Universitat Autònoma de Barcelona

Impact hazard associated with large meteoroids from disrupted asteroids and comets

Manuel Moreno Ibáñez

Impact hazard associated with large meteoroids from disrupted asteroids and comets

Manuel Moreno Ibáñez
Institut de Ciències de l'Espai (ICE, CSIC/IEEC)

Advisors: Dr. Josep Ma. Trigo Rodríguez
& Dr. Maria Gritsevich
Tutor: Prof. Dr. Jordi Mompart Penina

Universitat Autònoma de Barcelona
Departament de Física

A thesis submitted for the degree of

Doctor of Philosophy in Physics

Bellaterra, September 2018

Science is simply common sense at its best, that is, rigidly accurate in observation, and merciless to fallacy in logic.

— Thomas Huxley

ABSTRACT

Large meteoroid fragments disrupted from asteroids and comets may encounter the Earth along their orbits, posing extremely hazardous scenarios. Contemporary events like Chelyabinsk (2013), Carancas (2007) or Tunguska (1908) demonstrated that meteoroids in the diameter range of 1 to 100 m can devastate large areas and injure local population through the associated energetic blast, or even produce casualties due to localized crater excavation. Despite the relatively low frequency of these events, they have become a major concern within space agencies and other planetary defense initiatives which are currently developing impact mitigation tactics. This is in line with the growing popularity of this subject in the scientific community. The number of yet unresolved questions underlying the pre- and impact physics motivates the work carried out in this thesis. The study of meteoroids that encounter the terrestrial atmosphere provides valuable clues about their progenitors, their delivery mechanisms to Earth, and their ability to threaten our planet.

This thesis starts by exploring the complexity of meteoroid dynamics through two exceptional phenomena. On the one hand, a limited number of meteoroid dust trails detached from the comet 8P/Tuttle 620 years ago impact the Earth when the parent comet is in its aphelion, thus increasing the activity of the annual Ursid meteor shower. Aphelion-related increases in a meteor shower activity are uncommon and hence the Ursids offer a new perspective of orbital mechanics. On the other hand, meteorite falls, like Annama, can be orbitally linked to celestial bodies if their atmospheric trajectories are accurately recorded. Exploring these parental relationships offer the opportunity to overcome the uncertainties emerged from the short-term orbital evolution of near-Earth objects and ultimately predict future impacts.

The second part of this thesis focuses on the characterization of the atmospheric flight of a meteoroid. While up to-date re-entry models that account for the meteoroid ablation and fragmentation are common, no observational or modelling studies have resolved the intricacies associated with the mesosphere and lower thermosphere region for meteoroids travelling at hypersonic velocities and in rarefied gas flow conditions. This thesis presents the first observational validation of the flight flow regimes of centimeter-sized meteoroids and provides a new insight into the consequences for the meteoroid flight physics due to the generation of a shock wave. Meteoroid shock waves are also intimately related to the meteoroid energy deposition at different heights, which can alternatively be stated from the analysis of the terminal height of the meteoroid's trajectory. A new approach capable to predict the terminal heights is outlined in this thesis. The results show that, besides the great accuracy achieved, the calculated terminal heights are a valuable input to the derivation of atmospheric flight parameters. Furthermore, the approach taken provides a new way of classifying impacting meteor-

oids that improve previous classification scales.

Finally, a discussion of the implications of the previous analysis to impacting bodies of different sizes is carried out. Since Earth impacts by meter-sized or smaller bodies are more frequent, the study of sub-metric meteoroids provides a wide catalogue of events that can be crucial to understand the meteor physics. Being able to extrapolate the behaviour of these bodies to asteroid sizes can provide new clues on the underlying physics and make predictions concerning the degree of hazard associated with energetic events. The results of this work also provide feedback and an alternative approach to current and foreseen numerical simulations that were seen in the past essential to deal with these challenging encounters.

RESUMEN

El impacto de grandes fragmentos desprendidos de cometas y asteroides contra la Tierra puede llegar a ser muy peligroso. Recientemente, sucesos como Chelyabinsk (2013), Carancas (2007) o Tunguska (1908) han demostrado la capacidad que tienen los meteoroides con diámetros entre 1 y 100 m para devastar grandes extensiones y amenazar a la población local, ya sea mediante la liberación de energía en la atmósfera o el impacto en la superficie. A pesar de la baja frecuencia de este tipo de sucesos, la preocupación entre agencias espaciales y otras iniciativas de defensa planetaria es creciente, y ya están elaborando tácticas de mitigación ante posibles impactos. Este interés se extiende también en la comunidad científica. Además, el estudio de los meteoroides que impactan la atmósfera terrestre revela valiosa información sobre sus progenitores, los mecanismos que siguen para llegar a la Tierra, y su habilidad para amenazar nuestro planeta. Así, esta tesis tiene por objeto dar respuesta a una serie de interrogantes sobre la física asociada al impacto y a las condiciones pre-impacto.

Este trabajo comienza explorando aspectos complejos de la dinámica orbital de meteoroides a través de dos fenómenos excepcionales. Por un lado, la actividad anual de las Úrsidas aumenta cuando ciertos enjambres de meteoroides desprendidos del cometa 8P/Tuttle hace 620 años impactan la Tierra encontrándose el cometa en su afelio orbital. Los incrementos de actividad cuando el cometa está en su afelio no son comunes y por tanto las Úrsidas ofrecen nuevas claves sobre la mecánica orbital. Por otro lado, si la trayectoria atmosférica de un meteorito, como es Annama, se obtiene de manera precisa, éste se puede vincular orbitalmente con un cuerpo celeste. Dada la rápida evolución orbital de los NEA (considerados) posibles progenitores, este estudio nos permite acotar mejor sus órbitas y predecir futuros impactos.

La segunda parte de la tesis versa sobre la caracterización del vuelo atmosférico de un meteoroide. Los modelos actuales son capaces de considerar la ablación y fragmentación de un meteoroide en la atmósfera, pero aún no es posible comprender completamente, ni de manera observacional ni numérica, el vuelo hipersónico de un meteoroide en la región definida por la mesosfera y baja termosfera donde el gas se considera rarificado. Esta tesis presenta la primera comprobación observacional de los regímenes de vuelo para meteoroides centimétricos a estas alturas, y discute las consecuencias que origina la formación de una onda de choque en la física del vuelo del meteoroide. Además, las ondas de choque están íntimamente relacionadas con la energía depositada por el meteoroide a distintas alturas; magnitud que también se puede acotar conociendo su altura terminal. Así, esta tesis se ofrece también una nueva metodología para calcular estas alturas. Los resultados obtenidos son muy precisos y muestran que el cálculo de las alturas terminales es muy útil para derivar otros parámetros del vuelo del meteoroide. Es más, el planteamiento usado ofrece una nueva manera de clasificar los impactos de

meteoroides y mejorar escalas anteriores.

Por último, se discute la extrapolación de los estudios anteriores a cuerpos de diferentes tamaños. Aunque menos peligrosos, los impactos de cuerpos inferiores a 1 metro son los mas frecuentes y, en consecuencia, nutren las bases de datos y resultan fundamentales para abordar el estudio de meteoroides. La extrapolación de las conclusiones obtenidas previamente a objetos mas grandes puede revelar claves sobre la física subyacente y aportar nuevas predicciones sobre el riesgo asociado a impactos energéticos. Los resultados de esta investigación proveen también un enfoque alternativo al desarrollo de modelos numéricos, tanto actuales como futuros, que hasta hoy han sido fundamentales para afrontar el estudio de meteoroides.

ACKNOWLEDGMENTS

The research presented in this thesis was a result of team work. From the guidance of my directors to the daily support of my family, friends and girlfriend. Every tiny bit of positive encouragement, scientific lesson or understanding of my thesis obligations (that hindered weekend plans or special appointments) has contributed to the final submission of this work.

First, I am very grateful to my two directors, Dr. Josep María Trigo Rodríguez and Dr. Maria Gritsevich. I understand the difficulties of co-directing a thesis and so I appreciate your efforts to promote my learning on this fascinating field and to guide my work in a collaborative manner. I do also thank the support you gave me to temporally host my research in your institutes. These temporal stays were funded by the AYA 2011-26522 Spanish national plan research project, the Catalan Institute of Space Studies (IEEC), and by the project no. 260027 of the Academy of Finland, to which I gratefully acknowledge the support. Having such a wonderful couple (something like a mother and father) with such different profiles supporting my work has offered me the opportunity to learn a diversity of skills and to gain an insight into two alternative ways of seeing science and life. All I can say is Graciès! Спасибо!

Also, along these years I have been honoured by the generous and altruistic advice of other scientists. Particularly, I would like to express my deep gratitude to Esko Lyytinen, Dr. Elizabeth A. Silber, and Dr. Iwan P. Williams. Their availability at certain stages of this thesis have expanded my scientific grounds and have added a lot of value to our publications and my scientific career. I look forward to working with you soon. Similarly, I also appreciate the effort done by those meetings' LOCs that financially supported my attendance.

I also want to thank the welcoming received and the friendships made at my stays at ICE in Barcelona and at the FGI in Masala. I had a great time in both places and I enjoyed the afterwork activities we shared. I really improved my skills playing table games under the warm sun of Barcelona and trying to figure out my way out of a beautiful forest during orienteering competitions in Finland. I would specially thank Laura for being the one who involved me in all this PhD world, and the one helping me to complete my last steps. Also, and because I did not expect such amusement at that time, I am thankful of having met Luca, Bia, Angelina and Alba. You people made my couple of months in Helsinki awesome!

Two years ago, I joined a start-up company, Aistech Space. What was supposed to be a way of obtaining a daily income resulted to become the most amazing work experience I have ever had (and I have had a few...). Not only have I grown up as an engineer,

but I have meet outstanding people who is continuously supporting the achievement of my PhD degree. When it comes to the Space, I have always wanted to have a dual formation both in engineering and science, and Aistech Space is absolutely making that very easy.

Por último, siempre habrá un agradecimiento profundo a mi familia y amigos. A mi familia porque, aunque no terminan de tener muy claro en qué consiste mi investigación y por qué voy de un lado para otro, me lo han puesto siempre muy fácil y están siempre dispuestos a echar una mano. Muchos miembros de mi familia no están y esta tesis va dedicada a ellos, a mi abuelo porque me infundió la pasión por la lógica, a mi padre porque no escatimó un euro en darnos formación académica a ninguno de sus hijos, y al resto porque soy una persona equilibrada gracias a ellos. De otra parte, estoy muy agradecido con mis amigos del colegio porque hacen constantemente hincapié en "déjate de tesis y tonterías, y trabaja", y eso es su manera de decir "estás como un cencerro, pero vamos a flipar mogollón como lo consigas". Y al resto de amigos repartidos por el mundo porque entienden que no haya podido ir a verlos o dedicarles tanto tiempo especialmente durante la escritura de este documento. La lista seguro que está incompleta y extiendo mi agradecimiento a los olvidados.

Gracias a Mar, mi adorable novia, a la que este último año le he causado más inconvenientes que alegrías ¿Me quieres? A partir de ahora nos vamos de paseíto donde quieras.

CONTENTS

LIST OF FIGURES

LIST OF TABLES

1

INTRODUCTION

The impact of meteoroids with the atmosphere of the Earth, their ability to reach the ground as meteorites, and the associated source of risk to human beings is a serious issue that deserves a dedicated study. These objects consist of material that has detached from other bodies, mainly from minor solar system bodies like asteroids and comets, but also released from planetary bodies like the Moon or Mars. These bodies are defined according to the *International Astronomical Union* (IAU) definition as:

1. A *comet* is a body made of rock, organic compounds and ice, being typically kilometer-sized and orbiting the Sun. Comets usually go through the Solar System periodically, but some of them have extremely long orbits. A comet's tail is formed when the Sun's heat warms the coma or nucleus, which releases vapours into space.

2. An *asteroid* is a small and often irregularly shaped celestial body from one meter to less than 1000 km in diameter. Larger bodies are called planetary bodies.

3. A *meteoroid* is a solid natural object of a size roughly between 30 micrometers and 1 meter moving in, or coming from, interplanetary space.

4. *Interplanetary dust* is finely divided solid matter (basically tiny mineral grains), with particle sizes of few microns or less, much smaller than meteoroids, moving through interplanetary space.

Asteroids and comets are remnants of the formation of the solar system. In addition to being a valuable source of scientific information concerning the origin of our planetary system, these bodies are ultimately a potential threat to our planet, and humankind. Following various mechanisms, a wide variety of bodies ranging from sub-millimeter to kilometers in diameter are produced by collisional gardening (see e.g., Beitz et al., 2016). Once such fragments escape from the weak gravitational field of their progenitor they dynamically evolve towards shorter heliocentric orbits and evolve on time-scales of tens of millions of years through planetary perturbations (Williams, 1993; Jenniskens, 1998), and thermal forces: mostly radiation pressure and Poynting-Robertson drag (Williams, 2001). Thus, meteoroids can originate in asteroids or comets that may not intersect the heliocentric orbit of the Earth. Furthermore, collisions between large bodies against the surface of planets (i.e., Mars) or planetary moons, may have ejected (and continue to eject) new bodies into space, which stands as the main way by which pieces of the Moon or Mars are delivered to our planet (i.e., McSween & Huss, 2010; Moyano-Cambero et al., 2017). The hazard associated with these smaller pieces depends primarily on several parameters (Ceplecha et al., 1998; D'Abramo et al., 2001; Gritsevich et al., 2012): the impact velocity, the composition (including their density and porosity), their size, and the inclination of their orbit. Unlike prior epochs, nowadays the scientific community is better informed, with more detailed evidence

on the origin and statistics of suitably threatening sources. Furthermore, laboratories world-wide have large collections of meteorites, which have origins from various celestial bodies (Grady, 2000), as well as employing sizeable arrays of diverse instrumentation to continuously survey the sky. Through this, our knowledge on the vast amount of material from space that annually encounters our planet has expanded notably.

This Introduction addresses both the basics of meteor physics and the current state-of-the art so that the following chapters will be clearly understood in that wide context. Although the study of meteoroids can be approached from different points of view, the focus will be set on those items that show more evident links with impact hazard. Ironically, the term *disaster* has an etymologic origin on the Greek prefix *dis-*, which roughly means *bad*, and the word *aster*, meaning star or planet (for the people at that time any brilliant punctual light in the sky did not make much difference). Thus, in the context of this research, the word *disaster*, or *bad star* displays all its semantical meaning.

1.1 COMETS AND ASTEROIDS, WHERE THE RISK ORIGINATES

1.1.1 *Comets*

The first relevant source of meteoroids in the millimeter to centimeter-sized range are comets (Williams, 1993; Trigo-Rodríguez et al., 2013). These bodies populate large reservoirs in the limits of the solar system, where temperatures are lower and volatile elements remain in solid state. They predominantly originate in two delimited regions. At a distance of around 5,000 *astronomical units* (AU) it is believed that the *Oort cloud* extends approximately to 100,000 AU in a spherical distribution of icy debris where individuals are, on average, as separated one to another as the Earth is to Jupiter (Rickman, 2014, and references therein). This is the region where *long-period comets* (orbital period greater than 200 years) originate (Rickman, 2014, and references therein). Among them, it is remarkable the population of *Halley Type Comets* (orbital period shorter than 250 years, normally between 20 and 200 years) whose orbital period is proportional to that of Jupiter (this phenomenon is known as *resonance*), and are the source of several annual cometary material depositions on Earth (i.e., the Ursid meteor shower that will be addressed in Chapter 3 of this thesis). The resonance keeps this type of comets and their disrupted material away from other planetary perturbations temporally (Moreno-Ibáñez et al., 2017b). Therefore, their orbits do not vary much for larger times, the detached dust accumulates on the same orbit over multiple cycles, and the annual influx to Earth is more intense (Vaubaillon et al., 2005a,b). At a shorter distance, close to Neptune and between 30 and 55 AU, a disc-like region contains icy debris too. This region is known as the *Kuiper Belt* and it is the assumed origin of *short-period comets* (period between 3 and 20 years) known as *Trans-Neptunian Objects* (TNOs). The continuous disruption of TNOs produces smaller cometary bodies that cross the

orbits of giant planets and are the so-called *Centaurs*. Indeed, periodic comets are often pieces of larger ice-rich bodies stored in the Kuiper Belt or bodies scattered during the stage of planetary migration outwards (Sekanina, 1982; Trigo-Rodríguez et al., 2007; Trigo-Rodríguez & Williams, 2017). Although their orbits are quite stable, every now and then some of these bodies initiate their trip towards the Sun. Those comets that get trapped inside the orbit of Jupiter become part of the *Jupiter Family Comet* (JFC) type. JFCs tend to be retrograde, thus meteoroids originated in these bodies reach out the Earth at lower velocities (Jenniskens, 2006). They have their perihelia at Jupiter orbit and their orbits suffers from more planetary perturbations than TNOs. JFCs also periodically release material that reaches the Earth in the form of *meteor showers* (this term will be clearly defined later), and are suspicious of producing the fall of CI chondrites (Gounelle et al., 2006; Trigo-Rodríguez et al., 2015), whose bulk composition resembles that of the solar photosphere (Anders & Grevesse, 1989; Moyano-Cambero et al., 2017). Finally, other comets with no straight correlation to Jupiter's orbit penetrate the inner solar system and are prone to evolve to high inclination orbits. Dedicated literature describing the formation of cometary meteoroid swarms and streams can be found in Jenniskens (1998, 2006) or Vaubaillon et al. (2005a,b). For the following discussion note that a meteoroid *stream* is, as described by the IAU, a group of meteoroids with similar orbits and common origin, whereas a *swarm* is a group of meteoroids that results from the breakup of a larger body (Jenniskens, 2006).

As the comet reaches the orbit of Jupiter the solar irradiation increases, and its surface temperature rises. The immediate consequence is that the volatile components tend to evaporate and fine-grained dust components are released. Eventually, this forces the comet to lose material mainly due to the gas drag force that sweeps along other attached grains; or simply because as the evaporation process continues the local porosity increases, some grains become loose, and eventually detach (see for example Williams, 1993; Williams & Wu, 1993). Examples of this are the annual tiny cometary material streams that impact the Earth and cause meteor showers like the Leonids, the Ursids or the Perseids. Additionally, since comets are weak bodies composed of ices, dust and aggregates, they can fragment relatively easily, and so, a partial or complete disruption is possible (Jenniskens, 1998). Such a disruption may occur when the comet gets too close to a planet whose presence exerts gravitational tidal forces on the visitor(Hughes, 1994). It is then possible that meteoroid complexes that were produced by catastrophic disruption of comets may reach the Earth (Trigo-Rodríguez & Williams, 2017). Meteor showers can be also originated this way, examples of which are the Geminids, Phoenicids and Andromedids (e.g., Jenniskens & Lyytinen, 2005; Trigo-Rodríguez & Llorca, 2006; Trigo-Rodríguez et al., 2009b,c).

Once released from the parent body, the slightly different ejection velocity (Williams, 1993; Jenniskens, 1998) of the detached material, along with the solar radiation pressure, planetary forces, and the Poynting-Robertson drag change their orbital period and the particles can spread wide and along the orbit (Asher et al., 1999; McNaught & Asher, 1999; Asher, 2000; Lyytinen & Van Flandern, 2000; Vaubaillon, 2002). Particles released at roughly the same time tend to orbit in swarms (Vaubaillon et al., 2005a,b). Exception are those particles with sizes around 0.1 μm that will be ejected away by

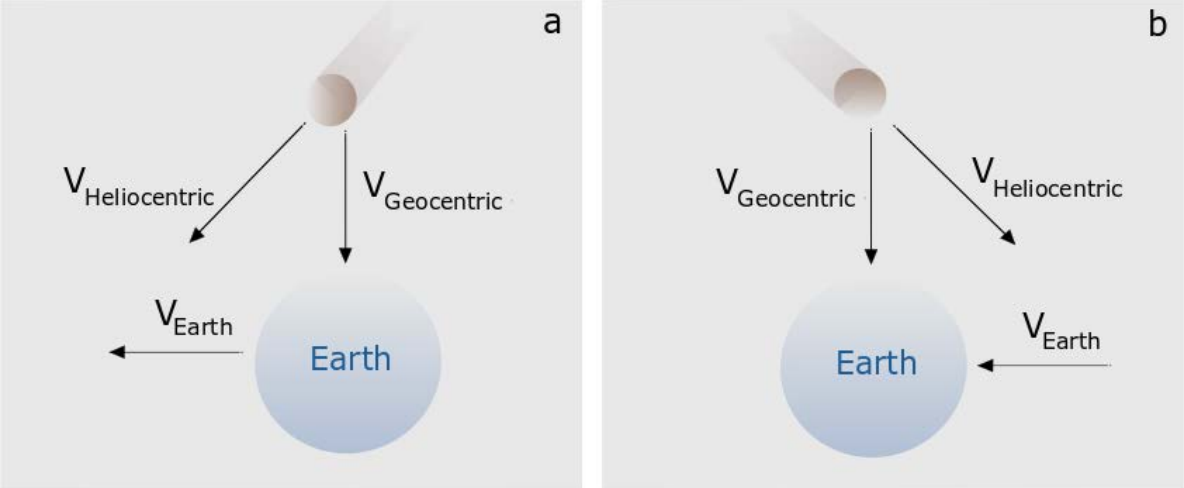

Figure 1: Geometrical encounter in two dimensions of a meteoroid and the Earth. The geocentric velocity results from: a) adding or b) subtracting the orbital velocity of the Earth ($\sim$ 30 km/s).

radiation forces (Wiegert et al., 2009). Those gravitational and non-gravitational effects alter the meteoroid swarm orbit in times that elapse from few years to thousands (Williams, 1993). Besides slight differences between the orbit velocity of the swarm members tend to spread the swarm along the orbit. With successive revolutions to the Sun these swarms are transformed into dust trails (e.g., Jenniskens, 1998; Vaubaillon et al., 2005a,b) Note that, as stated by Jenniskens (2006), the swarm cross section will not increase due to planetary perturbations, as these perturbations will affect all the swarm members in a similar level. The exact orbital distance from the Sun at which material can be detached from the comet depends on the properties of the comet and its orbit (Jenniskens, 1998).

The orbital evolution of the meteoroid swarm influences the impact velocities. Once a meteoroid is close enough to the Earth the velocity of the encounter depends on the configuration of the velocity vectors of both bodies (meteoroid and Earth heliocentric velocities) as shown in Figure 1. The resulting geocentric velocity (V_g) is also increased by the gravitational pull from the Earth. This effect slightly modifies the final entry velocity (V_e) by adding the escape velocity of the Earth. Consequently, the impact velocity may range from a free fall or Earth escape velocity, 11.2 km/s, to a parabolic orbital velocity (plus Earth movement), 73.1 km/s (Ceplecha et al., 1998).

The collision angle is quite diverse as the comet and the detached meteoroid swarms can arrive from a wide variety of orbital inclinations (Vaubaillon, 2003; Vaubaillon et al., 2005a,b). Since the Earth practically orbits on the ecliptic plane, the encounter with meteoroids shall occur when the meteoroids cross their orbital node, and these are located close to the Earth's orbit. When the Earth encounters a meteoroid swarm, the number of meteoroids that impact the Earth in a short time increases notably. The interaction between a meteoroid and Earth's atmosphere causes a luminous phenomenon called a meteor, and thus meteor showers are a celestial phenomena in which an increasing meteoroid impact activity is observed to radiate, due to the perspective in which

they are seen from the ground, coming from a conspicuous region in the sky called radiant. The major annual meteor showers are arranged in Table 1.

As discussed previously, most of the major meteor showers listed in Table 1 are originated in stable Halley Type Comets or trapped Jupiter Family Comets. However, two of these meteor showers, the Quadrantids and the Geminids, are associated with asteroids. Actually, asteroid 2003EH belongs to the 96P/Machholz complex (Abedin et al., 2018), which is thought to be the remnants of a larger comet breakup. As for asteroid 3200 Phaeton, it has been orbitally linked to the larger asteroid 2 Pallas (de León et al., 2010; Jewitt, 2012). It is also worth noting that the parent body of the Ursids, comet 8P/Tuttle, has a very short period and its considered an interloper within the Jupiter Family Comets (see Chapter 3).

Given the larger entry velocities and fluffier compositions of cometary meteoroids, the probability that they can survive the increasing atmospheric drag and the associated ablation phenomenology is very low (Blum et al., 2006; Trigo-Rodríguez & Blum, 2009a). Additionally, there is abundant evidence for the tendency of these meteors to burn out at high altitudes corresponding with a loading pressure of about 10 Pa (Trigo-Rodríguez & Llorca, 2006, 2007). Despite this, the observation and study of cometary meteors (and principally meteor showers) is crucial to unravel both the disposal mechanisms that occur when comets approach their orbit perihelion (see for example, Trigo-Rodríguez et al., 2007; Madiedo et al., 2014), the delivery of metals and condensates as a product of ablation into the upper atmosphere (Trigo-Rodríguez et al., 2003; Jenniskens, 2004b), and the dynamic mechanisms regulating their orbital evolution over time (Vaubaillon et al., 2005a,b).

1.1.2 *Asteroids*

Asteroids are either remnants of the original formation of the rocky planets, or large pieces of disrupted comets or asteroids. Unlike comets, asteroids do not usually preserve large deposits of volatiles and, thus, generally they do not show any activity. They also show relevant differences in their composition (chemical and mineralogy) and porosity (see e.g. Rietmeijer, 2000). The vast majority of the asteroid population is hosted in the *main asteroid belt* (MAB) located between 2 and 4 AU, that is, between Mars and Jupiter. According to their orbital characteristics, asteroids are classified in family groups, which represent a group of bodies that populate orbital regions where the density of asteroids is notable larger compared to the local background. Thus, the current registered family list may vary with time and new families can be outlined (Delbo' et al., 2017). As the collisions in the mean asteroid belt are relatively common, these families usually consist of the smaller bodies derived from larger asteroid breakups (Michel et al., 2002). Note that these impacts can either break, alter the orbit, or merge bodies, being also the source of delivery of small asteroids to the Earth's vicinity due to transportation mechanism that are outlined below.

Meteor Shower	Typical Activity	ZHR	Solar	Radiant		V_g		Orbital Elements						Parent	Type	References
			Longitude	RA	Dec.		Epoch	q	e	i	ω	Ω				
Quadrantids	Dec 28 - Jan 12	110	283.0	230.2	+49.5	40.7	J2000	0.979	0.690	71.05	171.2	283.3		2003EH	Asteroid	[6]
Lyrids	Apr 14 - Apr 30	18	32.0	272.0	+33.4	46.7	B1950.0	0.920	0.990	80.00	214.0	32.0		C/1861 G1 (Thatcher)	LPC	[1], [2]
η-Aquariids	Apr 19 - May 28	50	46.0	338.1	-0.8	65.7	B1950.0	0.568	0.938	163.80	95.6	43.9		1P/Halley	HTC	[1]
Southern δ-Aquariids	Jul 12 - Aug 23	25	128.0	341.3	-15.7	41.3	B1950.0	0.080	0.970	27.00	151.0	308.0		96P/Machholz	HTC	[1], [2]
α-Capricornids	Jul 03 - Aug 15	9	127.0	306.5	-9.2	23.0	J2000	0.602	0.921	7.68	266.7	128.9		169P/NEAT	JFC	[7], [9]
Perseids	Jul 17 - Aug 24	100	140.0	48.2	+58.1	59.1	B1950.0	0.950	0.950	113.10	150.3	138.3		109P/Swift-Tuttle	HTC	[1], [2]
Southern Taurids	Sep 10 -Nov 20	5	216.0	47.9	+12.8	26.6	J2000	0.352	0.825	5.40	115.4	37.3		2P/Encke	JFC	[3]
Orionids	Oct 02 - Nov 07	20	209.0	95.9	+15.7	66.3	B1950.0	0.570	0.970	164.00	83.0	29.0		1P/Halley	HTC	[1],[2]
Northern Taurids	Oct 20 - Dec 10	5	220.0	48.9	+20.7	28.0	J2000	0.350	0.832	3.10	294.9	226.2		2P/Encke	JFC	[3]
Leonids	Nov 6 - Nov 30	15	235.0	153.8	+21.8	70.2	J2000	0.986	0.897	162.70	174.7	236.6		55P/Tempel-Tuttle	HTC	[1], [5], [8]
Geminids	Dec 04 - Dec 17	120	262.0	113.2	+32.3	33.8	J2000	0.141	0.897	24.00	324.4	261.5		3200 Phaeton	Asteroid	[1], [7]
Ursids	Dec 17 - Dec 26	10	271.0	219.9	+75.4	32.9	J2000	0.944	0.795	51.50	204.9	270.6		8P/Tuttle	HTC	[4]

Table 1: Major Meteor Showers : (1) Meteor shower name; (2)-(3) Expected activity period and Zenith Hourly Rate (see the description in Chapter 3) for the year 2018 by the International Meteor Organization (IMO) following the guidelines in Rendtel et al. (1995) ; (4)-(5)-(6) Last solar longitude and radiant information (in [^{o}]; J2000) published according to the IAU Meteor Database: *https://www.ta3.sk/IAUC22DB/MDC2007/*; (7) Last published geocentric velocity, V_g in [km/s] (IAU Meteor Database); (8)-(13) The orbital elements of the average meteoroid pre-atmospheric orbit; (14)-(15). The associated celestial parent and its type: Long Period Comet (LPC), Halley Type Comet (HTC), Jupiter Family Comet (JFC) or Asteroid; (16) Orbits' references: [1] Neslušan et al. (1995), [2] Jopek et al. (1999), [3] Porubčan & Kornoš (2002), [4] Jenniskens et al. (2002) [5] Trigo-Rodríguez et al. (2004b), [6] Jenniskens (2004a), [7] Jenniskens (2006), [8] Jenniskens et al. (2008), [9] Jenniskens & Vaubaillon (2010).

There are several mechanisms that are behind the transportation of material from asteroids to the Earth. Due to gravity perturbations from the larger planets, most of the asteroid population is located at low inclinations. The gravitational influence of Jupiter and Saturn also depletes the asteroid population at those orbits where there exist resonances with these planets. These regions within the mean asteroid belt, called *Kirkwood gaps*, become escape routes toward inner planet-crossing orbits. These perturbations along with the Yarkosky effect are the driven mechanisms that feed the planet crossing orbits of the *Near Earth Object* (NEO) population (Bottke et al., 2002; Morbidelli et al., 2002; Morbidelli & Vokrouhlický, 2003; Granvik et al., 2016). The general term NEOs refers to those bodies with perihelion distances (q) located at < 1.3 AU. Typically, most NEOs are asteroids and so they are often referred to as *Near Earth Asteroids* (NEAs). Note that, since extinct comets or fragments of them are more difficult to identify, there could be a bias in the registered population of *Near Earth Comets* (NECs) compared to NEOs (Trigo-Rodríguez & Williams, 2017). Also, Granvik et al. (2016) observed a notable imbalance in the population of low albedo NEOs compared to those with high albedo in those orbits closer to the Sun. According to Granvik et al. (2016), as the perihelion distance of the NEO approaches a few tens of solar radii, the object undergoes a catastrophic breakup. The limiting value of the perihelion for low albedo NEOs is further from the Sun, and so their population is reduced at orbits closer to the Sun. These objects will be destroyed due to thermal effects (see for example Delbo et al., 2014). Asteroids that cross the Earth's orbit and have a size larger than 140 m can pose a serious hazard to Earth; these are classified as a *Potential Hazardous Asteroid* (PHA). A detailed description of the current NEOs groups can be found at the JPL website (*https://cneos.jpl.nasa.gov/about/neo_ groups.html*).

The question of whether NEAs could be a source of meteoroid streams that reach the Earth is a popular topic of research nowadays (see for example: Halliday, 1987; Jenniskens, 2006; Trigo-Rodríguez et al., 2007; Tóth et al., 2011; Borovička et al., 2015a; Trigo-Rodríguez & Williams, 2017). For instance, the Taurid complex, which causes several annual meteor showers (i.e., Northern and Southern Taurids in Table 1), is believed to have originated from a large comet that disrupted completely, giving rise to other minor asteroids and comets (Spurný et al., 2017b). Also, the orbit similarity to some recovered meteorites supports this idea (see Borovička et al., 2015a, and references therein).

Unlike meteoroid streams, sporadic meteoroids that have been formed by one-time collisions between asteroids or asteroids and other meteoroids can find their way to our planet. The time scale between the parent detachment and the collision with Earth is a minimum of hundreds of millions of years. During this time meteoroids lose their orbital coherence (Pauls & Gladman, 2005). The dynamic evolution of asteroid material is fast compared to the evolution of cometary dust. The mechanisms that dominate that evolution are described elsewhere (see Williams, 1993, 2001). Provided that the final pre-impact meteoroid orbit perihelion is located at a maximum in the mean asteroid belt, and that most of these orbits have low inclinations (close to the ecliptic plane), the impact velocities of these meteoroids shall be lower than that of the cometary meteoroids. Hence increasing their chances of surviving the aggressive interaction

with the Earth's atmosphere. These meteoroids are commonly the main source of fully unexpected meteorite falls (Trigo-Rodríguez et al., 2015).

The higher strength and increasing compaction associated with thermal metamorphism of asteroidal meteoroids (Trigo-Rodríguez & Blum, 2009a) also increase their chances to survive atmospheric entry. However, some recovered meteorites might be linked to a cometary origin. With the right circumstances, quite low strength meteoroids are able to survive atmospheric ablation and produce meteorite falls like the un-grouped carbonaceous chondrite Tagisk Lake (Brown et al., 2002b). For instance, the pre-atmospheric orbit from historical data of the Orgueil meteorite suggests a link to the Jupiter Family Comets (Gounelle et al., 2006). Although the orbital parameters of Orgueil, especially the aphelion distance, may vary slightly due to the rather large inaccuracy on the reported atmospheric entry velocity, the proposed origin seems to be in agreement with its composition. Orgueil's CI composition classification might be similar to the chemical composition of comet Halley's dust (Campins & Swindle, 1998). Another possible relationship of this kind is the one claimed by Trigo-Rodríguez et al. (2009c) regarding the comet Metcalf C/1919 Q2 and a swarm of meter-sized *meteorite-droppers* that produce meteorite falls. (this term will be described later). Additional evidence has been recently compiled that claims a connection between fragments of this comet and the fall of H/L chondrites (Trigo-Rodríguez & Williams, 2017). While these studies do not provide strong evidence because of the rarity of these meteorite falls and the absence of recordings capable of obtaining precise orbital data, continuous suggestions and studies on this regard will eventually lead to the recovery of meteorites with comet origins. This might ultimately imply a new impact hazard scenario, given the larger range of inclinations of cometary orbits.

Given the existence of mutual collisions in the Main Asteroid Belt, plausible breakups due to planetary approaches, long solar exposures, and continuous asteroid collisions, the composition of asteroids is not unique. If an association between a recovered *meteorite* and an asteroid is possible, then a detailed laboratory analysis will provide some clue on the physical properties of the asteroid (e.g., Wilkison & Robinson, 2000). As this association is rare, the study and comparison of meteorite surface reflectance (e.g., Trigo-Rodríguez et al., 2014) and reflected spectra of asteroids (Chapman et al., 1975; Gaffey et al., 1993; DeMeo et al., 2009, and references therein) are used to point out possible relationships and feasibly infer mechanical properties of the asteroids (Moyano-Cambero et al., 2017). However, it has been observed that meteorites exhibit higher bulk densities than their parent asteroids and show a bias towards the higher strength materials (Trigo-Rodríguez & Blum, 2009a). Asteroids tend to show lower densities, and this is associated with larger macroporosities (Britt et al., 2002). This also has an effect on other physical properties (e.g., the thermal conductivity, the strength, etc.; see for example Meier et al., 2017).

1.2 ATMOSPHERIC INTERACTION: METEORS, FIREBALLS AND METEORITES

The hypersonic encounter between meteoroids and the Earth's atmosphere occurs for different meteoroid sizes that may range from a few tens of microns to tens of meters in diameter (Hughes, 1994). Generally speaking, as the meteoroid reaches lower atmospheric layers the aerodynamic loading is more intense, and the braking it experiences is more abrupt. Also, the thermal and molecular collisional processes that ultimately imply a severe mass loss become gradually more efficient along the descending path. The complete phenomenology is called *ablation* and during this phase there is an associated emission of light that enables the visual observation of meteoroids from the ground; namely a *meteor*. At high altitudes the first atmospheric molecules provoke sputtering (Vinković, 2007), a process that removes and ionize the atoms in the meteoroid surface. Extensive meteoroid vaporization starts when the surrounding vapour temperature cloud increases at around 2500 K, which is usually over the vaporization temperature of rock-forming minerals (see Chapter 4; Bronshten, 1983; Ceplecha et al., 1998). At lower altitudes with the increasing air density, air friction becomes more relevant, and the sudden deceleration turns into fragmentation and heat that melts the external layers of the meteoroid. According to Yomogida & Matsui (1983) if the meteoroid is able to survive the atmospheric flight, the thermal effect of the heat will not get deeper than 0.3 centimeters in the resulting meteorite (Trigo-Rodríguez, 2012). Besides, if the meteoroid structure does not comply with certain strength premises the intensive dynamical loading may fragment the body (Popova et al., 2011; Trigo-Rodríguez & Llorca, 2006, 2007) that can continue ablating separately. Note though, that fragmentation may also take place due to thermal processes (Borovička et al., 2015a).

The study of meteor fragmentation is compelling and current mathematical approaches find difficulties in correctly representing the physical behavior. In two cases the mathematical approach is simpler: either when the fragmentation takes place at well-defined and observed points along the meteoroid trajectory, or when the fragmentation of small grains is more or less a continuous process. The former is known as *progressive fragmentation* (Babadzhanov, 1991), whereas the latter is referred to as *quasi-continuous fragmentation* (Revelle, 2002). The fragmentation model developed by Ceplecha & Revelle (2005) accounts for these two scenarios when observations are available. Note that this fragmentation model includes a set of free parameters that may be assumed or estimated and, consequently, it does not lead to a unique interpretation of the results.

Given the different ability of each meteoroid to penetrate deeper in the atmosphere and the intensity of its luminosity, a sub-seeded meteor classification is established. Typically, the brightness magnitude of a *fireball* or *bolide* reaches or overcomes that of Venus (-4). Very bright fireballs are generally able to get to much lower altitudes and can emit a continuous very bright light, at mid-way between the luminosity of the Moon and the Sun (absolute magnitude -16 or brighter). Such bright fireballs are named *superbolides* and can be observable at distances of more than 700 km (see e.g. Ceplecha et al., 1998; Trigo-Rodríguez et al., 2009a; Brown et al., 2013b). Once the

meteoroid is no longer subjected to ablation, the single body or fragments of it that do not disintegrate enter their last leg of the descending flight path, the *dark flight*, which is generally ruled by a nearly ballistic trajectory (Gritsevich et al., 2014; Vinnikov et al., 2016). Note that, when the meteoroid velocity is about 3 km/s, the thermal ablation is over (Borovička et al., 2015a). Meteoroids that partially survive their atmospheric flight and hit the Earth's surface are called *meteorites*. Ceplecha et al. (1998) stated that maximum entry velocities of 30 km/s are required to survive the ablation, which is in line with recorded meteorite falls to date (see Chapter 3). This limit is however under discussion (Borovička et al., 2015a) as the entry velocities of the recovered Maribo ($V_e \sim 28.5$ km/s; Haack et al., 2011) and Sutter's Mill ($V_e \sim 28.6$ km/s; Jenniskens et al., 2012) meteorites are close to that limit. Figure 2 illustrates the concepts of meteoroid, meteor, fireball and superbolide. The term *meteorite-dropper* is often coined to indicate those superbolides that may be followed by a meteorite fall.

Finally, micrometer dust particles orbiting in space may interact with the atmosphere at low velocities. If they are smaller than several hundredths of a millimeter, they can be decelerated at high altitudes before the initiation of the evaporation processes (Ceplecha et al., 1998). Consequently, these particles may survive to atmospheric deceleration with partial or no surface melting at all, and can be deposited on the ground as *micrometeorites* (Engrand & Maurette, 1998).

It has been estimated that less than 3% of the incoming (pre-atmospheric) mass can survive as meteorites (Ceplecha et al., 1998). Although it is complicated to estimate the total meteoroid mass influx on Earth, the data gathered using different observational methodologies has constrained this number owing to the size of the impacting body. Relevant studies on this regard are for example: Rabinowitz et al. (2000); Brown et al. (2002a); Ortiz et al. (2006); Silber et al. (2009); Brown et al. (2013b); Borovička et al. (2015a). These studies show a clear agreement in that a power law adjusts the annual flux with the diameter of the body, and that meter-sized bodies impacts, with the ability to become a meteorite, are less common.

Since meteorite falls could be unnoticed, when a reliable meteor observation linked to a meteorite exists, a more accurate insight on the processes that occur during the atmospheric flight is possible. This ultimately may derive in a better knowledge on the disruption mechanisms that took place when the meteoroid detached from its parent body, and its path towards its encounter with Earth. As will be detailed in Chapter 3, the number of recovered meteorites for which its atmospheric flight was observed is small. For one of these events, namely Annama (Trigo-Rodríguez et al., 2015), Chapter 3 of this thesis will outline the procedure that was followed to identify a suitable parent according to the pre-atmospheric orbit of the meteoroid. Conversely, unnoticed meteorite falls can be collected either by specific recovery campaigns or occasional finds. Up to date, the current meteorite collection contains 76,500 specimens (including provisional names, and according to The Meteoritical Bulletin Online Database: *https://www.lpi.usra.edu/meteor/*).

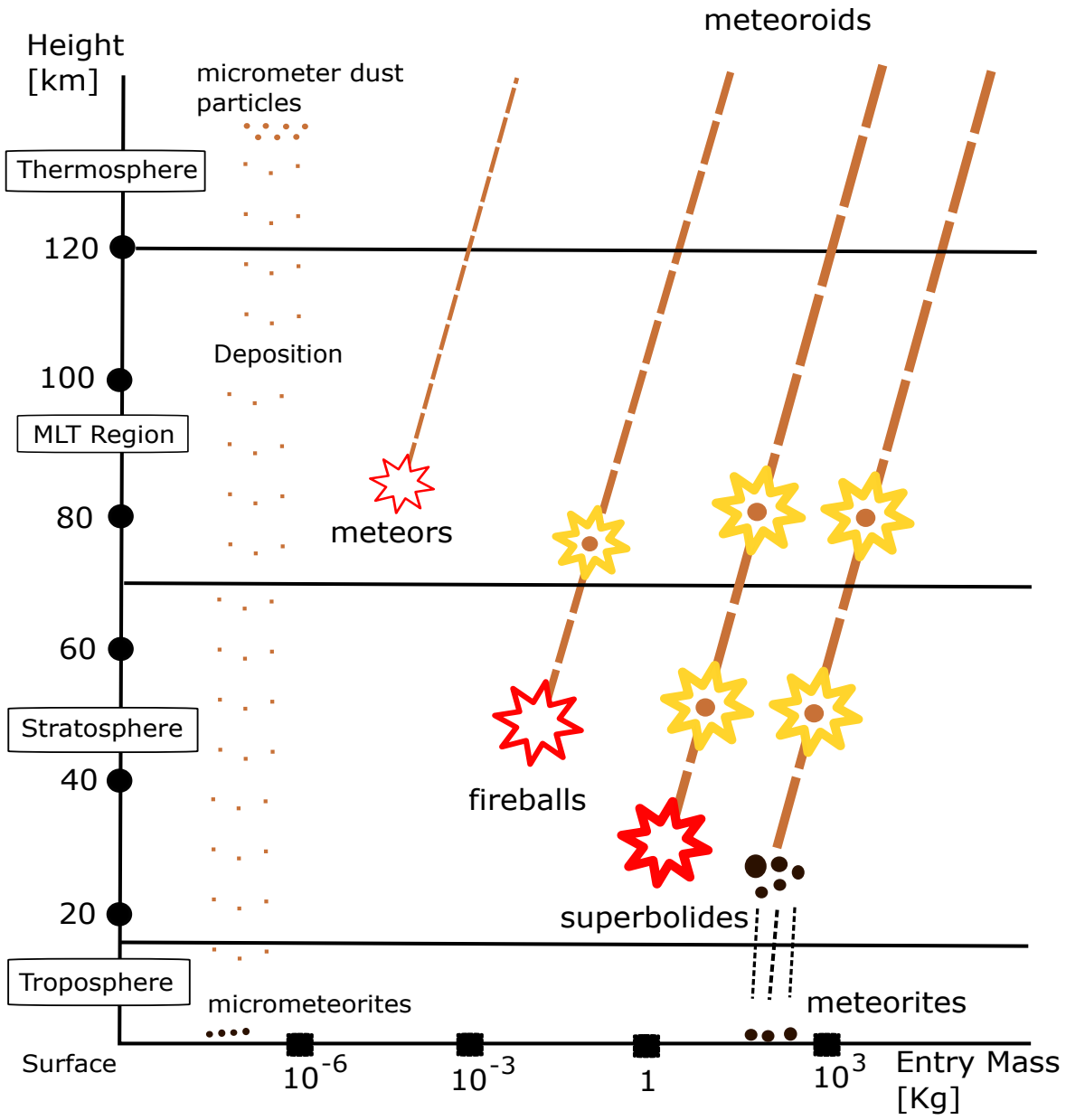

Figure 2: Graphical description of *meteoroids*, *meteors*, *fireballs*, *superbolides*, *meteorites* and *micrometeorites*. Figure adapted from Rendtel et al. (1995) and Trigo-Rodríguez (2012). MLT stands for the mesosphere and lower thermosphere region of the atmosphere.

Meteorites are classified owing to their petrology, which indicates their origins in differentiated (chondrites), or undifferentiated bodies (achondrites, iron and stony meteorites). While more details can be found in the extensive literature (Van Schmus & Wood, 1967; Brearley & Jones, 1998; Huss et al., 2006; Weisberg et al., 2006; Rubin et al., 2007; Martínez-Jiménez et al., 2017; Palme & Zipfel, 2017), for this thesis it will be more interesting to accurately constrain the bulk density of the meteoroid, which is quite well known for chondritic stones that dominate meteorite falls (Britt & Consolmagno, 2003; Macke et al., 2011). Although detailed and bulk compositions are intimately related, the range of meteoroid bulk densities is bibliographically constrained to between 270 kg/m^3 and 7000 kg/m^3 (Ceplecha & McCrosky, 1976).

For those meteors that disintegrate in the atmosphere, the study of their properties is done via the analysis of certain parameters retrieved from the observations. One of the earliest studies that exemplifies this issue was carried out by Ceplecha & McCrosky (1976) using a sample of 232 meteors that were observed using the most accurate techniques at that time. The orbits and the atmospheric trajectories of these meteors were derived, and further classification carried out. Ceplecha & McCrosky (1976) outlined a meteor classification based on several meteor atmospheric trajectory parameters: the terminal height (the last point of the atmospheric luminous path), the estimated meteor bulk density, and the orbit inclination, semi-major axis and eccentricity. Furthermore, they defined a classification parameter, namely PE, which ranked the meteor according to its entry mass, velocity, terminal height and zenith angle. Although this will be addressed in depth in Chapter 5, it is interesting to note at this point that Ceplecha & McCrosky (1976) stated that most of their sample consisted of cometary meteors. This is because at that time, it was quite challenging to state that fluffy bodies might have their origin in asteroids. Also, because as already mentioned, it is usually more complicated to relate dynamically the orbit of a meteor to that of an asteroid provided the planetary complex mixture of gravitational and non-gravitational effects that asteroids and their disrupted meteoroids suffer during their orbital lifetime.

1.3 THESIS GOALS AND OUTLINE

The aim of this thesis is to extend our current knowledge of the physical and dynamic properties of large meteoroids during and before their interaction with the Earth's atmosphere. The conclusion derived from this study shall serve a twofold purpose. On the one hand, the results shall help to set constraints on the hazard associated with the interaction between these bodies and the Earth. On the other hand, the following chapters will propose alternative means to delve into meteoroid dynamical properties that shall enhance future studies of these problems.

The introductory overview has provided a wide understanding of the general scenario and the associated phenomenology in a scientific field that still offers a lot of unexplored opportunities. More details will be described in detail in the following chapters, along with the implementation of new reliable methodologies and techniques to tackle meteor

physics problems.

This thesis is organized as follows:

- *Chapter 2*: provides a summary of the state-of-the art of the available instrumentation for meteor recording and the common data reduction procedures that are applied in following chapters. From naked eye observation to specialized equipment allocated in satellites, the data gathered shall be correctly processed by specific techniques (i.e. astrometry) that enable the calculation of trajectories and orbits through adequate mathematical models.

- *Chapter 3*: presents the results of the observation campaign of the expected outburst of the annual Ursid meteor shower. It is presented as a case study to understand the orbital evolution of cometary material before encountering the Earth.
  Besides, the observation and recovery of the Annama meteorite provide enough information to relate this meteorite with a feasible asteroid parent. The second part of this chapter is devoted to explain how to apply a methodology to finding such relationship. The orbital evolution of meteoroids detached from asteroids requires the use of simulations, an understanding of celestial mechanics, and valid assumptions to claim such a relationship.

- *Chapter 4*: proves how efficient the combination of infrasound and visual observations are to provide relevant clues on the properties and flight dynamics of meteors along their atmospheric flight. The study of a centimeter-sized meteor data set that generates shock waves at high altitudes is used to get the first observational evidence of the Knudsen number and flight flow regimes for these bodies.

- *Chapter 5*: focuses on the last bright point of the meteor atmospheric trajectory. The velocity, height and mass at this point are very relevant to gain comprehension on: (1) the pre-atmospheric properties of the meteoroid; (2) the flight dynamics; (3) and on the subsequent dark flight if the meteoroid is able to survive the ablation. It will be shown that the use of a recently introduced mathematical methodology to study meteors can decipher most of those parameters using either only the terminal height, or a combination of the terminal height with a couple of other observed parameters.

- *Chapter 6*: discusses the implications of the studies and conclusions of the previous chapters for impact hazard considerations. The risk posed to the Earth by large meteoroids depends on the physical properties of the meteoroid, on its impact configuration, and on the probability of future encounters between our planet and meteoroids of different sizes.

The last chapter is devoted to the conclusions that can be gathered after all the previous work, and suggestions of suitable future work that shall be undertaken to expand the current knowledge on subjects related to this thesis.

2

METHODS AND MODELS

2.1 INTRODUCTION

The trip of a meteoroid through the atmosphere is fast and generous in terms of the physical phenomenology triggered. According to the meteoroid properties and its flight configuration, the behavior could diversify significantly. The previous chapter outlined the main differences in terms of atmosphere penetration and survival between asteroid and cometary material. With the purpose of providing both, a complete understanding of the physics involved and unmasking possible unnoticed meteoroid encounters, the strategies and detection techniques are continuously evolving. In this chapter a general description of these techniques is provided. Likewise, a brief summary of the astrometric procedure applied to deal with photographic and video cameras is presented. Finally, the last part of this chapter caters for a synopsis of the three current mathematical approaches that allow meteor flight trajectory modelling.

2.2 METEOROID FLIGHT DETECTION TECHNIQUES

The physical phenomena revealed during the meteoroid atmospheric flight make the Earth atmosphere the largest sensor available to spot these events. The implementation of adequate techniques helps understanding the different phenomenology taking place. The direct naked eye observation is not only the oldest and more intuitive technique, but the one that has provided the best results to determine the intensity of meteor showers. The human eye is sensitive up to a stellar magnitude of +6. To enhance that sensitivity, additional equipment like binoculars and telescopes become useful for the observer. In this regard, it is worth mentioning the classical handling of Super-Schmidt cameras that were first introduced in the mid 50's (Jacchia & Whipple, 1956). These telescopes were especially suitable for very large fields of observation and removed the spherical aberrations from the optics using a correcting plate, thus becoming a powerful instrument for that time in meteor science. Although telescopes permit detection of faint meteoroids of about +11 limiting magnitudes, the field of view is too narrow, which ultimately hinders the detection of meteors and complicates the determination of their complete trajectory in the atmosphere. The use of wide-field automated photographic devices promoted extended observation campaigns and even more elaborate current techniques for meteor observations, such as international airborne campaigns (Vaubaillon et al., 2015) and possible future space-based monitoring systems (Bouquet et al., 2014). Nowadays, the advances in optical materials and surface polish-

ing, as well as the evolution of CCDs and CMOSs sensors, allows photographic cameras detecting limiting magnitudes between +3 and +5 (Madiedo & Trigo-Rodríguez, 2008; Kingery & Blaauw, 2017). One relevant asset associated with this technique is the inclusion of a controlled rotating shutter on all-sky CCD cameras (Trigo-Rodriguez et al., 2008), so the apparent path of the meteoroid is automatically chopped, and the accurate velocity of the meteoroid through the luminous trajectory can be derived. From this information, it is quite straightforward to derive the discrete meteoroid times, heights and velocities along its luminous flight. The new improvements on video cameras and their associated techniques allow the detection of larger volumes of faint meteoroids (standard video systems with zoom lenses can achieve a limiting magnitude between +7 and +9), and the meteoroid trajectory determination. Installing a video system is not complicated, and it can be fully operated automatically. Retrieving the desired information from the video frames is more compelling than when photographic data are in use. Fortunately, the current methodologies permits partial computational implementation, so data-retrieving tasks become easier. The main drawback of video systems is, paradoxically, their great sensitivity (Madiedo & Trigo-Rodríguez, 2008; Borovička et al., 2015a). While this property allows the detection of faint meteors (typically those belonging to meteor showers), brighter events, such as bright fireballs, may saturate a relevant number of the detector pixels. Note that nowadays most electronic devices (i.e., mobile phones) include a camera. While the information registered by these devices could be very valuable (i.e., Brown et al., 2013b), new techniques for calibrating the images are required (Lyytinen & Gritsevich, 2016).

Photographic cameras and video systems can be adapted to obtain meteoroid spectra and light curves. Wide band passes allow the panchromatic study of the energy released by the meteor in form of light. The analysis of the light curve provides valuable clues in terms of meteor motion and mass. The usual way of proceeding, as it will be described later in this chapter, consists of assuming negligible meteor deceleration and a fixed value of luminous efficiency, a parameter that relates the integrated emitted light to the kinetic energy of the object (Ceplecha et al., 1998). Although a large amount of studies relies on this approach, the results tend to overestimate the real mass of the meteoroid. It is therefore more convenient to combine this information to the astrometric observations of the event. On the other hand, narrow band filters are introduced in spectrometric studies to decipher the presence of meteoric elements that evaporate during the re-entry. Spectrometry techniques are generally implemented when the meteor wake and train are studied. The temperatures at the rear part of the meteor reach the local equilibrium and interpreting the observed spectra is more evident (Borovicka, 1993, 1994; Trigo-Rodríguez et al., 2003, 2004c; Berezhnoy & Borovička, 2010; Silber et al., 2017).

Meteors can also be detected using radio techniques (i.e., Simek, 1985; Šimek & Pecina, 2002; Madiedo et al., 2014). Radio forward scattering is the most common radio application (Ceplecha et al., 1998), which relies on detecting the radio signal emitted from a distant source (about hundreds of kilometers away). The signal would not be detected unless it reflects from the ionized trail of a meteor. The noticeable advantage of this technique is that it allows the detection of a larger number of meteors. The disadvant-

age is that, as the ionization is more intense at higher altitudes, there is a bias towards fast meteors that disintegrate soon and high in the atmosphere.

Other indirect means of retrieving information from meteors are mainly focused on the by-products of the energy released. The hypersonic velocities associated with the meteoroid atmospheric flight may eventually cause a shock wave in front of the meteor (Silber et al., 2017). For those bolides able to penetrate deep into the atmosphere, the largest part of the energy release occurs at low altitudes where the body could fragment violently and release energetic waves (blast waves) that may propagate down to the Earth surface. In fact, many large bolides end up with sudden fragmentations (Trigo-Rodríguez & Llorca, 2006; Trigo-Rodríguez & Blum, 2009a). If so, infrasound stations can detect the blast (Revelle, 1974; Brown et al., 2007; Silber & Brown, 2014) while seismic stations can record the ground shaking (i.e., Ben-Menahem, 1975; Llorca et al., 2005; Tauzin et al., 2013; Brown et al., 2013b; Tapia & Trigo-Rodríguez, 2017). These measurements support the understanding of violent events where no visual observations are available and/or allow gaining insight into complex fireballs associated with daylight meteorite falls where the astrometry is more complicated (i.e., Llorca et al., 2005; Trigo-Rodríguez et al., 2006; Brown et al., 2013b). In general, bolides move very fast and the overpressure due to the shockwave propagates as inaudible low frequency pressure waves (< 20 Hz) called infrasound. A theoretical approach to the meteor infrasound analysis assuming some premises, like direct arrivals, was developed by (Revelle, 1974, 1976), and was successfully implemented by Silber et al. (2015). There are, however, two main limitation to these two detection techniques. On the one hand, the maximum distance at which the signal stems from. Several atmospheric and geological phenomena dissipate the signal and reduce notably the quality of the signal to noise ratio. On the other hand, when several events take place in short time lapse, a visual observation counterpart is required to link each detection to each individual meteor. This is for example the case of using infrasound techniques during meteor showers.

As the industry and technologies of nanosatellites (i.e., standard CubeSats) moves on it is quite likely that the deployment of a devoted low-cost meteoroid monitoring satellite constellations will eventually become a reality. Indeed, military (Brown et al., 2002a) and science satellite (i.e., Rieger et al., 2014) payloads and subsystems have historically detected the meteor phenomena. In this line, new instrumentation and concepts of operation have been proposed (i.e., Bouquet et al., 2014) . In addition, the rise of new space business models, like asteroid mining, is promoting the apparition of companies demanding information on asteroid properties. Therefore, the interest in meteor science is gradually increasing and, if properly supported, this field will grow significantly over the next decades.

The combination of the techniques described above provides a more complete picture of the interaction between a meteoroid and the atmosphere. Provided the range of meteoroid geocentric entry locations on the sky and flight configurations, one single type of observations from one specific spot will limit the potential quality and quantity of the observations. For example, in order to accurately determine the trajectory of a meteor

using video systems, at least the combined information of two observation stations is required (Ceplecha et al., 1998). Note though that there exist notable discrepancies when the meteor phenomena are studied by coupling different techniques and caution must be taken (i.e., Gritsevich, 2008c) . Some approaches might be more adequate than others to address specific bits of the event. Nevertheless, when combined adequately, all the techniques described in the previous paragraphs are complementary. For example, as part of this thesis, Chapter 3 will benefit from the results obtained using video and radio scattering techniques, and Chapter 4 will explore the utility of using the information retrieved from the combination of infrasound and video systems.

While short term or specific observations can be successfully achieved with punctual co-joint collaborations of several observation stations, long-term meteor research projects do usually kick-off with the development of a potentially powerful array of well-equipped observation stations. As their main purpose is to investigate the bright meteor phenomena, these arrays are usually referred to as *Fireball Networks* (FN). Most Fireball Networks stations are arranged locally in the same country and implement the same acquisition and reduction software and procedures. They are usually ruled by the same organization and so they often fulfil the same institutional requirements. Nowadays there is a proliferation of national FN focused on observation based on photographic and video camera systems, especially in Europe. Good examples of this are the Spanish Photographic Meteor Network (SPMN; Trigo-Rodríguez et al., 2004c) , the French Fireball Recovery and InterPlanetary Observation Network (FRIPON; Colas et al., 2014), the Finnish Fireball Network (FFN; Gritsevich et al., 2014), or the recent Italian Meteor and Transient Luminous Event Network (IMTN). Outside the EU, it is worth mentioning the continental scale Desert Fireball Network (DFN; Bland, 2004) in Australia, which has proved to provide outstanding results. Yet, the first organized couple of cameras (that consisted of two Ross Xpress lenses of 1.5 inches apertures) that co-pointed to the same sky area was set up in 1936 and was ruled by F.L. Whipple at the Harvard Observatory. This project was called the Harvard Meteor Project (Jacchia & Whipple, 1956). From that moment on, the organization and capacities of the fireball networks improved. Networks gathering very relevant data are the European Fireball Network which was born in the Czech Republic in 1959 (Ceplecha, 1957) and lately expanded to Austria, Slovakia and Poland that is still operational (Oberst et al., 1998; Spurný et al., 2017b); the Prairie Network that operated in the United States in the period from 1963 to 1975 (McCrosky et al., 1978); and the Meteor Observation and Recover Project in Canada (MORP), whose operations dated from 1970 to 1985 (Halliday et al., 1978).

Although one of the fireball network's main goals is to detect and study fireballs, it also has a strong devotion to achieving the observation of an eventually recovered meteorite fall. Unfortunately, the statistics show that it has been historically difficult to succeed in this second goal; it usually occurred once per decade (see for example Gritsevich, 2008c). For instance, the MORP was able to register more than 1010 fireballs along the approximately 15 years of existence, including only one meteorite-dropper. Listed as MORP 285, the meteorite is commonly known as Innisfree. The following event in that reduced list did not occur until 15 years later. Other recent examples are Annama meteorite (Gritsevich et al., 2014; Trigo-Rodríguez et al., 2015) that was observed

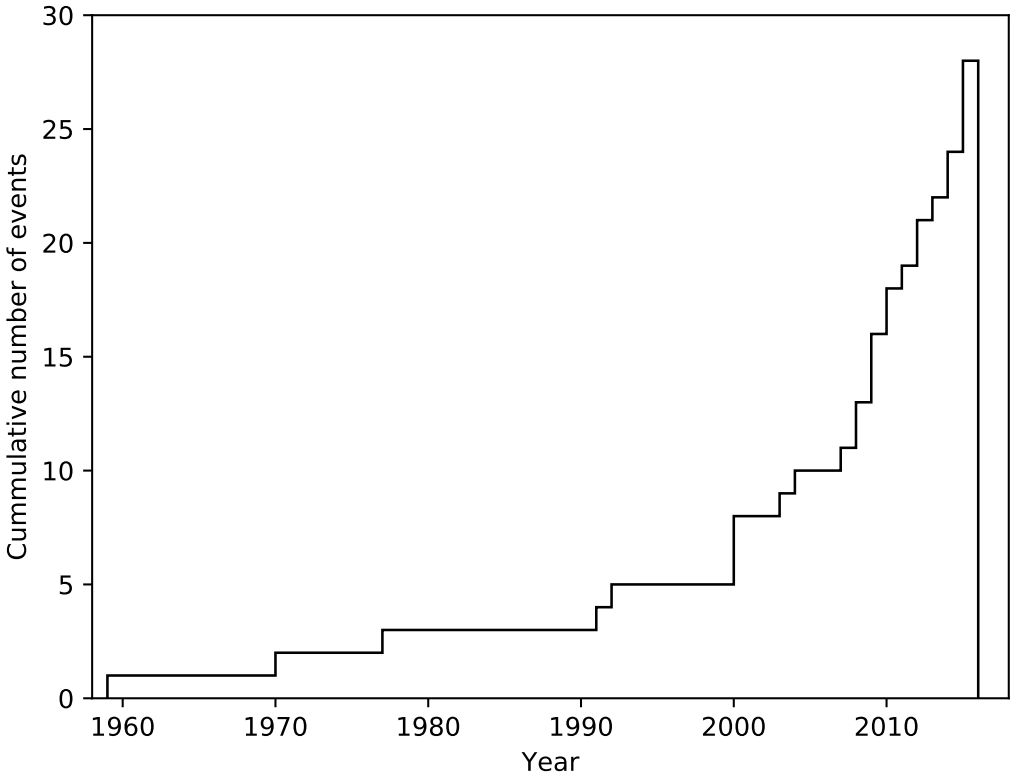

Figure 3: Cumulative histogram of all the recovered meteorites for which the atmospheric flight has been observed and the pre-atmospheric orbit calculated.

and recovered by the Finnish Fireball Network, or the SPMN's Villalbeto de la Peña occurred after approximately 10 years of the network operation (Llorca et al., 2005; Trigo-Rodríguez & Llorca, 2006). Although the orbits and dates of recovery of all these events will be provided in Chapter 3, here Figure 3 shows how the cumulative histogram of these events significantly increases over the recent years. As discussed in Bland et al. (2006), the rate of success has a lot to do with the extension of the networks and the orography of the prospective landing site. The Desert Fireball Network (DFN) benefits from these facts and in along the 14 years of its existence (Bland, 2004) it has allowed the observation and recovery of four meteorite falls: Bunburra Rockhole (Bland et al., 2009) in 2007, Mason Gully (Spurný et al., 2011) in 2010, Murrili (Bland et al., 2016) in 2015, and Dingle Dell (Devillepoix et al., 2018) in 2017. The improvement of the European Fireball Network equipment has also led to a higher rate of observed meteorite falls recoveries (Spurný et al., 2017b).

The technology improvements along with the strengthening of the collaboration between researchers is notably increasing the meteor observations and subsequent meteorite recovery. This is quite evident over the last 10 years. Besides, the continuous advances in mathematical approaches and technical capabilities is nourishing the meteoritic community with models and tactics to deal with data from current and past fireball network databases. For example, Chapter 5 of this thesis will validate the application of a new

mathematical approach to calculate the fireball terminal height using the MORP database.

2.3 ASTROMETRIC DATA REDUCTION

Each of the above-mentioned meteor detection techniques requires an appropriate data reduction procedure. As for the purposes of this thesis, the astrometric data reduction from video cameras followed in Chapter 3 is described here. Meteor detection performed by either wide field or all-sky video cameras encapsulate a lot of information that shall be treated before providing reliable data. Note that only night detections are considered here; daylight bolides might be studied somehow differently (i.e., Trigo-Rodríguez & Llorca, 2006; Blanch et al., 2017; Gritsevich et al., 2017).

The SPMN video cameras operate a "Phase Alterning Line" (PAL) system that performs at 25 frames per second. This encoding system uses interlaced frames to smooth the transition between motion steps. This way, the even and odd frames update the processed image alternatively. Ultimately this means that all the 25 frames per second can be doubled to 50 frames using even and odd sub-frames. This is quite convenient for difficult astrometry cases where more precision is required. For typical meteor trajectories ranging between 1 and 10 seconds, a 25-frames per second system provides between 25 to 250 images, which is usually enough to derive accurate information.

The apparent movement of the stars on the celestial sphere, as well as the meteor discrete positions over its trajectory, are registered in the camera sensor (CCD or CMOS detector) as a stereographic projection. The pixel coordinates on the sensor shall therefore be converted to the common used equatorial coordinates. Each of the recorded frames contains one projected position of the meteor along its path, and the position of the background stars. Since the equatorial coordinates of the stars are known and listed in the catalogues, these are used to perform the coordinate transformation between the detector image reference and the equatorial reference frames. However, this transformation is not straightforward and needs the inclusion of an extra intermediate set of coordinates. The alignment between the camera sensor and the stereographic projection might not be exact. The sensor could show a mismatch in terms of rotation, translation, or even not showing exact orthogonal axis. Thus, the pixel position on the sensor shall be first transformed to the stereographic projected coordinates before implementing the conversion to equatorial coordinates (see Figure 4). As per the all-sky cameras there are additional issues to be considered as detailed in Borovicka et al. (1995). The complete description of the transformation equations along with validation cases can be found in Steyaert (1990) and Trigo-Rodriguez (2002).

The information provided by one observation station (or one isolated camera) only indicates the apparent position of the meteor on the celestial sphere. For example, the final resulting image from the addition of the video frames of a meteor detected during the Ursid campaign is showed in Figure 5. This figure demonstrates the lack of information to procure the three-dimension movement of the body in the atmosphere. To

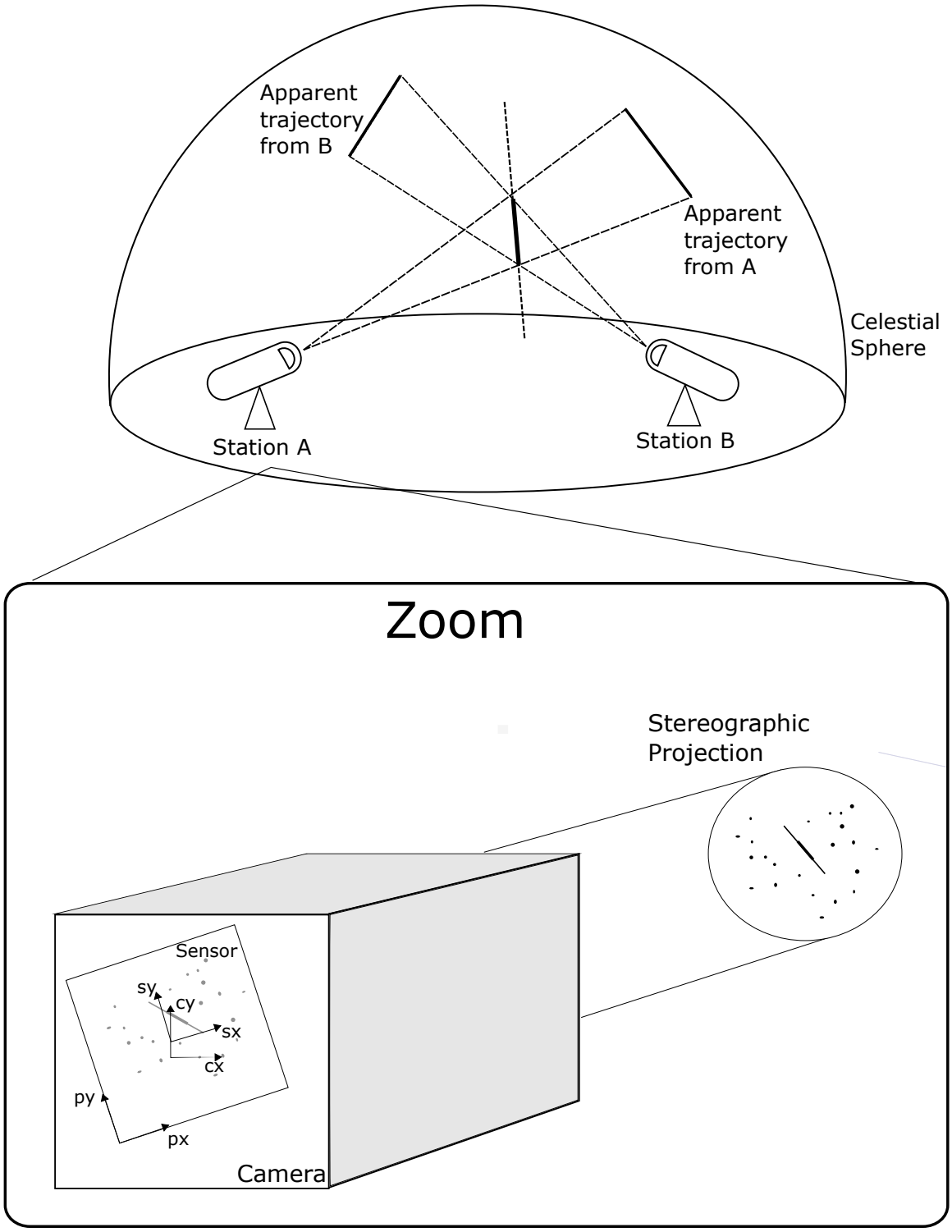

Figure 4: Schematic illustration of two stations (A, B) detecting a meteor (adapted from Roggemans, 1987). The zoom on the camera shows possible misalignments (translation and rotation) between the camera reference axis (cx, cy) and the sensor reference axis (sx, sy). The coordinates (px, py) indicate the pixel position on the sensor.

reconstruct the meteor trajectory at least two different observations are required. The intersection of the two planes defined by the apparent meteor trajectory (a line) and the station locations (a point for each) provides a line that corresponds to, approximately, the real meteor path. As the apparent trajectory derivation may have some associated errors, these might be propagated to the final plane intersection. The more observation stations that reliably detect the meteor the better is the adjustment of the meteor trajectory. The methodology to derive the meteor path and the ultimate refinement was outlined by Ceplecha (1987). It shall be remarked that the stations shall be separated by at least 20 km (Trigo-Rodriguez, 2002) and that the angle between the two planes shall be greater than 20°. Ceplecha (1987) called this angle Q, and it describes the statistical significance of the trajectory obtained by the combination of the information from the two stations considered. In case of being smaller than 20° the final adjustment of the resulting line intersection of the planes can be quite poor (regardless of the associated errors with the apparent trajectory calculation), leading to serious inaccuracies in the meteor trajectory determination. When there is information from more than two observation stations, the calculation is a bit more tedious as the triangulation requires more calculations, but it follows the same guidelines (Trigo-Rodriguez, 2002; Trigo-Rodríguez et al., 2004c; Trigo-Rodriguez et al., 2008).

Often video cameras dedicated to meteor monitoring are equipped with a rotating shutter for easier retrievals, so the trajectory is chopped into smaller bits whose length can be measured. Since the revolutions per second of the shutter are set beforehand, the time between trajectory cuts is known. The meteor velocity and deceleration at each luminous trajectory segment can be retrieved. Due to small imprecisions in the trajectory derivation some final adjustment is required. Normally the length of the meteor trajectory can be mathematically formulated as the sum of a linear and an exponential term (McCrosky & Posen, 1968; Gritsevich, 2008c):

$$D(t) = a + bt + ce^{kt} \tag{1}$$

Where the constants a, b, c, k are the outcome from a least squares adjustment between the observations and the velocity function (Equation (1)). The goodness of the adjustment depends on the reliability of the data, where the entry velocity plays a relevant role. The first (pre-atmospheric) value of the meteor velocity is normally difficult to retrieve, and despite notable efforts to approximate it (i.e., Gural, 2012) extra work on this subject shall be carried out. Since it is difficult to gather reliable information about the entry velocity, various approaches are commonly considered (Egal et al., 2017).

From the atmospheric luminous path, it is straightforward to derive the radiant (the apparent point in the sky where the meteoroid seems to originate). The radiant, the entry velocity, and the average velocity of the meteoroid are necessary to derive the pre-atmospheric orbit of the meteoroid (Ceplecha, 1987). Alternatively, the required input parameters for orbit computation are the topocentric pre-atmospheric velocity vector and the coordinates of the atmospheric entry point of the meteoroid, i.e. the beginning point of the visual path of a meteor, in an Earth centered-Earth fixed coordinate system (the International Terrestrial Reference Frame, ITRF; see Dmitriev et al., 2015). The

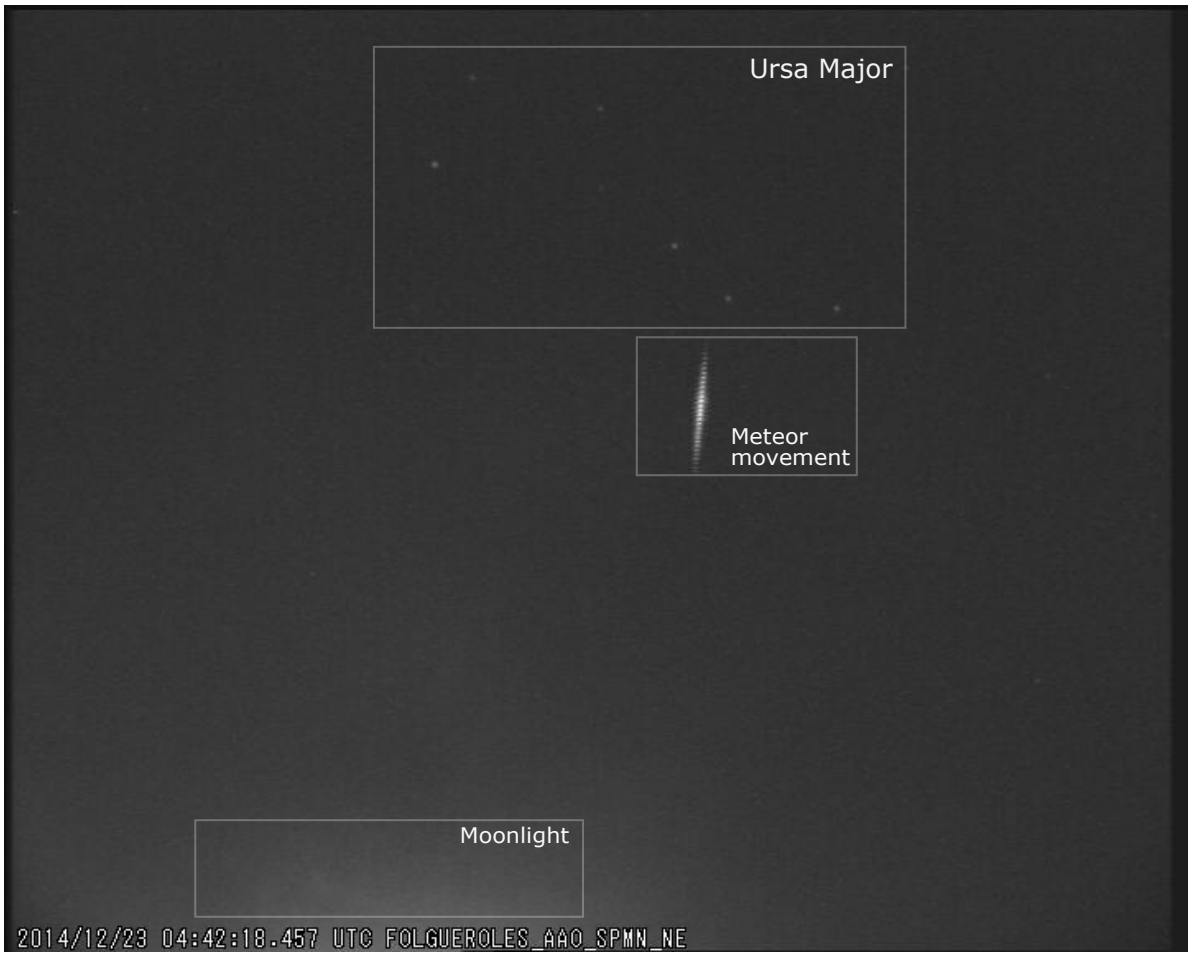

Figure 5: Example of one Ursid meteor studied during the Ursid outburst campaign. The image consists of the final sum of all the individual video frames. The background position of the Ursa Major constellations serves as a guide to locate the apparent trajectory of the meteor. Note that by varying the Point-Spread Function (PSF) distribution of the image dim stars can be also spotted and the effect of Moonlight constrained. The increase and decrease of brightness along the meteor path can be observed.

more accurate these values are, the more reliable the heliocentric orbit of the meteoroid results. Due to the difficulties in retrieving the geocentric meteoroid entry velocity, the orbital semi-major axis might show some inaccuracy (Betlem et al., 1999). Chapter 3 of this thesis will deal with this issue and show how it might affect parenthood determination.

2.4 METEOR DYNAMICS MODELS

The dynamics of the meteoroid during its atmospheric passage comprises various physical scenarios related to the flight configuration and the physical properties of the body. The general procedure to retrieve astrometric data from the observed meteor phenomena has been outlined above. The discrete positions, velocities and times of the meteor trajectory are then the input data to mathematical models whose output extent our knowledge, and help improving and validating those models. As per meteor dynamics studies these data have been historically treated using a mathematical model that results from the application of the Newton's laws. In this section the classical Newtonian formulation will be revisited, and two other formulations introduced. The decision on whether which formulation shall be chosen will ultimately depend on the characteristics and data available within each individual research.

2.4.1 *Meteor dynamics and Newton's second law*

The dynamical behaviour of a meteoroid that enters the Earth's atmosphere can be described using the equations of motion. The projection of the meteoroid movement along its trajectory provides an equation that relates the drag and the meteoroid deceleration:

$$M\frac{dV}{dt} = -\frac{1}{2}c_d\rho V^2 S \tag{2}$$

Where M is the mass, V the velocity, t is the time, S is the area of the middle section of the body, ρ is the density of the atmospheric air, and c_d is the drag coefficient. Note that the hypersonic entry velocities create a great drag effect that overcomes the effect of the gravity (Gritsevich, 2010) and therefore the gravity acceleration can be neglected from the above equations. If the slower entry velocity is taken (11.2 km/s) then:

$$\frac{c_d\rho V^2 S}{2Mg} \sim \frac{V^2}{g} \sim \frac{(11200)^2}{9.8} >> 1 \tag{3}$$

A second equation is obtained from the geometrical description of the differential increments of the distance over the meteor trajectory:

$$Vdt = dL = -dh \cdot sin\gamma \rightarrow \frac{dh}{dt} = -Vsin\gamma \tag{4}$$

Where γ is the slope between the trajectory and the horizon, and h is the meteor height above the Earth's surface. Equation (4) allows conversion between time and height. Additionally, the mass loss that the meteoroid experiences due to the ablation phenomena shall be accounted for. The flow dynamics mass variation equation leads to:

$$H^* \frac{dM}{dt} = -\frac{1}{2} c_h \rho V^3 S \tag{5}$$

Here it has been used c_h as the heat exchange coefficient and H^* as the effective destruction enthalpy.

From these premises, Hoppe (1937) and later Whipple (1938) elaborated a mathematical formulation assuming that the body does not experience any fragmentation. This is known as a *Single Body Theory* and it assumes that coefficients and ablation rates such as c_d or c_h remain constant along the trajectory. However, as the meteor flight parameters vary with time and at each event, it is more accurate to set these coefficients free and include as input data values retrieved from observations. In this case, for the system (2)-(4)-(5) to be resolvable additional relationships are needed. On the one hand, a shape factor coefficient, A, that relates the cross-sectional area to the meteoroid volume: $A = S/Volume^{2/3}$ is introduced. Note here that A has no dimensions, for a cube it has an unitary value, and for a sphere it is approximately $A = 1.21$. On the other hand, as the ablation phenomena remove mass from the meteoroid, its cross-sectional area (defined as the surface projected onto the normal plane to the trajectory) varies during the flight. Levin (1956, 1961) suggested that the cross-sectional area and the mass of the meteor body are connected as $S/S_e = (M/M_e)^{\mu}$, where μ is a constant and the subscript "e" indicates the values of the parameters when the meteoroid enters the atmosphere. The parameter μ characterizes the role of the body rotation during the flight and can be calculated based on the observed brightness of a fireball using the method proposed by Gritsevich & Koschny (2011). If $\mu = 0$ there is no body rotation, whereas if $\mu = 2/3$ the ablation of the body due to its rotation is uniform over the surface, and the shape factor does not change. Generally, $0 < \mu < 2/3$.

The additional equations can be obtained using various approaches. Hoppe (1937), following the work of Öpik (1933), introduced a luminosity equation which relates the light emission of the body to the meteor deceleration due to its mass loss times an efficiency factor. This can be put simple as:

$$I = \tau \frac{dM}{dt} \frac{V^2}{2} \tag{6}$$

Where τ is the luminosity coefficient (Gritsevich & Koschny, 2011), and I is the radiation efficiency. This equation has been normally used to derive the meteor mass from the photometric observations, and so this mass is usually referred to as "photometric mass" (e.g., Ceplecha & McCrosky, 1976). Conversely, the "dynamic mass" is obtained based on analysis of the meteoroid deceleration and ablation (Equations (2)-(4)-(5)),

see e.g., Gritsevich (2009).

Additionally, the work of Öpik (1958) and Bronshten (1965, 1983) also account for the vaporization of the meteoroid surface particles. The number of electrons ($\alpha^{'}$) that are created per unit of length of the meteor path because of the interaction of the evaporated meteor atoms with the atmosphere can be mathematically expressed as:

$$\alpha^{'} = -\frac{\beta^{'}}{m_a V}\left(\frac{dM}{dt}\right) \tag{7}$$

The average free electrons that result from the collisions between one meteor atom and other particles is $\beta^{'}$ (ionization coefficient); and m_a is the average mass of a meteor atom.

A bit different set of completing equations was introduced by Pecina & Ceplecha (1983, 1984). Their solution seeks for the refinement of the small distance increments over the meteor trajectory, $l = l(t)$, using the retrieved data from observations. As this approach is more geometrical, Equation (4) is expressed differently in terms of $l(t)$. A couple of new geometrical variables are introduced to express the γ slope, and the relationship between the trajectory height and local distance, which ultimately require the inclusion of two related equations. While the approach formulated by Bronshten (1965, 1983) strongly depends on the information derived from the observation, which is commonly difficult to obtain accurately, the formulation outlined by Pecina & Ceplecha (1983, 1984) softs that effect by providing a mathematical adjustment of the observed trajectory of the meteoroid luminous path. Note however that both approaches include the shape factor coefficient, A, and the ablation coefficient. This last coefficient is of notable interest as it describes how the ablation processes evolve with time. It is defined as:

$$\sigma = \frac{c_h}{2H^* c_d} \tag{8}$$

These two extensions of the initial layout of Hoppe (1937) equations are not the only ones in terms of direct application of the Newton's laws, but these are the most used in meteor physics. Other relevant formulations were outlined by Levin (1961) and Revelle (1979).

The Single Body Theory has been extensively used in common meteor studies and relies on considering as constant a series of characteristic parameters which are not known beforehand and cannot be obtained directly through the observations. In addition, other input flight parameters required in the formulation are assumed either to be the average values of previous studies or reasonable approximations for the event under study. For instance, the bulk density of the meteoroid is usually introduced in the equations of motion as a fixed value whereas it depends on the case under consideration. Due to the large number of unknowns required by the classical theory, the resolution of the equations and the results shall be treated with care. Slight modifications of some

parameters may lead to radically different results.

2.4.2 *Scaling laws and dimensionless variables*

The introduction of scaling laws and dimensionless variables in the mathematical formulation can overcome these problems. Stulov et al. (1995), Stulov (1997) and Gritsevich (2007, 2009) suggested a new way of resolving the equations of motion which reduces the number of unknowns down to two. These two new parameters, namely α and β, are easily retrievable from the observed set of trajectory points (h, V), providing only one unique case-matching solution in most of the cases. The methodology combines the system (2)-(4)-(5), and Levin (1956, 1961) relationship between the cross-sectional surface and the meteoroid mass.

Introducing dimensionless variables m, v, y, s and ρ ($M = M_e \cdot m, V = V_e \cdot v, h = h_0 \cdot y, S = S_e s$ and $\rho_a = \rho_0 \cdot \rho$) in the system (2)-(4)-(5), it turns into (see Gritsevich, 2009):

$$m\frac{dv}{dy} = \alpha\rho v s \tag{9}$$

$$\frac{dm}{dy} = 2\alpha\beta\rho v^2 s \tag{10}$$

These equations include the two mentioned parameters and show their physical meaning. The ballistic coefficient, α, is proportional to the mass of the atmospheric column with the cross section S_e along the trajectory divided by the meteoroid's pre-atmospheric mass. In other words, α expresses the drag intensity suffered by the meteor body during its flight. The mass loss parameter, β, characterizes the ablation of the meteor. It can be expressed as the fraction of the kinetic energy per mass unit of the body that is transferred to the body in the form of heat divided by the effective destruction enthalpy. These formulation of these two parameters is the following:

$$\alpha = \frac{1}{2} c_d \frac{\rho_0 h_0 S_e}{M_e sin\gamma} \tag{11}$$

And

$$\beta = (1-\mu)\frac{c_h V_e^2}{2 c_d H^*} \tag{12}$$

The system (9)-(10) can be resolved assuming an isothermal atmosphere: $\rho/\rho_0 = exp(-h/h_0)$, where ρ_0 is the atmospheric density at sea level and $h_0 = 7.16 \cdot 10^3$ m is

the atmosphere scale height. Using the initial conditions $y = \infty$ and $v = 1$ (for details see Gritsevich, 2007) it results:

$$m = exp[-(1 - v^2)\beta/(1 - \mu)] \tag{13}$$

$$y = ln2\alpha + \beta - ln\Delta, \quad \Delta = \bar{E}i(\beta) - \bar{E}i(\beta v^2), \tag{14}$$

where

$$\bar{E}i(x) = \int_{-\infty}^{x} \frac{e^t dt}{t} \tag{15}$$

The derivation of parameters α and β that match a particular event can be done via a least squares method which adjusts Equation (14) to the (h, V) data retrieved from the observations (see Gritsevich, 2007, for further details). In principle, at least three (h, V) points, including the entry velocity, are required to derive α and β this way.

This methodology was first validated by Gritsevich (2008c) to prove its accuracy through the study of four well-known meteorite falls. This first study did also remark that, similarly to the classical theory, more detailed account for meteoroid fragmentation might enhance the application of the approach.

Gritsevich (2009) derived α and β parameters for 143 objects from the Meteor Observation and Recovery Project (MORP, Canada; Halliday et al., 1996) and 121 objects from the Prairie Network (PN) database (McCrosky et al., 1979). This allowed the first large-scale classification of fireballs and meteorites using accurate parameters. This classification can be demonstrated using the logarithmic (α, β) plot (Gritsevich et al., 2012). As can be seen in Figure 6, meteorite-producing events (e.g. Innisfree, Lost City, Annama, Bunburra Rockhole, etc.) cluster in a defined localised region of the diagram compared to the rest of the fireballs. The location of the few Taurids registered in the MORP database is clearly indicated. These carbonaceous chondrites fall in another delimited area of the diagram. Thus, this methodology is useful to set up a new classification based on these parameters.

Gritsevich & Koschny (2011) implemented this scaling laws' methodology to additionally constrain the percentage of meteor kinetic energy emitted as light. This allowed them to completely perform the calculations as only the meteor mass and velocity variations were required, whereas further assumptions on meteor bulk density, shape and initial mass could be avoided in the analysis.

More recently, Lyytinen & Gritsevich (2016) suggested the way of successfully incorporating different atmospheric models in the dimensionless equation of motion (Equations (9)-(10)). Although the system solution (Equations (13)-(14)) is derived for isothermal atmospheres, the solution can be easily adapted when other atmospheric models

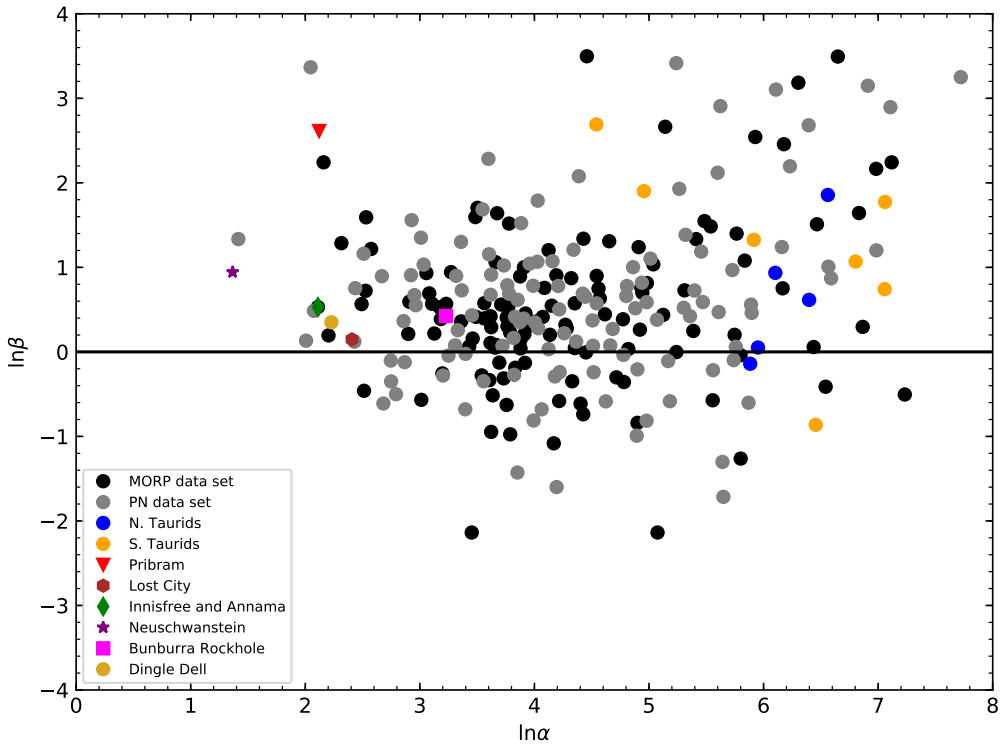

Figure 6: Diagram showing the combination of $ln\alpha$ and $ln\beta$ for MORP and PN database events based on Gritsevich et al. (2012), where the few Taurids registered by the MORP are marked separately. Marks for Pribram, Lost City, Annama, Innisfree, Neuschwanstein, Lost City, Dingle Dell and Bunburra Rockhole meteorites are also shown. Note that, as it will be seen in Chapter 6, Innisfree and Annama show the same α and β values.

need to be considered. Note that the use of the detailed height and atmospheric pressure measurements increase the accuracy of the results. This is especially critical for analysis of potential meteorite-droppers, to estimate the terminal mass, which also allows to narrow down the search area on the ground and to speed up the meteorite recovery. In this sense, if possible, the information provided by local weather station information should be used. However, for most meteor observations these data are not publicly available and have to be inquired upon request on a case-by-case basis. Detailed models such as the International Standard Atmosphere (ISA) model or MSIS-E-90 (Hedin, 1991) could also provide good results. The revised mathematical formulation to correctly account for other atmospheric models while avoiding a complex mathematical re-formulation is described in Lyytinen & Gritsevich (2016). In particular, for detailed atmospheric models, the exponential atmospheric model is still valid as long as individual heights are corrected according to the real pressure values at those heights.

Provided all these features, the application of this methodology becomes convenient to the analysis of large databases observations and allows the automation of meteor trajectory modelling. The main advantage when compared to the classical methodology is that the errors associated with the problem of defining characteristic parameters are more constrained, and therefore provides better adjustments when the quality of the observations is reliable enough.

Chapter 5 of this thesis will study the efficiency of this formulation to provide accurate information on the terminal heights of meteoroids. Moreover, it will also discuss the suitability of this formulation to tackle a meteoroid classification problem, similarly to the PE criterion of Ceplecha & McCrosky (1976).

2.4.3 *Stochastic estimator algorithms*

The atmospheric flight of a meteoroid through the atmosphere can be studied as a stochastic process where the subsequent values of the unknown variables could be considered to some extent random. The problem under discussion consists of finding the state of a group of variables, known as state vector, at a given time:

$$x_t = F(x_{t-1}, u_{t-1}, v_{t-1}) \tag{16}$$

$$y_t = G(x_t, n_t) \tag{17}$$

Where x_t is the unknown state vector at a given time t, u_{t-1} is previous state of the system (the initial condition at the time t), and y_t is the observed state vector at the time t. The variables v_{t-1} and n_t are the process noise (ultimately related to the mathematical equations used to model the physical problem) and the measurement inaccuracy at each time t respectively. The resolution of these equations involves an iterative process, which can be described analytically when certain conditions are fulfilled.

Otherwise the problem shall be tackled via implementing more specific mathematical tools.

One of such tools is the Kalman Filter which allows estimating the state vector of the system (16)-(17) when it is linear and the probability density distributions that gather the model inherent noise, v_t, and the measurement inaccuracies, n_t, are Gaussian (Grewal & Andrews, 1993). As the meteoroid's Equations (2)-(4)-(5) do not comply with these conditions, additional intermediate steps shall be carried out.

If the equation system is non-linear, the use of a Kalman Filter generates at each iteration step a probability density distribution that is not Gaussian. As a first approximation, these distributions could be approximated as Gaussian at each step and then propagated through the first-order linearization of the nonlinear system. This way of proceeding is known as Extended Kalman Filter (EKF). The result is a first-order approximation to the optimal solution. Unfortunately, as the nonlinearity of the system increases the results may largely diverge from the optimal solution. The first time a stochastic estimator algorithm was implemented to analyse meteor atmospheric flight was done by Sansom et al. (2015). Their study implemented an EKF to estimate the Bunburra Rockhole (Bland et al., 2009) event trajectory. Furthermore, they derived the dimensionless parameters (α and β) adjusting their predicted set of trajectory (h, V) values and the outcome matched the results obtained with the formulation outlined in Section 2.4.2.

An enhanced version of the EKF is the Unscented Kalman Filter (UKF). Both filters approximate the probability density distributions as a Gaussian at each iteration step, but the UKF overcomes possible divergences from the optimal solution by introducing a sampling approach. A set of sample points that properly represent the mean and covariance of the Gaussian distributions are chosen and propagated through the original nonlinear system. This way a second order accuracy level is achieved for the mean and co-variance values of the new gaussian distributions, improving the results of the EKF. Sansom et al. (2016) expanded their previous analysis of Bunburra Rockhole meteorite-dropper implementing a UKF. Their work provides a more complete description of the method along with the discussion of their results.

The implementation of Kalman filters to solve the meteor Equations (2)-(4)-(5) allows to encapsulate the error and its evolution along the time steps, however, the methodology still relies on the observed meteor flight values to both initiate the state estimation and to correct the results at each iteration step. The precision of these observed values constrains the outcome of the process. This inconvenience could be overcome by means of a particle filtering method (a.k.a. Sequential Monte Carlo). The particle filtering belongs to the Bayesian interference statistics and evaluates the probability of an estimation to be reliable. Taking into account the measurements available and also the probabilities of the estimations at previous steps it is possible to apply this approach to meteors (Sansom et al., 2017). The way particle filtering works is as follows:

- At a first step a cloud of particles is distributed over the whole range of possible state values.
- According to the values retrieved from observations, the particles within the probability distribution are assigned a weight which expresses the likelihood of the system to be in that state.
- Then, a resampling process takes over. The regions where the particles show higher weights are over re-populated whereas the regions where the likelihood of the state is poor are depleted.
- Once again, the information derived from observations at the following time step is used to re-assign probability weights and the process is repeated for as many steps as desired.

Sansom et al. (2017) implement the particle filtering to its previous work on the Bunburra Rockhole fireball. As stated by Sansom et al. (2017), the particle filtering allows them to explore a wider value range for the meteor flight parameters and to understand how the associated probabilities can provide a more complete picture of the event.

The application of these methodologies by Sansom et al. (2015, 2016, 2017) was initially aimed to exploit and automatize the considerable large number of event recordings the Dessert Fireball Network (Bland, 2004; Howie et al., 2017) is gathering and is expected to generate, but can be easily accommodated to any other FN or observational project.

The set of state variables propagated by Sansom et al. (2015, 2016, 2017) includes the meteor velocity, position, mass, ablation parameter, and shape-density parameter (which is related to the shape factor as $\kappa = (c_d A)/2$). Additionally, as noted in Sansom et al. (2017), the state vector could be expanded, and future studies may also include the meteor brightness or the internal heat.

The Kalman and particle filters provide a controlled way of managing and propagating errors in the meteor trajectory modelling. Compared to both the classical and the scaling laws methods, which estimate the numerical errors using the least-squares methods, the approach outlined in this section could be especially helpful when the meteor observations show large inaccuracies.

3

CHASING FOR METEOROID PARENTS. TWO CASE STUDIES

3.1 INTRODUCTION

Meteoroids are common decay products over the solar system for either rocky asteroids, or volatile-rich comets. As stated by Williams (1993) meteoroids detached from asteroids and short period comets shall follow orbits that are quite alike to those of their progenitors, but usually having lower kinetic energy. The inner solar system is not an easy playground because the proximity of the four terrestrial planets along with their relative short orbital periods increases the chances of the meteoroids to suffer a gravitational push or pull when they approach the planets' orbital nodes. In addition, the mutual periodical gravitational influence exerted by two celestial bodies help either maintaining their orbit fixed for long time scales or destabilizing them. This effect is known as *orbital resonance* and it does play an important role in the orbit evolution of asteroids, comets and meteoroids. An orbital resonance can be outlined by the evolution of different orbital parameters of the bodies involved (i.e., eccentricity, inclination), and can be considered at short time and long-time scales. For the purpose of this chapter, the interest is set on the *mean-motion* and the *secular resonances*. The former indicates that the two bodies have a periodical reciprocal gravitational influence which is determined by their orbital periods (which eventually involve their mean-motion and their semi-major axis). When a mean-motion resonance occurs, the orbital periods are related by a ratio of two small integers. Provided the larger masses of planets compared to meteoroids, the gravitational effect of meteoroids on the planets is negligible, and so the mean-motion resonances become a planetary mechanism to define the orbits that meteoroids can go through. On the other hand, the secular resonance expresses that the precession of two bodies occurs at the same long-term rate. In this case, the meteoroid will show a perihelion or an ascending node precession similar to that of a planet, which eventually alters the eccentricity and inclination of the meteoroid in times of 10^4-10^6 years (Froeschle & Scholl, 1986; Morbidelli et al., 1994). Note that the analysis of orbital resonances is complex and completely out of the scope of this thesis. Dedicated literature can be found in Nesvorný & Morbidelli (1998); Morbidelli & Nesvorný (1999); Smirnov & Shevchenko (2013); or Sekhar & Asher (2013).

Mean-motion and secular resonances are common in the Main Asteroid Belt (hereafter MAB). For example, asteroids in orbital resonance with Jupiter can be trapped in certain orbits and can be considered as an asteroid family, i.e., the Hilda family in the 3 : 2 mean-motion resonance (three complete asteroid orbits around the Sun per two orbits of Jupiter) with Jupiter (Brož et al., 2011). However, the most relevant resonances acting

in the MAB are the ν_6 secular resonance with Saturn, and the mean-motion resonances with Jupiter 3 : 1, 5 : 2, and 2 : 1 (Morbidelli et al., 2002). These resonances destabilize the orbit of the asteroid and thus are the reason behind the depletion of various orbital regions within the MAB (Bottke et al., 2002): the *Kirkwood gaps*. The asteroids are affected by non-gravitational forces that make them losing orbital energy until they cross the resonances. Once in an orbit affected by a destabilizing orbital resonance the asteroid orbit become more eccentric until they are transferred to the near-Earth region (Morbidelli et al., 2002) where they, or fragments of them, can cross the Earth orbit and become a threat. The second part of this chapter is devoted to the study of the parental origin of a recovered meteorite called Annama whose atmospheric flight was observed, and the orbital parameters accurately determined. The pre-atmospheric orbit of this meteorite suggested that the region of origin of this body was the inner edge of the MAB, from which it was removed by the ν_6 resonance (Trigo-Rodríguez et al., 2015).

Mean-motion and secular resonances along with close planetary encounters do also determine the dynamical evolution of Halley-type comets (Bailey & Emel'Yanenko, 1996). These comets are long period comets that come from the Oort Cloud reservoir and get eventually trapped in orbits with shorter periods where they can become stable for centuries if the number of close planetary encounters is low (Jenniskens, 1998, 2006). As a consequence of this stability, the orbital evolution of the dust particles detached from these comets is mainly subjected to non-gravitational effects that may largely affect smaller particles. Thus, the orbit of the dust particles and the comet can eventually evolve differently. Note though that, as outlined by Asher et al. (1999), mean-motion resonances can avoid orbital spreading and maintain the orbital configuration of the dust trails as long as close planetary encounters are avoided. It is then expected that the older the dust trail, the higher the chances to have suffered such encounters (Jenniskens et al., 2002) and the more dispersed are the dust particles along the orbit. This wide and stretched stream is usually referred to as a *filament* (Jenniskens et al., 2007). In this chapter, however, old dust trails detached from a Halley-type comet that conserve a fixed and compact orbital configuration are studied. The avoidance of close planetary encounters has caused these *trailets* to reach the Earth once the comet is at its aphelion.

3.2 THE PERIODICAL APHELION OUTBURST OF THE URSID METEOR SHOWER

The first identification of a possible meteor shower with a radiant point in the constellation of Ursa minor was by Denning (1912), occurring around the Winter Solstice. However, very few observations were subsequently made, except for Hoffmeister who recorded its activity in 1914. Additional observations of shower members were made, and its activity became confirmed in 1945 (Becvár, 1946). There are two reasons for the lack of records of the Ursids. First the Ursids have very low activity levels in most years, its *Zenith Hourly Rate* (the number of meteors that would be observed under good observing conditions in one hour if the radiant was at the zenith) is usually ZHR¡10

(Jenniskens, 1994). Second, the weather can be bad in mid-December and many observers choose to only observe the more predictable Geminids (which peak at mid-December but occur between the beginning and the 20^{th} of December approximately, see Table 1 in Chapter 1.

Concerning the parent body, Ceplecha (1951) showed that the annual Ursid meteor shower was related to comet 8P/Tuttle: a Halley-type prograde comet with an approximate diameter of 14.6 km (based on a 0.04 albedo; see Jenniskens, 2006), and a period of 13.6 years (JPL-HORIZONS, *ssd.jpl.nasa.gov*). The perihelion distance of 8P/Tuttle is slightly greater than 1 AU, which means that the comet is usually brightest (close to perihelion) and close to the Earth at roughly the same time. Hence it has been observed at all perihelion passages since discovery apart from 1953, when observing conditions were poor throughout. The subsequent observations of the perihelion passages are important to increase the accuracy of the comet's orbit determination, its periodicity, and the mechanisms that produce the release of material. As it can take a considerable time after being ejected from the nucleus for meteoroids to disperse away from the nucleus locality, a ZHR enhancement (a.k.a *outburst*) is generally to be expected in stream activity at the time when the comet is close to perihelion and new meteoroids are injected (see Williams et al., 1986, for an early discussion and mathematical formulation of this).

While perihelion passages took place in 1790, 1858, 1872, 1885, 1899, 1913, 1926, 1940, 1953, 1967, 1980, 1994 and 2008 (see Table 2), there has not been observed a ZHR increase in most of those years. Several ZHR enhancements (around 3 times larger than the usual ZHR) have been reported the following year after the perihelion passage. Therefore, the proximity to the perihelion is unlikely to be the explanation for the Ursid meteor shower activity increase. Instead, Jenniskens (2006) suggested that the ZHR increases are caused by cometary material released at very old comet perihelion passages between AD $300 - 1400$ that were subjected to orbital evolution and ultimately became a filament.

On the contrary, what is remarkable about the Ursids is that a much sharper increase in the ZHR to well over 100 was observed in 1795, 1945, 1986 and 2000 years when the parent comet is near aphelion at a heliocentric distance of over 10 AU, so that it will not be outgassing and inserting new meteoroids into the stream at this point. The comet perihelion passages, the large observed outburst that associated to the filament, and large outburst that took place when the comet is close to its aphelion are shown in Table 2. Outbursts when the comet is away from perihelion are not common and outbursts when the comet is close to aphelion are extremely rare. However, mean-motion resonances can offer a reasonable explanation on the subject.

Two body mean-motion resonances can play an important role in determining the behaviour of meteor showers as was first pointed out by Asher et al. (1999) who showed the importance of Jovian resonances in producing meteoroid storms. Other effects of resonances were described for the two body Saturnian resonances (Sekhar & Asher, 2013), two body Uranian resonances (Williams, 1997) and three body resonances involving both Jupiter and Saturn (Sekhar et al., 2016). Jenniskens et al. (2002), pointed out

Year	Observation	Reference	ZHR (/h)
1790	P	JPL	-
1795	O-CA	Imoto & Hasegawa (1958); Jenniskens (1995)	-
1858	P	JPL	-
1872	P	JPL	-
1885	P	JPL	-
1899	P	JPL	-
1900	O-F		-
1913	P	JPL	-
1914	O-F	Hoffmeister (1948)	-
1926	P	JPL	-
1940	P	JPL	-
1945	O-CA	Becvár (1946)	120
1953	P	JPL	-
1967	P	JPL	-
1980	P	JPL	-
1981	O-F	Ohtsuka (1994)	55
1986	O-CA	Hillestad (1987); Jenniskens (1995)	110
1993	O-F	Jenniskens et al. (2002)	100
1994	P	JPL	-
1995	O-F	Ohtsuka et al. (1995)	50
1996	O-F	Langbroek (1997)	25
2000	O-CA	Jenniskens et al. (2002)	90
2008	P	JPL	-
2011	O-F	International Meteor Organization	40
2014	O-CA	Moreno-Ibáñez et al. (2017b)	45

Table 2: List of: perihelion passages (P) of comet 8P/Tuttle from the JPL (JPL-HORIZONS, *ssd.jpl.nasa.gov*); large observed Ursid outburst associated with the filament (O-F); and Ursid outbursts that took place when the comet was close to its aphelion (O-CA). For the O-F and O-CA the ZHR is indicated when available.

the effect of Jovian resonances in the orbital evolution of the meteoroids detached from 8P/Tuttle. Since the comet 8P/Tuttle is trapped in a 15 : 13 resonance with Jupiter its period is fixed at about 13.6 years. Note that provided the high inclination ($i = 55^o$) and argument of the perihelion ($\omega = 207^o$) of the comet's orbit, the encounters with Jupiter are exceptional and poorly effective in altering the orbit of the comet. The orbits of the meteoroids initially released near the comet's perihelion slowly evolve due to the radiation pressure and become gradually trapped in a 7 : 6 mean-motion resonance with Jupiter. Consequently, these meteoroids have a roughly fixed period with 8P/Tuttle determined by this resonance, 13x7/15x6 = 1.011. Hence, in 45 or 46 orbits (around 620 years), the comet and meteoroids will be exactly out of phase (one at its perihelion, other at its aphelion). For such extended time ranges, close encounters with planets and non-gravitational effects can remove the meteoroids from the resonance with Jupiter (e.g. Dmitriev et al., 2015), and only some dust trails can eventually evolve to this fixed period.

The explanation provided by Jenniskens et al. (2002) was partially supported by the observations obtained during the observational campaign they carried out at the expected outburst of the year 2000. However, due to the lack of historical scientific record more observations were required to corroborate and fully understand the celestial mechanics behind the Ursid's outbursts.

Meteoroids in the filament and trapped in the resonance were both predicted (from theoretical and computationally approaches) to reach the Earth again in December 2014. In order to properly record this exceptional event, the SPanish Meteor Network (SPMN) set up a campaign with the collaboration of the recently established French Fireball Recovery and InterPlanetary Observation Network (FRIPON) to monitor the 2014 Ursid meteor shower. The use of several SPMN high sensitivity CCD video devices allowed the recording of Ursid meteors with good spatial resolution. As might be expected in December, bad weather hampered the continuous observations carried out at southern SPMN stations. However, three Spanish north-east stations located in Catalonia as well as south stations in France succeeded in detecting these meteors during the night of the 22^{nd} to 23^{rd} of December 2014. Note that, as it will be discussed later, the meteor data set for which a reliable analysis could be performed was limited. Thus, here the focus is only set on the observations and results of the aphelion outburst.

3.2.1 *Ursid ourburst predictions for December 2014*

The encounter between dust trails and the Earth can be numerically simulated if some considerations are assumed. Such simulations help constraining beforehand the meteor shower intensity, its duration and the meteor average magnitude. In order to plan the 2014 SPMN-FRIPON Ursids' campaign, a set of simulations using the software developed by Vaubaillon et al. (2005a,b) were carried out. The simulation involved computing the evolution of possible dust trails released from the comet 8P/Tuttle at 21 perihelion passages between AD 351 and AD 2008. The results suggested that only

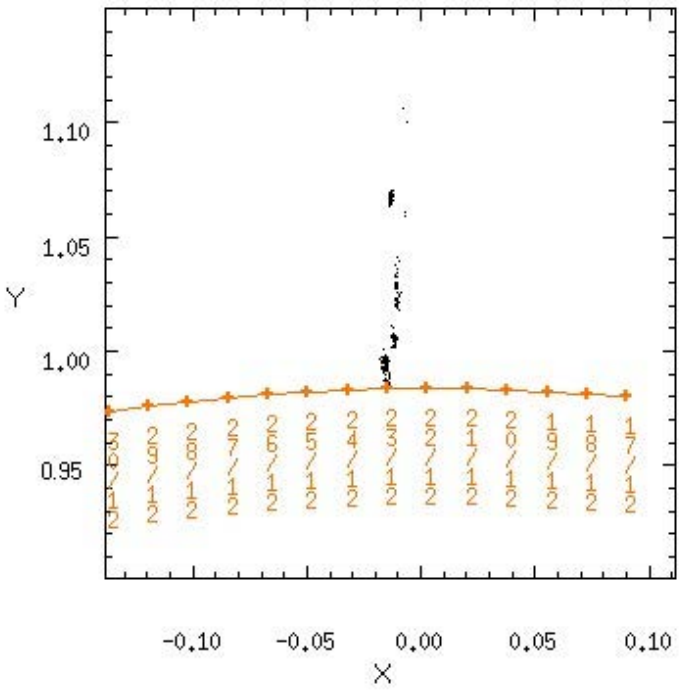

Figure 7: Nodes of the dust trails encountering the Earth in 2014. The trajectory of the Earth is also plotted. X and Y values indicate the coordinates on the ecliptic plane.

meteoroids released in year 1392 evolved in a way that would encounter the Earth in 2014 (exactly in line with the calculation given above of requiring about 620 years for the meteoroids to evolve). This encounter was predicted to be on December 23^{rd} at 00^h46 (UT), at a solar longitude of $\lambda_0 = 270.743^o$. The simulations carried out showed that the meteoroid swarm released in the year 1392 is the best candidate to encounter the Earth in this date because those particles within the swarm encountering the Earth belong to a single trail, cross the Earth in a single year, and show no close encounters with other planets that would have altered their orbit.The nodes of its orbit and the Earth trajectory are plotted in Figure 7.

Jenniskens (2006) claimed that the most likely trails to cause the previous Ursid aphelion outbursts are those released from the comet in 1392 and 1405, and also predicted that the 2014 Ursid outburst would be caused by a dust trail detached from the comet in 1405. This encounter was expected for December 22^{nd} 2014 at 23^h38 (UT) at a solar longitude of $\lambda_0 = 270.838^o$. In addition, the calculations carried out by Jenniskens (2006) indicated that the Ursid filament would encounter the Earth at 17^h05 (UT) on December 22^{nd}, with $\lambda_0 = 270.56^o$.

Network	Station (Province)	Longitude	Latitude (N)	Alt. (m)	Imaging System
SPMN	Montsec (Lleida)	00º 43´ 46” E	42º 03´ 05”	1570	AS
SPMN	Montseny (Girona)	02º 31´ 14” E	41º 43´ 17”	300	WFV
SPMN	Folgueroles (Barcelona)	02º 19´33” E	41º 56´ 31”	580	WFV
SPMN	Ebre Observatory	00º 29´ 44” E	40º 49´16“	50	WFV
FRIPON	Pic du Midi	00º 08´34” E	42º 56´11”	2876	AS
FRIPON	Dax Observatory	01º 01´49.8” W	43º 41´ 36.4”	470	AS

Table 3: Details of the SPMN and FRIPON stations involved in the Ursid aphelion outburst campaign. Acronyms for the different imaging systems are: AS (low-scan-rate CCD all-sky camera), and WFV (Wide field video cameras).

3.2.2 *Instrumentation and data reduction techniques implemented in the campaign*

The monitorization of the meteor shower was performed thanks to the joint effort of the SPMN and FRIPON. Although tens of stations were involved in the campaign, the bad weather conditions reduced the number of operational stations to six. The complete list of the stations involved is shown in Table 3.

The SPMN, which started its first operations back in 2002 (Trigo-Rodríguez et al., 2004c), has well-equipped facilities that use an array of low-light CCD video cameras (Water Co. models 920H and 902H Ultimate) which are provided with the UFO Capture software that allows autonomous continuous monitoring of the sky. The video cameras used in the campaign are equipped with a half-inch Sony interline transfer CCD image sensor with their minimum lux rating from 0.01 to 0.0001 lx at f1.4. The video cameras employ aspherical fast lenses with focal lengths ranging 4-12 mm, and focal ratios between 0.8-1.2. The detections are registered in a cluster of computers that synchronize according to GPS devices, providing meteor recording with an accuracy of 0.1 seconds (Madiedo & Trigo-Rodríguez, 2008; Madiedo et al., 2010). The system allows multi-area sky coverage with each camera, to obtain point-like star images and detect meteors showing an apparent magnitude of $+3 \pm 1$. The video system used consists of a PAL standard at 25 frames per second, and with a resolution of 720 x 576 pixels (Madiedo et al., 2016).

The reduction pipeline followed in this research is as in Trigo-Rodríguez et al. (2004c). The reduction software generates a composite image of the complete meteor atmospheric trajectory where the background stars can be identified. Then, a manual astrometric analysis is undertaken in order to retrieve the pixel position of the meteor trail and the surrounding stars that serve as calibrators (see Chapter 2). Introducing these data into the NETWORK software (Trigo-Rodríguez et al., 2004c), which follows the methodology developed by Ceplecha (1987), the trajectory, velocity and radiant data are derived. The AMALTHEA software, developed by Madiedo, is used to derive computationally

the orbital parameters (Trigo-Rodríguez et al., 2009b,c; Madiedo et al., 2011).

As for the FRIPON stations involved in the campaign, they have DMK 23*G*445 all sky cameras (from Imaging Source GmbH). This model contains a Sony Chip ICXX445 (1348 x 976 pixels, 5 x 4 mm). These cameras allow exposures of 30 ms and are equipped with a 8.5 mm sensor. A Focusave lens of 1.25 mm and a focal rate of 2.0 has been chosen to fulfill the focal length requirements (from 1 to 1.5 mm) of the stations (Colas et al., 2014). The information registered is transmitted to the store disks through a GigE Vision protocol.

Also, with the intention of elucidating the intensity of the outburst, the meteor shower was also studied using a forward-scatter radio system operating at a frequency of 143.05 MHz. The radio station is located in Jaén (south of Spain), it employs an 8 dBi six-element Yagi antenna and a Yaesu FT817 ND radio receiver, and listens to the Grand Réseau Adapté à la Veille Spatialle (GRAVES) radar located in Dijon, France (*http://www.onera.fr/dcps/graves*).

3.2.3 *Observations*

This rare phenomenon did not go unnoticed, and many other observers reported their results on the expected Ursid outburst of 2014. Gajdoš et al. (2015) registered 19 Ursids between 21^h20 UT, Dec. 22^{nd} and 05^h35 UT Dec. 23^{rd}. These were single station detection using the All-sky Meteor Orbit System (AMOS; Tóth et al., 2015) and so they could not derive the orbital data for these meteors. Note that, as described in Ceplecha (1987) at least two observations of the meteor are required to accurately determine the atmospheric trajectory of the body. The NASA's Camera for All-sky Meteor Surveillance (CAMS) project in California, detected 20 meteors during the main activity time (01^h32 UT Dec. 23^{rd} to 04^h00 Dec. 23^{rd}) and 15 more after this time (Brown et al., 2015) at $\lambda_0 = 270.85^o$. The Canadian Meteor Orbit Radar (CMOR) detected up to 85 meteors between 23^h15 UT (Dec. 22^{nd}) and 00^h45 UT (Dec. 23^{rd}) (Brown et al., 2015). There are also radio meteor detections (forward-scatter technique) by Yrjöla (Kuusankoski, Finland) reporting high Ursid meteor activity in this period (Brown et al., 2015).

The SPMN - FRIPON campaign optically detected 30 Ursid video meteors recorded at the SPMN stations listed in Table 3. The value of the *population index*, r, which is a factor that indicates how many times bigger is the meteor population of a magnitude regarding the population at a previous magnitude, is 1.8 ± 0.6 and it is similar to the 1.7 found by Molau et al. (2015). Low values of the population index usually indicate that the shower is old provided the smaller number of small members. This is in agreement with the meteoroid swarms under study which probably detached from the comet around 620 years ago. Table 4 shows the brightness magnitude distribution of the Ursids imaged during the campaign. The mean Ursid ZHR was around 19, in agreement with the ZHR=10 prediction of Jenniskens (2006); but peaking with a ZHR=45 ± 19 which

Magnitude	−5	−4	−3	−2	−1	0	+1	+2	+3	N	r
Number	1	2	1	1	2	4	6	8	5	30	1.8 ± 0.6

Table 4: Magnitude distribution of all Ursids imaged by SPMN video cameras during the night of December 22^{nd}-23^{rd}, 2014.

Time interval (UT)	Mean Solar longitude (^{o})	Ursids	Coma Berenicids	Sporadics
$18^h15 - 19^h15$	271.64	1	0	1
$19^h15 - 20^h15$	271.68	3	0	0
$20^h15 - 21^h15$	271.73	3	0	0
$21^h15 - 22^h15$	271.77	1	0	0
$22^h15 - 23^h15$	271.81	2	1	1
$23^h15 - 00^h15$	271.85	6	0	3
$00^h15 - 01^h15$	271.89	1	3	1
$01^h15 - 02^h15$	271.93	1	0	1
$02^h15 - 03^h15$	271.97	1	2	3
$03^h15 - 04^h15$	272.02	2	2	10
$04^h15 - 05^h15$	272.07	6	3	8
$05^h15 - 06^h15$	272.11	2	3	3

Table 5: Ursids, Coma Berenicids and sporadic meteors recorded from the Folgueroles SPMN video station, given every hour during the night of 22^{nd}-23^{rd} December 2014. Note that the meteor limiting magnitude recorded by the cameras was +4. The mean hourly rate was $ZHR = 19 \pm 3$, with a peak at 23^h45 UTC of $ZHR = 45 \pm 19$.

is also close to the value reported in Molau et al. (2015).

During the same period at which the Ursid meteor shower is active, there is another meteor shower showing active: Coma Berenicids (between December 12^{th} and 23^{rd}; see the reports available at the International Meteor Organization, IMO). All the meteors detected that night, between 18^h15 on December 22^{nd}, and 6^h15 on December 23^{rd}, from the SPMN station located in Folgueroles are compiled hourly in Table 5 (Ursids, Coma Berenicids and sporadic meteors). Note that Folgueroles is equipped with three wide-field video cameras that allow full sky coverage, and this was the darkest sky available that night. The meteor limiting magnitude recorded by the cameras is +4, which is practically the maximum visible magnitude acknowledged by Jenniskens et al. (2002) for the outburst of the year 2000. Two significant increases in the Ursid hourly rate occurred around 23^h45 and 04^h45 UT. Also, there was a notable activity of sporadics between 03^h15 and 05^h15.

The forward-scatter technique operating at a radio station in Jaén (Andalusia, Spain) provided some insight on the Ursid meteor activity. Despite the fact that the forward-scatter technique is unable to distinguish the source of each detection, the observations

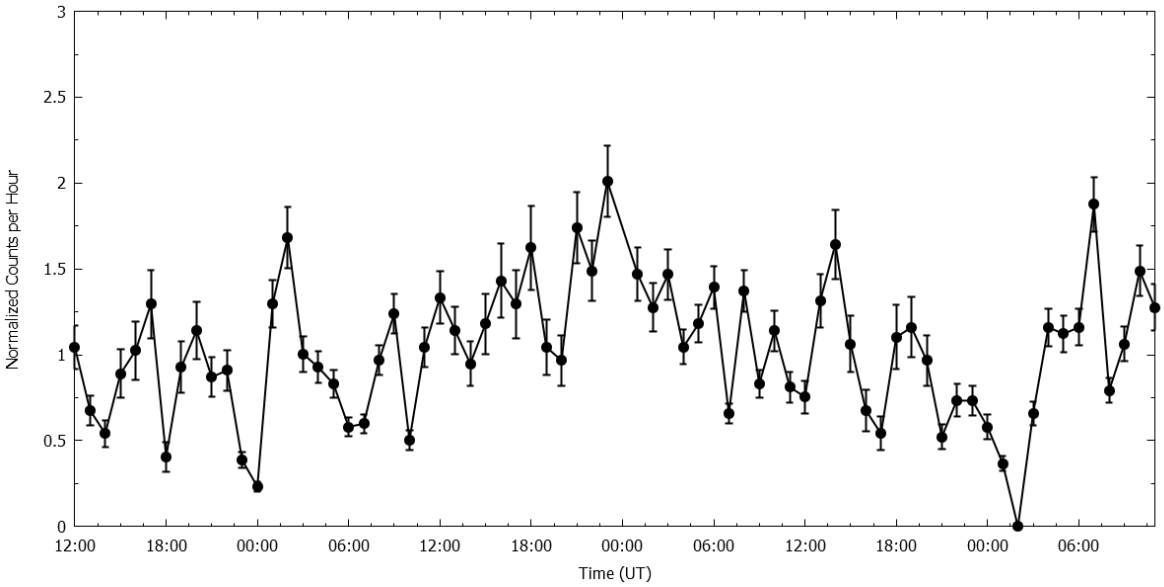

Figure 8: Radio meteors counts normalized per hour (over the mean number of counts each hour) detected at Jaén forward-scatter station, from December 21^{nd} at 12^h00 (UT) to December 24^{th} at 12^h00 (UT). An increase activity was observed in the night of 22^{nd} to 23^{rd} of December.

indicate significant activity between 00^h00 and 01^h00 on December 23^{rd}. In Fig. 8 the normalized echoes (over the mean number of echoes detected every hour) detected between 12^h00 UT (Dec. 21^{st}) and 12^h00 UT (Dec. 24^{th}) are plotted. The results prove an increasing activity that night starting close to the predicted time on December 23^{rd} at 00^h46 (UT).

3.2.4 *Result: trajectory, radiant and orbital data*

Due to bad weather conditions over the Iberian Peninsula the observations were limited to the northeast region of Spain and southeast of France. Also, it had been envisaged that collaboration between the SPMN and FRIPON would provide multi-station observations of any recorded Ursid meteors. Unfortunately, most of the meteors showed magnitudes below the limiting magnitude of the FRIPON cameras, and faint meteors could not be detected from the french side. The equipment of the SPMN is able to detect lower magnitudes and so the number of detected meteors was higher. Besides, due to the great distances between the stations and the weather conditions, there were no meteor detection coincidences that could lead to accurate trajectory determination. Despite this, the SPMN network successfully recorded 11 Ursid meteors at multiple stations that could be further analysed.

Multiple station detections can be used to derive the trajectory, radiant and orbital elements of the meteor atmospheric flight. The reliability of the intersection of planes methodology developed by Ceplecha (1987) to derived accurate results depends on the angle, Q, between the plane containing the two observing stations and the plane in

which the meteor is apparently moving. If Q is small, triangulation measurements become unreliable as the triangle has degenerated into a near straight line. Only meteors for which the Q value is higher than 20^o are accepted in this analysis. As a consequence of the bad weather already mentioned, which made observing difficult or impossible from some stations, most of the active station tended to be aligned in a rough North-South direction. Since the radiant point of the Ursids is close to the Pole Star, there was an inevitable preponderance of meteors moving in a roughly North-South direction. These two facts imply that for many observed meteors the angle Q was less than 20^o and so the determination of trajectories was unreliable. In addition to this, some of the meteor tracks were out the field of view of the cameras for some of the time and these have also been eliminated from the analysis as either the start or end point of the trail could not be accurately determined.

From the initial 11 multi-station Ursid meteor detections, complete and reliable data were only obtained for four meteors. The orbital elements, with errors, are obtained for these four meteors. In Table 6 the absolute visual magnitude (M_V), the entry and the terminal heights (h_e, h_t), the geocentric radiant (α_g, δ_g) expressed in J2000.0, and the pre-atmospheric, geocentric, and heliocentric velocities (V_e, V_g, and V_h) of these Ursid meteors are given. The SMPN nomenclature of each meteor indicates the date of its detection and its order of detection (i.e. A for the earliest and C for the latest). From this information it is also possible to estimate the meteoroid size (the radius) of SPMN data set. According to Jenniskens (2006) the mass of the meteoroid can be obtained from:

$$\log M = 6.31 - 0.40 M_V - 3.92 \log V_e - 0.41 \log(sin(h_r)) \tag{18}$$

Where h_r is the radiant altitude (which is 90^o at zenith). The above Equation (18) is derived considering the luminous efficiency (τ) described in Chapter 2. Since this efficiency is not fixed and it is under discussion (Gritsevich & Koschny, 2011), the results of Equation (18) shall be taken with care. The mass of the SPMN meteor data set is shown in Table 6. Finally, the sizes (the radii) can be derived assuming a spherical shape and a fixed density of 3500 kg/m^3 (Ceplecha et al., 1998). While cometary material may show a lower density value provided its icy composition, the trailets studied here were released from the comet nearly 620 years ago and so subsequent perihelion passages shall have reduced the number of volatiles. Note however, that a variation between 2000 and 7000 kg/m^3 in the density value of the SPMN meteor data set keeps the average meteoroid's size in the range of $1.5 - 2.5$ cm.

From these measured radiant positions and velocities, the orbital elements can be derived in a standard way (described in Trigo-Rodriguez et al., 2008, for example). These are given in Table 7. Figure 9 plots the resulting orbit of the meteoroid SPMN 221214A and that of 8P/Tuttle for comparison; together with the SPMN 221214A atmospheric trajectory and its projection on the ground.

Meteor Code	M_V	h_e (km)	h_t (km)	α_g (^{o})	δ_g (^{o})	V_g (km/s)	V_g (km/s)	V_h (km/s)	Mass (g)	Radius (cm)
SPMN 221214A	-3	93.5	85.5	225.43 ± 30.2	74.47 ± 0.21	33.8 ± 0.4	32.1	39.1	66.8	1.7
SPMN 231214A	-4	88.6	85.6	225.4 ± 0.3	75.88 ± 0.21	32.2 ± 0.4	30.1	39.0	99.8	1.9
SPMN 231214B	-5	96.3	69.7	229.6 ± 0.5	75.9 ± 0.4	33.7 ± 0.3	31.7	40.4	209.8	2.4
SPMN 231214C	-4	93.3	75.8	227.3 ± 0.4	76.7 ± 0.4	32.2 ± 0.4	30.1	39.4	117.7	2.0

Table 6: Trajectory, radiant, velocities, mass, and radius data for 4 multi-station Ursid meteors registered in December 2014 (J2000.0).

Meteor Code	Day	q (AU)	a (AU)	e	i ($^\circ$)	ω ($^\circ$)	Ω ($^\circ$)
SPMN 221214A	22.96484722	0.94861 ± 0.001	4.16 ± 0.17	0.772 ± 0.025	51.6 ± 0.5	203.3 ± 0.3	270.8240
SPMN 231214A	23.03800579	0.94500 ± 0.00052	3.15 ± 0.24	0.700 ± 0.023	48.9 ± 0.5	205.2 ± 0.3	270.8986
SPMN 231214B	23.05556839	0.9503 ± 0.0011	5.1 ± 0.6	0.815 ± 0.021	50.3 ± 0.4	202.4 ± 0.3	270.9165
SPMN 231214C	23.08608796	0.9448 ± 0.0011	3.5 ± 0.3	0.731 ± 0.020	48.4 ± 0.4	205.0 ± 0.3	270.9477

Table 7: Orbital elements for 4 multi-station Ursids meteors registered in December 2014 (J2000.0).

Number of values averaged	RA ($^\circ$)	Dec. ($^\circ$)	V_g ($km \cdot s^{-1}$)	Source
Prediction $N = 19$	220.85	$+75.4$	33.21	J. Vaubaillon (IMCCE)
Double station $N = 4$	219.85 ± 0.2	$+76.0 \pm 0.2$	32.3	This research
Single station $N = 19$	217.9	$+76.4$	–	Gajdoš et al. (2015)

Table 8: Predicted apparent radiant positions and averaged geocentric velocity V_g of the 2014 Ursid dust trail members according to J. Vaubaillon, compared with the current double station results and single station results from Gajdoš et al. (2015). Equinox (2000.0).

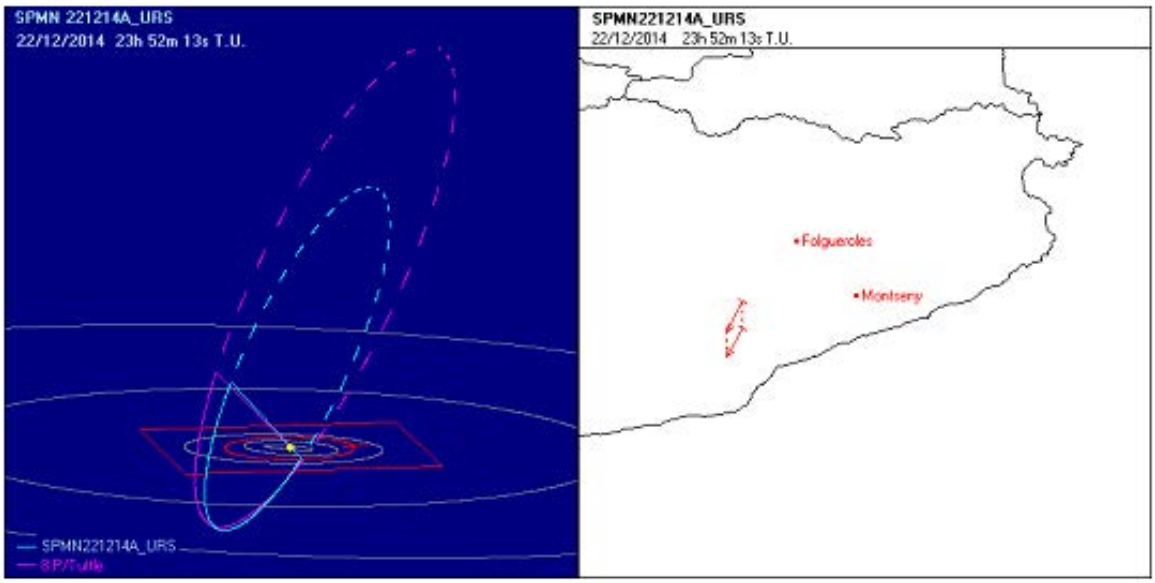

Figure 9: (Left) Heliocentric orbit of meteoroid SPMN221214A and comet 8P/Tuttle. (Right) Atmospheric trajectory and its projection on the ground. The SPMN stations from which this meteor was detected are indicated too.

The numerical simulation of the encounter with possible dust trails that was performed using the software developed by Vaubaillon et al. (2005a,b) and the theoretical apparent radiant for the expected encounter that was estimated using the Neslusan et al. (1998) code, method Q (Hasegawa, 1990) are compared in Table 8. Also, the average value derived for the four meteors reported, and the previous single-station results of Gajdoš et al. (2015) are shown. As it can be seen, there is excellent agreement between the observational results in this work and the predictions. There is a small discrepancy regarding the right ascension derived by Gajdoš et al. (2015), probably explained by the limitations in the accuracy of single-station observations. These results can also be compared to previous Ursid outbursts' apparent radiants in 1997 (filament) and 2000 (aphelion outburst) described in Jenniskens et al. (2002). Note that, the perihelion outburst (associated with the filament) described by Jenniskens et al. (2002) actually corresponds to the last remains of outburst activity from the comet perihelion passage of year 1994 (see Table 2). The largest activity took place between the years 1993 and 1995, however, the only reliable meteoroid orbits and meteor radiants related to this activity are those provided in Jenniskens et al. (2002). As it can be seen in Figure 10, the agreement between the value of the averaged apparent radiant presented in this campaign and the individual meteor apparent radiants of previous observations is clear.

3.2.5 *Discussion*

The last time there was an Ursid ourburst when the comet was close to its aphelion occurred back in the year 2000. At that time, Jenniskens et al. (2002) analysed a data set of 59 meteors. This was the first data set available on this event. Despite the data set

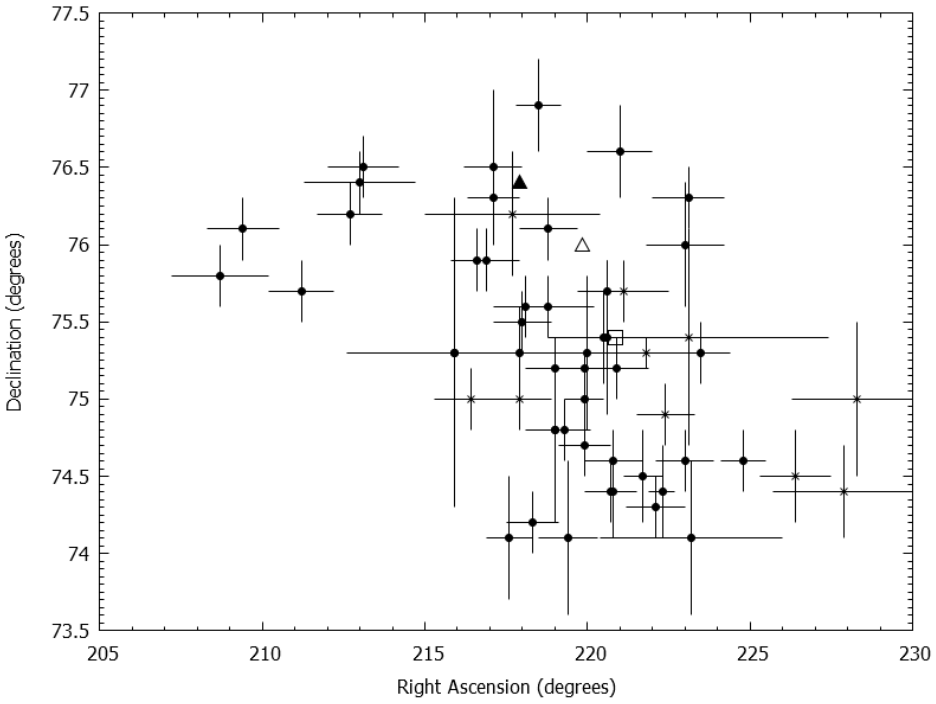

Figure 10: The empty triangle marks the averaged apparent radiant derived from the four meteors presented here; the empty square is the predicted apparent radiant according to J. Vaubaillon software; the filled triangle is the apparent radiant described in Gajdoš et al. (2015). The rest of points follow those given by Jenniskens et al. (2002), filled circles mark radiant positions for the 2000 aphelion outburst meteors, and asterisks indicate radiants for the 1997 perihelion outburst meteors.

Year	1997 (10 orbits) Filament	2000 (59 orbits) Aph. Outburst	2014 (4 orbits) Aph. Outburst
Date	Dec. 22.434	Dec. 22.32	Dec. 23.0375
h_e	104.9	107.1 (52 orbits)	92.93
h_t	94.2	96.2 (52 orbits)	79.15
RA_{geo}	222.1	219.0	219.85
$Dec._{geo}$	75.0	75.3	76.0
V_g	32.25	33.05	32.3
a	4.62	4.673	3.978
e	0.795	0.799	0.755
q	0.944	0.940	0.956
i	51.5	52.5	49.8
ω	204.9	205.9	203.9
Ω	270.64	270.76	270.9

Table 9: Averaged date, beginning and ending heights, geocentric radiant position, geocentric entry velocity and orbital elements for the filament observations in 1997 and the aphelion outburst observation in 2000 (Jenniskens et al., 2002) and 2014 (presented in this work).

presented in this study is considerably smaller, it is compared against Jenniskens et al. (2002) results. Besides, as the Ursid filament was also encountering the Earth at the same date, it could be possible that some of the current SPMN meteor data set could contain members of that filament. The last time the Ursid filament come into collision with our planet was in 1997 (Jenniskens et al., 2002). Table 9 gives the mean values of the trajectory and orbit for the 2000 and the 1997 outburst given by Jenniskens et al. (2002) as well as the SPMN results for the 2014 outburst. It can be seen that the SPMN meteor mean trajectory and orbital values slightly differ from those measured in the 2000 outburst.

The meteoroid stream that causes the outbursts of years 2000 and 2014 needed only one orbital revolution to encounter the Earth again. In this period, unless close planetary encounters may have altered its motion or orbital distribution, the mean values of the orbital elements shall have remained fairly similar. Figure 11 (top) is a plot of reciprocal semi-major axis versus perihelion distances for outburst taken from Jenniskens et al. (2002) as well as the four SPMN meteors. Also, meteoroids belonging to the outburst of 1997 related to the filament are plotted for comparison. As it can be seen, the values are well within the range of the larger data set of past outbursts. Also shown is the location of the 6 : 7 mean-motion resonance. According to Jenniskens et al. (2002), the dust trails producing the outburst when the comet is in its aphelion might be trapped in a 6 : 7 resonance with Jupiter. The orbits of the four meteors described in this work are slightly closer to the mean-motion resonance location than many of the meteors observed in 2000. Two of them (SPMN 221214A and SPMN 231214B) are in fact very close to the resonance line and the other two slightly further away.

To extend the comprehension of the behaviour of the SPMN data set a plot of the inclination against perihelion distance for the same set of meteors is shown in Figure 11 (bottom). Two of the meteors (SPMN 221214A and SPMN 231214B) studied here, have inclinations that are very much in line with the other observed meteors while two (SPMN 231214A and SPMN 23124C) have inclinations below 49^o, well below any other recorded value for the Ursids. The small size of the current SPMN data set hinders the discussion on whether the differences displayed in Figure 11 are significant or not. There are two meteors in the 2014 data set (SPMN 221214A and SPMN 231214B) that are very much in agreement with all the other evidence and two that do not fit so well. With a much larger data set it would be easy to determine whether the two discrepant ones are outsiders or not.

The discrepancies can be partially explained by the meteor detection and measurement limitations. These depend on the meteor luminosity, that in turns, is a function of the body pre-entry mass, the initial velocity to the power of three and the sine of the slope between the horizon and the trajectory (Gritsevich & Koschny, 2011; Bouquet et al., 2014, and Chapter 2). If the meteoroid's geocentric velocity is relatively slow, it is then possible that the meteor is not visible to detectors until it reaches lower atmospheric heights. In these cases, when the meteor trajectory is derived, the entry velocities outlined from the observations might be slightly underestimated. The orbital semi-major axis, the eccentricity and the inclination are obtained from the entry velo-

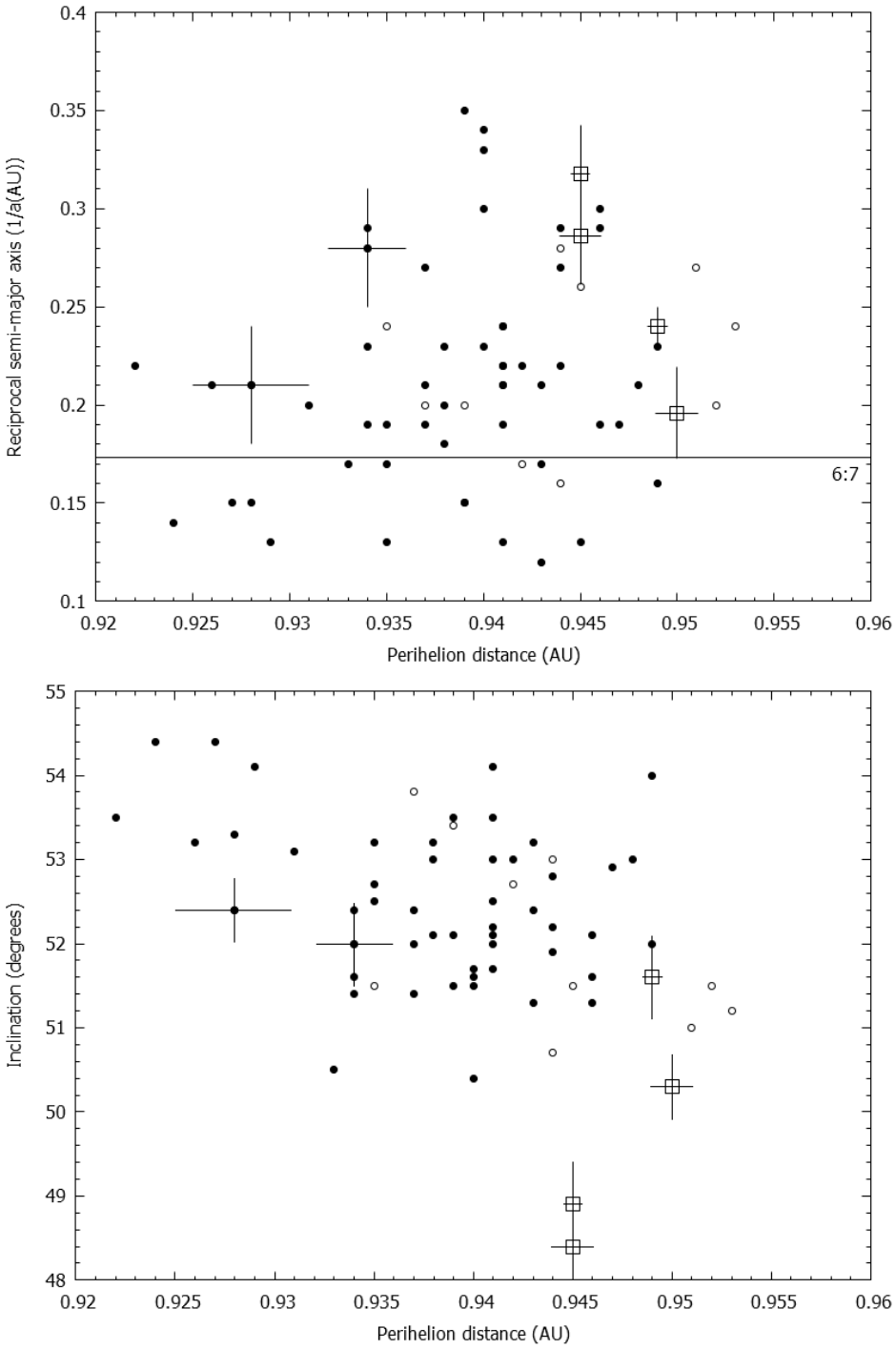

Figure 11: A plot of the perihelion distances versus the reciprocal semi-major axis (top) and versus the orbit inclination (Bottom)for the meteors registered at: the Ursid aphelion outburst in the year 2000 (filled circles) as in Jenniskens et al. (2002); the perihelion outburst of 1997 (empty circles) as in Jenniskens et al. (2002); and the four Ursids meteors studied in this work (open squares). Error bars of the four SPMN meteors and a couple of representative error bars of 2000 outburst data reported in Jenniskens et al. (2002) are plotted. The straight line indicates in the Top figure indicates the resonance 6 : 7 inverse semi-major axis.

city and the trajectory slope and could be affected by slight detection inaccuracies.

Otherwise, if the orbital elements derived for the meteoroids producing the four meteors are correct, then the possible effect of close Earth encounters on the orbits of the dust trails should be considered. The dust trails are closest to Earth when they are near perihelion and will thus be travelling with a slightly higher heliocentric velocity than the Earth. The cumulative effect of repeated encounters will be to decelerate the meteoroid. For a mathematical formulation of the effects of changing orbital energy on meteoroids, see Williams (2002, 2004). This could explain the different orbits obtained for two of the SPMN Ursid meteoroids. Unfortunately, the lack of reliable Ursid orbital data in past scientific literature on the meteor aphelion outburst before AD 2000 combined with this small meteor data set, makes it impossible to confirm that this occurred in the Ursids.

Finally, it could be argued that some of the four meteors reported here (especially the two discrepant ones) belong to a different perihelion release from the parent comet. An encounter with the filament material was predicted to occur in practically the same date as the aphelion outburst. This hypothesis can be ruled out because, despite the broader shape of the filament, previous studies (Jenniskens, 2006) indicate that they should exhibit higher inclination orbits, which is the opposite of what was found.

3.3 ASTEROID 2014UR116 AS THE PARENT BODY OF ANNAMA

Asteroid material with stony or iron bulk composition do normally encounter the Earth at lower entry velocities than cometary material provided the lower eccentricity their orbits usually exhibit. Besides, their mechanical strength is notably larger (Trigo-Rodríguez & Llorca, 2006, 2007; Blum et al., 2006; Trigo-Rodríguez & Blum, 2009a). Therefore, this material will bear the intense atmospheric aerodynamical load for longer times and reach lower atmospheric altitudes or even the Earth surface (i.e., Borovička et al., 2013a; Popova et al., 2011; Trigo-Rodríguez et al., 2015). Meteorite falls are usually related to meter-sized bodies (Ceplecha et al., 1998) and occur unexpectedly. Actually, most of the current meteorite collection has been recovered during campaigns on desserts (e.g., Bevan & Binns, 1989; Bischoff & Geiger, 1995; Reid et al., 1995) and the artic pole (e.g., Greely, 1915; Yoshida et al., 1971; Cassidy et al., 1992), or casual findings (usually reported to the Meteoritical Bulletin Online Database). Meteorites provide relevant clues about the nature and physico-chemical properties of asteroids, for example regarding the evolution of the asteroid composition (Madiedo et al., 2013a; Moyano-Cambero et al., 2017). However, as long as this information cannot be linked to a specific asteroid the overall picture will not be completed. In order to achieve this, it necessary to obtain both the atmospheric trajectory and the pre-atmospheric orbit of the impacting meteoroids from the accurate study of a bolide. Thus, observing the atmospheric passage increases the chances to understand the delivery mechanism

and possible source region in the MAB of the impacting body. Up to date, only the atmospheric passage of a short number of 30 recovered meteorites has been recorded. These cases are gathered in Table 10, which is an update of the tables presented in Trigo-Rodríguez et al. (2015) and Borovička et al. (2015a).

Although the scarce statistics available for this data set (Table 10), leaves many questions unresolved, there is clear evidence that most large meteoroids encountering the Earth originate in MAB asteroids (Trigo-Rodríguez et al., 2007). Collisions between asteroids in the MAB produce fragments that can escape and reach heliocentric orbits. When crossing destabilizing MAB resonances, the gravitational perturbation turns them into planet crossers. The average time that a mean belt asteroid orbits in a planetary crossing configuration depends on the resonance that rules its movement (Bottke et al., 2002; Morbidelli et al., 2002). If, eventually, are trapped in short NEO orbits, their behaviour could become chaotic because of continuous close encounters with the inner planets (Pauls & Gladman, 2005). In the case of larger bodies, i.e., meter-sized bodies, there are other non-gravitational effects that contribute to insert the meteoroid into planet crossing orbits. The forces and moments exerted on large bodies by the thermal radiation alter the orbit semi-major axis (*Yarkovsky* effect) and body spinning axis (*Yarkovsky - O'Keefe - Radzievskii – Paddack*, a.k.a *YORP effect*); see Bottke et al. (2006).

The perihelion distances of the meteorite data set listed in Table 10 points out that, except for the Bunburra Rockhole meteorite (whose orbit is classified within the Aten family type; Bland et al., 2009), the pre-atmospheric orbits of all these meteoroids belong to the Apollo Family type of NEAs. The large asteroid population of NEO at short orbits makes it very complicated to speculate on a plausible relationship between a recovered meteorite and a NEA. Nevertheless, for few events potential relationships were suggested in the past. The impact of Almahatta Sitta (2008) was predicted before the asteroid 2008 TC_3, its progenitor, partially disintegrated in the Earth's atmosphere and landed as a set of meteorites (Jenniskens et al., 2009). Maribo (2009) and Sutter's Mill (2012) are discussed to have originated in a NEO belonging to the Taurid Complex (Jenniskens et al., 2012; Tubiana et al., 2015). Three feasible parents were outlined for Košice (2015) using a dissimilarity criterion (see the next section) and numerical simulations that include meteoroid clones (Borovička et al., 2013b), although more data is required to provide more concluding results. Finally, for Chelyabinsk (2013) a preliminary relationship with asteroid 1999 NC_{43} is suggested according to a short-period (2000 years) simulation of a set of 1000 test particles (Borovička et al., 2013a).

Concerning Annama meteorite, the case-study outlined in this chapter, this event took place on April 19^{th}, 2014, at $22^h14^m09.3 \pm 0.1^s$ UTC, when a bright fireball flew over the border between Finland a Russia. The luminous phenomenon was recorded by photographic and video equipment patrolling the skies by the Finnish Fireball Network. With the compiled information, the atmospheric trajectory and the pre-impact orbit were accurately calculated. Also, the development of a well constrained dark flight path indicated a delimited strewn field on the Kola peninsula (Russia), where two meteorites (120 g Annama I, and 48 g Annama II) were found only about 100 meters from

Meteorite Name	Year	Type	V_g	q	$1/a$	e	i	ω	Ω	Reference
Pribram	1959	H5	17.43	0.789	0.416	0.671	10.48	241.75	17.79	Ceplecha (1961); Spurný et al. (2003)
Lost City	1970	H5	14.20	0.967	0.602	0.417	12.00	161.00	283.00	McCrosky et al. (1971)
Innisfree	1977	L5	14.20	0.986	0.534	0.473	12.27	177.97	316.80	Halliday et al. (1978)
Benešov	1991	LL3.5,H5	21.26	0.925	0.403	0.627	23.98	218.37	47.00	Spurný et al. (2014)
Peekskill	1992	H6	14.70	0.886	0.671	0.410	4.90	308.00	17.03	Brown et al. (1994)
Tagish Lake	2000	CM2	15.80	0.884	0.505	0.550	2.00	224.40	297.90	Hildebrand et al. (2006)
Morávka	2000	H5-6	19.60	0.982	0.541	0.470	32.20	203.50	46.26	Borovicka et al. (2003)
Neuschwanstein	2000	EL6	20.95	0.793	0.417	0.670	11.41	241.20	16.83	Spurný et al. (2003)
Park Forest	2003	L5	16.10	0.811	0.395	0.680	3.20	237.50	6.12	Brown et al. (2004)
Villalbeto de la Peña	2004	L6	16.90	0.860	0.435	0.630	0.00	132.30	283.67	Trigo-Rodríguez et al. (2006)
Bunburra Rockhole	2007	Achondrite	13.40	0.643	1.175	0.245	9.07	209.87	297.59	Bland et al. (2009)
Almahata Sitta	2008	Ureilite	12.42	0.899	0.764	0.312	2.54	234.45	194.10	Jenniskens et al. (2009) and NEO JPL database for 2008 TC_3
Buzzard Coulee	2008	H4	18.00	0.961	0.813	0.220	25.50	212.00	238.90	Milley (2010)
Maribo	2009	CM2	28.50	0.481	0.450	0.800	0.26	99.00	117.64	Haack et al. (2011)
Jesenice	2009	L6	13.78	0.997	0.571	0.431	9.60	190.50	19.19	Spurný et al. (2010); Bischoff et al. (2011)
Grimsby	2009	H4-6	20.90	0.982	0.490	0.518	28.07	159.87	182.96	Brown et al. (2011)
Kosice	2010	H5	10.30	0.957	0.369	0.647	2.00	204.20	340.07	Borovička et al. (2013b)
Mason Gully	2010	H5	14.53	0.982	0.405	0.602	0.83	18.95	203.21	Spurny et al. (2012)
Križevci	2011	H6	14.46	0.739	0.648	0.521	0.64	254.40	315.55	Borovička et al. (2015b)
Sutter's Mill	2012	CM2	28.60	0.456	0.386	0.824	2.38	77.80	32.77	Jenniskens et al. (2012)
Novato	2012	L6	13.67	0.988	0.478	0.526	5.51	347.35	24.99	Jenniskens et al. (2014)
Chelyabinsk	2013	LL5	19.03	0.738	0.581	0.571	4.98	107.67	326.46	Borovička et al. (2013a)
Annama	2014	H5	24.20	0.634	0.502	0.680	14.6	264.80	28.59	Trigo-Rodríguez et al. (2015)
Žďár nad Sázavou	2014	L3.9	18.60	0.671	0.476	0.681	2.83	257.75	257.26	Spurny et al. (2016)
Murrili	2015	H5	13.82	0.994	0.382	0.620	3.58	356.30	64.63	Bland et al. (2016)
Ejby	2016	H5-6	9.44	0.968	0.356	0,655	0,96	197,75	317.21	Spurný et al. (2017a)
Stubenberg	2016	LL6	14.00	0.924	0.656	0.395	2.07	221.2	346.52	Spurny et al. (2016)
Dingle-Dell	2016	LL5	10.05	0.923	0.444	0.590	4.05	215.77	218.25	Devillepoix et al. (2018)

Table 10: List of recovered meteorites for which the atmospheric trajectory and the pre-atmospheric orbit are available. The organization is as follows: (1) Meteorite name; (2) Year of the meteorite recovery; (3) Meteorite composition classification; (4) Geocentric entry velocity of the meteoroid [km/s]; (5-10) Orbital parameters of the meteoroid: distance of the perihelion [AU], inverse of the semi-major axis [1/AU], eccentricity, inclination [^{o}], argument of the perihelion [^{o}], longitude of the ascending node [^{o}]; (11) Reference for further information. Note that the associated uncertainties are not shown for simplicity.

the predicted landing path on May 29^{th} and May 30^{th}, 2014 (Gritsevich et al., 2014; Trigo-Rodríguez et al., 2015; Kohout et al., 2015). The Annama meteorite is classified as a H5 chondrite with a bulk density of 3500 kg/m^3 (Kohout et al., 2015, 2017), and its perihelion distance is also contained in the Apollo Family type asteroids.

Here, it is explored the possible relationship between Annama and a group of nine NEAs. This is done by comparing the pre-atmospheric heliocentric orbit of Annama, to the orbit of a selected group of NEA candidates, and a set of clones that are created to resolve any possible inaccuracy derived from the determination of Annama's orbit.

3.3.1 *Dissimilarity criteria*

The time duration that a meteoroid (i.e., Annama) conserves the same heliocentric orbit than its progenitor depends on the degree of effectiveness of the gravitational and non-gravitational forces to which the meteoroid is subjected (which depends on the meteoroid mass, volume, rotation, etc.). These effects are difficult to be evaluated from the information obtained either by the bolide trajectory on the atmosphere or the meteorite study when a fall occurs. When no other information regarding dynamic evolution constraints or compositional similarities are available, the obvious statement to claim a parenthood is that a meteoroid and asteroid shall show the same orbital origin. This is, the evolution of their orbits should have been the same till the disruption point. This point is important, since the population of asteroids in the inner solar system (i.e, NEAs) is particularly abundant (Bottke et al., 2000) and may change rapidly. A temporal orbital association can be casual, and many other orbital relationships cannot be dismissed. Conversely, just because a meteoroid and an asteroid do not show similar orbits at the time the meteoroid impacts the Earth a common origin cannot be disregarded.

The most straightforward comparison of orbits consists of studying the similitude of their orbital elements (semi-major axis, inclination, eccentricity, longitude of the ascending node, and longitude of the perihelion) or a combination of some them (i.e., using the longitude of the perihelion). However, provided the observational uncertainties in the asteroid orbit determination, and measurement inaccuracies in the pre-atmospheric orbit calculation of an impacting meteoroid, it is more convenient to seek for plausible orbital similarities. This is, instead of requesting a minimum level of error in the orbital elements individually, it is better to certify that none of the orbital elements differs notably and that the shapes of the two orbits show a reasonable degree of agreement. This approach is formulated through a dissimilarity criterion which weights the quadratic difference of the individual orbital elements. When this difference is equal or smaller than a cut-off value it can be claimed an apparent link between both bodies at that epoch (the time for which the calculated orbital elements are valid). There is no fixed cut-off value as it depends on the dissimilarity criterion used and the particulars of each study.

The first mathematical formulation of a dissimilarity criterion was carried out by Southworth & Hawkins (1963) when they discussed the association and possible link of new and previous identified meteor showers. Their study compared the orbital planes and the orbit shape of the streams. Given that the perihelion distance (q) was better determined from observations than the semi-major axis (a) the former was preferred and included in the formulation. This dissimilarity criterion is commonly known as D_{SH}, it is the one used in this study, and its mathematical expression is shown in Equation (19). For this criterion is usually assumed that a threshold value of $D_{SH} < 0.15$ (Lindblad, 1971a,b) is sufficient.

$$D_{SH}^2 = [e_B - e_A]^2 + [q_B - q_A]^2 + \left[2sin\frac{i_B - i_A}{2}\right]^2 + sin\, i_A\ sin\, i_B \left[2sin\frac{\Omega_B - \Omega_A}{2}\right]^2 + \left[\left(\frac{e_A + e_B}{2}\right) 2sin\frac{(\Omega_B + \omega_B) - (\Omega_A + \omega_A)}{2}\right]^2 \tag{19}$$

Among all the other perfectly valid dissimilarity criteria formulations, it is worth mentioning the one suggested by Jenniskens (2008). For those NEOs with a short orbital period, the orbital secular perturbations show some dynamic invariant relationships that can be used to derive a dissimilarity criterion. Based on the previous work of Lidov (1961, 1962), Babadzhanov & Obrubov (1989), and Babadzhanov (1990), Jenniskens (2008) outlined the three main invariants $C1$, $C2$ and $C3$, and the D_J criterion (which he initially called D_B) as in Equation (20). For D_J a cut-off value between 0.9 and 1.5 is commonly adopted (Madiedo et al., 2013b).

$$D_J^2 = \left(\frac{C_{A1} - C_{B1}}{0.13}\right)^2 + \left(\frac{C_{A2} - C_{B2}}{0.06}\right)^2 + \left(\frac{C_{A3} - C_{B3}}{14.2^o}\right)^2 \tag{20}$$

with

$C_1 = (1 - e)^2 cos^2 i$
$C_2 = e^2(0.4 - sin^2 i\ sin^2 \omega)$
$C_3 = \omega + \Omega$

As stated before, any other constraint that could be imposed to the parenthood analysis can be combined with the use of the dissimilarity criterion. For example, Steel et al. (1991) slightly modified the D_{SH} to avoid some nodal longitude selection that biased their analysis of the Taurids Complex. As the angles ω and Ω vary faster than other orbital elements, they decided to remove them from the dissimilarity criterion and include extra constraints. Finally, some reviews of other dissimilarity criteria can be found in Jenniskens (2008); Rudawska et al. (2012); Jopek & Williams (2013); or Madiedo et al. (2013b).

3.3.2 *Possible NEA parents for Annama*

The dissimilarity criterion outlines punctual orbital similarities between two bodies, however the only way to assure that both bodies share the same orbital origin is to have the dissimilarity criterion under a reasonable cut-off value (that accounts for possible inaccuracies in the orbital elements' determination at different epochs) for an interval of time. While it seems more logical to have the dissimilarity criterion below the cut-off value at all times from the moment the two orbits show a clear similarity, some inaccuracies in the derivation of the meteoroid pre-atmospheric orbit, the uncertainties on the asteroid orbits, and the propagation of errors in numerical simulations (used to derive the orbital elements at epochs back in time), could eventually lead to reasonable orbital differences. Furthermore, due to well explained facts (i.e., planetary close encounters) the orbits of the asteroid and meteoroid affected by the aforementioned inaccuracies could result into different orbital evolution paths, thus compromising the reliability of the dissimilarity criterion. In this sense, for example, Porubčan et al. (2004) suggest that a backwards integration of 5000 year shall suffice to provide enough clarity on the similarity orbit evolution of meteoroid streams and NEOs.

Before implementing the D_{SH} criterion a list of suitable NEO parent candidates is needed. The only orbital constraint that can be posed to this selection is the Apollo family type pre-atmospheric heliocentric orbit of Annama (Trigo-Rodríguez et al., 2015). A search in the NeoDys (2007) database of suitable Apollo family type NEOs (up to December 2014) resulted in 12 possible NEAs showing $D_{SH} < 0.2$. The possibility of identifying objects meeting a more restrictive $D_{SH} < 0.15$ is also explored, but no match was found at that date. Note that the number of NEOs detected and for which their orbit is calculated increases with time.

The orbital elements of nine of these NEAs (as collected by the Minor Planet Center, *www.minorplanetcenter.net*) along with the corresponding epoch, and the orbital elements of Annama (from Trigo-Rodríguez et al., 2015) are shown in Table 11. Note that three of the original list of 12 were preliminary explored in that paper and they were rejected and not included in this study.

The orbits of the NEAs listed in Table 11 and Annama's orbit are integrated back in time for 20,000 years to gain understanding on the evolution of the D_{SH} criterion. The integrations are performed using the MERCURY6 program (Chambers, 1999), which is a hybrid symplectic integrator designed to numerically simulate N-body problems. While the gravitational effects of the planets and the Sun are included into the simulations, the software would require extra programming tasks to account for non-gravitational perturbations. The comparison between the orbit of Annama and each of the NEAs allows the calculation of D_{SH} at all the simulated time; these are plotted in Figure 12. Although none of the NEAs holds a similar orbit to Annama ($D_{SH} < 0.2$) over the about 20,000 years of simulation, it is remarkable that the D_{SH} criterion for NEAs 2002EB3, 2003GR22, 2004VY14 and 2014UR116 remains low for that time. A sinusoidal behaviour is expected as a result of the different fast orbit evolution of both, the

ID	Epoch	a	e	q	i	ω	Ω	M
2000EJ26	2458000.0	1.383	0.615	0.532	9.226	285.861	10.520	211.531
2002EB3	2458000.0	1.758	0.684	0.555	9.922	300.264	1.597	196.541
2002GM5	2458000.0	2.113	0.695	0.644	7.281	274.512	13.467	345.980
2003GR22	2458000.0	1.385	0.318	0.944	55.833	273.047	21.139	247.162
2004HA1	2458000.0	2.711	0.718	0.764	19.077	259.059	28.943	348.511
2004VY14	2458000.0	1.961	0.650	0.686	7.026	230.344	60.416	278.095
2005TU50	2458000.0	1.426	0.596	0.576	12.422	259.541	22.304	25.517
2006JO	2458000.0	2.377	0.667	0.791	8.200	248.319	41.073	21.737
2014UR116	2458000.0	2.070	0.727	0.565	6.574	286.794	6.003	2.021
Annama	2456762.0	1.988	0.690	0.634	14.65	264.770	28.611	342.10

Table 11: Orbital elements (semi-major axis, eccentricity, perihelion distance, inclination, argument of perihelion, longitude of ascending node, and mean anomaly) of the 12 NEAs (data from the Minor Planet Center) which might be dynamically related to Annama at the Epoch of the meteoroid impact with the Earth's atmosphere. The orbital elements of Annama are also shown (from Trigo-Rodríguez et al., 2015). All the orbital elements refer to the Equinox (J2000.0).The columns are: (1) NEA identification code, ID; (2) Epoch [JD]; (3) semi-major axis [AU]; (4) eccentricity; (5) perihelion distance [AU]; (6) inclination [^{o}]; (7) argument of the perihelion [^{o}]; (8) right ascension of the ascending node [^{o}]; (9) mean anomaly [^{o}];

NEA and Annama.

3.3.3 *Clones and feasible parenthood*

The reasonable similarity of NEAs 2002EB3, 2003GR22, 2004VY14 and 2014UR116 with Annama's orbit motivates a more detailed study made on a case by case basis. At this point, it is important to note that, unlike the study of meteoroid streams where the analysis of the stream mean orbit can alleviate individual extreme behaviours of the stream members (see Jones, 2007; Porubčan et al., 2004), the study of an individual meteoroid relies only on the derived orbital parameters and the associated inaccuracies. Thus, remarking the relevance of deriving accurate pre-atmospheric orbits for the impacting meteoroids. According to this, although Annama's orbit could be directly used for this case by case comparison, the slight pre-atmospheric meteoroid velocity uncertainty that remains due to the complexity of retrieving the meteoroid atmospheric trajectory (Trigo-Rodríguez et al., 2015) requires an alternative approach. Following the methodology implemented in Porubčan et al. (2004); Jones (2007); Madiedo et al. (2013b); and Borovička et al. (2013a,b), a series of Annama clones are created. These clones inherit the orbit shape and configuration of Annama's nominal orbit, except for the little variation in their pre-atmospheric velocity (V_e). This slightly alters the values of the semi-major axis, the eccentricity, the inclination and the perihelion distance. Additionally, the nominal values of the argument of the perihelion, the right ascension of

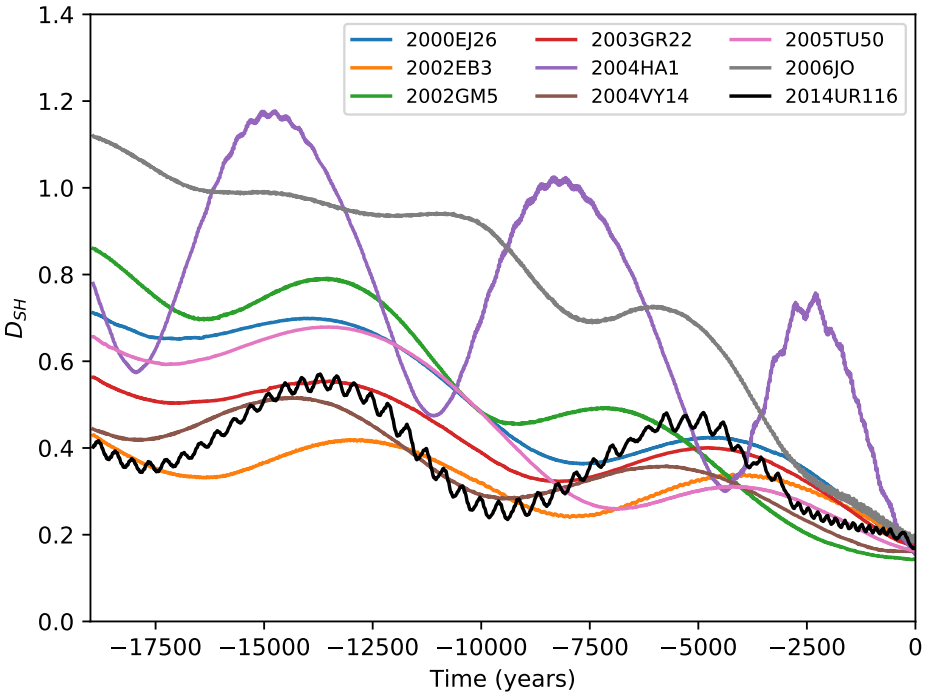

Figure 12: Evolution of the D_{SH} criterion that compares Annama and the following NEAs' orbits: 200EJ26, 2002EB3, 2002GM5, 2003GR22, 2004HA1, 2004VY14, 2005TU50, 2006JO and 2014UR116. The figure shows the backward orbital integration over 20,000 years.

the ascending node and the mean anomaly are indirectly affected. The resulting clones show, however, a very similar orbit shape and plane than the nominal orbit of Annama (indeed clone A6 is a slight different variant of the nominal orbit). As the uncertainty in V_e is ± 0.5 km/s (Trigo-Rodríguez et al., 2015), a total number of 11 clones are created considering velocity increments (or decrements) of 0.10 km/s. The orbits of the clones are shown in Table 12.

For each of these clones a numerical backwards integration is performed, and the D_{SH} criterion analysis for each one of the four NEA candidates carried out. The results show that only for NEA 2014UR116 most of the clones exhibit a low dissimilarity criterion. The D_{SH} evolution for 2014UR116 is plotted on Figure 13 (Top). From this figure, it can be seen that all the clones (except for A2) show a $D_{SH} < 0.4$ for the last 5000 years. Although this value is slightly greater than the desired cut-off value ($D_{SH} < 0.2$), the fact that it can be hold for 5000 years is in line with the approach taken by Porubčan et al. (2004). Hence, this result is suggestive of a possible relationship between the Annama meteoroid and the NEA 2014UR116. Furthermore, from Figure 13 (Top) it can be stated that those clones with lower pre-atmospheric velocities (A1, A3 and A4) keep the $D_{SH} < 0.4$ for a period of around 9000 years. As per the rest of clones (from A5 to A11), the DSH stays below 0.6 back to 9000 years too, although their D_{SH} value is generally below 0.3 for the first 3000 years.

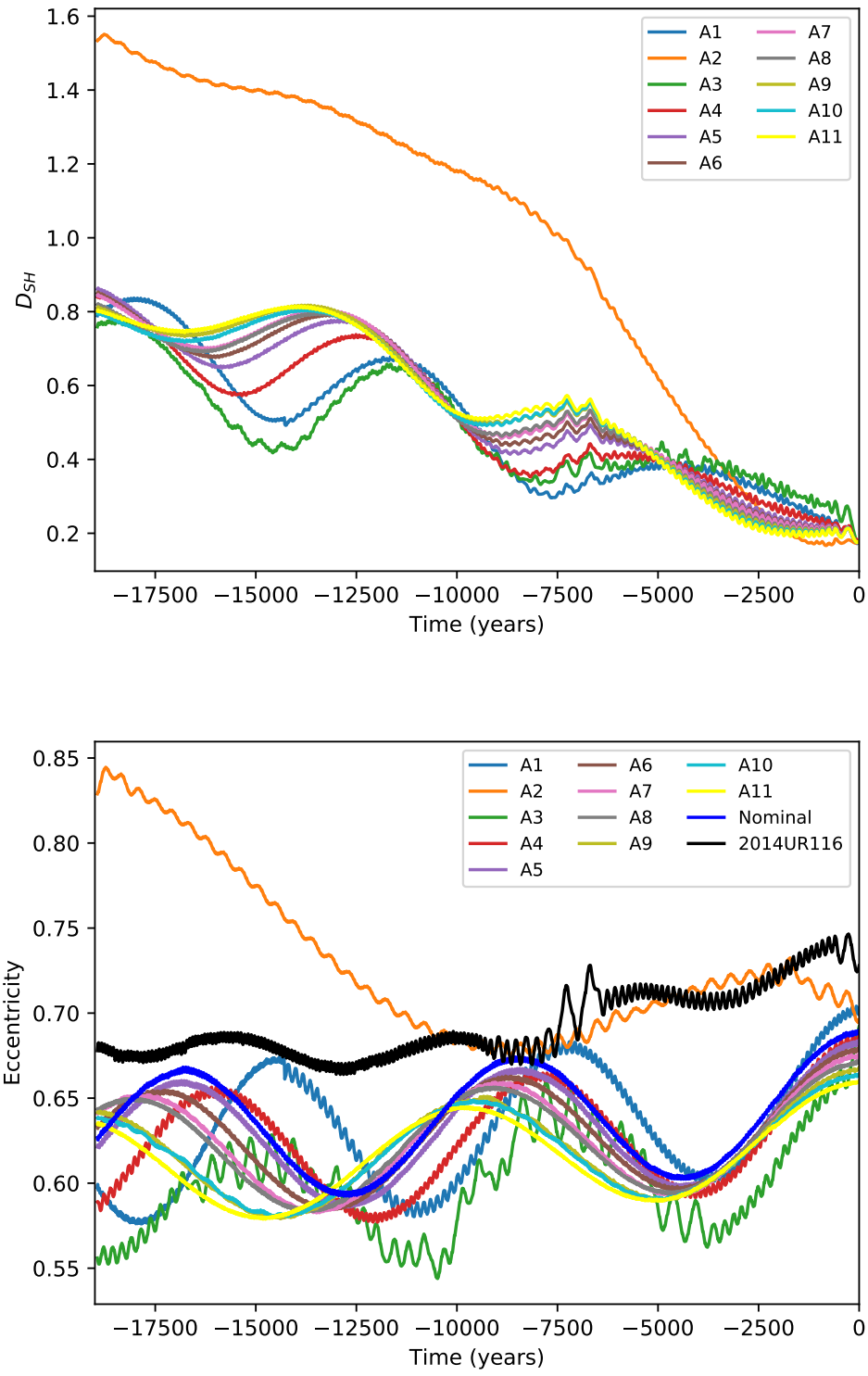

Figure 13: Top: D_{SH} evolution over 20,000 years for Annama's clones and NEA 2014UR116. Bottom: Orbit eccentricity evolution over 20,000 years for Annama's clones and NEA 2014UR116.

ID	a	e	q	i	ω	Ω	M	V_e
A1	2.10	0.700	0.630	15.02	264.53	28.595	344.940	24.70
A2	2.07	0.696	0.631	14.93	264.60	28.595	344.545	24.60
A3	2.05	0.692	0.632	14.83	264.67	28.595	344.285	24.50
A4	2.03	0.688	0.633	14.74	264.73	28.595	344.018	24.40
A5	2.00	0.684	0.633	14.65	264.80	28.595	343.587	24.30
A6	1.98	0.680	0.634	14.56	264.87	28.595	343.303	24.20
A7	1.96	0.676	0.635	14.47	264.94	28.595	342.975	24.10
A8	1.94	0.672	0.636	14.38	265.01	28.595	342.674	24.00
A9	1.92	0.668	0.637	14.28	265.08	28.595	342.366	23.90
A10	1.90	0.664	0.637	14.19	265.15	28.595	342.011	23.80
A11	1.88	0.660	0.638	14.10	265.23	28.595	341.685	23.70

Table 12: Clones of Annama. The columns are: (1) Clone identification code, ID; (2) semi-major axis [AU]; (3) eccentricity; (4) perihelion distance [AU]; (5) inclination [^{o}]; (6) argument of the perihelion [^{o}]; (7) right ascension of the ascending node [^{o}]; (8) mean anomaly [^{o}]; (9) pre-atmospheric velocity [km/s].

The evolution of the orbital eccentricity, perihelion distance and inclination of the clones and NEA 2014UR116 are plotted in Figure 13 (Bottom) and Figure 14. While the evolution of the orbital eccentricity and perihelion distance do not suggest any clear similarity between the clones and the NEA, the evolution of the orbital inclination indicates some degree of similarity between those clones with higher entry velocities (A1, A3 and A4) and 2014UR116. Note that the geocentric velocity of an impacting meteoroid is commonly underestimated from the meteor observations. This uncertainty is propagated to the calculation of the pre-atmospheric meteoroid velocity and, consequently, it shall be expected that those clones with higher values of the pre-atmospheric velocity could possibly show a more similar evolution pattern. This statement is only in agreement with the evolution of the orbital inclination.

For the shake of a complete understanding of Figure 13 (Bottom) and Figure 14, the clone A2 (with $V_e = 24.6$ km/s) deserves a separate study. Not only the D_{SH} criterion between this clone and NEA 2014UR116 diverges at around 3000 years back in time, but also its orbital elements follow a different evolution compared to the rest of the clones. Both, its orbital inclination and the D_{SH} criterion, increase notably when the numerical integration reaches 3000 years back in time. Conversely, the orbit eccentricity and perihelion distance of A2 show the best adjustment to the corresponding NEA 2014UR116 orbital parameters for $10,000$ years. This ultimately means that the semi-major axis of both bodies shall be similar too. Given the semi-major axis, possible mean-motion resonances can be studied. Additionally, if the eccentricity and the inclination are known, then the *Tisserand parameter* can be derived. The Tisserand parameter states close encounters with solar planets (Morbidelli et al., 2002) and is expressed a function of the semi-major axis of the planet (a_p), the semi-major axis of the body (a), the eccentricity

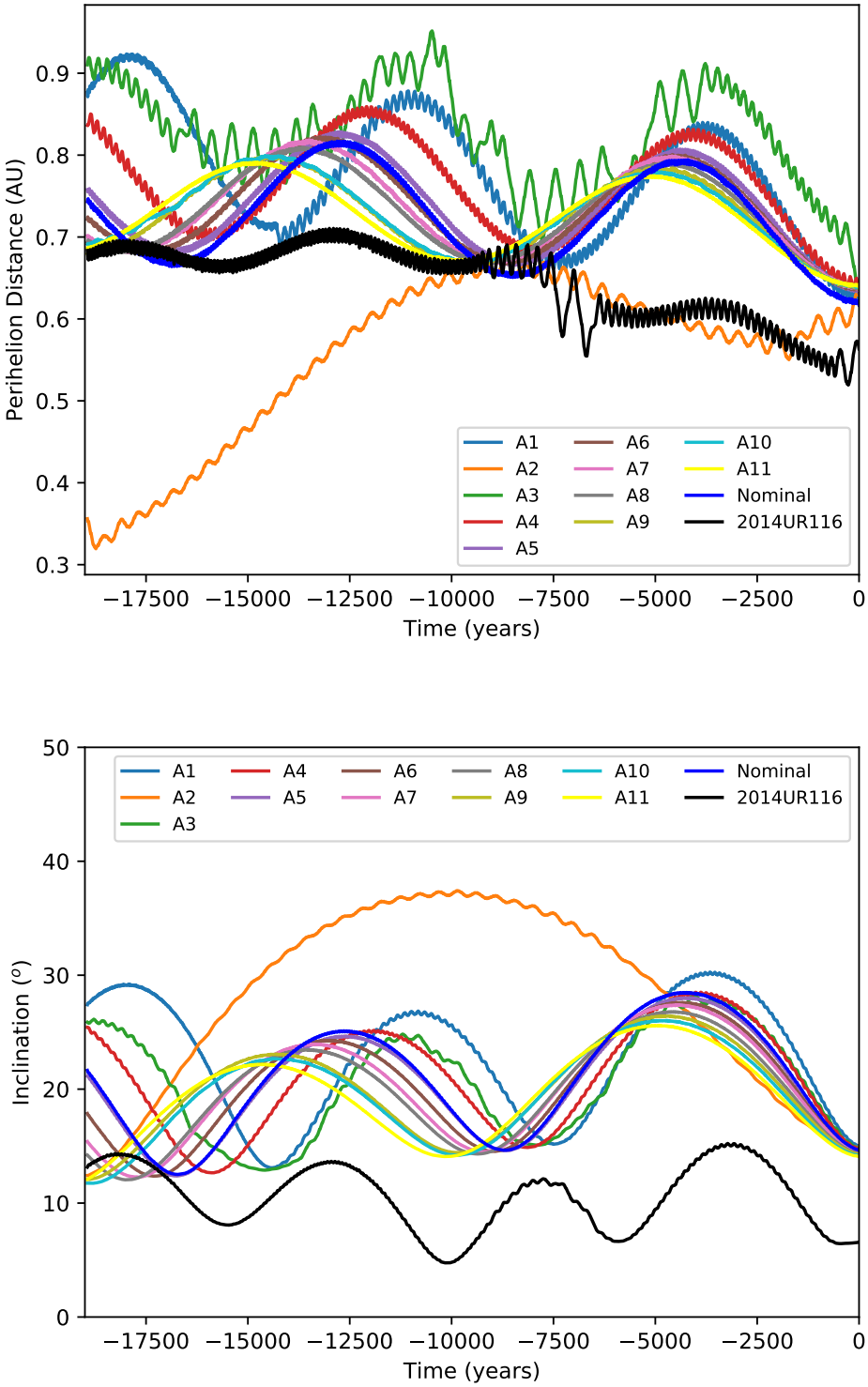

Figure 14: Orbit perihelion evolution (Top) and inclination (Bottom) over 20,000 years for Annama's clones and NEA 2014UR116.

(e) and inclination (i) of the body's orbit:

$$T = \frac{a_p}{a} + 2\sqrt{\frac{a(1-e^2)}{a_p}}\, cosi \tag{21}$$

After exploring several options, it is found that among all the clones, only A2 shows an integer period ratio with Jupiter, $T_{Jupiter}/T_{A2} = 3.98$ at the moment Annama impacted the Earth. Thus, suggesting that clone A2 is gravitationally ruled by the $4:1$ resonance with Jupiter. The small difference from 4 is due to the slight oscillations that the orbit of the meteoroid experiences around resonant orbit; this phenomenon is called *libration*. This is also the case of NEA 2014UR116 which also shows $T_{Jupiter}/T_{NEA} = 3.98$. To explore the consistency of this gravitational link, the backwards evolution of the rates $T_{Jupiter}/T_{A2}$, $T_{Jupiter}/T_{NEA}$, $T_{Jupiter}/T_{AnnamaNominal}$ are calculated. The results for clone A2, NEA 2014UR116 and the nominal orbit of Annama are plotted in Figure 15 (Top). The orbit's libration of the clone A2 around the $4:1$ mean-motion resonance can be stated from Figure 15 (Top). Note that this mean-motion resonance is responsible of one of the innermost MAB Kirkwood gaps. The abrupt change in the orbital eccentricity and inclination (while keeping the semi-major axis fixed) agrees with the effect of the resonance (see Morbidelli et al., 2002). On the contrary, this is not the case of the NEA 2014UR116 as it is only trapped by this resonance during short periods of time. During these short resonant periods the evolution of the eccentricity and perihelion distance experiences sharper amplitude variations (as it can also be observed in Figure 13 (Bottom) and Figure 14 (Top).

Interestingly, the clone A2 is also subjected to a mean-motion resonance with Saturn ($10:1$). The evolution of this resonance is shown in Figure 15 (Bottom). As stated before the analysis of resonance is a complex issue and requires a deep insight. On top of that, 3-body mean-motion resonances are even more complicated and not so common in the solar system (Sekhar et al., 2016). As this is out of the interest of this thesis, no conclusions are derived regarding the effects of this 3-body resonance that rules the orbital movement of the clone A2.

The evolution of the Tisserand parameter is shown in Figure 16. This time, the Tisserand parameter is mostly constant for the NEA 2014UR116 and the nominal orbit of Annama, while there is an evident variation of this parameter for clone A2 over time. This suggests that encounters between the NEA and Annama (assuming its nominal orbit) with Jupiter are common. Planetary encounters are enough to remove a body from a resonance and so this might explain why the NEA 2014UR116 and Annama (nominal orbit) are usually kept away from the effects of the jovian $4:1$ and saturnian $10:1$ resonances. On top of that Trigo-Rodríguez et al. (2015) indicate that statistically Annama shall be coming form the ν_6 secular resonance with Saturn.

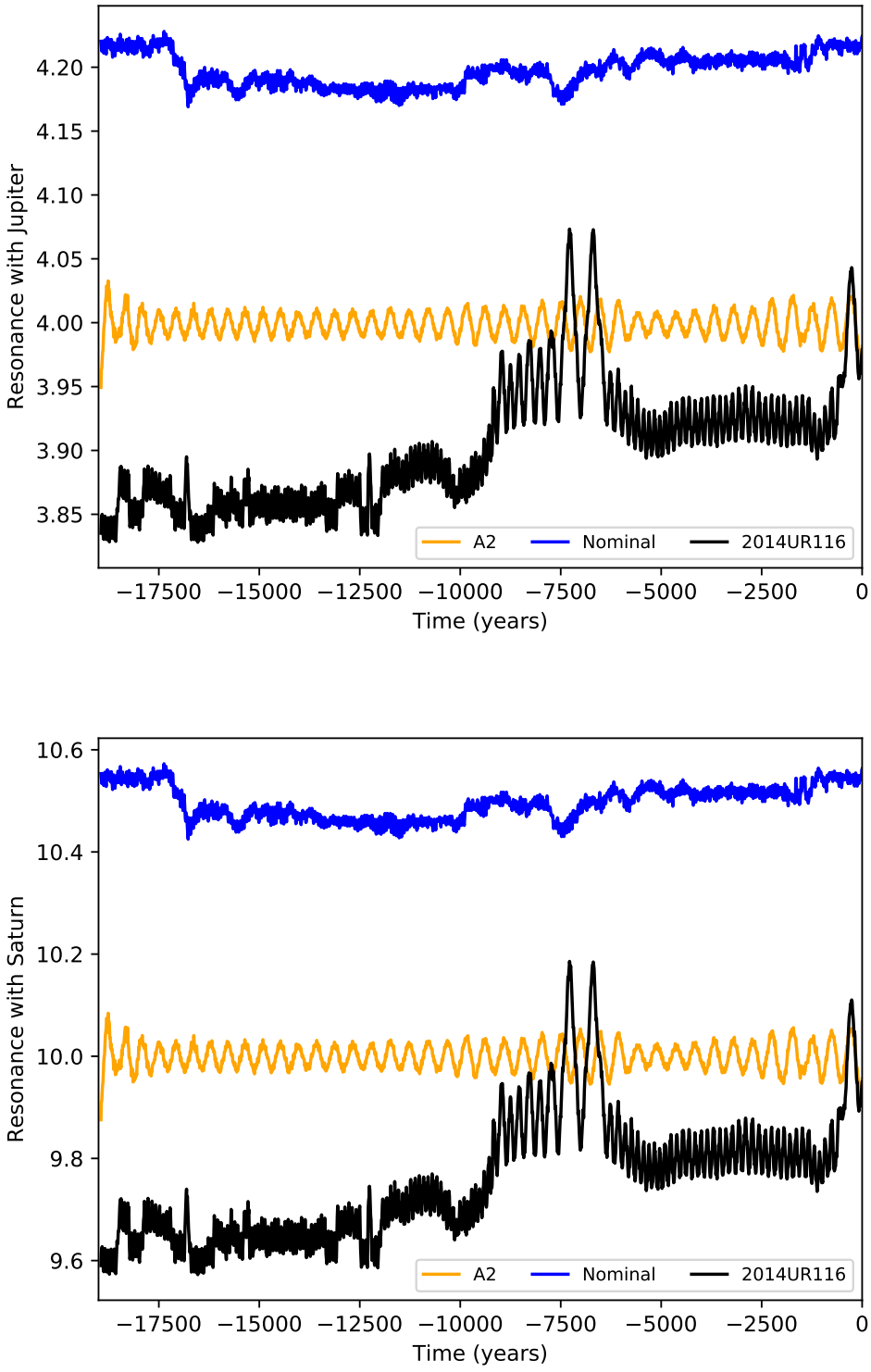

Figure 15: (Top) Evolution of the Tisserand parameter ratios: $T_{Jupiter}/T_{A2}$, $T_{Jupiter}/T_{NEA}$, $T_{Jupiter}/T_{AnnamaNominal}$ over 20,000 years. (Bottom) Evolution of the Tisserand parameter ratios: T_{Saturn}/T_{A2}, T_{Saturn}/T_{NEA}, $T_{Saturn}/T_{AnnamaNominal}$ over 20,000 years.

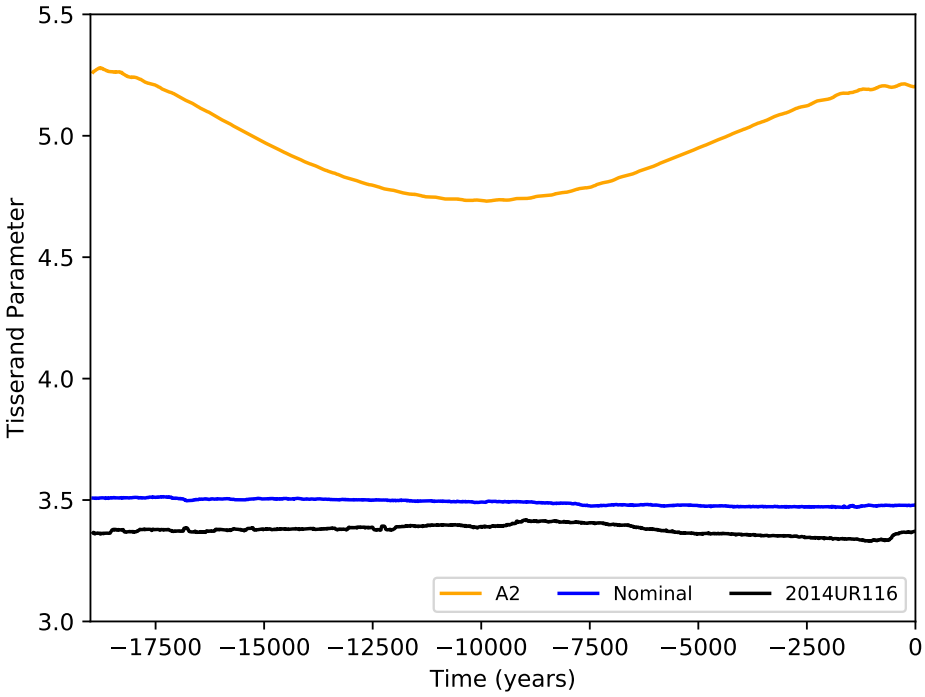

Figure 16: Evolution of the Tisserand parameter over 20,000 years for Annama's nominal orbit, the NEA 2014UR116, and clone A2.

3.4 CONCLUSIONS AND OUTLOOK

This chapter explores two different topics concerning Celestial Mechanics. On the one hand, the observation of the Ursid meteor shower outburst on December 2014 has provided four reliable meteor trajectories from which accurate orbital information based on double-station detections is obtained. This outburst corresponds to cometary material released from the comet 8P/Tuttle in one of its perihelion transits that encounters the Earth when the comet is close to its aphelion. On the other hand, the search for a potential progenitor for Annama meteorite results in a possible candidate. The origin of meter-sized meteoroids like Annama is complicated to track provided the chaotic changing orbital conditions within the near-Earth environment.

The results concerning the Ursids' outburst can be summarized as following:

1. Video and forward-scatter detections along with other reports indicate high meteor activity associated with an Ursid dust trail crossing the Earth's orbit at solar longitude at $\lambda_0 = 271.8^o$ on Dec. 23^{rd}, 2014.

2. The outburst was characterized by centimeter- sized meteoroids (population index of 1.8), producing bright meteors and some fireballs recorded by the SPMN cameras.

3. The mean Ursid ZHR was around 19 meteors/hour, peaking with a ZHR of 45 ± 19.

4. Two of the four Ursid orbits (SPMN 221214A and SPMN 231214B) exhibit similar orbital elements to the previously recorded meteoroids during outbursts. The other two are measured slightly below the expected geocentric velocity, and their measurements are probably affected by low meteor brightness on the very beginning trajectory segment. However, the meteor orbits retrieved are within the range of values of previous aphelion outbursts.

5. Despite some slight discrepancies in the orbital parameters, the four meteoroids have orbits that seems to be associated with the 1405 or 1392 dust trails which provoked the outburst and are captured in the two body mean-motion resonance with Jupiter.

And as per the Annama event:

1. The pre-atmospheric orbit of Annama resembles a NEA Apollo Family type orbit.

2. The dissimilarity criterion of Southworth & Hawkins (1963) is used to select nine possible NEA parental candidates. To assure a reliable dynamical relationship, a numerical backward simulation is carried out to study the evolution of the dissimilarity criterion for $20,000$ years.

3. Only NEAs 2002EB3, 2003GR22, 2004VY14 and 2014UR116 show a reasonable long-term low value of the dissimilarity criterion. In order to remove the uncertainty due to the calculation of the meteoroid atmospheric entry velocity, a set of Annama clones are created. The re-evaluation of the dissimilarity criterion for the shorten list of NEA candidates and the clones indicates that only 2014UR116 shares reasonable orbital elements evolution with Annama and most of the clones.

4. The study of the orbital elements of the clones and 2014UR116 suggests a very probable relationship.

5. A 3-body mean-motion resonance with Jupiter and Saturn may be the reason behind the orbital divergence of the clone A2, which shows different orbital parameters' evolution compared to the rest of Annama clones.

4

METEOROID FLIGHT FLOW REGIMES

4.1 INTRODUCTION

Among the instrumental observation techniques reviewed in Chapter 2, infrasound monitoring has proved to be effective in detection of the meteor-generated shock waves. When combined with optical observations of meteors, this technique is also reliable for detecting centimeter-sized meteoroids that usually ablate at high altitudes, thus offering relevant clues that open the exploration of the meteoroid flight regimes. Indeed, the presence of a meteor-generated shock wave can be used to outline the state of the meteor surrounding gas and can be used to determine the meteor flow regime. This chapter analyses the flow regimes of a data set of 24 centimeter-sized meteoroids for which well-constrained infrasound and photometric information is available, and thus becoming the first time that the flow regimes for meteoroids in this size range are validated from observations. Here, the Knudsen and Reynolds numbers are calculated, and two different flow regime evaluation approaches are compared in order to validate the theoretical formulation.

4.1.1 *Definition of the flow regimes*

It was already discussed in Chapter 1 that meteoroids are solid objects that originate from comets, asteroids, and other solar system bodies and impact the Earth's atmosphere at hypersonic entry velocities, ranging between 11 - 73 km/s. These velocities correspond to a *Mach number* (Ma), which represents the ratio of the meteoroid velocity to the local speed of sound at the meteoroid surrounding flow conditions, between 35 and 270 (e.g., Ceplecha et al., 1998; Jenniskens, 1998; Baggaley, 2002; Gritsevich, 2009).

During their atmospheric passage, given the increasing gas density, these bodies are subjected to an increasing number of collisions with atmospheric particles. The number and energy of these collisions is related to the velocity (i.e., the Mach number) and the size of the body. In this regard, several possible physical flight scenarios known as *flow regimes* can be outlined. There are four commonly accepted flow regimes: free-flow, transitional, slip-flow, and continuum-flow. These are characterized by a dimensionless parameter called the *Knudsen number* (Kn), which is defined as the ratio between the mean free path of the gas molecules (l) and a characteristic length scale (L) of the body immersed in the gas, and thus $Kn = l/L$. It is quite common to use an equivalent ra-

dius of the meteoroid (r) as the characteristic length (e.g., Gritsevich & Stulov, 2006). However, when a *boundary layer* exists (a region in the vicinity of the body where the viscous effects are significant), the thickness of the boundary layer (δ) is used as the characteristic scale, $Kn = l/\delta$ (Bronshten, 1965, 1983). Alternatively, the Kn number can be described as the inverse product of the intermolecular collision rate (ν) and a characteristic flow time (t), thus $Kn = 1/(\nu \cdot t)$. The latter definition demonstrates that the larger the number of the collisions for a given time, the smaller the Kn value. Note that the collision rate applies only to the gas molecules; the collisions against the body surface are not accounted for in this scenario. The rate of collisions controls the distribution of velocities of the impinging molecules and thus the mathematical formulation to be applied to the physical scenario. This eventually hinders a sharp delineation of the flow regime limits, since it is not trivial to constrain the molecular collision rate at each stage of the meteoroid's descent through the atmosphere.

The first Kn expression, $Kn = l/L$, is the most common and practical, although defining l can be challenging, as its definition is not unique, and it can be regarded differently owing to the molecules and the reference frame considered in a given study. As explained in Bronshten (1983), there are more than eight possible scenarios, out of which two are usually the most commonly adopted. On the one hand, blunt bodies (i.e., reentry vehicles) are generally studied using a reference frame moving with the gas and the equilibrium air molecules. On the other hand, as discussed by Rajchl (1969) and Bronshten (1983), for meteor problems where the immersed body loses material during its movement and the shape of the meteoroid is not known, it is more realistic to fix the reference frame to the meteoroid and study the mean free path of the reflected (or evaporated) molecules relative to the impinging molecules. Furthermore, this approach allows a separate analysis of the various local scenarios in the vicinity of the meteoroid (Josyula & Burt, 2011). To make a distinction between these scenarios, the latter Kn is renamed to B (Rajchl, 1969) or Kn_r (Bronshten, 1983). Hereafter, the nomenclature Kn_r will be adopted to refer to this second definition of the Kn approach, where the reference frame is fixed to the meteoroid.

There are various flow regime classifications based only on Kn or a combination of Kn with other parameters. The most widely used classification (hereafter referred to as the classical scale) accounts for the number of intermolecular collisions in a specific time (recall that Kn is proportional to the inverse product of the intermolecular collision rate); it is as follows:

(i) Free molecular regime, Kn¿10. The number of intermolecular collisions is scarce. Single molecules hit the immersed body.

(ii) Transitional-flow regime, $0.1 < Kn < 10$. The mean free path of the molecules is of the same order of magnitude as the characteristic size of the body. There are collisions between molecules.

(iii) Slip-flow regime, $0.01 < Kn < 0.1$. There is a slightly tangential component of the flow velocity in the boundaries of the body's surface, but there is no adhesion of the flow to the body's surface.

(iv) Continuum-flow regime, $Kn < 0.01$. The flow is considered to be continuous.

Another typical strategy is to delimit the flow regimes considering the relevance of the viscous effects. This is done via the value of the *Reynolds number*, Re. This physical parameter compares the convective forces to the viscous forces of a fluid, $Re = \rho v L/\mu$ (where ρ is the gas density, v is the flow speed and μ is the gas dynamic viscosity). It will be seen later, in the Section 4.2 (Equation (23)), that Kn_r, as defined using a frame fixed on the meteoroid, is a function of the Re number, and thus, using this scale the actual conditions for each event are more explicitly considered. Tsien (1946) noted the importance of these viscous effects and outlined a flow regime classification based on the comparison of the mean free path of the gas molecules (l) to the thickness of the boundary layer (δ). This scale is then described as in Tsien (1946):

(i) Free molecular regime, $Kn > 10$.

(ii) Transitional-flow regime, $Re^{-1/2} < Kn < 10$.

(iii) Slip-flow regime, $10^{-2} \cdot Re^{-1/2} < Kn < Re^{-1/2}$.

(iv) Continuum-flow regime, $Kn < 10^{-2} \cdot Re^{-1/2}$.

While the flow regime boundaries are fixed in the classical scale according to the intermolecular collision rate, the Tsien's scale accommodates for each event taking into account the viscous effect evolution. For instance, if Re increases, the transition and slip-flow regime ranges shift to higher Kn numbers for that meteoroid. Conversely, as the Re decreases, the transitional and slip-flow regime boundaries tend to shift to lower Kn values (and the continuum-flow regime appears later). Note that these scales refer to the more general Kn definition (the reference frame moves with the gas flow), and the particulars derived from the use of another frame should be studied individually. In this study, in line with Bronshten (1983), the consideration of Kn_r instead of Kn, which accounts for the mean free path of the reflected (evaporated) molecules relative to the impinging molecules (l_r) instead of the mean free path of the gas molecules (l), allows for the use of the two flow regime scales (classical and Tsien's) described above. Additionally, Tsien (1946) originally suggested the classical scale to be used when the Kn is defined with the thickness of the boundary layer Bronshten (1965).

Another classification was introduced by ReVelle (1993). He developed a meteoroid flight regime scale using Kn and three related parameters: a variation of the shape coefficient (effective mass/area), a variation of the ablation coefficient, and the height at which the kinetic energy has been reduced down to 1% of its initial entry value. This classification describes six different regimes. However, these parameters cannot be retrieved accurately from observations, and thus the reliability of the results depends on

the accuracy of the input data. This flight regime classification will not be accounted for in this study.

4.1.2 *The screening of the meteoroid: the vapour cloud and the shock wave*

The increasing number of high-energy particle collisions along the meteoroid descending path evaporates the first layers of the body surface. This effect ultimately creates a surrounding vapour cloud that screens the meteoroid from further high energetic impacts (also known as *hydrodynamic shielding*). The vapour cloud can virtually increase the cross-sectional area of the meteoroid (that collides with the atmosphere) by up to 2 orders of magnitude (Boyd, 2000; Popova et al., 2000) leading to a more efficient screening that decelerates the impinging particles (Rajchl, 1969; Bronshten, 1983). When the mean free path of the vapour particles becomes an order of magnitude smaller than the meteoroid radius the screening acts more efficiently (Popova et al., 2000). Due to the reduction of high-energy impacts, the atoms and ions within the hydrodynamic shielding cap can no longer be considered to be embedded in a hypersonic flow (see Bronshten, 1965, 1983), and the hypersonic flight scenario becomes complex. Finally, the main dependences of the hydrodynamic shielding parameters for centimetre-sized meteoroids are the size and the altitude of the meteoroid (Popova et al., 2000).

It is when the vapour cloud reaches a pressure that exceeds that of the surrounding atmospheric gas (the vapour cloud is highly compressed), that the vapour cloud expands like a hydrodynamic fluid into the surrounding, less dense environment (Popova et al., 2000). The outer layers of the cloud expand at supersonic speeds, and a detached shock wave forms ahead of the body. The extent of the *shock layer* (defined as the space between the shock wave and the meteoroid surface) determines the amount of ionization and dissociation of the gas molecules (Bronshten, 1965; Rajchl, 1969). Further mathematical formulation and discussion on the physical phenomena that take place in the shock wave front, shock wave layer and meteor trail can be found in Bronshten (1965). Besides, Silber et al. (2017, 2018b) provide a detailed scheme and a complete description of the meteor generated shock waves, the flow fields and the near wake. Note here that identifying the moment when the meteor-generated shock wave sets on is not fully understood and is out of the scope of this chapter.

Based on necessary simplifying assumptions, the computational work carried out by Popova et al. (2000) and Boyd (2000) indicate that the vapour cloud should form during the transitional-flow regime. This agrees with Rajchl (1969), who suggests that the vapour cloud should persist up until the beginning of the slip-flow regime.

4.1.3 *Infrasound observation to understand the flow regimes*

Optical instrumental observations can be used to visually detect a meteor; however, this technique cannot provide solid evidence of the presence of the shock wave, especially for sub-centimetre and centimeter-sized meteoroids at high altitudes (e.g., the mesosphere and lower thermosphere or MLT region of the atmosphere). The high luminosity of the meteor phenomena, coupled with the fact that the shock front is very thin and attenuates very rapidly (Silber et al., 2017, 2018b), does not allow for direct optical detections of the shock wave (e.g., Schlieren photography). Indeed, previous attempts of observing meteor-generated shock waves using photometric measurements provided only preliminary conclusions (Rajchl, 1972). The introduction of infrasound techniques to gain more insight in this phenomenon has been recently proved to be reliable.

Infrasound is low-frequency (< 20 Hz) sound lying below the human hearing range and above the natural oscillation frequency of the atmosphere. Due to its very low attenuation rate, infrasound is an excellent tool for monitoring and studying impulsive sources in the atmosphere (e.g., Revelle, 1974; Silber et al., 2015; Silber & Brown, 2019, and references therein). A shock wave, initially in the highly nonlinear strong shock regime, eventually decays to a weakly nonlinear acoustic wave that could, given favourable conditions, be detected infrasonically at the ground (Silber et al., 2015). A theoretical approach to derive meteoroid parameters from infrasonic signatures, conceived by Revelle (1974, 1976), was recently improved and subsequently validated (Silber et al., 2015) using a database of well-constrained centimeter-sized meteoroids (Silber & Brown, 2014). Using optical measurements and infrasound detections of bright meteors, Silber & Brown (2014) constrained the altitude of the meteor-generated shock wave by finding the point along the meteor trajectory from which infrasound signal originated. Although this altitude is not diagnostic of the initial onset of the shock wave, it represents the earliest detected point at which the shock wave is proved to exist, which is an important prerequisite for the purpose of this chapter. While there is strong evidence suggesting that in some cases the onset of meteor shock waves could take place much earlier than predicted by classical methodologies (Silber et al., 2017, and references therein), the Knudsen scale has never been verified against observations of centimeter-sized meteoroids.

This study analyses the homogeneous database of 24 centimeter-sized meteoroids detected simultaneously by optical and infrasound systems and previously published by Silber et al. (2015). The meteoroid size (radii) was also constrained in Silber et al. (2015) using five different methodologies to derive the meteoroid mass. The derivation of the flow regimes depends on the meteoroid size, and so using five different approaches to obtain the meteoroid mass can help understanding the accuracy of the results of this study. Note that constraining the meteoroid mass could be challenging, as it may vary according to the methodology used (see, e.g. Gritsevich, 2008c). The first mass derivation approach relies on an empirical law described by Jacchia et al. (1967). It relates the following parameters to the meteoroid mass: the meteor magnitude in the photographic

bandpass, the zenith angle of the radiant, and the speed at that point. Second, the photometric mass derivation method is applied as described in Ceplecha et al. (1998). It is known that some portion of the kinetic energy lost by a meteoroid is converted to light emission, which can be mathematically expressed with the use of the luminous efficiency factor. The approach of Ceplecha et al. (1998) considers an equation describing the change in kinetic energy along with the assumption that a variation in the meteoroid velocity due to deceleration can be neglected compared to the loss of meteoroid mass. The magnitude of luminosity emitted by the meteor is then a function of the mass loss exclusively. Along with this, the rate of mass loss is assumed to be constant during ablation. The third photometric approach applied in the present work uses a more complex correlation between the fragmentation model (see Chapter 2) and the light curve, described in Ceplecha & Revelle (2005). These three mass estimates will be hereafter referred to as JVB, IE (integrated energy), and FM, respectively, as previously defined and published in Table S3 of Silber et al. (2015). For comparative purposes, the meteoroid mass estimates derived from the infrasound analyses (Silber et al., 2015) are also included as the final two approaches. The fourth mass estimate is calculated from the observed information of the infrasonic signal period in the linear regime, and the fifth mass from the observed infrasonic signal period in the weak shock (ws) regime (Revelle, 1974, 1976). This will be described in the Section 4.2.1, and further details regarding the derivation of all the five masses can be found in Silber et al. (2015).

4.1.4 *Implications of the identification of meteor flow regimes*

Using infrasound analysis, it is possible to determine the earliest confirmed height along the meteor trail at which the shock wave is present. This knowledge can be used to determine the surrounding atmospheric gas conditions and ultimately the meteoroid flight flow regime. Moreover, since the shock wave is an indicator of the energy released by the event, the association of meteor flow regimes with the presence of a shock wave will provide relevant clues on the meteoroid flight parameters required to deposit energy in the upper atmosphere.

The flow regimes of small meteoroids impacting the Earth at hypersonic velocities have not been studied in depth previously. Only numerical simulations carried out by Boyd (2000) and Popova et al. (2000) have tackled this problem. Also, in their work, Campbell-Brown & Koschny (2004) developed a meteoroid ablation model for faint meteors under the free-flow regime conditions and illustrated the differences in the meteoroid flow regimes with sizes up to one meter depending on whether the vapour cloud is taken into consideration or not. However, no study has described and validated the meteoroid flow regimes by means of observations that account for the existence of the hydrodynamic shielding.

According to Popova et al. (2000) and Silber et al. (2017), overdense meteors (as described in Silber et al., 2017, particles sized between $4 \cdot 10^{-3}$ m and a few centimeters) may reach the continuum-flow regime below $90 - 95$ km altitude, as the flow pressure at that point will be smaller than the vapour gas pressure. It is well defined, though, that most meteoroids do ablate (which involves the possible onset of the vapour cloud and the shock wave) between 70 and 120 km; this region corresponds to the MLT region of the atmosphere. At these heights, the atmospheric conditions are dominated by large-amplitude thermal and gravitational tidal waves which increase inner momentum of the fluid. Among other effects, this causes a rapid change in the gas molecular density, which ultimately leads to a variation in the molecular mean free path.

The meteoroid data set of Silber et al. (2015) is the only well-documented and well-constrained set of centimeter-sized events to-date. The following sections of this chapter will elucidate the complexities associated with the meteor flow regimes of bright meteors. Using the classical theory along with this homogeneous, observational data set of well-constrained meteoroid events recorded both optically and infrasonically, the aim is to determine and validate the flow regimes of centimeter-sized meteoroids in the upper atmosphere. In order to get a deeper insight on the suitability of this approach, both the classical and the Tsien (1946) Knudsen scales are implemented to determine the flow regimes. It will also be examined whether these two Kn scales can be employed as useful proxies in determining the flow regimes of meteoroids in the centimeter-size range in future studies. This also allows to elucidate the flow regimes associated with an apparent early onset of meteor-generated shock waves by linking the observations to a theoretical approach.

4.2 METHODOLOGY

The data set in use (taken from Silber et al., 2015) consists of only the best-constrained events, for which at least one infrasound source height is accurately obtained, have reliable optical measurements, and do not show abrupt deceleration or fragmentation. Several cases for which two infrasound sources are obtained are also included in this study, but only the earliest source is considered. This is because only the highest altitude associated with the shock wave is relevant to the analysis of the flow regimes, as this is where the most uncertainty exists. Low altitudes (e.g. below 70 km) are usually associated with the continuum flow, where the verification is then no longer a practical task.

The meteors in the data set were recorded simultaneously by all-sky cameras (the All-Sky and Guided Automatic and Realtime Detection (ASGARD) network) and infrasound array (the Elginfield Infrasound Array (ELFO)), which are the part of the regional fireball observations network located in Southwestern Ontario (Canada). The advantages of having both optical and infrasound systems within the same network, and thus close together, are twofold. First, given favourable conditions, some meteors (such as those analysed in this chapter) can be recorded by both optical and infrasound systems simultaneously. Second, it is more likely to detect direct arrivals, or infrasound

sources within $\sim$ 300 km of the receiver. The relevance of this lies in the fact that there is a rapid decrease of the infrasound signal-to-noise ratio (SNR) for events that originate too far from the infrasound array ($>$ 300 km). Provided that the shock wave typically forms at high altitudes (Popova et al., 2000; Silber et al., 2017), the atmospheric conditions along the propagation path can adversely affect the signal and therefore hinder the detection efficiency of infrasound. Thus, direct arrivals are less likely to suffer from irreversible changes (Silber & Brown, 2014, 2019). Only about 1% of optically detected centimeter sized meteoroids are also captured by infrasound (Silber & Brown, 2014). More details regarding the detailed methodology outlining data collection, reduction, and analyses pertaining to the data set can be found in Silber & Brown (2014).

4.2.1 *Derivation of meteoroid sizes from masses*

The estimation of the meteoroid characteristic size, its radius (r), is derived from the meteoroid masses. The masses used in the current study have been derived using the five different methods, as described in the Section 4.1.3, three of them based on the analysis of the photometric light curve produced by the meteor and the remaining two using infrasound techniques. The infrasound masses are calculated using Equation (8) in Silber et al. (2015):

$$M_{infra} = \left(\frac{\pi \rho_m}{6}\right)\left(\frac{R_0}{Ma}\right)^3 \tag{22}$$

where ρ_m is the meteoroid density and R_0 the blast radius. The blast radius is proportional to the product of the meteoroid diameter (d) and the Mach number ($R_0 \approx d \cdot Ma$), and it is defined as the distance between the shock source and the point where the overpressure (the excess pressure over the local atmospheric pressure generated by the shock wave) approaches the local atmospheric pressure. Thus, it is a way of determining the instantaneous energy deposition. Kinetic energy and R_0 are interconnected (Figure 17 (a)), especially if there is no abrupt deceleration or gross fragmentation that would skew the magnitude of R_0 (see Silber et al., 2015, for further disussion). Figure 17 (a) proves that none of the events analysed here undergo fragmentation or abrupt deceleration, which attests to the suitability of the data set for the purpose of this chapter. The blast radius can be obtained through correlating the observed infrasonic signal period with the modelled period in the linear and weak shock regimes (for a more detailed discussion, see Silber et al., 2015). It should be stated that while infrasound is a reliable tool for detecting meteors and estimating the source function, it has not been validated sufficiently well for the purpose of estimating the meteoroid masses. Hence, infrasound masses are often either under- or overestimated compared to photometric masses. Despite this shortcoming, meteoroid radius estimates from infrasonic masses are included for the purpose of direct comparison and for the sake of completeness.

When calculating the five meteoroid sizes from their respective masses (photometric and infrasonic) there is one source of uncertainty to be considered: meteoroids do not

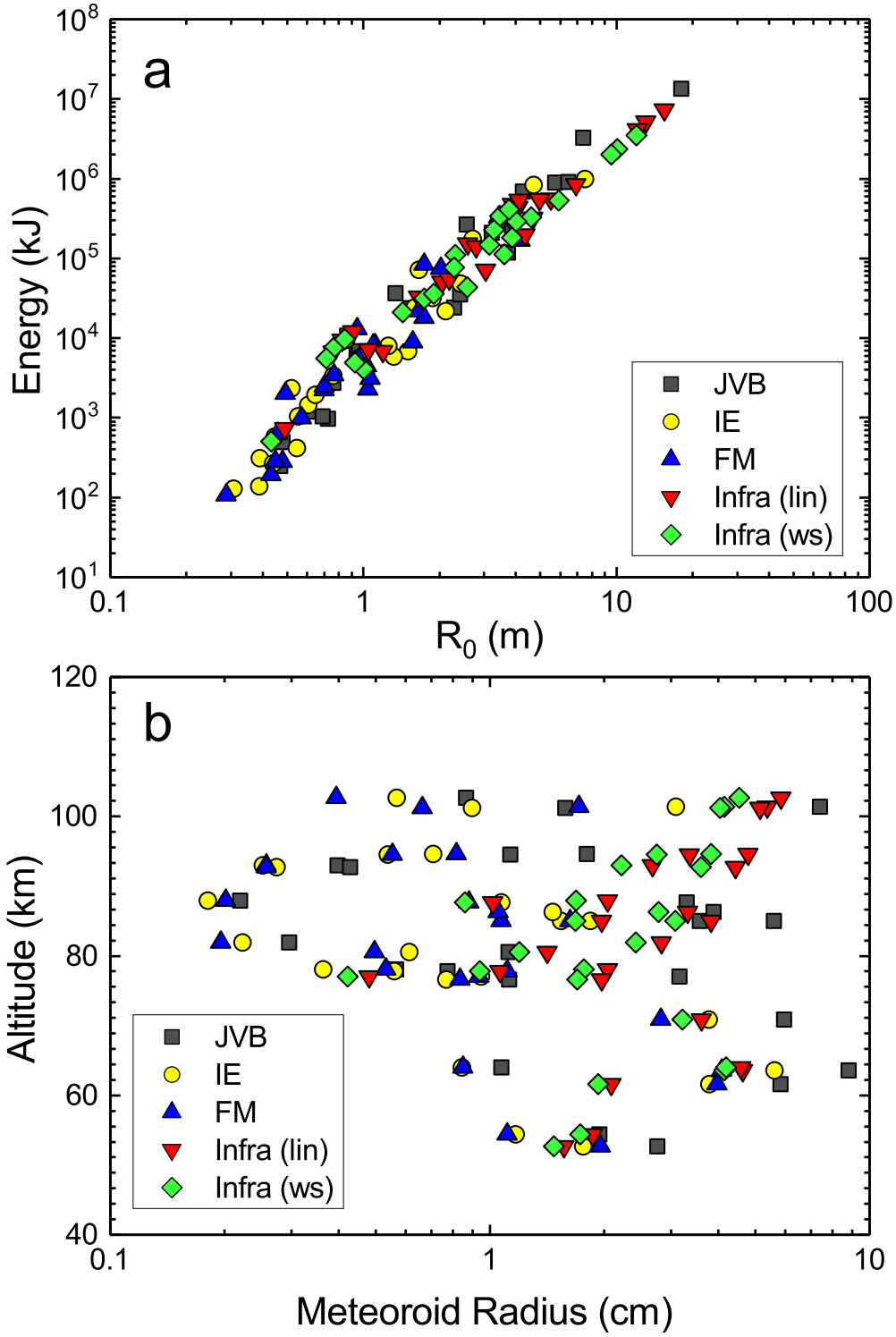

Figure 17: (a) The meteoroid kinetic energy plotted against infrasound blast radius (R_0) for the five masses derived in this study; (b) The shock source altitude plotted against meteoroid radii, as retrieved from the JVB, IE, FM, and infrasound masses (from linear and weak shock methodologies).

have a fixed bulk density value. While this value is usually assumed to be fairly similar to a certain reference density according to the meteorite classification (see Chapter 1), other parameters such as the micro- and macro-porosity or case-specific mineral inclusions can alter it significantly (Britt & Consolmagno, 2003; Babadzhanov & Kokhirova, 2009; Meier et al., 2017).

Possible meteoroid associations with well-studied annual meteor showers (i.e., Chapter 3) were explored by Silber & Brown (2014). Previous studies of known meteor showers could provide additional clues on the meteoroid density. However, since only five of the events in the current data set show such a relationship, providing insufficient statistics, for this work the possible density values for each meteor shower are disregarded. From the observational data, Silber et al. (2015) retrieved the PE parameter (see table S4 in Silber et al., 2015) described in Ceplecha & McCrosky (1976) and Chapter 2. The use of this parameter as a meteor classification criterion has been widely adopted (e.g. Brown et al., 2013a) and will be revisited in Chapter 5. The range of densities assigned to each PE value relies on the statistics built up with the density derivation for each meteoroid using a dynamic analysis of the trajectory of accurately observed meteors; however, individual density errors may ultimately affect the statistics of the result. The PE values for some meteors of the current data set lead to a meteoroid density value of 270 kg/m^3. Such a value is smaller than that of water ice (916.8 kg/m^3). Though these density values might be possibly depending on the packing factor of fractal-like structures (see, e.g., Blum et al., 2006), typical meteoroid bulk densities are usually larger (e.g., common chondritic meteorite bulk density ranges between 3000 and 3700 kg/m^3; see Consolmagno & Britt, 1998; Flynn et al., 1999; Wilkison & Robinson, 2000). On the other hand, as per the classical classification of meteoroids accepted for stony bodies, a reasonable bulk density approximation corresponds to the value of 3500 kg/m^3 (Levin, 1956). This value has been widely in use (see, e.g., Halliday et al., 1996; Ceplecha et al., 1998; Gritsevich, 2008a, 2009; Gritsevich & Koschny, 2011; Bouquet et al., 2014), and it is thus chosen for this work. Note that this value could be large for fragile meteoroids as discussed in Britt & Consolmagno (2003), who suggest density close to 2500 kg/m^3 for carbonaceous chondrites. Nonetheless, the assumption of either value does not significantly affect the resulting Kn_r number. The meteoroid data set under this study consists of centimeter-sized bodies whose exact characteristic size may show only slight variation, according to the mass and density chosen. Furthermore, this variation could be neglected, as the Knudsen number is principally affected by the characteristics (velocity, density, and temperature) of the incoming flow. In the scenario studied in this work, the high-energy collisions with the ambient species are effective in slowing down the ablated species in the meteor flow field. This consequently leads to high ranges of temperature and density in the shock layer, which play the main role in varying the value of Kn_r. Thus, the most critical input parameter in this analysis is the incoming gas flow velocity.

The characteristic meteoroid radii were derived for each of the five mass estimates by considering a spherically shaped object of the same mass and the bulk density. It is evident that the mass estimates obtained from each methodology (photometric and infrasound) differ notably owing to intrinsic assumptions associated with each. It will

be discussed shortly what the implications are to the overall results in this study (see the Section 4.3). The radii, along with other parameters obtained from the meteor infrasound detection and luminous path observations by Silber et al. (2015), are shown in Table 13. Note that all the five meteoroid sizes vary from $r \sim 0.18$ to $r \sim 8.8$ cm. The spread in meteoroid radii as a function of altitude is shown in Figure 17 (b).

4.2.2 *Calculation of the Knudsen number*

As already stated in the Section 4.1, the meteoroid reaches a point at which the surrounding screening vapour gas expands like a hydrodynamic fluid into the surrounding, less dense environment (Popova et al., 2000). This forces the incoming atmospheric gas density to adapt abruptly to the expanding vapour gas and creates a shock wave through which the atmospheric gas increases its pressure and temperature. The state of the gas at both sides of the detached (if the Mach number of the gas flow behind the shock layer is subsonic) shock wave is ruled by the equations of Rankine-Hugonoit if one-dimensional compressible, inviscid, and adiabatic fluid is assumed. Thus, these equations do not consider viscosity effects, radiation, or conduction heat transfer, or gravitational acceleration.

Although in the following calculation a fixed value of the constant ratio of specific heat ($\gamma = c_p/c_v$) will be used, it is important to note the following. The density and temperature jump of the shock wave strongly depend on the adopted γ value. Thus, increasing or decreasing γ could vary the magnitude of this jump. While the best approach would be to vary γ according to the atmospheric conditions and the physical scenario, the dynamical changes in the value of γ in the flow field can only be tracked through sophisticated numerical simulations. Even so, the existing numerical models are unable to accurately describe the hypervelocity flow conditions associated with meteoroids propagating at velocities greater than about 35 km/s, especially in the upper atmosphere, where the object might be on the boundary of the transitional flow. Thus, in the current study, the gas is assumed to be calorically ideal, with γ equal to 1.4 (this is the value for an ideal diatomic gas). This assumption is generally considered to be a valid approximation for explosive sources with a narrow channel (when the shock wave can be approximated as a cylindrical line source; see Taylor, 1950) including meteoroid entry problems, and as such is also employed in other studies (e.g., Popova et al., 2000; Zhdan et al., 2007; Sansom et al., 2015; Chen et al., 2017). The reasoning for such an approach is that the rarefied ambient density (e.g., the MLT) decreases the value of γ, while the presence of strong radiative phenomena (associated with meteors) increases the value of γ. While this might be an oversimplification, any other assumptions implemented in the analytical approach and the classical theory could introduce additional uncertainties and skew the results.

In order to obtain the gas state behind the detached shock wave using the Rankine-Hugoniot equations and eventually derive the Ma, Re, and Kn numbers, the incoming gas flow atmospheric conditions need to be estimated first. The incoming flow is ob-

tained in this study using the NRLMSISE-00 atmospheric model (Picone et al., 2002). This model provides the atmospheric profile above a specific geocentric location (longitude, latitude, and ground altitude) for a required date and time and is among those recommended for the use in meteor analysis (Lyytinen & Gritsevich, 2016). The geographical location of the infrasound array and the infrasound wave arrival time for each event (Table 13) are used in order to retrieve the atmospheric conditions from the NRLMSISE-00 model. The meteor events in the data set in use have shock source height uncertainties that range between 0.3 km and 4.2 km (see column (3) in Table 14), although for most of the cases this uncertainty is ≤ 1 km. For such a limited height uncertainty, the surrounding atmospheric gas conditions will not show large variations, and therefore it is possible to assume that the gas pressure, density, and temperature values are fixed.

From the gas state at both sides of the shock wave, the sound speed and the Mach number upstream and downstream relative to the shock wave (note that the upstream and downstream, respectively, refer to the flow regions ahead of and behind a reference point, which in this case is the shock wave), and the gas state in the shock layer are calculated. Here, a normal front shock wave has been assumed. In principle, the bow shock wave tends to wrap around the meteoroid; however, the Mach cone angle, defined as the angle between the body movement direction and the normal vector of the shock wave, is equal to the $\arcsin(1/Ma)$, and thus it deviates only marginally from zero for the incoming gas flow. The gas flow conditions upstream and downstream of the shock wave can be found in Table 14.

The resulting atmospheric gas conditions behind the shock wave are used to derive the Knudsen number. As discussed in the Section 4.1, the Kn_r is the most suitable Knudsen number description for meteor physics problems. Equation (23) shows the relationship between the Kn_r and the gas physical variables (Bronshten, 1983):

$$Kn_r = \frac{1}{Re} \cdot \frac{\overline{V_e}}{c_s} = \frac{1}{Re} \cdot \frac{1}{c_s} \cdot \left(\frac{8T_w R}{\pi M}\right)^{1/2} = \frac{1}{Re} \cdot \frac{(8T_w)^{1/2}}{\sqrt{\gamma \pi T}} = \frac{\mu}{v \rho r} \cdot \left(\frac{8T_w}{\gamma \pi T}\right)^{1/2} \quad (23)$$

Here cs is the local speed of sound, $\overline{V_e}$ is the average velocity of the vaporizing molecules (Bronshten, 1965), R is the universal constant of the gases, M is the molar mass of the gas, T_w is the meteoroid's surface temperature, γ is the constant ratio of specific heat, μ is the gasdynamic viscosity, v is the velocity of the incoming gas flow, ρ is the gas density, r is the equivalent radius of the meteoroid (derived assuming a spherical body), and T is the gas temperature. Note that, according to Equation (23), Kn_r can be expressed in terms of the Re number and the local speed of sound.

The dynamic viscosity in Equation (23) is a function of the gas temperature, and it is given by Sutherland (1893):

$$\mu = \frac{1.458 \cdot 10^{-6} \sqrt{T}}{1 + \frac{110.4}{T}} \quad (24)$$

As per the velocity of the incoming gas flow, it is the velocity of the meteoroid when the frame of reference is set on the meteoroid surface. For simplicity, this velocity was assumed to be equal to the initial velocity observed along the meteor luminous trajectory path. While this value will remain temporally constant only for those fast meteors within the study data set that experience little deceleration, it will be argued later that the Kn_r results are not largely affected and this assumption is valid. Additionally, meteoroids typically undergo notable deceleration at lower altitudes, where the atmospheric density is greater. Thus, at altitudes investigated here, deceleration can be assumed to be negligible. Furthermore, as stated in Silber et al. (2015), the meteoroids in the current data set did not undergo abrupt deceleration, as that was one of the prerequisites of the weak shock model validation.

Finally, the most challenging issue is the estimation of the meteoroid surface temperature as there is no unique methodology to determine it. It is generally assumed that when the ablation phenomena takes over, the main evaporation phase begins once the temperature reaches 2500 K (Ceplecha et al., 1998; Boyd, 2000; Popova et al., 2001; Jenniskens, 2006) and it shall not largely increase afterward, as the kinetic energy is mainly employed in the ablation process itself. On the other hand, using emission spectroscopy techniques, Borovicka (1993, 1994) and Trigo-Rodríguez et al. (2003, 2004c) compared synthetic spectra with the observed meteor spectra and found an excellent match for most lines. These spectroscopy studies determined that there were two separate ranges of temperatures that could match the two differentiated spectral components that the meteors produced at 3500 - 5000 K for most of the excited composition elements, and at around $10,000$ K for some specific ionized elements. As the infrasound analysis reveals the altitude at which the shock wave originated (but not the earliest point at which the meteoroid started generating the shock wave upon entering the atmosphere), a conservative approach is used assuming that the meteoroid surface temperature is close to 2500 K. Furthermore, as the shock source altitude was constrained by Silber et al. (2015) to within ± 1 km for more than half of the cases (although eleven events have an altitude uncertainty of up to 4.2 km; see Table 14, column (3)), there exists a difficulty in accurately determining the level of evolution of the ablation process of the meteoroid. It should be noted, though, that the temperature rise in the shock layer will reach and even exceed $\sim 10^6$ K. Hence, depending on material properties and velocity of the meteoroid, the meteoroid surface temperature T_w will be two or three orders of magnitude smaller than the gas flow temperature, and as stated by Equation (23), variations between $T_w \sim 2500$ and 5000 K will not largely affect the rate T_w/T. The remaining uncertainty is well within the uncertainties in the radius size.

4.3 RESULTS AND DISCUSSION

4.3.1 *Exploring the Kn results*

The assumptions and guidelines of the previous sections are used to obtain the gas state upstream and downstream the shock wave (see Table 14) and to calculate the values of Kn_r and Re (Table 15) for all the five mass estimates considered (JVB, IE, FM, linear period and shock weak period). Also, in order to map the influence of each mass estimate (and thus radius estimate) on the flow regime calculation, Figure 18 illustrates the relations between Kn_r obtained for each mass estimate and various quantities: the altitude (Figure 18 (a)), the kinetic energy (Figure 18 (b)), the meteoroid velocity (Figure 18 (c)) and the meteoroid mass (Figure 18 (d)). The first thing to be noted in Figure 18 is that it offers an insight into how these variables behave at the different flow regimes of the classic scale. For instance, no meteoroid is observed in the transitional-flow regime ($10^{-1} < Kn_r < 10$) when the infrasound masses are considered. In addition, the linear relationship between the shock source and the Kn_r shown in Figure 18 (a) demonstrates that for well-constrained centimeter-sized meteoroids, the formation of the hydrodynamic shielding may affect the meteoroid flow regime by shifting it to lower Kn_r. Besides, it can be seen that if the meteoroid velocity is kept constant but the mass (and consequently the effective radius) is increased, the flow regime shifts to lower Knudsen numbers for the shock source altitudes observed.

The amount of kinetic energy released at the shock source height shows little variation when all the masses and their respective Kn_r are compared. Figure 18 (b) indicates a slight shift toward higher Kn_r of those meteoroids with lower energies. However, care must be given here, as the statistically small meteoroid data set might lead to a weak relationship. It can, however, be acknowledged that the energy deposition at the shock altitudes (50 to 100 km) varies by three orders of magnitude, from 10^3 kJ to 10^6 kJ. The combination of different values of the velocity and entry angle affects how the meteoroid releases energy and produces infrasound that can be detected on the ground (Silber & Brown, 2014). The results obtained here expand this discussion and allow us to determine the flow regime associated with the point along the meteor trajectory at which the energy was deposited (and subsequently recorded by infrasound). The results (Table 15) suggest that the shock waves could, in principle, form prior to the continuum-flow regime and mainly during the slip-flow regime (or even the transitional if the classical scale is considered). This may be attributed to the formation of the hydrodynamic shielding, which, as explained in the Section 4.1.2, acts to increase the effective size of the meteor cross section (Bronshten, 1983; Popova et al., 2000; Campbell-Brown & Koschny, 2004; Silber et al., 2018b). While this result suggests that infrasound can be used to obtain relevant meteoroid flight parameters, more sophisticated numerical models (yet to be developed) are recommended to further investigate this assertion and to determine the earliest possible point at which the shock wave forms when a meteoroid undergoes strong ablation in rarefied flow conditions.

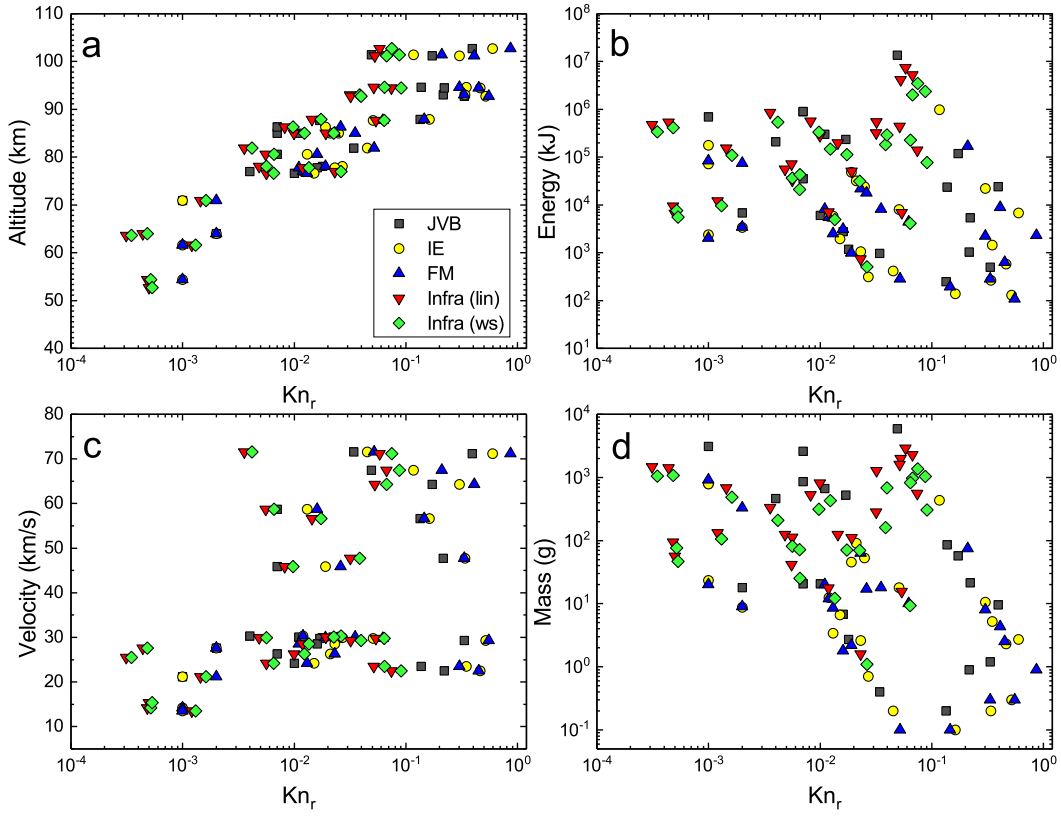

Figure 18: Relation between Kn_r, as derived from the five masses retrieved from observations (JVB, IE, FM, linear period and weak shock period) with: (a) the shock source altitude; (b) the kinetic energy; (c) the meteoroid entry velocity; (d) the meteoroid mass. Note that the legend in panel (a) is applicable to the rest of plots (b-d).

Figure 18 (c) shows that for the fastest meteoroids the associated shock wave is detected when these bodies are between the transitional and slip-flow regimes according to the classical scale. Although it will be discussed later, the results in Table 15 indicate that if the Tsien's scale is used, all meteoroids are within either the slip-flow or continuum-flow regime. Note that for these fast meteoroids the shock wave is detected at higher altitudes than usually expected for a typical meteoroid (see Table 14). The current results corroborate the results of Popova et al. (2000) which suggest that in fast-moving meteoroids, the flow regime will be shifted upward and the shock wave should, indeed, form at higher altitudes. Moreover, the presence of the vapour cap in strongly ablating meteoroids will also affect the flow regime (Popova et al., 2000). This might explain why, typically, fast meteoroids can be visually observed sooner than slow meteoroids. Conversely, slow meteoroids will reach lower altitudes before the shock wave can be detected (see, e.g. Silber et al., 2018a).

As per Figure 18 (d), it illustrates that infrasound masses have a tendency toward lower Kn_r, while photometric masses show a spread across all Kn_r and thus exhibit a weak relationship. In principle, this tendency is due to the already-mentioned mass overestimation through infrasound analyses. A plausible explanation for this apparent discrepancy is the formation of hydrodynamic shielding, which could, in principle, affect the energy deposition and thus the size of the blast radius. In fact, Equation (22) assumes that no or very little ablation is taking place, which, in reality, is rarely the case. Therefore, the infrasound mass derived from the energy deposition (and the blast radius) might not necessarily correspond to the physical mass of the object itself. In some cases, both infrasonic and photometric JVB masses may differ notably relative to the photometric IE and FM masses. In principle, the larger the meteoroid cross section, the larger the number of collisions against atmospheric particles, and the sooner the vapour cap is formed. Consequently, larger masses (which represent larger sizes if the same value of density is assumed) are consistent with lower Kn_r, which agrees with the results shown in Figure 18 (d). This is in line with the discussion in Popova et al. (2000), that indicates that the presence of the vapour cap effectively increases the cross section of the region colliding with air molecules and will shift the meteoroid continuum-flow regime to higher altitudes. Finally, given that the meteoroid mass (or size) is only one of several factors (e.g., altitude, velocity) controlling Kn_r, the broad distribution of IE and FM masses is expected.

4.3.2 *Application of two Knudsen classification scales to validate the results*

The uncertainties in the mass (and thus size) derivation lead to different values of Kn_r for each meteoroid, thus making it possible to associate a different flow regime according to the mass estimate used. However, as shown in Table 15, despite minor differences, the three Kn_r numbers obtained from the JVB, IE, and FM photometric masses show little variation in terms of the flow regimes. The task of assigning a flow

regime when the Kn_r value lies near the flow regime boundaries is strictly related to the precision at which it is accepted that these boundaries are sharp, although, in reality, this transition is not necessarily sharp. Slight Kn_r variations around these 'edges' are merely nominal, and so in this study it is considered that if two different masses lead to the same flow regime, this is accepted as the current state. According to this scheme, 33% of the meteoroid data set is in the transitional-flow regime, 46% in the slip-flow, and the remaining 21% has already reached the continuum-flow regime. Note that these statistics are only used to get a preliminary view of the phenomenology; indeed, for some events the Kn_r is on the boundary between the slip-flow and continuum-flow regimes. A similar discussion can be applied to the Tsien (1946) scale. In this case, the meteoroid data set shows the following distribution: 88% in the slip-flow regime and 12% in the continuum-flow regime.

In view of these results, the use of three different masses (JVB, IE, and FM) for each meteoroid proves that the effect of the assumed meteoroid bulk density value is not critical. Even in the case of the largest difference between mass estimates (meteoroid ID 20110808), the Kn_r number does not vary by much (this is so in both scales). Furthermore, the effects of the extreme meteoroid bulk densities (according to the PE scale: 270 and 7000 kg/m^3) were explored, showing that for the lowest-density case (270 kg/m^3), the flow regime may vary for 33% of the events in the classical scale and 12% in the Tsien's scale. In the classical scale, these events shift either from the transitional to the slip-flow regime, or from the slip-flow to the continuum-flow regime. However, it should be mentioned that most of these cases were previously lying in between the two flow regimes using the assumed stony meteoroid bulk density. Moreover, the use of the Tsien's scale shows that only three cases move to the continuum regime, but once again, these were close to the boundary cases. The use of the highest bulk density (7000 kg/m^3) leads to the variation in two cases in the classical scale and one case in Tsien's scale, all shifting from the continuum-flow to the slip-flow regime. These small variations due to the bulk density are expected, as the effect of either the mass or the bulk density only affects the meteoroid characteristic size, which was determined to be well constrained.

Even though the meteoroid data set in this study is not considered to undergo abrupt deceleration (Silber et al., 2015), a certain level of deceleration is examined in order to overcome the effect of any measurement inaccuracy in the results. This is because the meteoroids, by their very nature, will undergo ablation (more or less strong), which in turn will result in deceleration, especially at lower altitudes. A new value of this velocity was applied assuming a deceleration of 30% (this value exceeds typical deceleration values for centimeter-sized meteoroids, see Jenniskens et al., 2011, but will help in understanding the effect of the velocity on the derivation of the Kn_r). It must be emphasized that the entry velocity used here was that obtained at the first luminous observed point of the meteor trajectory; at that point, the shock wave may have already been formed. Although the shock source heights shown in Table 14, column (2), indicate points within the luminous trajectory, these points represent the earliest point in the trajectory at which the shock wave was detected. However, the shock wave could

certainly have appeared even earlier.

According to this, the results show that there are only two different event flow regimes that change in the classical scale and the Tsien's scale. Thus, introducing deceleration in order to account for any inaccuracies in the calculation of the entry velocity does not affect the results at these heights, and only two events shift from the continuum-flow to the slip-flow regime. The reason behind this apparent flow regime invariability is the energy conversion at the shock front. The transformation of the kinetic energy of the incoming gas flow at the shock front elevates both the temperature and the density in the shock layer. However, on the one hand, the gas density, which remains too low, and the small size of the body still balance the increase due to the velocity variation (see Equation (23)); on the other hand, these high-temperature conditions provide dynamic viscosity values that are well below 1. Consequently, the Re number does not vary significantly. However, this small variation still alters the boundaries of Tsien's scale (see the comments in the Section 4.1), which tend to shift toward higher Kn_r. Using this new velocity value, all meteoroids in the data set propagate under the slip-flow conditions, except for one case, which remains in the continuum-flow regime. Although this new velocity, accounting for deceleration, is more extreme than the one that should occur in the MLT, it is used to test the parameter space bounds in the calculations.

The two Kn_r numbers derived from the infrasound linear and weak shock period masses are quite similar (see columns (5) and (6) in Table 15), and generally different from the JVB, IE, and FM Kn_r numbers. It shall be reiterated here that the JVB masses do remarkably differ from the IE and FM masses and in several cases resemble the mass of the infrasound linear and weak shock methodologies. This could open the discussion on whether the JVB methodology is accurate enough. A previous study that critically compared photometric masses to those derived through dynamic approach (Gritsevich, 2008d) also demonstrated that more work is required to reconcile the apparent differences. However, its use helps understanding the effects of possible erroneous measurements on the Kn_r determination. The use of exclusively the infrasound masses leads to 54% of the events in the slip-flow regime and a 46% in the continuum-flow regime according to the classical scale. As for the Tsien's scale, 79% of the cases are in the slip-flow and the remaining 21% in the continuum-flow regime. Despite the small size of the data set, it can be recognized that these results agree with those derived using the classical scale. In fact, except for one case, all the five masses provide the same flow regime when the Tsien's scale is in use. This is because, as derived from the previous discussion and Equation (23), the value of Kn_r is strongly influenced by the entry velocity and the atmospheric gas conditions at the height where the shock wave is detected. These parameters are principally gathered in the Re number. Moreover, the importance of the viscous effects that are already relevant in the expanding vapour gas is held in the Re number; this suggests that the use of the Tsien's scale is more appropriate in this study. Conversely, the use of the classical scale does not take into account the actual physical scenario that viscosity may create. It is therefore interesting to note that there could be other more complex combinations of fluid dynamics dimensionless characteristic parameters that could delimit more appropriately the meteoroid

flight regimes.

The results provided indicate that the flight flow regime for most of the meteoroids in this data set is between the lower half of the slip-flow regime and the beginning of the continuum-flow regime (Tsien's scale is assumed here). If it could be further verified that the shock wave forms in these regimes, it would be in agreement with the work of Rajchl (1972). However, there is no clear evidence of that, and the suggestion of Probstein (1961), by which the shock wave may gradually form once past half of the transitional-flow regime, cannot be rejected. Future studies should be done in this regard.

Note that while the assumption that $\gamma = 1.4$ might be a simplification, it still provides reasonable results that are consistent with the observations. For example, as expected, no meteor event is found to be in the free molecular flow at altitudes that suggest the presence of the shock wave. The consideration of varying γ is best suited for numerical models, although some modelling studies did apply $\gamma = 1.4$ and found that the main dependences of the vapour (hydrodynamic shielding) parameters, and consequently the temperature and density jumps, are the size and the altitude of the meteoroid (see Popova et al., 2000, and the Section 4.1.2). Also, the consideration of an ablating centimeter-sized meteoroid entering at velocities up to 73 km/s is very different and profoundly more complex than, for example, a much larger reentry vehicle at significantly lower velocities (e.g., 7 km/s; see Silber et al., 2018b, for discussion).

Finally, the current study uses a reference frame located on the surface of the meteoroid (see the discussion in the Section 4.1), thus moving with the body (i.e. local phenomena). However, although well beyond the scope of this study, it could also be possible to combine this information (Kn_r, local) with the information that arises from the global picture, that is, the Kn study of the immersed body (meteoroid plus the vapour gas cap) in the surrounding gas flow. The global and local outcome retrieved from studying both parameters could be of interest in analysing individual cases and should be considered in future studies.

4.3.3 *Understanding the implications of the shock wave information in the study of the flow regimes*

Infrasound indicates the earliest confirmed point at which the shock wave originated (Silber & Brown, 2014; Moreno-Ibáñez et al., 2018) and so this technique can only provide partial information on the whole event (see Chapter 2). The question of what the maximum altitude is at which the shock waves can form remains open. This is indeed a source of uncertainty, but it also validates the fact that meteor shocks form at much higher altitude than they would by theoretically considering their size alone. For instance, it can be found within the meteoroid data set that some members show high-altitude infrasound, which is in line with previous studies for centimeter-sized bod-

ies (Brown et al., 2007; Silber & Brown, 2014, and references therein). Thus, there is already a shock wave at these altitudes. Even in those cases, this chapter shows that the Tsien's scale appropriately describes the flow regimes even for these high-altitude events. Note that thus far no observational or modelling studies have resolved the intricacies associated with the formation of a shock wave in the MLT region for meteoroids traveling at hypervelocity and in the rarefied flow conditions. Furthermore, at present there are no numerical models that account for all meteor-associated phenomena (e.g. ablation, radiation) in the rarefied flow conditions. Thus, this should be the focus of future studies.

The analysis carried out by Popova et al. (2000) explores the flow regimes for a Leonid meteoroid with entry velocity of $\sim$ 72 km/s. As stated before, the meteoroid propagates under the free molecular flow conditions until the onset of intense evaporation at lower heights. Due to this mass loss, the vapour cloud (or hydrodynamic shielding) forms gradually, and when the mean free path within the vapour cloud is much smaller than the meteoroid radius ($l_v \sim 0.1r$), the screening acts more efficiently and the meteoroid is no longer in the free molecular regime. The vapour cap is then formed, and the meteoroid enters the transitional-flow regime between the free-flow and the continuum-flow regimes. Note, however, that Popova et al. (2000) use the classical scale and so $l_v \sim 0.1r$ represents the boundary between the transitional and slip-flow regimes when Kn_r is considered. Note also that the transition regime mentioned by Popova et al. (2000) should really account for the slip-flow regime in the classical scale, as it is derived from the use of the classical scale ($0.01 < l_r/r < 0.1$).

Popova et al. (2000) additionally acknowledge the moment the vapour cloud becomes optically thick, and so it hinders the release of the increasing energy in form of radiation from the the vapour cloud. This moment occurs when the vapour temperature exceeds 4000 K, and it may have an effect in increasing the vapour pressure as described in the Section 4.1.2 of this work, leading to the formation of a shock wave.

To put the current results in perspective, the data set under study is plot on an adaptation of Figure 1 of Popova et al. (2000). This comparison is of interest as this current study deals with the meteoroid flow regimes from an observational aspect and upon the formation of the shock wave, while the work of Popova et al. (2000) provides a numerical approach. This comparison is shown in Figure 19. This figure includes the boundaries and flow regimes as described by Popova et al. (2000) for 10^{-2} to 10 centimeter-sized Leonid meteoroids considering a dense vapour cloud in front of the body. The altitude used to plot the data of this study is that at which the shock wave is detected (the shock source height), whereas for the meteoroid size a mean value for the estimated sizes (see Table 15) through various methodologies is chosen. Figures 19 (a,c) show the average meteoroid radius for the JVB, IE, and FM masses, while Figures 19 (b,d) display the mean value for the infrasound linear and weak shock wave period derived sizes. Note that since the altitude is a fixed value, the position of the meteoroids in each panel of Figure 19 may only vary along the abscissa according to the methodology used in the meteoroid radius derivation. The intense evaporation line, the beginning of the vapour cloud formation ($l_v \sim 0.1r$), the limit below which the vapour

temperature (T_V) exceeds 4000 K, and the boundary for the continuum-flow regime for the Leonid meteoroid studied in Popova et al. (2000) are also plotted.

In order to provide a deeper insight into the results, different shapes and colours are used in Figure 19 to indicate the flow regime of each meteoroid as derived in the current study (Table 15), namely: blue circles illustrate that the meteoroid is in the transitional-flow regime, orange triangles represent the slip-flow regime, and green squares represent the continuum-flow regime. Since two Kn scales are under analysis, in the panels on the left (Figure 19 (a,b)) the meteoroid flow regime results of this chapter as derived from the use of the classical scale are plotted, while the panels on the right (Figure 19 (c,d)) illustrate the meteoroid regimes when the Tsien's scale is considered. Note again that the flow regime areas labelled in the plots are those obtained by Popova et al. (2000) for their Leonid meteoroids, and so they do not represent the calculated flow regimes for the meteoroid data set in use.

The first thing to be noted is that the presence of a shock wave indicates that the meteoroids of the studied data set are located below the line of $T_V \sim 4000$ K, which is indeed the case. However, the existence of a shock wave changes the conditions in the vapour cloud, and thus the meteoroid could reach the lower Kn earlier. Although the division of flow regimes by Popova et al. (2000) does not directly apply to the data set under study, it can serve as the basis for visualization. It can be seen that the continuum-flow regime is not reached by nearly any of the meteoroids in the data set. Indeed, the slip-flow regime is achieved at a wider range of heights. Another consideration that should be noted is that the delimitation of the flow regimes by Popova et al. (2000) applies to Leonid meteoroids with a roughly fixed entry velocity of 72 km/s, whereas the meteoroid data set studied shows a range of entry velocities (13.5 - 71.2 km/s, as shown in Table 14). However, the data set in use contains three meteoroids with entry velocities close to 72 km/s, namely: 20060805, 20070125, and 20081107. Two of these, 20060805 and 20070125, show a Kn_r that is on the boundary between the transitional and slip-flow regimes (classic scale), and their position on Figure 19 (a) is closer to the free molecular flow outlined by Popova et al. (2000). These two meteoroids are located around 20 km below the free molecular flow delimitation line, thus supporting the statement that the appearance of a shock wave is suggestive of the alteration of classically defined meteor flow regimes.

Regarding the use of the mean meteoroid size, although it is not completely accurate, it is still representative of the realistic scenario. Using either end member estimate of the radius for a given meteoroid would move the position of the data point along the x-axis (Figure 19) to the right or the left (note that the x-axis is in logarithmic scale). The x-axis error bars in Figure 19 indicate the standard error from the mean values. As stated before, the masses derived from the infrasound linear and weak shock periods are very similar, and thus this error is small. However, the meteoroid sizes derived using the JVB methodology show larger discrepancies when compared to the IE and FM results; this causes the large error bars. If the JVB masses were disregarded in the study, the meteoroid radii in the figure would be practically fixed. Nevertheless, as the sizes of the meteoroids in the data set are well constrained and the flow regimes

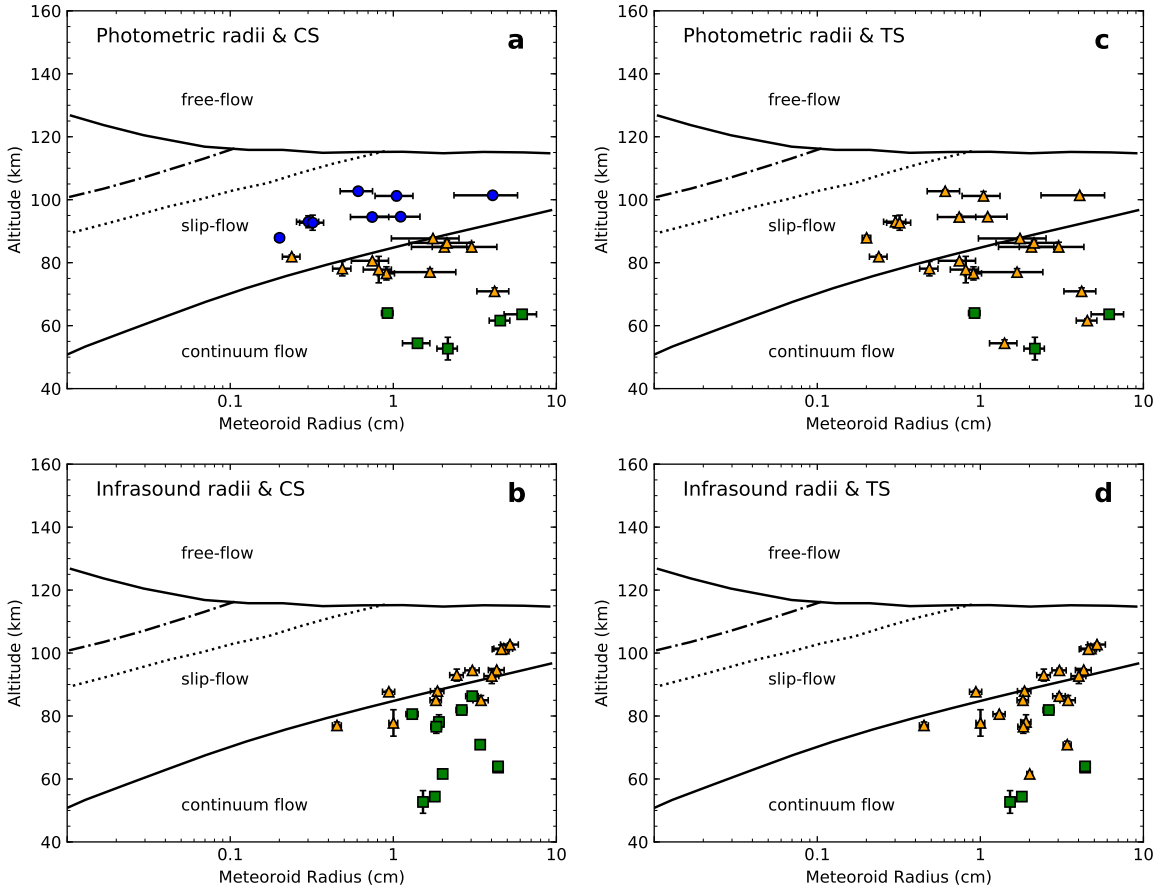

Figure 19: Adaptation of Figure 1 of Popova et al. (2000). The lines and regions are as in Popova et al. (2000): the intense evaporation line (solid top line) and the continuum-flow (solid bottom line) boundary for the Leonids (0.01 centimeter-sized meteoroids with entry velocities around 72 km/s); the boundary that indicates the moment the mean free path (l_v) becomes 0.1 times the meteoroid radius ($l_v \sim 0.1r$) or, conversely, the beginning of the slip-flow regime when the classical scale is in use (dashdotted line); and the line below which the vapour cloud temperature (T_w) exceeds 4000 K (dotted line). The flow regime regions for these Leonid meteoroids as derived by Popova et al. (2000) are labelled. The mean meteoroid radii from the JVB, IE, and FM photometric masses are shown in panels (a) and (c). While panels (b) and (d) plot the results for the mean meteoroid radii derived from the infrasound methodologies (linear and weak shock periods). The flow regimes as derived from the two scales analysed in this study are represented by data points with distinct colours and shapes. Blue circles are used for meteoroids in the transitional-flow regimes. Orange triangles represent those meteoroids in the slip-flow regime. Green squares indicate the continuum-flow regime. The panels on the left (a, b) account for the flow regimes when the classical scale (CS) is considered, whereas in the panels on the right (c, d), the meteoroid flow regimes are based on the results using the Tsien's scale (TS). Finally, the horizontal error bars represent the standard error from the mean, and the altitude error as described in Table 14. Note that some error bars are small and contained within the data points.

are determined, these large error bars are useful to indicate the extent of uncertainty that might be expected in these types of studies. It can be stated from Figure 19 that the results derived from the infrasound linear and weak shock period radii are generally within the size errors of the mean photometric radius (JVB, IE, and FM).

The formation of the hydrodynamic shielding and eventually the shock wave alters the mean free path in the vicinity of the meteoroid and therefore the flow regime conditions. This implies a dynamical scenario that could be difficult to track using a fixed classification of the classical Knudsen scale. As per the results obtained in this chapter, it can be suggested that the formation of the vapour cap (or hydrodynamic shielding) should be reevaluated in the definition of the meteoroid flow regimes. In fact, the vapour cap plays an important role in the generation of the shock wave, and the extent of this role should be the scope of more sophisticated models (yet to be developed) and future studies. In these terms, the introduction of a classification scheme that accounts for changes in the surrounding conditions, such as Tsien's scale, seems more reliable.

4.4 CONCLUSIONS

This chapter has explored the utility of meteoroid infrasound to unravel new clues on the atmospheric flight regime of centimeter-sized bodies. Coupled with optical observations, infrasound provides conclusive evidence of the existence of meteor-generated shock wave at a given altitude. As the meteoroid penetrates deeper into the atmospheric layers, the incoming flux of atmospheric particles increases, and the ablation process starts. Sporadic gas molecular collisions become more regular, triggering an intense vaporization process. This leads to the formation of a vapour cloud in front of the meteoroid. Once the pressure of this cloud exceeds that of the surrounding atmospheric gas, it expands, and a detached shock wave is formed in front of the meteoroid. The acoustic by-product of the shock wave (infrasound) can be detected under certain conditions from ground-based instruments. The use of that information has been implemented here to reach the following conclusions:

1. Previous works based on infrasound analysis demonstrated that the infrasound study could positively identify the earliest point at which it can be claimed that a shock wave is present. Furthermore, those studies also suggest that the meteor shock wave could form much earlier than predicted by classical methodologies. On the other hand, despite the limited information provided, infrasound seems to be a robust means to determine the flow regime of meteoroids. This study provides the first observational verification of the Knudsen scale using information obtained through infrasound for a data set of centimeter-sized meteoroids. This data set represents the only well-documented and well-constrained set of such events to date.

2. The results of this chapter are consistent with the use of a reference frame attached to the meteoroid body, in contrast to the gas flow attached reference frame. Such

an approach is not only more convenient but also more representative of realistic conditions. Moreover, it has been shown that the flow regimes could be considered within boundaries delimited as a function of several fluid dynamic dimensionless parameters (i.e. Kn, Re, Ma). The results reinforce the theoretical approach that claims that a scale based on the Kn and Re numbers illustrates the physics of the problem more accurately. The differences between the flow regimes derived from the theoretical and observational approaches have been discussed. While no strong conclusion could be derived, as the formation height of the shock wave cannot be determined yet, this study suggests that the shock wave for centimeter-sized meteoroids is already formed in the slip-flow regime (or even the late transitional-flow regime).

3. This chapter also explored whether the use of information derived from different meteoroid observation techniques could lead to similar results. In this sense, photometric measurements provide the robust means of estimating centimeter-sized meteoroid masses (under the condition of negligible deceleration). While infrasound alone does not provide sufficient insight into meteoroid masses, it remains an excellent tool in monitoring and detection of meteors. Moreover, infrasound measurements, when coupled with other techniques, provide useful estimates in meteor flow regimes and thus could serve as another mode of validation. This chapter shows that simultaneous observations of meteors, using both infrasound and photometric techniques, can provide relevant clues on the meteoroid flight regimes and the energy deposition at the point of origin of the shock wave.

4. This study confirms that the formation of a vapour cap shifts the flow regimes upward and acknowledges the necessity of developing new and more sophisticated models to describe the flow regimes of meteoroids encountering the Earth's atmosphere. These new models should also constrain and evaluate the impact on the hydrodynamic shielding in those events where a strong ablation takes place. This fact would eventually play a relevant role on the formation of the meteor-generated shock wave and shift the flow regimes. Several questions remain open and shall be the scope of future research: Once the maximum height at which the shock wave can form is more accurately determined, would the flow regime vary by much?; What is the most suitable flow regime scale?; Is there any use in combining the information obtained using different reference frames (Kn vs Kn_r)?. A natural step toward further refinement would include numerical studies and determination of how the dynamic changes in the hypervelocity flow field might affect the flow regimes.

Date	Hour	Minute	Seconds	H_{begin}	H_{end}	Mass (JVB)	Mass (IE)	Mass (FM)	Mass Infrasound (linear p.)	Mass Infrasound (weak shock)	Radius (JVB)	Radius (IE)	Radius (FM)	Infra. Radius (linear p.)	Infra. Radius (weak shock)
20060419	7	5	56	72.0	47.7	107.4	23.5	20.0	94.9	75.9	1.94	1.17	1.11	1.86	1.73
20060805	8	38	50	126.4	74.5	5927.6	432.9	74.0	2292.7	1038.3	7.39	3.09	1.72	5.39	4.14
20061104	3	29	29	89.9	65.8	459.9	12.5	12.0	1.6	1.1	3.15	0.95	0.94	0.48	0.42
20070125	10	2	5	119.2	88.5	9.5	2.7	0.9	2924.5	1375.2	0.86	0.57	0.39	5.84	4.54
20070727	4	51	58	96.2	70.6	2583.9	91.5	63.0	816.4	428.6	5.61	1.84	1.63	3.82	3.08
20071021	10	26	25	130.8	81.7	57.5	10.6	4.3	2005.9	967.5	1.58	0.90	0.66	5.15	4.04
20080325	0	42	3	76.2	32.8	2912.0	792.9	917.0	133.0	105.4	5.83	3.78	3.97	2.09	1.93
20080511	4	22	17	95.2	77.3	85.8	5.2	8.0	1603.0	822.5	1.80	0.71	0.82	4.78	3.83
20080812	8	19	29	105.7	82.0	0.2	0.1	0.1	125.0	70.6	0.22	0.18	0.20	2.04	1.69
20081028	3	17	35	81.2	41.1	309.8	79.6	110.0	56.7	46.8	2.76	1.76	1.96	1.57	1.47
20081102	6	13	26	96.5	62.6	663.9	53.3	18.0	112.1	69.5	3.56	1.54	1.07	1.97	1.68
20081107	7	34	16	113.5	81.5	0.4	0.2	0.1	332.7	208.7	0.30	0.22	0.20	2.83	2.42
20090428	4	43	37	83.5	38.0	3086.5	784.1	330.0	686.0	489.3	5.95	3.77	2.82	3.60	3.22
20090523	7	7	25	95.9	72.4	2.7	0.7	2.2	125.0	81.1	0.57	0.36	0.53	2.04	1.77
20090812	7	55	58	108.5	80.4	20.6	3.4	1.8	41.8	25.1	1.12	0.61	0.50	1.42	1.20
20090917	1	20	38	85.7	72.4	20.7	6.6	8.5	112.7	71.8	1.12	0.77	0.83	1.97	1.70
20100421	4	49	43	108.5	74.6	861.5	45.7	17.0	534.3	314.6	3.89	1.46	1.05	3.32	2.78
20100429	5	21	35	105.7	89.9	0.9	0.2	0.3	283.7	159.8	0.40	0.25	0.26	2.68	2.22
20100530	7	0	31	96.0	78.3	1.2	0.3	0.3	1281.4	682.6	0.43	0.27	0.26	4.44	3.60
20110520	6	2	9	95.7	84.1	21.3	2.3	2.5	555.6	304.7	1.13	0.54	0.55	3.36	2.75
20110630	3	39	38	100.5	71.7	527.5	18.0	10.0	15.6	9.3	3.30	1.07	0.88	1.02	0.86
20110808	5	22	6	86.6	39.9	9990.9	2586.4	1003.0	1465.3	1045.3	8.80	5.61	4.09	4.64	4.15
20111005	5	8	53	96.2	64.5	6.8	2.6	20.0	17.7	12.2	0.77	0.56	1.11	1.06	0.94
20111202	0	31	4	97.0	53.8	18.0	8.8	9.0	1413.9	1075.8	1.07	0.84	0.85	4.59	4.19

Table 13: Basic data retrieved from the meteor infrasound detection and luminous path observations. Photometric meteoroid masses taken from Silber et al. (2015) are calculated as described in Jacchia et al. (1967), JVB; using the kinetic energy as in Ceplecha et al. (1998), IE; using the fragmentation model and the light curve described in Ceplecha & Revelle (2005), FM. Infrasonic masses (linear period and weak shock period) has been calculated using Equation (23) and following the work of Silber & Brown (2014). The meteoroid radii are derived from these masses. The columns are organized as follows: (1) meteoroid ID (which coincides with the date of its detection); (2-4) the time at which the infrasonic wavetrain reached the detector; (5-6) the beginning and ending heights of the meteor luminous path in [km]; (7-11) the meteoroid masses derived using five different methodologies in [g]; (12-16) the results of the meteoroid radius calculation using the masses listed in previous columns in [cm]. Except for the infrasound masses and meteoroid radii, all the other data shown in this table was previously published by Silber et al. (2015).

			Flow Conditions Upstream					Flow Conditions Downstream					
ID	Shock Source Height	Error S.S. Height	V_{entry}	T	Density	Sound Speed	Mach	T	Density	Mach	Sound Speed	V	Atmospheric Viscosity
20060419	54.4	1.1	14.2	255.1	6.461E-07	320.0	44.32	97651.9	3.867E-06	0.3785	6260.5	2369.4	0.0005
20060805	101.4	0.4	67.5	191.8	3.379E-10	277.5	243.32	2208143.7	2.026E-09	0.3780	29770.3	11252.6	0.0022
20061104	77	1.1	30.3	218.5	2.461E-08	296.1	102.18	443808.2	1.477E-07	0.3781	13346.5	5045.7	0.0010
20070125	102.7	0.5	71.2	181	3.396E-10	269.5	264.31	2458858.3	2.037E-09	0.3780	31415	11874.2	0.0023
20070727	85	1.5	26.3	165.6	8.244E-09	257.8	102.05	335505.5	4.946E-08	0.3781	11604.3	4387.1	0.0008
20071021	101.2	1.4	64.3	185.6	4.722E-10	272.9	235.59	2003159	2.832E-09	0.3780	28354.9	10717.6	0.0021
20080325	61.6	0.6	13.5	237.2	2.414E-07	308.6	43.75	88516.3	1.445E-06	0.3785	5960.5	2255.9	0.0004
20080511	94.6	0.4	23.5	188.5	1.418E-09	275.1	85.58	268631.1	8.502E-09	0.3781	10383.6	3926	0.0008
20080812	87.9	0.8	56.6	174.5	4.952E-09	264.6	213.87	1552152.8	2.970E-08	0.3780	24959.6	9434.4	0.0018
20081028	52.7	3.6	15.4	252.1	6.790E-07	318.1	48.41	115132	4.063E-06	0.3784	6797.8	2572.1	0.0005
20081102	85	0.5	30.1	209.7	7.222E-09	290.1	103.75	439121.2	4.329E-08	0.3781	13275.8	5019	0.0010
20081107	81.9	0.6	71.6	214.4	1.137E-08	293.3	244.08	2483801.8	6.821E-08	0.3780	31573.9	11934.3	0.0023
20090428	70.9	1.1	21.2	217.7	7.448E-08	295.6	71.72	217940.1	4.466E-07	0.3782	9352.7	3536.8	0.0007
20090523	78.1	2.3	29.9	194.4	2.772E-08	279.3	107.04	433293.2	1.661E-07	0.3780	13187.5	4985.5	0.0010
20090812	80.6	0.3	58.7	186.4	1.780E-08	273.5	214.61	1669465.6	1.068E-07	0.3780	25885.6	9784.4	0.0019
20090917	76.6	2.1	24.2	206.5	3.051E-08	287.9	84.06	283912.6	1.830E-07	0.3781	10674.9	4036.2	0.0008
20100421	86.3	0.8	45.9	190.7	6.602E-09	276.7	165.91	1020839.5	3.961E-08	0.3780	20241.8	7651.4	0.0015
20100429	93	1.9	47.7	186.3	2.019E-09	273.4	174.44	1102456.7	1.210E-08	0.3780	21035.4	7951.3	0.0015
20100530	92.7	2.4	29.3	171.7	1.973E-09	262.5	111.61	416063.9	1.183E-08	0.3780	12922.6	4885.3	0.0009
20110520	94.5	0.7	22.5	183.6	1.465E-09	271.5	82.89	245429.9	8.786E-09	0.3781	9925.1	3752.7	0.0007
20110630	87.7	0.5	29.8	161.4	5.042E-09	254.5	117.08	430369.9	3.025E-08	0.3780	13142.9	4968.5	0.0010
20110808	63.6	0.3	25.5	230.9	2.229E-07	304.4	83.76	315236.4	1.336E-06	0.3781	11248.3	4253	0.0008
20111005	77.8	4.2	28.5	208.7	2.276E-08	289.4	98.47	393697.5	1.365E-07	0.3781	12570.5	4752.4	0.0009
20111202	64	0.6	27.6	234.6	1.474E-07	306.9	89.94	369261.7	8.842E-07	0.3781	12174.1	4602.8	0.0009

Table 14: Shock wave analysis: shock source height and its error values derived from infrasound study; and gas flow conditions upstream and downstream calculated using the Rankine-Hugoniot equations. Columns are organized as follows: (1) the meteoroid ID; (2-3) the source height of the shock wave and the associated error in [km]; (4) the entry velocities (which are used to estimate the incoming gas flow velocity, as described in the main text) in [km/s]; (5-8) the gas temperature [K], gas density [g/cm^3], sound speed [km/s] and Mach number upstream, respectively; (9-14) the downstream conditions in the following order: (9) gas temperature [K], (10) gas density [g/cm^3], (11) Mach number, (12) sound speed [km/s], (13) gas velocity [km] and (14) the gas dynamic viscosity [kg/(m·s)].

Date	Kn_r (JBV)	Kn_r (IE)	Kn_r (FM)	Kn_r (linear p.)	Kn_r (weak shock p.)	Re (JBV)	Re (IE)	Re (FM)	Re (linear p.)	Re (weak shock p.)	Classical Scale	Tsien Scale	Classical Scale for infr. masses	Tsien Scale for infr. masses
20060419	0.0000	0.001	0.001	0.000	0.0010	391.0	235.6	223.3	375.2	348.3	Continuum	Slip	Continuum	Continuum
20060805	0.0490	0.117	0.210	0.067	0.0870	0.8	0.3	0.2	0.6	0.4	Transitional	Slip	Slip	Slip
20061104	0.0040	0.012	0.012	0.023	0.0260	24.2	7.3	7.2	3.7	3.2	Slip	Slip	Slip	Slip
20070125	0.3930	0.599	0.862	0.058	0.0750	0.1	0.1	0	0.6	0.5	Transitional	Slip	Slip	Slip
20070727	0.0070	0.021	0.023	0.010	0.0120	14.4	4.7	4.2	9.8	7.9	Slip	Slip	Slip	Slip
20071021	0.1720	0.302	0.408	0.053	0.0670	0.2	0.1	0.1	0.8	0.6	Transitional	Slip	Slip	Slip
20080325	0.0000	0.001	0.001	0.001	0.0010	438.9	284.5	298.6	156.9	145.2	Continuum	Slip	Continuum	Slip
20080511	0.1370	0.348	0.301	0.052	0.0640	0.8	0.3	0.4	2.1	1.7	Transitional	Slip	Slip	Slip
20080812	0.1340	0.162	0.146	0.014	0.0170	0.3	0.3	0.3	3.2	2.6	Transitional	Slip	Slip	Slip
20081028	0.0000	0.000	0.000	0.001	0.0010	584.9	371.9	414.2	332	311.6	Continuum	Continuum	Continuum	Continuum
20081102	0.0110	0.025	0.035	0.019	0.0230	8.0	3.5	2.4	4.4	3.8	Slip	Slip	Slip	Slip
20081107	0.0340	0.045	0.052	0.004	0.0040	1.0	0.8	0.7	10	8.6	Slip	Slip	Continuum	Continuum
20090428	0.0010	0.001	0.002	0.001	0.0020	138.1	87.4	65.5	83.6	74.7	Slip	Slip	Continuum	Slip
20090523	0.0180	0.027	0.019	0.005	0.0060	4.9	3.1	4.6	17.6	15.3	Slip	Slip	Continuum	Slip
20090812	0.0070	0.013	0.016	0.006	0.0070	6.2	3.4	2.8	7.9	6.6	Slip	Slip	Continuum	Slip
20090917	0.0100	0.015	0.013	0.006	0.0070	10.7	7.3	7.9	18.8	16.1	Slip	Slip	Continuum	Slip
20100421	0.0070	0.019	0.026	0.008	0.0100	8.0	3	2.2	6.8	5.7	Slip	Slip	Continuum	Slip
20100429	0.2160	0.339	0.332	0.032	0.0390	0.2	0.2	0.2	1.7	1.4	Transitional	Slip	Slip	Slip
20100530	0.3320	0.519	0.553	0.032	0.0400	0.3	0.2	0.2	2.7	2.2	Transitional	Slip	Slip	Slip
20110520	0.2200	0.463	0.450	0.074	0.0910	0.5	0.2	0.3	1.5	1.3	Transitional	Slip	Slip	Slip
20110630	0.0170	0.051	0.062	0.054	0.0640	5.2	1.7	1.4	1.6	1.3	Slip	Slip	Slip	Slip
20110808	0.0000	0.000	0.000	0.000	0.0000	611.2	389.6	284.1	322.3	288	Continuum	Continuum	Continuum	Continuum
20111005	0.0160	0.023	0.011	0.012	0.0130	5.5	4	7.9	7.5	6.7	Slip	Slip	Slip	Slip
20111202	0.0020	0.002	0.002	0.000	0.0000	49.1	38.7	39	210.6	192.3	Continuum	Continuum	Continuum	Continuum

Table 15: Knudsen numbers, Reynolds numbers and meteoroid flow regime analysis: (1) event ID; (2-6) Kn_r as derived from the five possible masses discussed in the Section 4.3; (7-11) the Re number using these five masses; the flow regime according to the classical scale (see the Section 4.1) and the scale described in Tsien (1946) as obtained from the JVB, IE and FM masses (12-13), and the masses derived from the infrasound detected signal (linear and weak shock period) (14-15).

5

TERMINAL HEIGHTS

5.1 INTRODUCTION

Retrieving the meteoroid trajectories in the atmosphere is of interest to researchers. On the one hand, orbital parameters can be derived based on the impact time, meteor radiant and initial velocity allowing us to estimate their parental relationship with parent bodies - asteroids and comets. On the other hand, a knowledge of physical parameters such as mass, velocity, deceleration or height at different points of the meteor trajectory turns out to be very useful to locate a meteorite fall, or to predict the energy deposition either on the Earth atmosphere or surface. The temporal analysis of the energy released during the meteoroid atmospheric path is additionally important to provide a complete understanding on the ablation and other mass loss mechanisms occurring along the flight.

Despite ablation and drag processes associated with atmospheric entry of meteoroids have been a subject of intensive study over the last century, little attention has been devoted to interpreting the observed fireball terminal height. This parameter indicates the final point of the luminous part of the meteoroid trajectory. This is the point where a fireball disintegrates, or for meteorite-droppers, the last point where luminous radiation can be observed. This is a key parameter because it not only depends on the initial mass, but also on the bulk physical properties of the meteoroids and hence on their ability to ablate in the atmosphere. The terminal height also describes the amount of deceleration experienced by the meteor, which in turn means the degree of penetration into the atmosphere.

This chapter provides a different insighti into the way of calculating terminal heights for either disintegrating meteoroids and meteorite falls. This will be done using the scaling laws meteor modelling described in Chapter 2 and the accurate data sample gathered by the Meteor Observation and Recover Project which includes a meteorite.

5.2 PREVIOUS STUDIES ON THE TERMINAL HEIGHTS

Provided past limitations that techniques and methodologies set on the observation and processing of meteor data, previous studies relied on the combination of observed meteor flight parameters to derive further conclusions and reinforce previous hypothesis.

Besides, all these studies relied on the Single Body Theory (see Chapter 2) which assumes the values of some meteoroid flight parameters beforehand. An example of this is the work of Ceplecha & McCrosky (1976) using the Prairie Network database. This network operated in USA between 1963 and 1975 and registered more than 2,700 fireballs, one of them being the Lost City meteorite (McCrosky et al., 1971). The goal of Ceplecha & McCrosky (1976) was to outline the means to distinguish between ordinary and carbonaceous chondrites within the recorded fireballs. Their driving idea was that carbonaceous chondrites are more fragile than ordinary chondrite. Consequently, the former should, in principle, suffer larger rates of ablation and show higher terminal heights, while the later may reach lower altitudes. As the ability of a meteoroid to reach lower atmospheric layers do also depend on the entry angle, velocity and shape, these should be also accounted for when a classification criterion is outlined. Ceplecha & McCrosky (1976) derived an empirical criterion (Equation (25)) that established a weighted relation (PE criterion) between the fireball terminal height and these other flight properties of the fireball, namely: the air density at terminal height, ρ_t [g/cm^3], the pre-atmospheric mass, M_e [g], pre-atmospheric velocity, V_e [km/s], and the zenith distance of the meteor radiant, Z_R [^{o}].

$$PE = log\, \rho_t + A\, log\, M_e + B\, log\, V_e + C\, log\, (cos\, Z_R) \tag{25}$$

Where coefficients A, B and C are obtained by imposing a least square fit to 156 fireballs of the Prairie Network (McCrosky & Boeschenstein, 1965). Note that in Equation (25) the terminal height is included through the air density at that point, ρ_t. According to this PE criterion, Ceplecha & McCrosky (1976) classified the Prairie Network fireballs into four different meteor groups.

All the parameters involved in the PE criterion express the atmospheric dynamic behaviour of the meteor, and so Equation (25) does not include the bulk properties of the impacting body. Indeed, there is extra information that can be directly extracted from the meteor observation that could help to refine the classification provided by the PE criterion. The ablation coefficient, σ [s$^2\cdot$ cm^{-2}], and a geometrical coefficient depending on the shape of the object, the drag coefficient and the bulk density, the shape-density coefficient K [cm$^2\cdot$ g$^{-2/3}$], are also determined from the trajectory when the observations and the Single Body Theory equation are compared. Ceplecha & McCrosky (1976) build up a secondary criterion comparing the average values (for all the observational measurements) of these later parameters. This new criterion, called SD is expressed as:

$$SD = < log\, K > \; + \; < log\, \sigma > \tag{26}$$

The average numbers, $< log\, K >$ and $< log\, \sigma >$, are weighted by the ratio of the deceleration to its formal rms error. Then, SD is a parameter that has little influence from observational errors and it describes globally the physical changes that the meteor suffers during its atmospheric flight (change in mass, surface, ablation, etc.). It is relevant that the shape-density coefficient (K) is a function of the object's shape and its density, thus providing an indirect means of accounting for the meteor fragmentation.

This way, one of the Single Body Theory main weaknesses is partially overcome.

Ceplecha & McCrosky (1976) showed that both the PE and the SD criteria are theoretically related. Moreover, PE was initially intended to be empirical, but it can be outlined using the Single Body Theory. As a final remark, Ceplecha & McCrosky (1976) stated that SD depends on the second derivative of the observational measurements and therefore it is less affected by observational errors than PE.Thus, reducing the uncertainties of PE and becoming somehow supplementary. Note that these two criteria (Equations (25) and (26)) turned out to be mathematically related when the meteor initial mass could be considered small or the ablation was large. Additionally Ceplecha & McCrosky (1976) also stated that the results obtained using the ablation and shape-density coefficient values at the recorded last luminous point of the meteor trajectory in Equation (26) instead of the average values seem to provide better results.

Previously to the work of Ceplecha & McCrosky (1976), Ceplecha (1967, 1968, 1988) suggested a meteor classification that relied on the meteor beginning height and its pre-atmospheric orbit. Ceplecha & McCrosky (1976) discussed a possible relationship between both classifications but found that only objects with Taurid-like orbits could be compared as they were available in both samples. This small sample of nine bodies leads to a poor statistic so as to derive strong conclusions.

Few years later, Wetherill & Revelle (1981) suspected that a large number of ordinary chondrite falls might be hidden within the Prairie Network database and not found because of their small terminal masses. Wetherill & Revelle (1981) also discussed that the commonly accepted low-bulk density values may relevantly affect the outcome in meteoroid impact studies. Based on the previous work of Revelle & Rajan (1979) and Revelle (1980), Wetherill & Revelle (1981) claimed that masses derived photometrically could be ten times higher than real masses, whereas dynamic masses could be twice smaller. Additionally, Wetherill & Revelle (1981) spotted that the cross-sectional area, which is related to any possible fragmentation occurred during the atmospheric flight (fragments flying very close to the main fragment increase the effective cross-sectional area) could have been previously overestimated for the dataset. Implementing a correction to these values may increase the expected number of small ordinary chondrites meteorite falls. Note though that the chances of an ordinary chondrite meteoroid to survive its atmospheric flight do also depend on its initial mass and entry geometry. Given that bodies with different compositions were available in the Prairie Network database, and these can show similar terminal heights, this parameter cannot be the only distinctive parameter to characterize ordinary chondrites. Nonetheless, Wetherill & Revelle (1981) assumed that chances of having other than ordinary chondrites with such terminal heights within the studied sample were less than 16%.

As a further way of classification Wetherill & Revelle (1981) stated four criteria to differentiate feasible ordinary chondrites within the Prairie Network sample. Among these criteria Wetherill & Revelle (1981) highlighted the importance of the observed terminal height and stated that any ordinary chondrite inside the sample shall behave, scaled up to a certain point, alike the Lost City meteorite. This was otherwise expressed consider-

ing that for any meteorite-producing fireballs the observed terminal height should agree with the dynamic mass value obtained through the equations of the Single Body Theory, as well as with that of Lost City fireball to within 1.5 km, when appropriately scaled for mass, velocity, and entry angle. Note that Wetherill & Revelle (1981) required an agreement between the observed and theoretical terminal heights as an indicator of a good adjusted meteoroid atmospheric trajectory; this is, Wetherill & Revelle (1981) showed similar deceleration, drag coefficient, ablation, etc. Wetherill & Revelle (1981) stated that despite of the different methodologies applied, the final amount of ordinary chondrite fireballs identified within the Prairie Network is similar to the previous work of Ceplecha & McCrosky (1976).

Another work in this regard was carried out by Halliday et al. (1989a,b). They studied 44 fireballs recorded by the Meteor Observation and Recover Project (MORP) to derive possible correlations between some observed flight parameters, i.e.: the initial velocity, total light emitted by the fireball, initial and end masses, initial and end heights, orbital elements etc. The correlations analysed were ultimately evaluated as strong, moderate, weak or none. Despite of the observational errors (meteor trajectories not fully observed, not clear sky, etc.), two strong correlations were derived: the mass lost during the ablation versus the peak brightness, and the duration of the luminosity recorded versus the zenith distance of the radiant.

Here the terminal heights along with suitable approximations are obtained to a large number of MORP fireballs, including suspected meteorite-producing events included in the Table 6 by Halliday et al. (1996). To do so, the mathematical approach (see Chapter 2) developed by Stulov et al. (1995), Stulov (1997) and Gritsevich & Stulov (2007) that gathers the meteoroid flight unknown values into two new variables, α (ballistic coefficient) and β (mass loss parameter), is used; thus, mathematically introducing the similar idea of parameters' scaling as suggested by Wetherill & Revelle (1981). The combination of these two new parameters allows the derivation of other important parameters, such as pre-atmospheric and terminal mass values, ablation and shape change coefficients, and the terminal height. Although a methodology to determine terminal height using this mathematical approach was previously implemented by Gritsevich & Popelenskaya (2008), it was only limited to fully ablated fireballs and not applied to a large dataset.

5.3 FORMULATION

The basic equations of motion of a meteor in the atmosphere require a concise knowledge about the body physical properties, such as the bulk density, shape, mass, etc. These properties do change during the flight and they also depend on the observations reliability and camera resolution. The usual way of tackling this problem relies on using average values which are retrieved either from previous experience or from the observations available from the astrometric reduction of each event (see Chapter 2). Alternatively, a different approach is suggested. Instead of using the average values

as input data, all unknowns can be gathered into dimensionless parameters, retrievable from the observations with the help of inverse techniques. As already outlined in Chapter 2, the resulting analytical solution of the scaled meteoroid equations of motion is:

$$m = exp[-(1-v^2)\beta/(1-\mu)] \tag{27}$$

$$y = ln2\alpha + \beta - ln\Delta, \quad \Delta = \bar{Ei}(\beta) - \bar{Ei}(\beta v^2), \tag{28}$$

$$\bar{Ei}(x) = \int_{-\infty}^{x} \frac{e^t dt}{t} \tag{29}$$

Where m and v are the dimensionless values of the meteoroid mass and velocity respectively, μ is a constant, and α and β the dimensionless unknowns. As explained in Gritsevich (2007, 2008b) a weighted least-squared method is applied to the observed height and velocity values using Equation (28) to derive α and β. While a manual assignation of the weighted factors could be quite complicated, Gritsevich (2008b) suggests that taking an exponential form of Equation (28) proves to perform better since the height and velocity of a meteoroid decrease while it gets closer to the Earth's surface. Mathematically it means that instead of laying a direct comparison between y_i (observed) and y_i (calculated) the comparison is made between e^{-y_i} values. The obtained results are then compared with the original data leading to a very good agreement (see e.g., Gritsevich, 2008c). Then, Equation (28) turns into the following form:

$$\alpha exp(-y) - \Delta exp(-\beta) = 0 \tag{30}$$

with $\Delta = \bar{Ei}(\beta) - \bar{Ei}(\beta v^2)$.

When the analytical expression (30) accurately adjusts the set of observed trajectory (y_i, v_i) values then α and β are derived by minimizing the following expression:

$$Q(\alpha, \beta) = \sum_{i=1}^{n} (F_i(y_i, v_i, \alpha, \beta))^2 \tag{31}$$

where

$$F_i(y_i, v_i \alpha, \beta) = 2\alpha exp(-y_i) - \Delta_i exp(-\beta) \tag{32}$$

At least 3 points along the trajectory ($n \geq 3$) are required to solve Equation (31). One of such points should contain the initial velocity value, V_e, as it is needed for scaling. It is also assumed that deceleration was noticeable during the luminous trail, i.e., there are at least 2 other than the beginning points $(k, j \leq n)$ along the trajectory such as $V_k < V_j < V_e$. In principle, recent proliferation of meteor observational instruments and methodologies makes it possible to fulfil this condition even for such small meteoroid particles as the Draconids (Borovička et al., 2007; Kero et al., 2012; Ye et al., 2013;

Vaubaillon et al., 2015). In ordinary cases, when equally reliable data are provided along the observed trajectory (e.g., Halliday et al., 1996), it is more convenient to input all available (h_i, V_i) values. However, sometimes specific initial filters on observational data may apply to correct inaccurate information. Indeed, although α and β derivation only requires three observed (h_i, V_i) values, since α and β mainly describe the meteor deceleration, and this is remarkably present in the last part of the luminous trajectory of the meteoroid flight, it is highly recommendable to include (h,V) values of the part where the main deceleration is present. This will generally decrease the error in the results which, otherwise, may differ from the real behavior of the meteoroid. This is particularly relevant for meteoroids that penetrate deeper into the atmosphere due to the great amount of deceleration that they suffer.

This methodology does not directly account for any large meteoroid fragmentation during its atmospheric flight. A way to overcome this issue consists of analyzing the individual trajectories of the resulting fragments. This is in principle possible if the height and velocity values of the meteoroid are accurately known at the instant the fragmentation occurs. It shall however be done with care as there is a change of the dynamical energy of the bodies involved. This is, the initial velocities of the fragments at the height where the fragmentation occurs might be larger than the last velocity of the parent meteoroid prior to fragmentation. Thus, a correction shall be imposed to the initial velocities of the new fragments, and this correction might be different for each fragment as the distribution of energy could not be equally distributed.

The exact solution of the problem (Equations (30) and (31)) will normally require a computational implementation to provide the desired parameter values at each trajectory point. Nonetheless, for certain problems, only the value of these parameters at specific trajectory points is requested. This is, for instance the case of the beginning and terminal trajectory points. It is notable then than Equations (30) and (31) admit some simplifications that bring a more direct approach to these points. For quick meteors, one can neglect the deceleration and set the velocity as constant for the luminous segment of the trajectory, then $v = V/V_e = 1$. In this case, a strong evaporation process takes place so β becomes high ($\beta >> 1$). This means that the meteoroid ablation occurs rapidly in the absence of drag. For this situation, Stulov (1998, 2004) developed an asymptotic solution:

$$v = 1, \quad m^{1-\mu} = 1 - 2\alpha\beta e^{-y}, \quad ln2\alpha\beta < y < \infty \tag{33}$$

It should be noted that Equation (33) does not describe the drag process until the point where $m = 0$. The meteor velocity begins to decrease in a certain vicinity of this point. In order to account for this change in velocity it was proposed to combine Equation (33) suitable for high β values with Equation (27) suitable for arbitrary β values (see Gritsevich, 2008c, and references therein). Such substitution of Equation

(27) into Equation (33) fully escapes the dependency on μ and gives a direct height and velocity relationship for high β values:

$$v = \left(\frac{ln(1 - 2\alpha\beta e^{-y})}{\beta} + 1 \right)^{1/2}, \quad ln2\alpha\beta < y < \infty \tag{34}$$

It is notable that, since a condition of changing velocity was applied in the derivation of Equation (34), the Equation (34) is no longer applicable for constant-velocity meteors. Thus if condition $v = V/V_e = 1$ is strictly set then solely Equation (33) should be considered.

In the opposite case, when $\beta = 0$, the analytical solution (27), (28) and (29) becomes (Gritsevich, 2008c):

$$m = 1, \quad y = \ln \alpha - \ln(-\ln v) \tag{35}$$

Meteoroids suffering no evaporation process at all $\beta = 0$ are not common, however β could certainly very low at some cases. For such small β values ($\beta < 2$), Kulakov & Stulov (1992) and Stulov et al. (1995) suggested an asymptotic expression which provides very good results:

$$y = \ln \alpha - \ln(-\ln v) + 0.83\beta(1 - v) \tag{36}$$

Now, the terminal height is the last point of the registered luminous path of the meteor atmospheric trajectory (when ablation processes are over). For disintegrating fireballs this point is reached when $m = 0$ (given that the fireball suffers little or no deceleration, and so v remains constant) and it is calculated at the point where $v_t = V_t/V_e$. Note that the terminal velocity of a fireball is the velocity at its terminal height, and this velocity is represented as V_t. Thus, from the simplified solutions (33) and (34) of the analytical expression (28) two approximation for the terminal heights are obtained. For the sake of clarity in the following discussion the dimensional height values (h) for the mentioned points will be used. Also, subscripts I, II, III, etc., will be assigned to indicate the different ways of expressing the terminal height according to the simplifications made in Equations (33) and (34) and so on. The resulting terminal height for fast meteors (Equation (33)) will be called hereafter h_I, and for the simplified solution where some deceleration is considered (Equation (34)) it will be used subscript II, h_{II}:

$$h_I = h_0 \cdot y_t = h_0 \cdot ln(2\alpha\beta) \tag{37}$$

$$h_{II} = h_0 \cdot y_t = h_0 \cdot ln\left(\frac{2\alpha\beta}{\left(1 - e^{\beta \cdot (v_t^2 - 1)}\right)} \right) \tag{38}$$

Given Equations (37) and (38), it can be pointed out that, for fast meteors, where deceleration is not accounted for, the terminal height (h_I) is a function of the dimensionless parameters α and β. Although this simplification is not always true it can be applied in some well-studied cases. Meteoroids do decelerate before disintegrating or starting its dark flight when they are meteorite-droppers, therefore a second approximation is suggested for these terminal heights (h_{II}). This new terminal height depends on α, β and the terminal velocity.

As it will be seen later the simplifications h_I and h_{II} will adjust better in the range of validity of their assumptions. When these simplifications are used to study a large set of observations with a notable variety of entry velocities and decelerations, the results might not be accurate. In these cases, the original analytical solution of the problem, Equation (28), shall be implemented. Nonetheless, there is another possibility. It is possible to derive a simplified terminal height formulation via mathematical means. Gritsevich et al. (2016) carried out a mathematical analysis so as to get a better performance of h_{II} compared to the analytical solution of the problem. More specifically, Gritsevich et al. (2016) obtained an approximation function that corrects Equation (38). Their work accounted for the following premises:

1. Both, the analytical solution (28) and the simplified calculated height for decelerated meteors (Equation (38)) have no singularities and are monotonous on the interval $0 < v < 1$.

2. The α dependency is the same (through $\ln \alpha$) for both equations.

These facts allow the use of an approximation function which shall only affect parameter β. It shall be remarked that this approximation function is thought to improve accuracy in those cases where $\beta > 3$, otherwise the previous simplified solutions and the asymptotic solution are, in principle, more reliable.

This function is ultimately adjusted to the range of meteoroid velocities values of interest, this is $v \in [0.3, 1)$. Moreover, this function works for fixed values of α and β but the error analysis carried out by Gritsevich et al. (2016) proves that it works more efficiently for a range of β values (depending on the approximated function used). Note that α is not strictly required in this analysis since Equations (28) and (38) can be expressed in terms of $y - \ln 2\alpha$. The approximation function suggested by Gritsevich et al. (2016) is introduced through a shift on the β parameter where it is substituted by $\beta - A$ in Equation (38), and A represents the approximation function. Introducing this shift on the expression (38) and comparing it to the analytical solution (28) it follows:

$$\ln\left(\frac{2\alpha(\beta - A)}{1 - e^{(\beta - A)\cdot(v^2 - 1)}}\right) \approx \ln \alpha + \beta - \ln \frac{\Delta}{2} \tag{39}$$

Gritsevich et al. (2016) describe how A is a function of both β and v, $A = A(\beta, v)$, resulting in a quite complex expression. In line with the simplified shape of the terminal expression sought, instead of directly considering the full formulation of $A = A(\beta, v)$ two reliable simplifications of A are taken. Gritsevich et al. (2016) came out with two

efficient simplifications for function $A = A(\beta, v)$ for which the attached errors are well constrained:

1. $A_0 = 1.1$
2. $A_1 = 1.0 + (1.0 - v) \cdot \frac{2.5}{\beta}$

The error analysis performed when using A_0 and A_1 in Equation (38) suggests that the optimal performance of these approximations (given 20-30 meteor trajectory points observed) occurs at $\beta \approx 2.89$ for A_0, and at $\beta \approx 2.1$ for A_1. The average statistical deviation for any derived parameters using A_0 is $5-10\%$ and $1-2\%$ for A_1 (Gritsevich et al., 2016).

The terminal height obtained using A_0, namely h_{III} is:

$$h_{III} = h_0 \cdot \ln\left(\frac{2\alpha(\beta - 1.1)}{1 - e^{(\beta-1.1)\cdot(v^2-1)}}\right) \tag{40}$$

Figure 20 demonstrates the quality of the approximation of Equation (40). It shows the comparison functions $y(\beta, v) = y(\alpha, \beta, v) - ln(2\alpha)$, where y is the dimensionless height (h_i/h_0, where $i = I$, II or III) taken according to Equations (37), (38) and (40). The comparison made for different β values confirms that Equation (40) has better accuracy than previously used Equation (38).

Using A_1, the terminal height expression for h_{IV} results:

$$h_{IV} = h_0 \cdot \ln\left(\frac{2\alpha(\beta - (1.0 + (1.0 - v_t) \cdot \frac{2.5}{\beta}))}{1 - e^{(\beta-(1.0+(1.0-v_t)\cdot\frac{2.5}{\beta}))\cdot(v^2-1)}}\right) \tag{41}$$

One important note about Equations (40) and (41) is that they approximate the analytical solution of the terminal height correcting a simplification for fast meteoroids. Thus, it is expected that some inaccuracies may appear for some events. Nonetheless, the goal of using Equations (40) and (41) is to keep a simple formulation capable of constraining the number and extent of these inaccuracies.

5.4 RESULTS

The reliability of the simplified expressions for h_I, h_{II}, h_{III} and h_{IV} is studied using the database of the Meteorite Observation and Recover Project in Canada, MORP (1970-1985). As described by Halliday et al. (1978) the goal of this project was to gain further knowledge on the origin and properties of fireballs and meteorites. The project consisted of twelve observatories located mainly in the south of Canada while the control headquarters were located at the campus of the University of Saskatchewan in

Saskatoon. Each of the observatories had five cameras each of which covered 54° of azimuth near the horizon. Neighbor stations covered the part of the unrecorded azimuth area. The cameras used photographic films (see more details in Halliday et al., 1978) which gives an idea of the relative complexity compared to the current digitalization era.

MORP was able to register more than 1010 fireballs, including a meteorite-dropper. MORP 285, known as Innisfree, was recorded on the 6^{th} of February of 1977, and was recovered twelve days later (Halliday et al., 1977, 1978, 1981). The accurate observations of the meteor phenomena allowed the derivation of its pre-atmospheric orbit (see Table 10 in Chapter 3). Here, these data has been used to calculate the corresponding terminal heights. This has been done using:

1. The α and β values previously obtained by Gritsevich (2009) for MORP data set.
2. The observed terminal height (h_t), the entry (V_e) and terminal velocity values (V_t) retrieved by Halliday et al. (1996) from MORP fireballs observations.

These calculated heights are finally compared to the fireballs observed terminal heights (Halliday et al., 1996). The results of the calculations are shown in Table 16.

Additionally, Figure 21, Figure 22, Figure 23, and Figure 24 compare the calculated terminal heights h_I, h_{II}, h_{III} and h_{IV} to the observed terminal height h_{obs} respectively. For reference the line $h_i = h_t$ (where $i = I, II, III, or IV$) is plotted; this way a visual understanding of the main differences is quickly provided. From these figures, it can be appreciated that the range of terminal heights is approximately between 20 km and 80 km, thus combining meteoroids with moderate and high penetration skills.

As it will be discussed later, the differences between the observed terminal height h_t and the theoretical h_I, h_{II}, h_{III} and h_{IV} do depend on the value of the β parameter. Figure 25, Figure 26, and Figure 27 plot these differences for h_I, h_{III} and h_{IV} between the calculated and observed values against the β parameter. Note that no figure in this regard has been included for h_{II} as it does not add extra information for the current analysis.

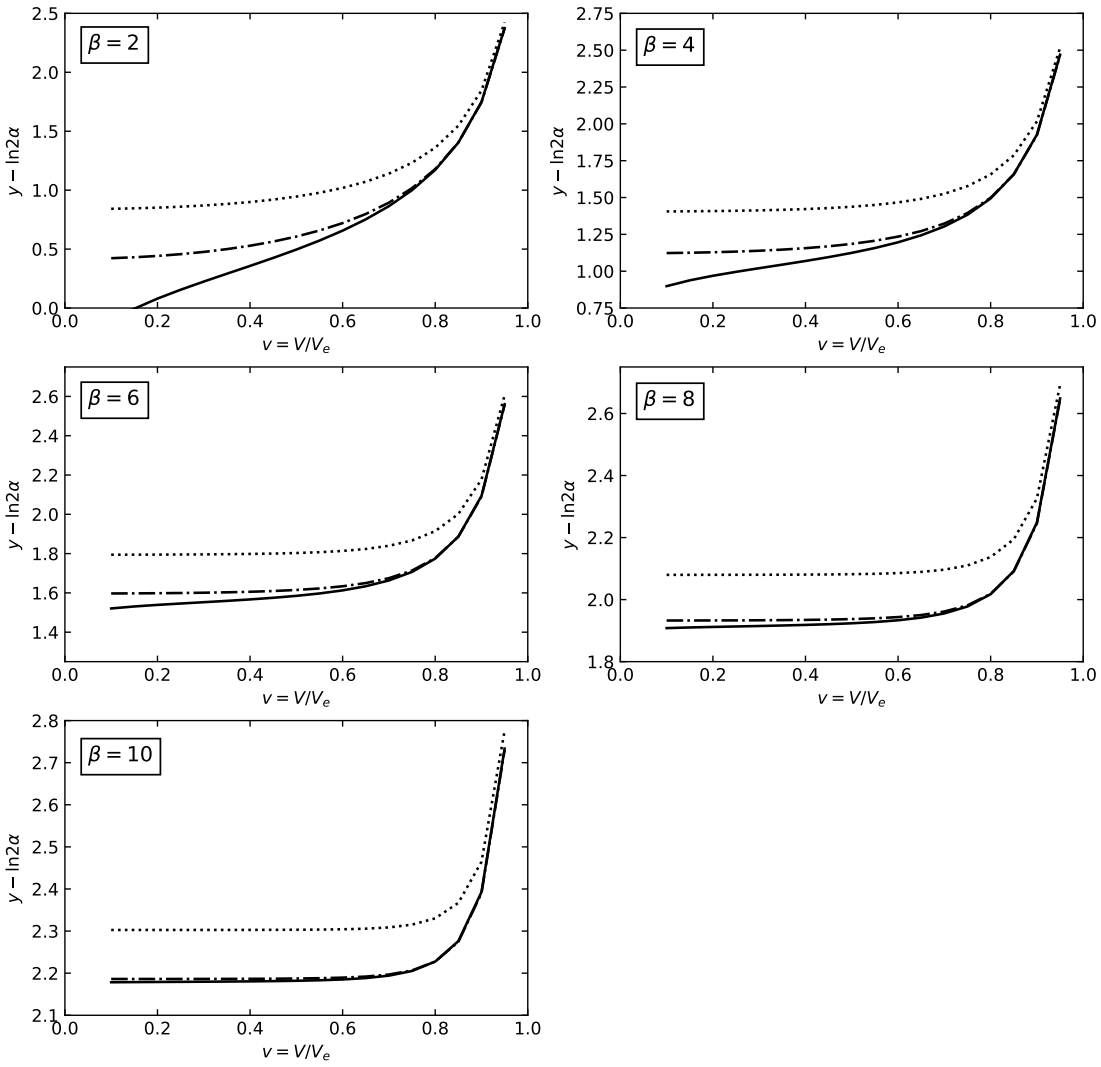

Figure 20: Graphical comparison of Equation (28) (dotted line), Equation (38) (dashdotted line), and Equation (40) (continuous line) for the selected β values. Note that for real fireballs the terminal velocity $v_t = V_t/V_e$ is usually higher than the one shown on the graphs (see experimental V_t and V_e values given in Table 16), so only the range $v_t < v < 1$ would be applicable for practical purposes.

Table 16: Terminal Heights

ID	V_e	V_t	α	β	h_I	h_{II}	h_{III}	h_{IV}	h_t
18 [a]	18.5	5.7	24.13	1.475	30.54	32.73	29.65	26.09	27.6
123 [a]	16.3	8.7	37.22	1.111	31.61	35.92	33.29	30.72	32.6
138	16.9	9.5	38.90	2.889	38.77	39.84	37.83	37.28	37.0
141	32.1	29.0	707.19	6.403	65.24	67.87	67.28	67.31	65.1
144	23.5	13.5	137.13	1.301	42.08	45.96	43.54	41.79	42.9
169	22.9	9.3	50.52	1.575	36.30	38.54	35.71	33.21	34.0
172 [a]	12.5	8.1	13.13	3.379	32.12	33.20	31.52	31.25	31.2
177	15.8	8.7	77.63	1.777	40.24	42.69	40.33	39.07	39.8
187	18.4	14.0	83.76	3.815	46.25	47.86	46.57	46.50	46.3
189	14.5	4.8	34.47	0.757	28.32	33.42	30.02	21.95	27.9
192	21.0	14.6	94.01	2.458	43.93	46.29	44.59	44.24	44.4
195 [a]	25.2	7.6	35.22	1.486	33.30	35.45	32.37	28.79	30.4
204 [a]	13.0	8.7	10.13	3.620	30.75	31.80	30.21	30.01	29.5
205 [a]	19.7	7.5	36.84	0.716	28.39	33.99	30.70	23.16	28.9
207 [a]	17.9	6.5	24.45	0.775	26.03	31.14	27.83	20.65	25.9
218	18.5	13.2	64.65	0.339	27.07	40.49	38.53	34.49	37.9
219 [a]	18.4	7.8	12.51	2.060	28.23	29.69	27.11	25.50	26.1
223 [a]	27.1	9.5	18.33	1.809	30.03	31.67	28.84	26.45	27.1
225	21.2	10.0	75.92	0.706	33.47	39.64	36.64	30.91	35.4
229	12.3	6.1	43.73	4.564	42.88	43.12	41.46	41.16	40.7
231 [a]	27.9	11.7	52.72	1.371	35.61	38.41	35.52	32.61	34.2
232	35.0	29.8	434.10	0	...	...	56.58	...	56.5
235	19.1	17.5	171.01	14.343	60.85	61.60	61.19	61.22	60.7
241	16.7	9.8	50.27	0.878	32.08	38.00	35.51	32.77	34.9
245 [a]	13.5	8.9	83.60	0.478	31.37	41.68	39.44	35.57	39.0
261 [a]	12.4	7.8	39.13	1.084	31.80	37.04	34.79	33.09	34.4
268 [a]	19.1	15.7	39.44	5.157	43.02	44.51	43.54	43.55	42.9
276 [a]	23.5	6.5	18.15	1.237	27.24	29.99	26.74	21.86	24.4
285 [a,b]	14.54	2.7	8.25	1.700	23.87	25.41	22.30	18.53	19.8
287	23.4	10.5	40.85	1.750	35.53	37.57	34.91	33.03	34.6
288 [a]	12.4	4.1	9.05	1.215	22.13	25.09	21.93	17.54	20.2
299 [a]	23.6	14.7	48.36	1.042	33.03	38.41	36.12	34.28	35.7
300	21.5	10.2	202.36	2.071	48.20	49.80	47.33	45.99	46.2
301	36.1	24.4	693.65	0.662	48.85	57.42	55.30	52.92	55.6

Continued on next page

Table 16: Terminal Heights (continued)

ID	V_e	V_t	α	β	h_I	h_{II}	h_{III}	h_{IV}	h_t
303 [a]	14.1	8.2	44.15	1.260	33.74	37.82	35.41	33.64	34.9
304	16.2	6.6	48.17	2.442	39.10	40.10	37.64	36.36	36.8
307 [a]	21.0	3.8	12.08	1.760	26.85	28.29	25.21	21.60	22.0
310	17.0	10.5	67.74	0.559	30.98	39.79	37.36	33.30	36.8
313 [a]	16.7	10.2	134.20	0.432	34.03	44.33	41.83	36.14	41.1
314	14.6	9.3	159.93	0.118	26.00	45.27	42.83	20.25	42.1
331	13.3	7.0	37.94	0.598	27.32	34.81	31.98	26.29	31.1
340	29.1	25.6	1165.35	5.894	68.22	70.41	69.70	69.73	69.1
345 [a]	17.4	10.6	46.21	0.829	31.07	37.52	35.11	32.48	34.3
346	15.7	8.5	21.81	1.997	31.98	33.99	31.67	30.56	31.0
364 [a]	11.3	5.3	20.34	0.567	22.47	29.84	26.77	19.22	25.4
384	21.1	12.1	476.52	2.121	54.50	56.47	54.28	53.40	53.8
388	21.9	14.8	81.67	0.542	32.10	41.88	39.74	36.72	39.4
390	19.7	16.7	958.47	1.344	56.24	64.51	63.44	63.26	63.4
391	19.5	9.0	72.46	1.323	37.63	40.75	37.96	35.30	36.9
410	31.0	27.3	901.17	2.912	61.33	66.59	65.78	65.78	64.9
414	29.9	27.7	375.26	12.707	65.61	66.90	66.49	66.53	66.5
419	24.7	16.2	329.97	0.962	46.21	52.38	50.23	48.52	49.8
425	17.6	12.3	43.41	1.699	35.76	39.65	37.83	37.22	37.2
436	29.0	25.9	224.06	3.797	53.27	57.73	57.02	57.04	57.0
445	21.3	13.7	119.22	0.700	36.64	44.44	42.16	39.46	41.6
462	19.1	10.6	140.03	2.015	45.36	47.40	45.13	44.10	44.5
481	13.7	5.9	77.70	1.046	36.45	40.43	37.44	33.43	35.8
486	33.2	26.4	624.60	1.059	51.46	59.57	58.16	57.65	58.1
503 [a]	14.8	10.5	25.27	1.765	32.15	36.01	34.25	33.72	34.1
511 [a]	18.1	9.8	48.38	1.156	33.78	37.95	35.36	33.00	31.7
516	20.5	13.3	104.87	3.703	47.65	48.54	46.92	46.70	46.3
518	15.5	8.7	75.32	2.391	42.15	43.70	41.55	40.78	40.8
521	18.8	12.8	188.55	0.998	42.46	48.77	46.74	45.34	46.4
528	19.5	8.4	37.25	1.525	33.89	36.33	33.54	31.11	32.4
529	18.5	10.2	35.26	1.779	34.60	37.05	34.69	33.43	34.0
536	12.9	9.3	61.78	3.332	43.11	44.72	43.24	43.08	42.8
549	26.5	12.1	111.65	0.740	36.57	42.39	39.35	33.66	38.1
555	25.5	24.1	481.92	11.668	66.79	69.22	68.88	68.90	68.8
557	36.5	27.8	138.83	2.139	45.73	49.47	48.00	47.75	47.9

Continued on next page

Table 16: Terminal Heights (continued)

ID	V_e	V_t	α	β	h_I	h_{II}	h_{III}	h_{IV}	h_t
559	26.0	20.1	135.61	3.454	48.99	51.04	49.76	49.68	49.6
561	16.0	11.7	154.14	2.817	48.45	50.70	49.18	48.98	48.6
565 [a]	13.2	10.7	12.57	4.913	34.49	35.95	34.93	34.93	34.8
567 [a]	23.4	8.1	101.02	1.560	41.19	43.28	40.32	37.33	38.7
577	22.0	21.6	86.30	33.029	61.92	64.52	64.40	64.41	64.3
589	24.3	12.0	167.95	1.549	44.78	47.44	44.83	42.91	43.9
593	20.3	16.1	313.35	1.224	47.56	54.78	53.38	52.95	53.1
598	17.9	11.1	118.26	1.471	41.90	45.61	43.41	42.22	42.9
610	29.7	25.7	384.29	1.053	47.94	58.39	57.42	57.22	57.4
615	20.5	8.8	55.62	1.434	36.32	38.98	36.15	33.49	34.9
626 [a]	13.50	10.0	31.59	0.118	14.38	35.57	33.74	22.76	33.5
628	28.9	21.6	600.34	1.850	55.17	59.35	57.78	57.41	57.6
635	35.5	18.5	96.63	1.883	42.22	44.32	41.90	40.59	41.2
654	13.8	6.9	43.15	1.356	34.10	37.31	34.65	32.40	33.8
661	30.9	17.5	218.48	1.281	45.30	49.19	46.74	44.88	46.1
664	22.1	13.0	145.75	2.257	46.46	48.32	46.21	45.47	45.8
669 [a]	20.6	8.6	28.80	1.434	31.60	34.22	31.36	28.61	30.6
672 [a]	13.7	10.0	22.79	1.243	28.90	34.77	33.03	32.29	32.7
683 [a]	17.6	9.3	37.46	1.340	33.00	36.43	33.86	31.81	33.1
687 [a]	16.7	5.9	42.83	0.534	27.37	34.43	30.97	19.27	28.9
702	28.7	19.9	306.92	0	...	...	48.52	...	48.2
708	15.7	10.8	63.51	1.727	38.60	42.29	40.42	39.79	40.1
715	31.7	27.9	141.98	6.700	54.06	55.85	55.16	55.20	54.8
725	29.5	28.0	93.72	14.748	56.74	58.63	58.33	58.35	57.9
727	31.3	27.7	1160.73	2.100	60.80	68.00	67.20	67.17	67.2
741	31.9	28.5	370.61	3.764	56.81	61.32	60.61	60.63	60.6
751	18.9	8.9	44.19	0.377	25.10	34.91	31.78	19.52	30.5
752	13.6	11.9	8.67	9.418	36.48	37.32	36.69	36.73	36.5
763	27.6	25.2	254.30	4.410	55.24	59.93	59.34	59.37	59.4
769	17.4	10.5	50.00	1.233	34.47	38.84	36.52	34.88	36.0
771 [a]	17.1	7.8	41.75	0.731	29.44	35.32	32.28	26.49	31.0
774	33.0	27.1	85.66	0.994	36.78	45.99	44.74	44.32	44.7
776	13.1	10.0	33.21	5.497	42.25	43.01	41.89	41.88	41.6
792 [a]	17.3	7.7	37.43	0.388	24.12	33.57	30.34	17.36	28.9
819	17.7	11.1	123.90	1.034	39.71	45.18	42.90	41.08	42.4

Continued on next page

Table 16: Terminal Heights (continued)

ID	V_e	V_t	α	β	h_I	h_{II}	h_{III}	h_{IV}	h_t
823	25.0	19.4	32.61	4.927	41.33	42.42	41.28	41.27	40.0
829	28.9	15.1	359.02	0.869	46.08	51.51	48.76	45.10	47.7
835	24.2	8.2	66.13	2.474	41.46	42.31	39.77	38.25	38.4
840	23.6	6.1	22.35	1.766	31.28	32.81	29.81	26.73	27.7
843	36.5	33.7	642.92	4.526	62.07	67.22	66.69	66.72	66.6
844 [a]	14.9	9.8	23.89	1.694	31.46	34.91	32.92	32.12	32.6
852	15.9	4.6	21.27	2.541	33.53	34.26	31.69	30.06	29.9
857	18.5	12.0	62.52	1.224	36.02	40.87	38.74	37.43	38.3
860	23.3	17.6	330.46	0.283	37.46	52.98	51.25	47.67	51.1
861	13.3	7.2	49.82	2.720	40.11	41.24	39.14	38.47	38.6
865	26.5	18.1	258.85	0.564	40.65	50.29	48.20	45.44	47.8
868	27.8	25.6	1234.31	9.416	71.99	73.94	73.47	73.51	73.4
871	23.9	20.2	134.32	0	...	...	47.87	...	47.8
872 [a]	14.8	5.8	12.34	0.631	19.66	25.98	22.68	14.15	20.8
873	16.5	14.8	927.96	5.170	65.65	68.89	68.24	68.27	68.0
878	15.5	14.1	58.70	1.512	37.08	47.62	46.96	46.93	46.9
883	26.1	8.8	95.53	2.115	42.97	44.16	41.45	39.50	40.1
884 [a]	12.4	8.3	26.37	2.569	35.15	37.13	35.35	34.97	34.9
886	13.8	7.4	55.66	0	...	...	33.18	...	32.0
888 [a]	25.5	9.0	31.85	1.171	30.87	34.06	30.92	26.57	29.2
892	28.9	6.2	32.77	1.514	32.92	34.84	31.65	27.45	28.9
901	32.6	27.3	636.32	0.422	45.01	60.28	59.10	58.13	59.0
902	29.6	22.4	447.06	2.547	55.35	58.29	56.85	56.65	56.7
920	16.7	12.7	318.85	4.052	56.26	57.69	56.42	56.36	56.3
921	28.1	22.4	1077.86	8.721	70.47	70.77	69.96	69.99	69.3
925 [a]	26.4	4.2	42.87	1.503	34.79	36.67	33.42	28.70	29.8
929	35.0	30.1	342.27	2.944	54.48	58.95	58.03	58.01	58.0
930 [a]	13.4	9.5	38.75	1.052	31.51	37.94	36.06	34.98	35.6
933	15.4	11.1	43.80	1.779	36.15	40.12	38.41	37.93	38.0
937 [a]	17.9	6.4	40.19	0.881	30.50	34.96	31.69	25.49	29.8
947	24.9	24.0	771.47	32.917	77.58	78.31	78.13	78.14	77.9
966	31.3	27.8	1384.16	0.604	53.14	68.34	67.51	67.23	67.5
967	30.0	15.0	239.38	0	...	...	43.09	...	41.9
977 [a]	23.3	9.4	30.90	1.065	29.98	33.76	30.69	26.43	29.4
984	36.2	26.1	128.24	0	...	...	43.00	...	42.7

Continued on next page

Table 16: Terminal Heights (continued)

ID	V_e	V_t	α	β	h_I	h_{II}	h_{III}	h_{IV}	h_t
995	28.9	26.0	240.98	4.700	55.31	59.07	58.42	58.45	58.8
996	26.9	14.1	59.56	2.133	39.65	41.36	39.04	37.97	38.4
1010	18.4	10.1	71.58	1.378	37.84	41.28	38.79	36.98	38.1
1011	37.6	36.6	546.56	24.155	72.90	75.26	75.10	75.11	75.0

The table columns are organized as follows: (1) The ID name of the fireball; (2) the V_e which is the velocity of the body when it enters the atmosphere; (3) the terminal velocity observed, V_t; (4) α; (5) β; (6) h_I; (7) h_{II}; (8) h_{III}; (9) h_{IV}; (10) the observed terminal heights h_t. Velocities are expressed in [km/s], and heights in [km].
Notes:
[a]Probable meteorite fall according to Halliday et al. (1996).
[b]This calculation corresponds to the Innisfree meteorite and it is based on the data from Halliday et al. (1981), see Gritsevich (2008c). The total mass of the recovered Innisfree L5 meteorite was 4.58 kg (Halliday et al., 1981).The estimated pre-atmospheric mass of the Innisfree meteoroid was around 35 kg (Ceplecha & Revelle, 2005; Gritsevich, 2008c). Pre-atmospheric data about the Innisfree meteoroid can be found in Table 10 of Chapter 3.

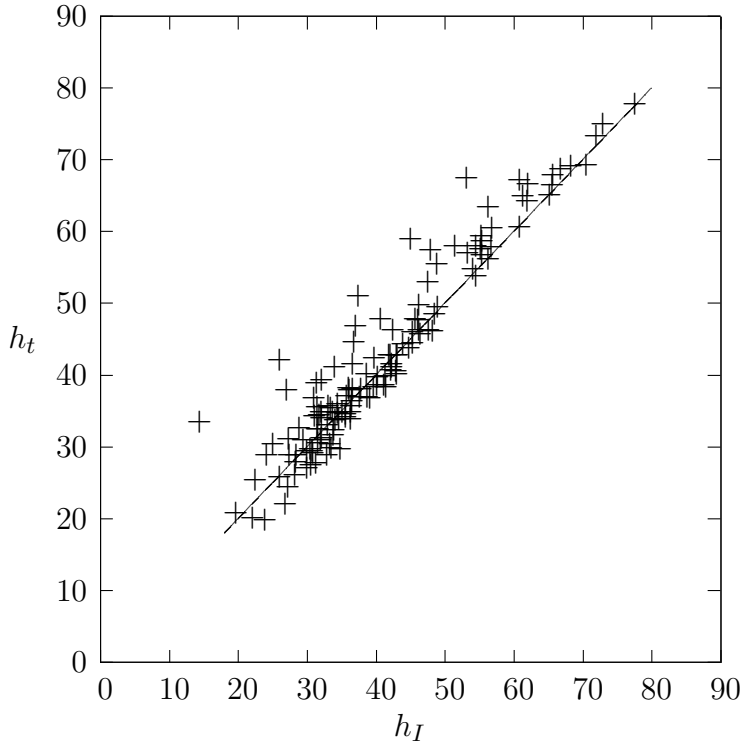

Figure 21: Representation of derived terminal heights using Equation (37), h_I versus the observed terminal height, h_t. Line indicating $h_I = h_t$ is also plotted.

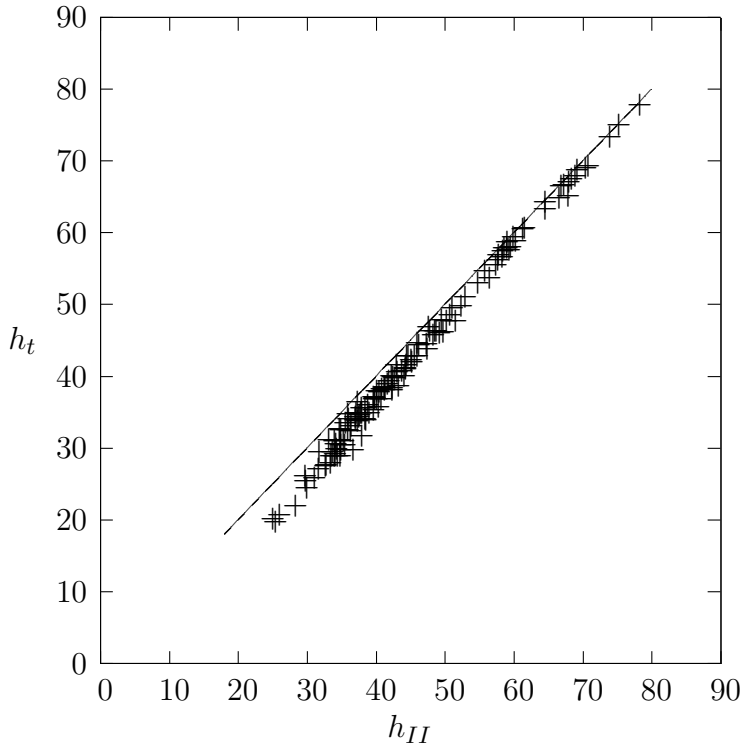

Figure 22: Representation of derived terminal heights using Equation (38), h_{II} versus the observed terminal height, h_t. Line indicating $h_{II} = h_t$ is also plotted.

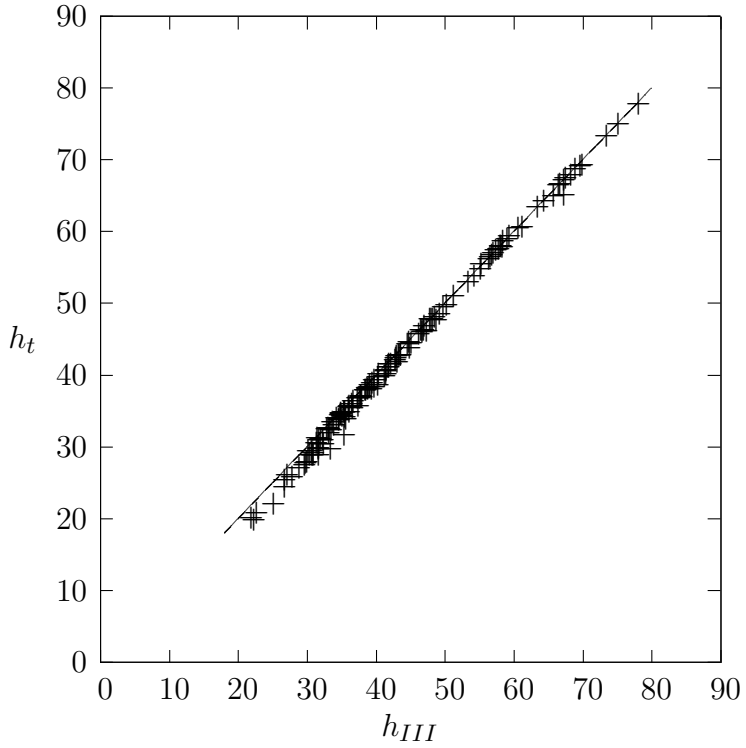

Figure 23: Representation of derived terminal heights using Equation (40), h_{III} versus the observed terminal height, h_t. Line indicating $h_{III} = h_t$ is also plotted.

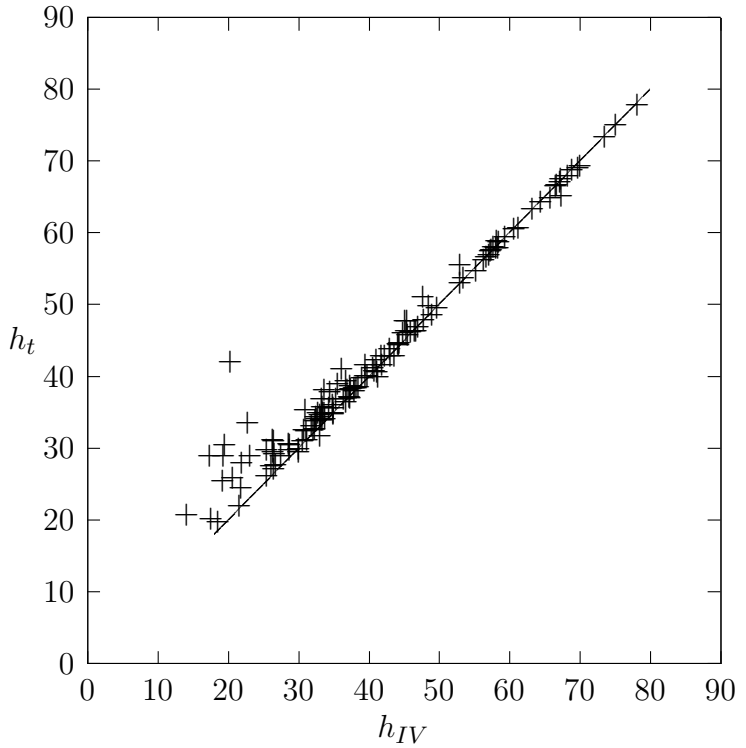

Figure 24: Representation of derived terminal heights using Equation (41), h_{IV} versus the observed terminal height, h_t. Line indicating $h_{IV} = h_t$ is also plotted.

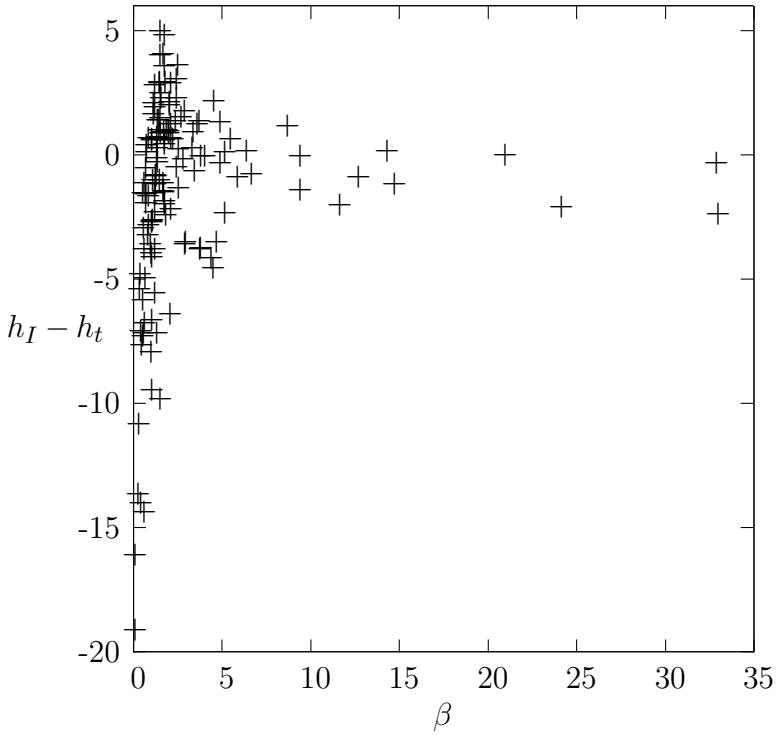

Figure 25: Representation of the differences between derived and observed terminal heights ($h_I - h_t$) versus β values.

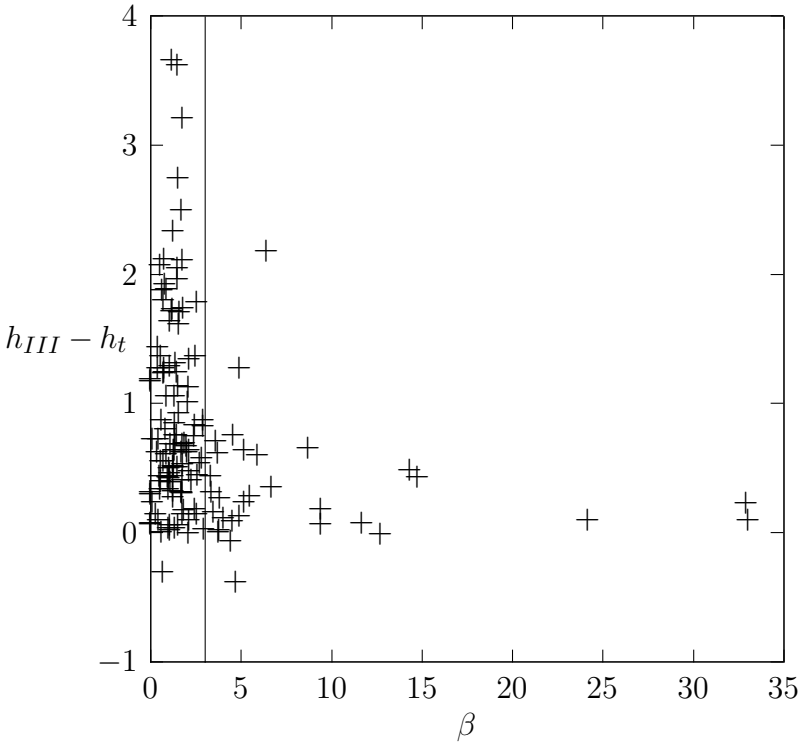

Figure 26: Mass-loss parameter (β) against $h_{III} - h_t$. The vertical line indicates $\beta = 3$.

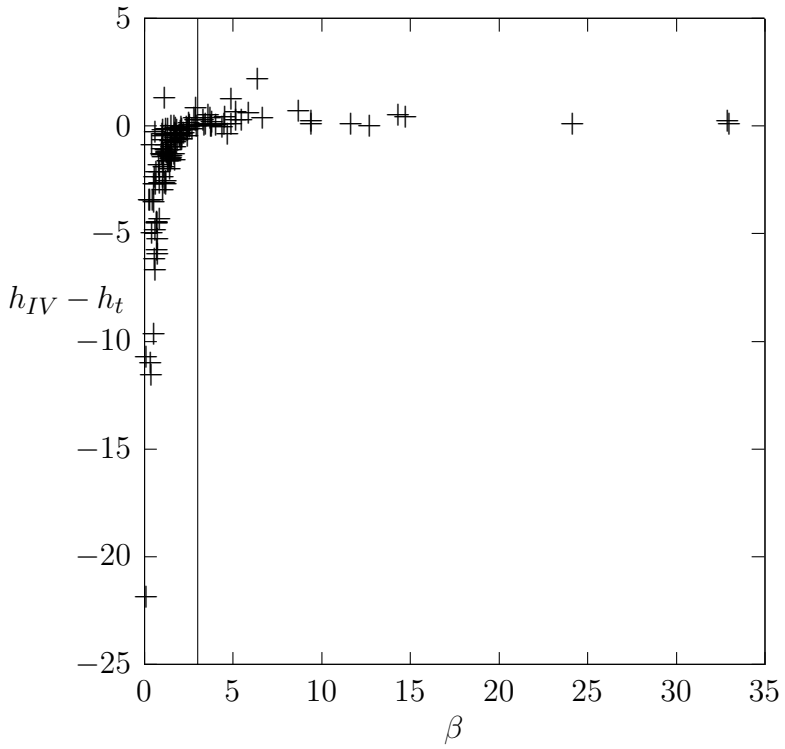

Figure 27: Mass-loss parameter (β) against $h_{IV} - h_t$. The vertical line indicates $\beta = 3$.

5.5 DISCUSSION

The results offered in the previous section clearly show that each of the four terminal height formulations described achieve a different level of accuracy. According to the results in Table 16, differences between observational and analytical terminal height values generally improved from h_I to h_{II}, and from h_{II} to h_{III}. It can be stated from Figure 21 that h_I tends to underestimate the observational values. The standard deviation is $\sigma = 4.11$ km which is a bit higher than the typical error for MORP observational heights (around 2 km, see Halliday, 1988). This result implies that the method proposed by Gritsevich & Popelenskaya (2008) cannot be extended to be applicable for decelerated fireballs without further modification, though it is usable to derive parameters of small meteoroids with constant velocity (Popelenskaya, 2010). This is, Equation (37) should lead to good results when β values are high. In Figure 25 it can be noticed that for $\beta > 5$ the differences between derived and observed terminal heights are small. Note that, this equation does not take into account the decrease in velocity close to the terminal point of the trajectory.

As it can be seen in Figure 22, though differences between derived and observed terminal heights (h_{II}, h_t) have decreased, there is still a wide spread in the results. Deviations are larger for low β values and moderate for medium and large β values.This time the standard deviation of the results is $\sigma = 1.52$ km which is well within the observational error. Besides, Figure 22 also illustrates that a global linear tendency can be found. This indicates that this terminal height formulation, h_{II}, may provide a reasonable first-order approximation to observations.

The modification made by introducing the proposed approximation by Gritsevich et al. (2016) in the formulation leads to higher accuracy. As displayed in Figure 23 the agreement between the calculated h_{III} and the observational terminal heights is very good. Now, the standard deviation becomes $\sigma = 0.75$ km. Despite the fact that observations could carry different kind of errors: bad astrometric measurements, incomplete recording of the luminous trajectory of the meteor, blurring effects, etc., the analytical values deviate little from the observed ones. This could be explained if acknowledging that the observations of MORP are indeed quite accurate and that the h_{III} approximations seems to work very good with the sample used, which even allows to derive terminal heights in those few cases where β values are null.

Though the mathematical approximation achieved with Equation (40) provides a global good adjustment, it can be noticed on Figure 23 that the best fit for h_{III} is for those fireballs that terminate at higher altitudes. This result is expected since fireballs which survive ablation reach lower atmospheric layers, and they have, on average, lower values of mass loss parameter β. Since the approximation A_0 is supposed to show a better performance for higher values of the mass-loss parameter, these differences were expected to appear. Note that h_{III} is the result of a simplification made on the analytic solution of the equations of motion. Thus, despite including the mathematical modification suggested by Gritsevich et al. (2016) it may still be appreciated a residual error

due to the original simplification assumed.

Finally, results for h_{IV} are plotted on Figure 24. Once again, there exists a lack of correlation between the observed and calculated terminal heights for low height values (low β values). Note that now the differences between the calculated and the observed terminal heights are negative. The explanation can be found in β values. As it has been discussed, these approximations are thought to work efficiently for $\beta > 3$, and its accuracy should only be considered for that range of results. Graphically, Figure 26, and Figure 27 show the relationship between the mass-loss parameter, and h_{III} and h_{IV} respectively. The sudden change in accuracy is quite clear at the right side of the dashed line indicating $\beta = 3$. Lower β values show different levels of terminal height accuracy. It is important to recall here that the mathematical functions derived by Gritsevich et al. (2016) reaches its highest accuracy close to $\beta \approx 2.89$ for A_0 and to $\beta \approx 2.1$ for A_1. This is clearly in line with what Figure 26, and Figure 27 show, and shall help choosing between h_I, h_{II}, h_{III} and h_{IV} when a case-by-case meteoroid analysis is carried out.

Additionally, it is quite interesting to note that, for the MORP database, the use of h_{III} leads to better global results (including those fireballs with $\beta < 3$) than h_{IV}; conversely, h_{IV} shows better adjustment when only meteors with $\beta > 3$ are considered. The global results for h_{IV} are biased by five cases at very low β values; hence, avoiding the contribution of these events to the global accuracy the adjustment enhances dramatically.

According to the previous results it can be stated that the general accuracy improves when using h_{III} and h_{IV}. Despite the mathematical formulation introduced by Gritsevich et al. (2016) aims to solve accuracy problems for high β values, here it has been explored its applicability for events that show low β values. Further study should be addressed but up to now it has been proved that the use of A_0 enhances the global accuracy of Equation (38). This is partially because this solution improves the accuracy at moderated β values, which may include some of the meteoroids that are able to penetrate to lower heights.

The formulation of Equations (37), (38), (40) and (41) require either two or three input parameters (α, β, $v_t = V_t/V_e$) which can be directly derived from the observations. Sometimes the final part of the trajectory could not be visible or even recorded and thus the terminal velocity may require further assumptions, but the derivation of α and β only needs three observed (h, V) points, one of which should be the entry point (the entry velocity). Using these three points it is possible to obtain the remaining (h,V) trajectory points from the adjusted fireball trajectory (see Whipple & Jacchie, 1957). Though the terminal point of the trajectory would not be exactly determined using this adjustment, a combination of this adjustment with other methodologies and/or hypotheses shall lead to a good estimation. Consequently, the dimensionless methodology allows the calculation of the terminal height accounting for either two (α and β) parameters for h_I, or three (α, β and V_e) parameters for h_{II}, h_{III} and h_{IV}.

Regarding the entry velocity (V_e), which is required to obtain α and β, and to scale the velocity values, in principle it is possible to consider it as another unknown and derive it along with α and β values as discussed by Gritsevich (2009). Future study will be done on this subject in order to improve the methodology.

It is also notable, that Equations (37), (38), (40) and (41) outline the meteoroid height as a function of time. Thus, the ability of predicting a terminal height may be directly linked with the forecast of a total duration of the meteor phase (Moreno-Ibáñez et al., 2015a, 2017a). This can create a new scope to a new class of problems, such as, for example, insights into the determination of luminous efficiency based on meteor duration and calculation of critical kinetic energy needed to produce luminosity. In the future, several other tightly related problems may be considered, including a possibility of determining the initial meteor height or deriving parameters α and β without the beginning part of a meteor trail. Furthermore, it is possible to tackle the inverse problem. There are still large amount of archived data and many new meteor registrations for which the recorded deceleration was not significant, and/or it is in the order of the observational errors. For these cases observed terminal heights will be crucial in setting margins on possible α and β values based on Equation (37). Some initial steps in solving this problem were taken in Popelenskaya (2010).

Moreover, even for obviously decelerated and well-studied cases, such as Innisfree meteorite (fireball No. 285 in Table 16), published terminal heights may differ depending on a taken data-reduction approach (e.g. 21 km in Halliday et al., 1981; 19.8 km in Halliday et al., 1996) and, therefore, any additional theoretical constrains on the terminal height and fireball duration may be very helpful.

Undoubtedly, the estimation of the terminal height has a strong impact on planetary defense applications. Large objects that might release large amount of energy at low heights and/or may become meteorite-droppers can penetrate below 40 km, with an average terminal height of 29 km. As it can be derived from Figure 22, Figure 23, and Figure 24 the approach presented in this chapter tends to overestimate the terminal heights for bodies reaching heights below 40 km. Hence, the approximations h_{II}, h_{III} and h_{IV} shall be taken with care when planetary awareness tactics are to be applied. Note thought that the general solution described by Equation (28) is as accurate as the observations available and it only require some computational outline. In addition, the combination of α and β parameters could provide relevant clues on impact hazard (see Gritsevich et al., 2012).

Finally, the results obtained prove the validity of using scaling laws and dimensionless variables in meteor science problems. Particularly, it has been proved that this methodology accurately retrieves one important meteor flight parameter (the terminal height) for most members of a large data set.

5.5.1 *The PE criterion*

It is interesting to analyse if the current approach could override the PE criterion introduced by Ceplecha & McCrosky (1976) and reviewed in the Section 5.1 of this chapter. The PE criterion has been proved to be useful to provide a first reliable approximation on the type of meteor body that has been observed. This criterion basically provides and estimation of the terminal heights for fast meteors by means of the atmospheric density at that height. By introducing scale laws and dimensionless variables the derivation of coefficients A, B, C coefficients of the PE criterion is replaced by the derivation of α and β (only two parameters). Moreover, by definition, α and β gather all the unknowns. Note that V_e is also required to be known from the observations in the PE criterion. In principle, α depends on the pre-atmospheric cross-section-to-mass ratio (the ratio which can be easy converted into dependency on bulk density, pre-atmospheric mass and shape coefficient) and trajectory slope γ related to Z_R. The mass-loss parameter is proportional to pre-atmospheric velocity in power of 2 and inversely proportional to the effective destruction enthalpy. Thus, it is obvious that a similar set of physical parameters affecting the degree of deepening of meteoroids in the Earth's atmosphere are accounted for in both the PE criterion and a combination of α and β parameters.

Although Equation (25) is an empirical approximation, the PE criterion as described by Ceplecha & McCrosky (1976) can be derived from the Single Body theory basic equations. Thus any other mathematical approach that branches from these equations shall lead to the same PE formulation. Using the Single Body Teory equations and assuming no terminal mass ($M_t = 0$), an isothermal atmosphere $\rho/\rho_0 = exp(-h/h_0)$, and a negligible average meteoroid deceleration ($< V^2 >= V_e^2$), Ceplecha & McCrosky (1976) got:

$$-\log \rho_t = \log \sigma + \log K - 0.33 \cdot \log M_e + 2 \cdot \log V_e - \log cos(Z_R) + const. \qquad (42)$$

In Equation (42) the nomenclature used in this chapter is applied, and Z_R is the zenith distance of the meteoroid radiant (trajectory angle to the vertical), σ is the meteoroid ablation, and K is the shape-density factor. Note that Equation (42) is indeed the relationship between the PE and SD parameters (see Ceplecha & McCrosky, 1976). Now, if the dimensionless parameters α and β are adequately combined it results:

$$\log(\alpha \cdot \beta) = \log\left(\frac{c_d \cdot \rho_0 \cdot h_0 \cdot S_e \cdot (1-\mu) \cdot c_h \cdot V_e^2}{4 \cdot M_e \cdot sin\gamma \cdot c_d \cdot H^*}\right) = \\ = \log\left(\frac{c_d \cdot \rho_0 \cdot h_0 \cdot S_e \cdot (1-\mu) \cdot \sigma \cdot V_e^2}{4 \cdot M_e \cdot sin\gamma}\right) \qquad (43)$$

Where:

1. From Levin (1956, 1961): $S/S_e = (M/M_e)^{\mu}$
2. The shape-factor $A = S/(Volume)^{2/3}$

3. The shape-density factor $K = A \cdot c_d \cdot \rho^{2/3}$, where ρ is the meteoroid bulk density.
4. The slope between the trajectory and the horizon at each time γ is related to Z_R as $cosZ_R = sin\gamma$

Including these definitions into Equation (43), it follows that:

$$\log(\alpha \cdot \beta) = \log\left(\frac{const. \cdot K \cdot \sigma \cdot (1-\mu) \cdot V_e^2}{M_e^{(1-\mu)} \cdot cosZ_R \cdot M^{(\mu-2/3)}}\right) = \tag{44}$$

$$= \log\sigma + \log K + 2\log V_e - \log cosZ_R - (1-\mu)\log M_e - (\mu - \frac{2}{3})\log M + const.$$

Equations (42) and (44) are quite similar. There are however some differences. The shape parameter μ is present at those terms accounting for the mass. As already explained in Chapter 2, $0 < \mu < 2/3$. Nonetheless Bouquet et al. (2014) discussed that most meteors show $\mu = 2/3$. In this latter case, the term depending on M could be removed or considered negligible, and $\log M_e$ would be multiplied by 0.33. Additionally, there is no terminal height related term in Equation (44). This is because up to this point only the combination of α and β have been accounted for. The link between these two parameters and the terminal heights has been outlined in the Section 5.3 of this chapter. Consequently, the relationship between ρ_t and $\log(\alpha \cdot \beta)$ could be more complex than the formulation offered by the PE criterion. Note that α and β gather most of the meteoroid flight parameters as described by the Single Body Theory basic equations, and their values are obtained once the particularities of each meteoroid trajectory are included in the study. These particularities vary with the observations and assumptions considered at each event. Thus Equation (44) outlines a general formulation where simplifications and further assumptions could be made according to the event under analysis.

Following the assumptions made by Ceplecha & McCrosky (1976) (namely: no meteor deceleration, meteoroid final disintegration and isothermal atmosphere), the resulting scenario is that of h_I in Equation (37):

$$\frac{h_I}{h_0} = -\frac{\ln\rho_t}{\ln\rho_0} = \ln(2\alpha\beta) \Rightarrow -\frac{\log\rho_t}{\log\rho_0} = \log(2\alpha\beta) \Rightarrow -\log\rho_t = \log(2\alpha\beta) - \log\rho_0 \tag{45}$$

And then using Equation (44):

$$-\log\rho_t = \log\sigma + \log K + 2\log V_e - \log cosZ_R - 0.33\log M_e + const. \tag{46}$$

It results that Equations (42) and (46) are exactly the same. While coefficients A, B, and C in Ceplecha & McCrosky (1976) are derived via a least squares adjustment to 156 meteor trajectories obtained by the Prairie Network, their theoretical approach was based on the assumptions that lead to the current h_I formulation. Hence, if as discussed

h_I does not provide a good adjustment to the observed terminal heights, the PE criterion suffers from similar inaccuracies. Moreover, since it has been proved that it is possible to derive the PE criterion from a combination of two dimensionless parameters that are directly retrieved from observations, it can be stated that Equation (44) provides a more general classification criterion. This new approach relies on the observations and does not need any approximation for unknown parameters nor an specific atmospheric model (Lyytinen & Gritsevich, 2016), thus avoiding any model bias.

5.6 CONCLUSIONS AND OUTLOOK

The study carried out in this chapter has proved that it is possible to accurately calculate the terminal heights of meteoroids only accounting for two parameters. This was possible thanks to the introduction of the scaling laws and dimensionless variables (Stulov et al., 1995; Stulov, 1997; Gritsevich, 2007).This methodology had only been tested on several fully ablated fireballs with large β values by Gritsevich & Popelenskaya (2008). It was then interesting to determine whether this new mathematical approach works equally accurately with fully ablated fireballs and meteorite-producing ones, and whether any additional modification could be applied to improve the accuracy and extend the applicability range for the proposed methodology. The results shown in this chapter are summarized in the following points:

1. Several simplifications of the terminal height formulation have been verified using an accurate data sample from the Meteor Observation and Recovery Project. The use of Equation (37) that neglects meteor deceleration and is applicable to fast bodies shows a standard deviation of $\sigma = 4.11$ km which seems to be high. However, if a modification is introduced to account for some degree of deceleration (Equation (38)) a linear tendency is found, and the global accuracy improves notably ($\sigma = 1.52$ km). This is the motivation to find a better adjustment. By applying a newly suggested mathematical approximation function Equations (40) and (41) provide different levels of improved adjustment. While Equation (40) leads to $\sigma = 0.75$ km, Equation (41) show some discrepancies at low β values. This unexpected discrepancy of of h_{IV} can be explained due to five cases with low β values. However, in this case, the adjustment using the approximated function A_1 is more precise for values of $\beta > 3$ (see Figure 27). This is in agreement with the results discussed in Gritsevich et al. (2016). Mathematically, these authors concluded that close to $\beta \approx 2.89$ for A_0 and at $\beta \approx 2.1$ for A_1 (provided $v \in [0.3, 1)$) the difference between Equation (38)) and the resulting expression using approximated functions is optimized. This statement has been tested with a large amount of real cases in this chapter, supporting the analytical study.

2. The discrepancies between observed and calculated terminal heights found at low β values shall be studied in more detail. Typically, meteorite-droppers show low β values, which mean low ablation and thus, higher chances of survival. In other words, tough bodies (such as ordinary chondrites) may be affected by this error. While these discrepancies could be due to simplifications arising from the analytical solution, the mathematical modification introduced by means of the

approximation function A_0 is able to correct the global accuracy of the results for the sample under study. The local deviation at low β are of particular relevance for any planetary defense study. At low β values the suggested calculated terminal heights have lower values than observed values. This would mean that any prediction about the atmospheric penetration of fireballs based on h_{II} or h_{III} would indicate higher values that the observed ones. On the contrary, the values suggested by h_{IV} would be lower than the real recordings. Note that given errors attached to the observations (i.e., atmospheric conditions, whole trajectory recording, resolution of the camera, etc.), this subject should be studied in more detail.

3. It is worth noticing that a good estimation of terminal heights opens new fields of studies. First, it is possible to forecast terminal heights when the last part of the fireball trajectory has not been recorded, which happens quite often. The more number of recorded points, the better the accuracy (α and β do strongly depend on the deceleration, and this is better described with an increasing number of (h, V) trajectory observations), but it is still possible to obtain α and β with only three recorded points. Depending on each event this may have little influence on their derivation. This is quite advantageous if we consider a fast meteoroid because, no more parameters are required (see Equation (37)). On the contrary, for decelerated bodies with high β values, the missing (h,V) at the end of the trajectory could be adjusted based on the rest of the trajectory data (Whipple & Jacchie, 1957). Thus, as discussed in this chapter, V_t (the terminal velocity) could be obtained (provided some assumptions or extra data from other observational techniques) for most of the registered fireballs and h_{III} or h_{IV} could be derived.
   Secondly, it is also notable, that meteor height may be expressed as a function of time. Thus, the ability of predicting terminal heights may be directly linked with the forecast of a total duration of meteor phase. This leads to a new class of problems, such as, for example, insights into determination of luminous efficiency based on meteor duration and calculation of critical kinetic energy needed to produce luminosity.

4. Direct comparison between h_{III} and h_{IV} could be used for other purposes. The results presented here correspond only to one fireball network. It is still difficult to conclude whether h_{III} or h_{IV} would provide better general results for other fireball network data. It could be interesting to find out whether h_{III} is able to absorb better the widespread in results for different β values. According to MORP results, h_{III} achieves a better global accuracy. This is in part due to the five cases that bias the global accuracy achieved with h_{IV}. Nonetheless, it seems that terminal heights of fireballs showing moderate β values are more accurately determined using h_{III}. Resolving whether better global results are obtained either with h_{III} or h_{IV} might be quite useful in two senses, to detect and avoid systematic errors in database recordings, and to derive fast accurate results for large sets of data.

5. The dimensionless methodology is able to describe in a simple way the physical event. Given the difficulties of deriving the exact values for some physical properties (i.e. bulk density, shape, etc.) from the observation, the reduction of

unknowns achieved with this methodology could be used as a powerful tool to pursue a classification based on α and β parameters (see Gritsevich et al., 2012). In some cases it could be quite convenient to use h_{III} or h_{IV} and β to characterize different events instead of using a combination of α and β. Particularly, members of meteor showers (generally carbonaceous chondrites) can be classified using these two parameters, given the excellent behavior of h_{III} or h_{IV} for high α and β values.

6. For significantly decelerated bolides and a few well-studied cases, such as the Innisfree meteorite, the published terminal heights may differ depending on the data-reduction approach used (e.g. 21 km in Halliday et al., 1981; 19,8 km in Halliday et al., 1996). This not only affects the accuracy between calculated and observed terminal heights for any individual fireball, but also the global accuracy obtained for larger databases as studied here. Nonetheless, this could be taken as an opportunity. The current approach could set constraints on terminal heights and fireball flight duration values, which may help to put adequate restrictions verification guidelines on the recorded values.

7. The PE criterion outlined by Ceplecha & McCrosky (1976) can be derived using the current formulation. The mathematical definition of α depends on the ratio of pre-atmospheric cross-section to pre-atmospheric mass (a ratio easily convertible to bulk density, pre-atmospheric mass and shape coefficient, all of these parameters are used in the PE criterion), and on the trajectory slope γ related to Z_R of the PE criterion. Respectively, the mass-loss parameter is proportional to pre-atmospheric velocity with a power of two and inversely proportional to the effective destruction enthalpy. It has been proved that the PE criterion corresponds to the mathematical expression of h_I and thus it can be applied under the same assumptions: no meteor deceleration, homogeneous loss of mass ($\mu = 2/3$), meteoroid final disintegration and isothermal atmosphere. However, here it has been demonstrated that a more general formulation of the PE criterion which does not need these assumptions can be outlined combining only α and β parameters. Furthermore, this result reinforces the validity of the current approach to study the atmospheric flight of meteoroids.

8. Future studies shall envision the calculation of terminal height to be useful when the lower part of the trajectory was not instrumentally registered (e.g. limited field of view of the camera, shadowing of fireball trail by other objects, weather conditions, detection of meteoroids using radar techniques with limited observation beam etc.). It also brings critical knowledge into the problem when one needs to predict how long will be a total duration of the luminous flight or at which height a fireball produced by a meteoroid with given properties would terminate. Based on the current results the recommendation is to use of Equation (40) also to solve inverse problem when terminal height and velocity are available from the observations, and parameters α and β need to be derived.

6

IMPLICATION OF THE RESULTS IN THE IMPACT HAZARD

6.1 INTRODUCTION

The work carried out in previous chapters for meteoroids with estimated radii between 1 to 10 cm is essential to understand the atmospheric behaviour of larger bodies. Despite that the energy release per unit of time and the possible meteorite impact consequences are different between centimeter-sized and tens-of-meters sized bodies, meteoroids in both ranges of sizes experience similar physical phenomena during their atmospheric passage. The goal of this chapter is to extrapolate the discussion held in previous chapters to larger meteoroids and small asteroids. Note that, according to the IAU, asteroids can be as small as 1 meter in diameter, and so this terminology is assumed here (see also Chapter 1 for definitions).

6.2 IMPACTS OF LARGE METEOROIDS

The data set of Ursid meteoroids with radii between 1 to 3 cm studied in Chapter 3 is an evidence of the meteoroid orbital evolution under the complexity of celestial mechanics and the effects of non-gravitational forces. A better understanding of these processes allows to constrain orbital meteoroid swarm evolution models (Trigo-Rodríguez, 2000; Trigo-Rodríguez et al., 2005; Vaubaillon et al., 2005a,b; Tóth et al., 2011). Besides, the study of meteor showers is essential to gain understanding in the aggregation processes that took place in the formation of their progenitors (Trigo-Rodríguez & Llorca, 2006). Ultimately, this will contribute to shed more light on the mechanisms that lead to cometary break-ups and mass loss, and even reveal the presence of extinguished comets within the current NEO population (Jenniskens, 1998, 2006; Trigo-Rodríguez et al., 2004a, 2007; Madiedo et al., 2013b). As stated by Jenniskens (2006) the study of meteor showers may also announce the orbital change of their parent comet, and thus announce a future impact of that larger body. Moreover, meteoroid swarms that cause meteor showers could pose a risk on satellites either by direct impact, or by high energetic plumes that may electrically charge the spacecraft and create overcurrents that can affect critical satellite systems (Jenniskens, 2006). Finally, asteroids with slightly larger sizes (up to 100 m) are subjected to the same gravitational and non-gravitational

effects in similar quantities than centimeter-sized bodies (Bottke et al., 2000). Hence, the study of meteor showers and their parent meteoroid swarms is a suitable approach to understand the orbital evolution of larger meteoroids.

While the Earth atmosphere is efficient in disintegrating small meteoroids, larger meteoroids can survive the atmospheric passage. Centimeter-sized meteoroids reach the top of the atmosphere at hypersonic velocities with energies ($E_k = 1/2 \cdot M_e \cdot V_e^2$) between 10^{-3} to 10^{-6} kilotons. Most of this energy is deposited at high altitudes, mainly in the mesosphere and lower thermosphere (or MLT) region of the atmosphere, as it was proved in Silber et al. (2015) and revisited in Chapter 4, where the hazard to the local population is negligible. Even though centimeter-sized meteoroids can ablate till an altitude of around 20 km (see the terminal heights in Chapter 5, Table 16), these bodies usually experience fragmentation and disruption into smaller fragments that rarely provoke *airbursts* (defined as a detonation in the air that yields an explosive load comparable to or greater than a weapon of war). When these bodies survive the atmospheric passage, the remaining meteorites deposit their remainig energy on the ground, where their ability to create a small hole does not pose a serious damage. For instance, regarding the short list of the recovered meteorites for which the atmospheric flight was observed (see Table 10 in Chapter 3), it can be noticed that half of them had a pre-ablation meteoroid radius between 10 to 50 cm. Table 17 compiles the values of density, entry mass and approximated radius (assuming a sphere shape) of those events of listed in Table 10 in Chapter 3 that have a pre-entry size of 10 to 50 cm in radius. The values shown in Table 17 bring to discussion two points. On the one hand, most of these meteoroids have an estimated bulk density of 3500 kg/m^3, which is the value used in Chapter 4 to derive the flow regimes. Thus, the density assumption taken in that study is also valid for centimeter-size meteorite-droppers. On the other, there are several cases (i.e. Bunburra Rockhole, Mason Gully, or Grimsby) that are close to the 1 - 10 cm meteoroid size and are in line with the size range of the data set studied in Chapter 4. However, while meteorite-droppers usually suffer fragmentation, the analysis of Chapter 4 was made for high altitudes shock wave detections, close to the initial formation of the shock wave, where abrupt deceleration or fragmentation are uncommon. Indeed, the data set chosen complies with these facts. Although these phenomena shall be taken into account when revealing the meteoroid flight regime and the onset of the shock wave, the inclusion of fragmentation when dealing with the meteoroid flight regimes is complex and there is not much work done in this regard (for a brief review see e.g. Silber et al., 2018b). Basically, for large fragments the shock wave of individual fragments can play an effect on other's fragments shock waves which still remains to be studied. For meteoroids in the range of millimeters and centimeters the initial shock wave could even disappear after the fragmentation. The reduced size of the resulting fragments may suffer a lower ablation intensity, the flow regime could change, and the generation of a shock wave in the MLT region can be compromised (Silber et al., 2018b). It is therefore important to revisit the effect of fragmentation on the identification of the meteoroid flow regimes and the generation of the shock wave (Moreno-Ibáñez et al., 2018). Unfortunately, given the sporadic nature of these events and the recent implementation of infrasound techniques within the fireball networks, the information compiled in databases is still poor and

Meteoroid	Density	Entry Mass	Radius	Reference
Prîbram	3700	1300	43.8	[1], [2]
Lost City	3730	163±5	21.9±0.2	[1], [3]
Innisfree	3500	35±2	13.4±0.3	[1], [3]
Morávka	3590	1500±500	46.4±5.2	[4]
Neuschwanstein	3490	300±100	27.4±3.0	[5], [6]
Villalbeto de la Peña	3420	550±150	33.7±3.1	[7], [8]
Bunburra Rockhole	2700	22±0.3	12.5±0.1	[9]
Maribo	2100	1500	55.5	[10]
Jesenice	3400	170±80	22.9±3.6	[11]
Grimsby	3370	33±16	13.3±2.1	[12]
Mason Gully	3320	14	10.0	[10], [13]
Kirzevci	3500	50±25	15.1±2.5	[14]
Novato	3400	80±35	17.8±2.6	[15]
Dingle Dell	3450	81.6	17.8	[16]
Annama	3500	472	31.8±0.2	[17], [18]

Table 17: Radius of the instrumentally observed centimeter-sized meteorite falls (in [cm]). The densities are given in [kg/m^3] and masses in [kg]; these values are taken from the references in the last column: [1] Gritsevich (2008c); [2]Borovicka & Kalenda (2003); [3] Ceplecha & Revelle (2005); [4] Borovicka et al. (2003); [5] Gritsevich & Stulov (2008); [6] Spurný et al. (2003); [7] Llorca et al. (2005); [8] Trigo-Rodríguez et al. (2006); [9] Spurny et al. (2012); [10] Borovička et al. (2015a); [11] Spurný et al. (2010); [12] Brown et al. (2011); [13] Dyl et al. (2016); [14] Borovička et al. (2015b); [15] Jenniskens et al. (2014); [16] Devillepoix et al. (2018); [17] Kohout et al. (2015); [18] Kohout et al. (2016).

could hinder the derivation of strong conclusions.

Terminal heights were calculated in Chapter 5 avoiding the necessity of assuming or approximating the value of a set of unknown meteoroid properties and flight parameters, thus reducing the attached uncertainty. While the formulation outlined in Chapter 5 does not include fragmentation, the implementation of fragmentation in the formulation is possible if further work to adjust the change in the momentum of the disrupted fragments is carried out. Centimeter-size meteoroids suffer minor fragmentation during its flight and the main meteoroid does not experience an abrupt change in its momentum. It is at the end of their atmospheric luminous path (where the terminal height is defined) that they can either disintegrate or experience a larger fragmentation, thus allowing the inclusion of fragmentation in the equations of motion. In any other situation, when there is a soft variation of the meteoroid momentum during fragmentation, the methodology outlined in Chapter 5 allows a straight-forward determination

Meteorite	V_e	V_t	v_t	α	β	h_{obs}	h_I	h_{II}	h_{III}	h_{IV}	Ref.
Prîbram	20.89	20.46	0.98	8.34	13.64	44.80	38.86	44.96	44.82	44.83	[1]
Lost City	14.20	3.40	0.24	11.11	1.16	19.90	23.27	26.19	22.83	17.06	[1]
Innisfree	14.54	2.70	0.19	8.25	1.70	19.80	23.87	25.41	22.30	18.53	[1]
Neuschwan.	20.95	2.40	0.11	3.92	2.57	16.04	21.50	22.09	19.42	17.20	[1]
Bunburra Rockhole	13.31	5.68	0.43	25.23	1.53	29.59	31.12	33.53	30.74	28.29	[2]
Annama	24.20	-	-	8.25	1.70	21.80	23.87	-	-	-	[3]
Dingle Dell	15.44	3.24	0.21	9.28	1.42	19.12	23.41	25.55	22.29	17.63	[4]

Table 18: Entry velocity [km/s], terminal velocity [km/s], dimensionless velocity (V_e/V_t), α and β parameters, observed terminal height [km] and the four derived terminal heights [km] as described in Chapter 5 for some instrumentally observed meteorite falls with sizes within a centimeter range. The last column indicates the references from which α and β were obtained: [1] Gritsevich (2008c); [2] Sansom et al. (2015); [3] Trigo-Rodríguez et al. (2015); [4] Devillepoix et al. (2018).

of the terminal heights. To further explore this statement the terminal height of those meteoroids shown in Table 17 for which the α and β values were elsewhere derived are calculated. The same formulation outlined in Chapter 5 is used. The calculated and the observed terminal heights for 7 meteorites are shown in Table 18. Note though that as the terminal velocity of Annama meteorite is not available, only h_I is derived.

The first thing to be noted from the results in Table 18 is that, in spite of experiencing fragmentation, the terminal height for these bodies can be correctly retrieved using the approach of Chapter 5. This is relevant, as previous studies (Moreno-Ibáñez et al., 2015a, 2017b) proved the validity of using scaling laws and dimensionless variables to derive the terminal height for meteorites on a one case-basis (Innisfree fall, Halliday et al., 1981). Now it has been proved that a similar level of accuracy as that obtained in Chapter 5 can be obtained for centimeter-sized meteorite-droppers. Moreover, the methodology can be applied to meteoroids with a pre-atmospheric diameter close to a meter (the pre-atmospheric radius of Prîbram is around 44 cm) that suffer fragmentation (see Gritsevich, 2008c). This fact also proves that if the meteoroid atmospheric trajectory can be accurately observed and the change of momentum due to fragmentation constrained, then the derivation of α, β and the terminal height is accurate. Note that the change in the fragments' momentum when they disrupt depends on the height at which it occurs, the size of the fragments, the vapour-pressure produced when volatiles are released during break-up, and the resulting flight configuration (see Gritsevich, 2008c). This is for example the case of Prîbram meteor (see Table 18). Its large β value indicates that the intensity of the meteoroid ablation was large during its meteor phase. Ablation is intrinsically related to mass-loss, and this can be experienced in several ways. As for the Prîbram meteoroid, the estimated mass of most of the 17 fragments observed during its meteor phase (Ceplecha, 1961) were three orders of magnitude smaller than the main fragment (Gritsevich, 2008c), thus not altering by much the momentum of the

larger fragment and increasing the mass-loss and consequently the value of β.

Secondly, it seems that the value of h_{IV} achieves the best accuracy for all the events displayed in Table 18. Note that, even though only h_I was derived for the Annama meteorite, this value only diverges 2 km from the observed one (which is well within the standard deviation for h_I estimated in Chapter 5, $\sigma = 4.11$ km). Annama was a daylight fall which usually require more effort to be correctly analysed since the astrometric study (see Chapter 2) cannot be based on background stars. Hence, the use of a mathematical approach using scaling laws and dimensionless variables could be a reliable complement to retrieve further information in these situations.

The α parameter for the events posted in Table 18 is generally low; only exception made for Bunburra Rockhole. Similarly, the β values are small with the already mentioned difference of Prîbram meteorite. As discussed by Gritsevich et al. (2012) meteorite-droppers are located in a well constrained area in a $\ln \alpha - \ln \beta$ diagram. The diagram accounting for the meteorites listed in Table 18 is shown in Chapter 2, Figure 6. From that figure it comes quite straightforward that meteor showers (i.e., Northern and Southern Taurids) are allocated in a separated area of the diagram, and thus the use of α and β can serve as fireball classification. This has been demonstrated mathematically in Chapter 5 through the reformulation of the PE criterion (Ceplecha & McCrosky, 1976) using a logarithmic combination of α and β. Also, as suggested in Chapter 5, the combination of β and the calculated terminal heights could be of use to understand possible bias in meteor databases.

It was also discussed in Chapter 5 that the Equations (37) ,(38), (40) and (41) could be used to derive the duration of the meteoroid atmospheric time till it reaches its terminal height if only a limited part of the luminous trajectory is detected. This information allows the adjustment of photometric light curves and can be of interest to describe the amount of energy per unit of time released by the body during its flight. A combination of this information, along with the presence of the shock wave, and the knowledge of the flow regimes' evolution of a given meteoroid can be helpful to understand the energy released per unit of time during the fireball flight.

Finally, the ability of a meteoroid to survive the atmospheric passage is related to the aerodynamical load it can stand (Trigo-Rodríguez & Llorca, 2006, 2007; Popova et al., 2011) and its flight configuration. The increasing air density that the meteoroid encounters along its descending path increases the load on the meteoroid according with $\rho \cdot V^2$ (Trigo-Rodríguez & Llorca, 2006, 2007; Popova et al., 2011). Provided that the meteoroid often exhibits a heterogeneous composition, fragile aggregate structure, high porosity, and some spin, loading forces act differently and promote the meteoroid fragmentation. Thus, the rotating meteoroid could delay fragmentation if the increasing aerodynamic load acts in a more favourable way. Flow regimes, shock waves and terminal heights can also be useful to gain a deeper insight into the meteoroid bulk strength and its macroporosity (e.g. Revelle, 2002). For instance, the stresses suffered by the meteoroid could be better estimated if the flow regime and the gas density in the shock layer (if a shock wave is already generated at the first fragmentation point) are known. Also,

as mentioned above, the terminal heights could be useful to outline the amount of energy released by the body at a certain point. The more clues obtained for the meteoroid bulk strength, its macroporosity and the orbit mechanics of a meteoroid, the better is the understanding of the physical processes and evolution paths that meteoroids may have experienced since their accretion (Blum et al., 2006; Trigo-Rodríguez & Blum, 2009a). This ultimately is of relevance to outline and implement planetary defense tactics for larger bodies.

6.3 EXTRAPOLATION TO METER-SIZED ASTEROIDS

The study of centimeter-sized meteoroids is essential to understand the underlying physics of small asteroids. While the formers do encounter the Earth more often, the later have proved to be a source of damage to the Earth in two ways: either by a direct surface impact (resulting in a crater) or releasing most of its energy at low atmospheric altitudes.

6.3.1 *Past hazardous events*

The last century was quite relevant in terms of meteoroid impact hazard caused by meteoroids with diameters in the tens-of-meters range. Three large bodies encountered the Earth during their orbits and the consequences were notable. Tunguska in 1908 provoked a great devastation over a forest area of about 2150 km^2 in Russia (Chyba et al., 1993; Vasilyev, 1998), and local inhabitants felt an Earthquake that was lately estimated to range within 4.5 to 5 on the Ritcher scale (Chyba et al., 1993; Vasilyev, 1998). The estimated energy released in the atmosphere was around 10 to 50 Mt TNT (1 kT TNT = 4.185 $\times$ 10^{12} J), and the airburst was able to bend down forest trees over an area of around 100 km^2 (Chyba et al., 1993; Vasilyev, 1998). Probably all the meteoroid was disintegrated in the airburst as no resulting meteorite was found. The radius of the meteoroid was initially constrained to be about 20 - 30 meters (Chyba et al., 1993), and has been recently revisited using more accurate entry models (Boslough et al., 2015) to around 40 m.

One century later, on September 15th, 2007, the local population of the Carancas village (near the Lake Titikaka in the border between Peru and Bolivia) spotted the atmospheric passage of another hazardous body (Le Pichon et al., 2008; Tancredi et al., 2009; Kenkmann et al., 2009). This time several fragments corresponding to a H4-5 chondrite meteorite were recovered from the walls of the resulting crater (Le Pichon et al., 2008; Tancredi et al., 2009; Kenkmann et al., 2009). The diameter of the crater diameter had a mean value of 13.5 meters and a depth of 5 meters (Le Pichon et al., 2008; Tancredi et al., 2009). The study of the crater dimensions and soil composition lead to a

very constrained meteoroid velocity entry values, entry angles, and energy release. The general conclusion delimits an entry angle of 60 degrees, the entry velocity lower than 16 km/s, the meteoroid initial diameter around 2 meters, and the energy deposition in the atmosphere around 1 to 3 tonnes TNT (Le Pichon et al., 2008; Brown et al., 2008; Tancredi et al., 2009; Kenkmann et al., 2009). Carancas was an homogenous monolithic meteoroid with a likely strength larger than 20 MPa, which is higher than any other meteoroid observed (Borovička & Spurný, 2008; Popova et al., 2011). Hence, the Carancas event clearly showed that the meteoroid strength shall be studied individually for each event (Borovička & Spurný, 2008).

More recently, (February 15^{th}, 2013) over the Russian region of Chelyabinsk, another hazardous meteoroid was reported. The sonic boom associated with Chelyabinsk caused serious damage in the surrounding building glassware (Brown et al., 2013b; Popova et al., 2013). Note that this event took place only six years later than Carancas. However this time, thanks to the dashcams that most Russian population have installed in their vehicles for security reasons, there was a wealth of well reported observations that eventually allowed to accurately retrieve the meteor trajectory (see Borovička et al., 2013a; Brown et al., 2013b; Popova et al., 2013). Furthermore, this was the first time that important fragmentation was observed for meteoroids in this size. This meteoroid was an LL5 chondrite, had an entry velocity of 19.03 km/s, an entry angle of 18.5 degrees, and the atmosphere energy deposition estimated using infrasonic, seismic and satellite data resulted in approximately 500 kt TNT (Borovička et al., 2013a; Brown et al., 2013b; Popova et al., 2013). The only crater found was a 9 meters hole in ice, and was produced by the largest meteorite recovered from the bottom of the lake. Chelyabinsk suffered a lot of fragmentation and thus, a wide variety of meteorites with various masses were recovered. Chelyabinsk was 19 meters in diameter, and the total mass recovered was around 2 tonnes (Popova et al., 2013). The main hazard of Chelyabinsk was associated with the shock wave that broke roofs, doors and windows causing more than one thousand of injured people (Tapia & Trigo-Rodríguez, 2017).

6.3.2 *Potential hazard*

Although the number of historical registered events is low, it is evident that early detection and follow-up of bodies of tens-of-meters in diameter, together with the study of the mechanical properties of their rock-forming minerals (Moyano-Cambero et al., 2017) is crucial to understand the risk and develop adequate planetary protection tactics. The astrometric follow-up of PHAs is of key relevance to understand some key physical parameters of these bodies; more details can be found in the contributions made by our group, i.e.: Trigo-Rodriguez et al. (2008), Trigo-Rodríguez et al. (2010), and Moreno-Ibáñez et al. (2015b). The current level of completeness of the size distribution in observational programs is such that nowadays the new discoveries are mostly limited to detect bodies with absolute magnitudes well below +16 (Pravec et al., 2012). Basically focusing on small asteroids which are difficult to be detected due the unfavourable combination of the distance, absolute magnitude and albedo, and thus mak-

ing the detection of NEAs with tens-of-meters diameters complicated (Binzel et al., 2004). Indeed, only in few cases a NEA impact was predicted beforehand i.e., 2008 TC_3 (Jenniskens et al., 2009); 2014AA (de la Fuente Marcos et al., 2016); or the recent 2018 LA (de la Fuente Marcos & de la Fuente Marcos, 2018)). In the rest of cases (Carancas, Tunguska or Chelyabinsk) the approach of the body happened without previous warning. However, the impact from undetected objects could be more catastrophic. And example in this regard was the close Earth approach of the 660 m in diameter NEO 2015 TB_{145}, whose closest orbital point to Earth was only 0.1 lunar distances from Earth, and was discovered only twenty days before the close approximation (Müller et al., 2017). Although this object was catalogued as a NEA, its large orbit eccentricity ($e = 0.866$) and inclination ($i = 39.7^o$) suggest that it could be an extinct comet (Trigo-Rodríguez & Williams, 2017). Indeed, the number of detected Near Earth Comets (NECs) is roughly 107, whereas the number of NEAs is way larger, 18617 (JPL website: *https://cneos.jpl.nasa.gov*). NECs are usually few kilometer in diameter TNOs that decay to inner orbits after close planetary encounters and perihelion passages (Jewitt, 2008). Given their cometary nature (weakly bounded conglomerates icy grains; Britt et al., 2002), these objects can fragment and create orbital related complex of objects (i.e., 2P/Encke, Spurný et al., 2017b). The main disruption mechanisms are probably an increasing spin of the comet or collisions with asteroids and meteoroids (Jenniskens et al., 2007). The range of sizes in the resulting complex of disrupted fragments goes from dust particles to few kilometers in diameter objects. The cometary complex objects can eventually become more compact (Binzel et al., 2004), thus hindering its localization. In this line, the close encounter of NEO 2015 TB_{145} brings to discussion the current weaknesses in terms of planetary defense and detection of large dark objects with high encounter velocities (this is, with high eccentric orbits). As suggested by Trigo-Rodríguez & Williams (2017), some recent events (such as Damocloids, Madiedo et al., 2013c) could set evidence of the existence of high eccentric comets with high mechanical strengths. Besides, comets with high inclinations (and thus subjected to a lower number of orbital collisions) may not be as fragile as previously assumed (Jones & Williams, 2008). This fact shall be taking into consideration in future NEO surveying projects.

In order to partially address the difficulties in the prompt detection of threatening bodies the use of statistical approaches is implemented. For instance, D'Abramo et al. (2001) suggested to use a re-detection ratio which considers that every NEA is equally easy to be discovered given the impossibility of determining their exact population and their accurate location. Boslough et al. (2015) derived a completion curve (a curve that shows how frequent an impact from a meteoroid with a determined size is) using this re-detection parameter, the absolute magnitude of the NEA, and the limiting magnitude of a simulated survey involving $100,000$ synthetic NEA orbits. These results were also calibrated and compared against previous completion curves. This curve shows for example that Chelyabinsk-like events take place every 50 years, and suggests that the disruption of *rubble piles* (bodies that result from the weak gravitational link between several boulders) or even detachment of large boulders in high spin asteroids, particularly during close approaches with Earth, could play a role in increasing the impact rate for bodies of few tens of meters in diameter (Trigo-Rodríguez & Williams, 2017).

Indeed, according to Michel et al. (2001, 2002), most NEAs are rubble piles that can ultimately be split easily under gravitational events and collisions, and thus give birth to smaller asteroids. Given that up to date most of the identified PHOs are PHAs, which usually originate in the MAB and are subjected to frequent collisions, it is expected that most of the meter-size bodies originated in larger objects show low strength properties like for example fragile carbonaceous chondrites or fractured ordinary chondrites (Trigo-Rodríguez & Blum, 2009a,b; Popova et al., 2011; Moyano-Cambero et al., 2017). Note that most catalogued NEAs are related to an ordinary chondrite composition (Pravec et al., 2012).

Although as stated by Boslough et al. (2015), large NEOs represent a tiny fraction of the population but the large threat in terms of the ratio of impact probability to damage consequences. The consequences of their encounter could generate blasts which are able to devastate large areas as exemplified by Tunguska (Boslough et al., 2015). The effectiveness of asteroids in the size of tens-of-meters to deposit energy at an optimum height where the devastation power is higher, depends basically on the zenith angle, the entry velocity, and the strength properties of the body (exemplified by the Tagish Lake bolide; Brown et al., 2002b). This is, they can reach the troposphere at hypersonic velocities, releasing an enormous energy at low altitude. For instance, Chelyabinsk had a low bulk strength value that fostered its fragmentation (Popova et al., 2013) and alleviated the amount of energy deposited at low heights. This is the most common output that explains the relative absence of craters of few hundred meters in diameter (Bland & Artemieva, 2003). Also, the damage caused by Chelyabinsk could have been worst if the zenith angle would have been higher (Boslough et al., 2015). The effect of fragmentation is essential to understand the mechanism, amount, and the altitude of energy release. Depending on the fragmentation suffered, the resulting fragments could maintain their flight close to the main fragment and fly behind the same shock wave, thus keeping the energetic profile of the initial shock wave (Silber et al., 2018b). However, more complex scenario could take place.

The airbursts that meter-sized bodies could create at low atmospheric heights can reach energy levels of several Mt TNT, as it was the case of Tunguska (Chyba et al., 1993; Vasilyev, 1998). While small asteroids could reach the surface and create a crater, the hazardous consequences of such impacts are far less important compared to the airburst. Furthermore, as stated by Boslough & Crawford (2008), the asteroids with sizes from few to hundreds-of-meters in diameter will continue releasing energy after their atmospheric disintegration. Due to their downwards momentum, the descending cascade of energy will still propagate downwards and reach lower atmospheric altitudes (or even the surface, explaining some *tektite fields* with no associated crater) thus enhancing the heat transportation to the surface and their destructive power. The set of hydrocode simulations carried out by Boslough & Crawford (2008) also revealed that, unlike war weapons, low-altitude airbursts generate upward ballistic plumes. The formation of a shock wave creates a low-density region at the rear side of the meteoroid (Silber et al., 2018b) through which the expanding hot gas jet is able to propagate and reach back higher atmospheric altitudes. Boslough et al. (2015) explains that this effect, called *plume*, can be appreciated at altitudes of 300 km. At these heights the human presence

is increasing with time. For instance, the International Space Station (ISS) orbits at around 400 km, and private space travel companies are now offering space tourism trips between sub-orbital heights and the ISS. Hence, plumes require further study since they can become a potential threat to humans.

The combination of the collision probability and expected energy deposition at low atmospheric altitudes serves to outline the two main current hazard predicting scales. On the one hand, the Torino scale (Binzel, 2000) is generally used to illustrate the civilian population about the associated risk of a detected object. However, among other limitations, it does not progressively re-evaluate the hazardous level of a NEO as the uncertainty associated with its size is reduced (i.e., the body approaches the Earth and new measurements can be carried out). Besides, the scale is not continuous and similar objects can have very different classification ranks. On the other hand, the Palermo scale (Chesley et al., 2002) includes an extra parameter to evaluate the hazard. The *background hazard* is a normalization of the potential risk of an object over all the registered associated risks of other potentially hazardous objects detected in the meantime of the impact of the studied object. The classification is therefore based on previous and future statistics for similar objects. This is, it claims whether the threatening of the studied object is lower, equal or higher than the rest of registered objects threats before the date of the studied object's impact. Unlike the Torino scale, the Palermo scale is continuous, as it states the potential risk posed by a body considering the risk level of the background hazard. All in all, these scales are useful to provide an impact prediction in terms of quality, and they serve to concern about the likelihood and level of an eventual impact, but they fail to quantify the potential damage that might be caused.

6.3.3 *Application of the previous work on meteoroid hazard*

While future implementation of planetary defense tactics will allow orbital tracking of large meteoroids and meter-sized asteroids before collision with Earth, the current sporadic nature of events like Chelyabinsk reduces the chances to obtain an accurate atmospheric flight instrumental observation. In any case, the impact hazard challenge comes from the aleatory (and unexpected) nature of the projectiles. This will ultimately derive in difficulties to accurately determine their heliocentric orbit. For instance, as discussed in Chapter 3, the study of the orbital evolution of these challenging bodies, and their effects requires a precise knowledge of the pre-atmospheric flight parameters, especially the velocity. Although the calculation of the meteoroid entry velocity has been addressed by previous studies (see Ceplecha et al., 1998; Gural, 2012; Egal et al., 2017), more work must be done in this regard. The expanded use of meteoroid clones to map possible orbital trajectories helps solving this issue. However, constraints in the numerical models (i.e., not inclusion of non-gravitational effects) do not allow further accuracy. The validation of the preliminary parental association and orbital evolution models, as done in Chapter 3, is constantly needed to solve the yet remaining questions in celestial mechanics and to validate simulation assumptions.

In the same way that ablation provides centimeter-sized meteoroids with an hydrodynamical shielding so does it to meter-sized asteroids. Similarly, the flow regime at which the shock wave is formed is not clear. The ability of these bodies to reach low atmospheric altitudes at hypersonic velocities allows them to release most of its energy at lower heights where the meteoroid and its disrupted fragments are under continuum-flow conditions. Note that according to Equation (23) in Chapter 4, if the same flight conditions are considered, the larger the meteoroid radius, the smaller Kn_r and thus the faster is achieved the continuum flow regime. The radius of Chelyabinsk is around 10 meters, which is 3 orders of magnitude larger than the average radius of the data set used in Chapter 4. Consequently (assuming equal flight conditions), the flight flow regime of Chelyabinsk at the highest height the initial shock wave was observed (90 km, according to Popova et al., 2013) is the continuum-flow regime. This is so using both, the classical and Tsien's scales. Indeed, the inclusion of the fragmentation and collateral effects (change in velocity, shape and direction, ablation rate, etc.), creates a complex scenario that may require on the one hand understanding the complete set of physical events occurring at very short timescales, and on the other, the use of simulation tools (e.g., hydrocodes) capable of reaching such level of resolution (Silber et al., 2018b). Reciprocally, determining the height at which the shock wave forms shall provide relevant feedback to understand the fragmentation mechanisms, the energy released per unit of time, and the flow regime at which it happens. For instance, as discussed by Popova et al. (2013), the mutual separation distance of the disrupted fragments of Chelyabinsk was long enough so as to let them decelerate sufficiently before reaching lower atmospheric heights, and also short enough to host them under the same shock wave. This way, for favourable meteoroid orbital configurations, planetary defense tactics could envision to fragment the threatening body before it impacts the Earth. Moreover, as previously discussed, understanding the generation of the meteoroid shock wave and its flight regimes is a valuable help to unravel the meteoroid and its parent's bulk properties. This is obviously a very relevant input when selecting the most adequate planetary defense or impact mitigation techniques to implement on a given impact scenario. A summary of current planetary defense techniques is outlined in Capozzi (2018).

The cascade of intense fragmentations that meter-sized projectiles can suffer can be hard to follow with instrumental observations (see for example Borovička et al., 2013b; Popova et al., 2013; Gritsevich et al., 2014). The pre-atmospheric meteoroid splits into several fragments that follow a normal distribution of sizes (Gritsevich, 2008c) with different momentum and flight directions. These new bits can break apart into new fragments with new velocities and trajectory vectors, and so on. Due to this, the determination of the terminal height for any of these sub-fragments using the formulation of Chapter 5 requires an accurate registration of momentum and trajectory direction variations. Future improvements of this mathematical approach should at least ease the analysis for certain well-constraint fragmentation models (see Chapter 1 for a brief discussion), and reproduce the atmospheric energy release rate (note that the formulation of the terminal heights calculated is time dependent) and the combination of entry velocity and slope required to provoke certain level of damage to the Earth population (via either by a direct impact or an energetic blast wave). In addition, the PE criterion

was envisioned to understand the nature of fireballs subjected to no large fragmentation that deposit their energy at high altitudes, and to discuss their ability to penetrate into the lower atmosphere (Ceplecha & McCrosky, 1976). According to the previous discussion, for meter-sized bodies this criterion could be only applicable in certain fragmentation scenarios. However, as per Chapter 5 , the new PE criterion outlined could be used as long as the values of α and β are accurately derived. This fact expands the range of applicable events that can be added to this classification. Regarding meteoroids penetrating at lower altitudes, Boslough & Crawford (2008) outlined a two-type low altitude airburst classification that acknowledges the limiting meteoroid size that can hit the Earth surface. Thus, assessing the risks and damage that these penetrating bodies could cause. Type 1 accounts for Tunguska-like events, and Type 2 for bigger bodies able to melt Earth surface silicates that suffer a quick quenching right afterwards to form glasses (i.e., the Libyan Desert Glass). The new PE criterion could be used to expand this classification and reach a higher level of discrimination.

In terms of impact hazard simulations, there exist several asteroid impact simulation applications and programs freely available in internet. Their purpose is to allow any eager user to estimate the consequences that an impact of meter-sized meteoroids like Chelyabinsk or Tunguska can cause. The different characteristics of these simulators along with the simulation of a test case (Chelyabinsk) is discussed in Moreno-Ibáñez et al. (2016). The results suggest that despite of being very interesting tools for science diffusion they need notable improvements prior to become powerful tools for scientific analysis. This brings into discussion the need to develop reliable software tools that allow the estimation of the impact hazard of different bodies, flight configurations and impacting sites. This task can be quite challenging given that fragmentation and energy release conditions require the evolution pattern of a set of variables. Furthermore, the new phenomena identified (e.g., ballistic plumes, downward jets, and large-scale vortices) shall be better adjusted in hydrocodes and included into impact risk awareness tactics (Silber et al., 2018b). The work carried out in this thesis provides suitable information and mathematical tools that shall be taken into consideration to undertake these developments. Some possible utilities could be: the use of scaling laws and dimensionless variables to reduce the uncertainty in mathematical models (Moreno-Ibáñez et al., 2016); the exploration of the relationship between shock waves and fragmentation to help introducing and refining efficiency factors in meteor flight models and to understand the evolution of the atmospheric energy release per unit of time; the implementation of meteoroid clones to sample the measurement uncertainties; etc.

6.4 CONCLUSIONS

The work carried out provides relevant understanding about the physics behind the entry of meter-sized bodies in the terrestrial atmosphere. In this chapter the focus was set in understanding the implications and lessons learnt concerning impact hazard. The main conclusions of the discussion held in this chapter are:

1. The study of bolides produced by more frequent centimeter-sized bodies is fundamental to constrain the impact hazard associated with meter-sized PHAs. Recent impact rate estimations indicate that these small asteroids produce much frequent hazard that previously known.

2. To gain insight on meter-sized events means to have new clues to validate current analysis models (e.g. atmospheric flight, ablation, energy release and impact consequences) and assumptions.

3. As stated by Bottke et al. (2000), the orbits of asteroids with sizes up to 100 m suffer the same gravitational and non-gravitational effects in similar quantities. This fact implies that a better comprehension of the orbital evolution of meteoroid swarms produced by cometary material detachment, catastrophic disruption of NEAs, or by detachment during close approaches can be fundamental to predict the impacts of larger bodies.

4. Meteor showers can also state the presence of extinct comets in the NEO population as it is well exemplified by the discovery of 2015 TB_{145}. The study of meteoroids associated to these PHAs can provide clues about the strength and composition properties of these challenging bodies.

5. Concerning their ability to penetrate deep into the atmosphere, most meteoroids have structural defects caused by their collisional histories (e.g. Chelyabinsk) that shall be accounted for, but others are monolithic and high-strength materials that can excavate craters and pose in risk human beings (e.g. Carancas). In view of that, our modelling efforts should be addressed to study the ability of meteoroids to reach low altitudes as a function of the different degrees of fragmentation that the bolide experiences during its atmospheric flight.

6. Once a meteoroid or small asteroid is fractured in the atmosphere, the fragments could continue their flight under different flow regimes and change the surrounding conditions that promote the generation of a shock wave or compromise the existence of an already existing one. Moreover, it is unknown how the shock waves of the fragments may interact with one another. Consequently, the formation, configuration and evolution of the shock wave when there is fragmentation requires further study.

7. The inclusion of fragmentation in the meteor dynamic equations is complex and generally it is done assuming well constrained scenarios. For the mathematical formulation used in this thesis, the calculation of the terminal heights accepts certain degree of fragmentation. Indeed, for approximately half of the current meteorite-droppers (with few-centimeters sizes) for which the meteorite was recovered and the atmospheric trajectory observed, the terminal heights were accurately derived. Thus, as long as α and β parameters can be accurately retrieved the terminal height can be calculated and the PE criterion implemented. This opens the doors to new impact hazard classifications and simulation scenarios.

8. The ability of a meteoroid to release energy is related to its terminal height and to the flow regime. While centimeter-sized meteoroid release most of their energy

at high altitudes and mainly in the MLT region. Asteroids in the range of tens-of meters reach lower altitudes were the energy release could occur in the form of an airbursts (e.g. Tunguska). Although some of these latter meteoroids may reach the ground at high velocities and therefore create a crater, the low-altitude airburst and the phenomenology associated are more hazardous.

9. The methodologies carried out and the results obtained in the previous chapters of this thesis are valuable information that shall be considered for planetary defense assessment and improvement of current numerical models such as hydrocodes.

7

CONCLUSIONS AND FUTURE WORK

The main goal of this thesis has been to provide a deeper understanding on the physical and dynamical properties of large meteoroids disrupted from asteroids and comets during and before their ablation in the Earth's atmosphere. These bodies may pose a serious hazard to Earth and so this study tries to unravel relevant clues that help implementing planetary defense tactics and mitigation actions. For instance, the highest hazard source are those meteoroids that yield large quantities of energy at low atmospheric altitudes. Although these bodies may disintegrate at that point, the kinetic momentum is able to transport most of the energy downwards to the Earth's surface in different ways (i.e, shock, thermal waves, radiation, etc.) that will devastate large areas. The work presented in previous chapters provides a multidisciplinary approach to the analysis of the Earth's impact of meteoroids with radii between 1- 10 cm. These bodies can be quite limited source of danger, but the analysis implemented have demonstrated the necessity of modelling and understanding these bodies to assess the risks and effects of the impact of larger hazardous bodies. The results outlined in these chapters can also be of interest to different scientific communities such as (but not limited to) astronomy, aeronomy, shock physics, meteor science, and near-Earth object (NEO) research.

In summary, the most relevant conclusions of this thesis are:

1. The prevention of future hazardous meteoroid impacts starts by understanding the dynamic evolution of the impactor, and their bulk physical properties. The gravitational and non-gravitational effects that cause changes in the orbital evolution of meteoroids also makes it difficult to identify and track their parent bodies. Since these dynamic processes affect meteoroids with a range of diameters between 1 cm to 100 m in a comparable way, the study of meteor showers can be used to obtain additional information about the nature and evolution of larger bodies. In addition, the study of meteor showers could inform about the existence or the return of hazardous comets, or provide clues on the presence of extinct/dormant comets in the NEO population which can be large, compact, and impact at high velocities (due to their high eccentricity). Also, this knowledge is useful to build up a catalogue of possible hazardous bodies, their bulk physical properties and their impact consequences. The observation and orbital analysis of the extraordinary and periodical Ursid meteor shower outburst (Chapter 3), that occurs when its parent comet (8P/Tuttle) is at its aphelion, is an illustrative example of the orbital dynamics complexity and the interest of understanding the orbital evolution of meteoroid streams. In this case, those meteoroid trailets detached from

the comet 620 years ago, are able to dynamically evolve to a different fixed orbit than that of the 8P/Tuttle.

2. Those meteoroids detached from asteroids that reach the Earth can be used to obtain more information about their NEAs parents. Indeed, if the pre-atmospheric orbit of an impacting meteoroid can be accurately retrieved, it is possible to orbitally link it to a NEA and so to constraint the orbit dynamics of this latter body. However, the orbital behaviour of NEAs changes rapidly in the short-term, thus making it complicated to accurately predict their position. This implies that identifying a parental relationship between a meteoroid and a NEA requires both the accurate determination of the meteor sky radiant and the entry velocity to obtain a very accurate heliocentric orbit. Also, the observational uncertainties in the observation of NEAs shall be acknowledged. The reduction of the uncertainty in the meteoroid entry velocity has been the goal of previous studies, however, more work must be done in this regard. In this sense, future work on the formulation used in Chapter 5 will allow the simultaneous derivation of the entry velocity along with α and β parameters from the meteor trajectory observations. In Chapter 3 a set of meteoroid clones to map possible uncertainties when obtaining the meteoroid pre-atmospheric orbit, along with a dissimilarity criterion have been used to state a likely relationship between the meteorite Annama and the NEA 2014UR116. Note that although numerical clones are required to claim such parental relationships, many times these are not used. The lessons learnt on celestial mechanics are particularly relevant for bodies like Chelyabinsk as, they help gaining understanding in the delivery mechanisms (i.e., resonances after collisions) that put these meteoroids into the Earth's path.

3. Studies of meteoroids entering the Earth's atmosphere offer insight into the characteristics of these objects, as well as the conditions under which they produce shock waves. Despite recent advancements in meteor science, the classically derived flow regimes of meteoroids in the centimeter size range have never been validated against a well-constrained observational data set. Validation and better characterization of the flow regimes associated with bright meteors are essential for further considerations of the onset of shock waves produced by these objects in the upper atmosphere, as well as for developing new atmospheric flight models, the examination of ablation processes assumptions, and the improvements of the studies derived from meteor observations. A key result of this thesis is that the shock wave of centimeter-sized meteoroids might be already formed under slip-flow conditions (or even during the late transitional-flow regime). It is also presented that the formation of an hydrodynamic shielding has an effect on the Knudsen number calculation and that a classical approach shall be disregarded in favour of a formulation that accounts for viscosity effects and where the reference frame is attached to the meteoroid's surface.

4. Infrasound is a way to detect the entry of large meteoroids in the Earth's atmosphere, or detecting large blasts associated with their disruptions. Coupled with other techniques it enhances the monitoring and detection of meteors and performs as a reliable tool to validate meteor flow regimes. The use of infrasound

data is indeed essential to detect the existence of the shock wave, which is of valuable interest to derive the meteoroid mass or the energy released. Given that the shock wave is a consequence of the energy deposited by the meteoroid, further association with the meteoroid flow regimes can reveal other relevant clues on the meteoroid flight parameters that are required to deposit this energy. However, the infrasound technique still requires more development and improvement to provide alone sufficient insight into these parameters.

5. The analysis of the flow regimes in larger bodies that experience intense fragmentation is not straight-forward. Disrupted fragments could change their velocity, shape and trajectory, thus changing the flight flow regime conditions. Whether the pre-fragmentation shock wave will remain, or the formation of separated shock waves will interact somehow between them do still require more study. Possible future expansions of the work carried out in Chapter 4 could envision the analysis of the flow regimes for centimeter-sized meteorite-droppers that show well-understood fragmentation patterns. Chapter 4 also focuses on meteoroids in the centimeter size that release most of their energy at high altitudes, mainly in the MLT region, where the flow regimes are less understood. However, meter-sized bodies are capable of reaching lower altitudes at hypersonic velocities where they deposit most of their energy. Moreover, these bodies yield high energy levels through an intense airburst. If disintegrated in the airburst, the high kinetic momentum propagates the released energy downwards to the surface where their destructive power is higher than crater-forming events. The study carried out in this work can set the basis for a new scope of approaches to deal with the yet remaining open questions in this regard.

6. Another valuable outcome of this thesis is that the mathematical formulation used allows to make predictions concerning the terminal heights of large bolides. For meteoroids with diameters in the centimeter to meter size it is possible to accurately determine their terminal height (the last point of their luminous trajectory). This height is important, as it determines the ability of a meteoroid to penetrate to deeper altitudes, outlines its rate of energy deposition, and can constrain the critical kinetic energy to produce luminosity. Here, the implementation of a recently developed mathematical formulation results in the accurate derivation of the terminal heights of centimeter-sized fireballs (Chapter 5), and tens-of-centimeters to one-meter sized (in diameter) meteorite-droppers (Chapter 6). The results obtained for meteorite-droppers demonstrates that the current formulation can be applied to accurately calculate the terminal heights even if the meteoroid experiences fragmentation. Furthermore, this thesis acknowledges that the terminal heights can be obtained if only a reduced set of points is observed at the beginning of the meteoroid atmospheric flight. Hence, the knowledge of the accurate terminal height is also interesting to refine data derived from observations, and to complete missing trajectory information.

7. The renewed PE criterion outlined in Chapter 5 could help to assess the level of hazard associated with a meter-sized meteoroid. As seen in Chapter 5, this criterion can be constrained in most cases to a dependency on α and β parameters.

Previous studies on this subject showed that a meteoroid classification considering the combined values of α and β parameters can describe the type of event in hand. Here, a deeper exploration of the combination of α and β yields a broader and more general formulation of the PE criterion (commonly used to set such a classification). While previously the PE criterion was envisioned to provide an empirical classification of fireballs that experienced little fragmentation, the renewed PE criterion could be implemented to meteorite-droppers. Future work will be set on analysing how this renewed formulation of the PE criterion could contribute to enhance meteoroid impact hazard scales and planetary defense assessment.

8. Finally, the technological update of observational instrumentation is based on the prospective research focus. The results obtained in Chapters 3, 4, and 5 are valuable information to the planetary science community which may request new devices' designs for their observations. In terms of impact hazard simulation tools, current hydrocodes have been determinant to gain insight into the impact phenomenology and the meteoroid energy release at different altitudes. These hydrocodes focus, however, on a specific item of the impact. Currently there is no simulator able to outline the complete impact scenario and it is expected that the outcome of this thesis will become valuable input for improving such simulators. It is also worth mention that the mathematical approach used in this thesis can be implemented under different atmospheric density profiles, hence, it can be potentially applied to study impact hazard in other planets under future exploration, like e.g. Mars.

APPENDIX

A

LIST OF SYMBOLS

Symbol	Definition
a	Constant.
A	Shape factor of meteoroid.
A_e	Pre-entry shape factor of meteoroid.
A_0	Simplification function used for the terminal height calculation.
A_1	Simplification function used for the terminal height calculation.
b	Constant.
c	Constant.
c_d	Drag coefficient.
c_h	Heat-transfer coefficient.
c_p	Specific heat coefficient at constant pressure.
c_s	Local speed of sound.
c_v	Specific heat coefficient at constant volume.
d	Meteoroid diameter.
D	Distance between two meteor trajectory points.
D_J	Dissimilarity criterion of Jenniskens (2008).
D_{SH}	Dissimilarity criterion of Southworth & Hawkins (1963).
E	Energy.
E_k	Kinetic energy.
g	Earth gravity constant.
h	Height.
h_e	Observed entry height of the meteor.
h_r	Radiant altitude of the meteor.
h_t	Observed terminal height of the meteor.
h_I	First approximation of the calculated terminal height of the meteor.
h_{II}	Second approximation of the calculated terminal height of the meteor.
h_{III}	Third approximation of the calculated terminal height of the meteor.
h_{IV}	Fourth approximation of the calculated terminal height of the meteor.
h_0	Scale height.
H^*	Effective destruction enthalpy.
I	Radiation efficiency.

Continued on next page

Symbol	Definition
k	Boltzmann constant.
-	also, a constant used to adjust trajectory information to an exponential curve.
K	Shape-density parameter.
Kn	Knudsen number.
Kn_r	Knudsen number referred to the meteoroid surface.
l	Mean free path of the gas molecules.
l_v	Mean free path within the hydrodynamic shielding.
L	Small distance increments along the meteor atmospheric trajectory.
-	also, the characteristic length scale of the body immersed in the gas.
m	Dimensionless meteoroid mass.
m_a	Mass of a meteor atom.
M	Meteoroid mass.
-	also, molar mass of the gas.
M_e	Pre-entry meteoroid mass.
M_{infra}	Mass derived from infrasound information.
M_v	Absolute visual magnitude.
Ma	Mach number.
n_t	Measurement inaccuracies at a time (t) in a stochastic process.
Q	Angle between the two planes that contain the meteor trajectory and the observing station.
r	Radius of the meteoroid.
-	also, meteor population index.
R	Universal constant of the gases.
Re	Reynolds number.
R_0	Blast (or characteristic) radius.
s	Dimensionless middle section area of meteoroid.
s_e	Dimensionless pre-entry middle section area of meteoroid.
S	Middle section area of meteoroid.
S_e	Pre-entry middle section area of meteoroid.
t	Time.
-	also, characteristic flow time.
T	Temperature in the shock layer.
T_w	Temperature of the meteoroid surface.
T_V	Temperature in the vapour cloud in front of the meteoroid.
T_0	Temperature of the ambient air.
v	Dimensionless meteoroid velocity.

Continued on next page

Symbol	Definition
-	also, the velocity of a fluid.
v_t	Dimensionless meteoroid velocity at the terminal height.
-	also, inherent noise at a time (t) in a stochastic process.
V	Meteoroid velocity.
V_e	Pre-entry meteoroid velocity.
V_e^*	Average velocity of the vaporized molecules.
V_g	Geocentric velocity of the meteoroid.
V_h	Heliocentric velocity of the meteoroid.
V_t	Meteoroid velocity at the terminal height.
x_t	State vector at a given time (t) in a stochastic process.
u_t	Previous state of the system at a time (t) in a stochastic process.
y	Dimensionless meteoroid height.
y_t	The observed state vector at a given time (t) in a stochastic process.
Z_R	Zenith distance of the meteor radiant.

Greek Symbols

α	Ballistic coefficient
$\alpha^{'}$	Number of electrons that are created per unit of distance of the meteor path.
α_g	Right ascension of the meteor radiant.
δ	Thickness of the boundary layer.
δ_g	Declination of the meteor radiant.
β	Mass loss parameter.
$\beta^{'}$	Ionization coefficient.
γ	Slope between horizon and the meteor trajectory.
-	also, the specific heat ratio.
κ	Shape factor.
μ	Shape-change coefficient.
-	also, dynamic viscosity coefficient.
ν	Intermolecular collision rate.
ρ	Gas density.
ρ_0	Gas density at sea level.
ρ_m	Meteoroid bulk density.
ρ_t	Gas density at the terminal height.
σ	Ablation coefficient.
-	also, the Stefan-Boltzmann constant.
τ	Characteristic time in a fluid.

Continued on next page

Symbol	Definition
-	also, the luminous efficiency factor.

Orbital Elements

a	Semimajor axis.
e	Eccentricity.
i	Inclination.
Ω	Longitude of the ascending node.
ω	Argument of periapsis.
M	Mean anomaly at the epoch.
T	Tisserand parameter.
ν_6	Secular resonance with Saturn.
λ_0	Solar longitude.

B

GLOSSARY OF TERMS

Ablation: is a mass-loss process that bodies entering the atmosphere experience due to the increasing air density.

Airburst: is a detonation in the air that yields an explosive load comparable to or greater than a weapon of war.

Asteroid: is a small and often irregularly shaped celestial body. An asteroid shall be larger than a meteoroid, it must not behave as a comet, and must not comply with the definitions of planets and dwarf planets coined in the IAU 2006 General Assembly.

Asteroid Absolute Magnitude, H: is the visual magnitude that an observer would record if the asteroid is placed 1 AU away, 1 AU from the Sun, and at a zero-phase angle.

Astronomical Units: is the average distance between the Earth and the Sun, which is 149,597,870,700 m ($\sim$150 million kilometers).

Background Hazard: is a normalization of the potential risk of an object over all the registered associated risks of other potentially hazardous objects detected before the impact of the studied object.

Bolide: is a meteor whose brightness magnitude reaches or overcomes that of Venus (-4). It can also be referred as fireballs.

Boundary Layer: is the fluid layer in the vicinity of a body's surface where the viscosity effects are significant.

Carbonaceous Chondrite: is a type of stony chondritic (this is, that contains chondrules) meteorite that is usually characterized by particularly high abundances in carbon and water. Some of the most primitive recovered meteorites are of this type. Carbonaceous chondrites are divided into 8 groups: CB, CH, CI, CK, CM, CO, CR and CV.

Centaurs: are small bodies orbiting the Sun between Jupiter and Neptune. These objects can cross the orbits of the giant planets.

Comet: is a body made of rock, organic compounds and ice, being typically kilometer-sized and orbiting the Sun.

Crater: is the resulting hole on an icy or solid terrain caused by a meteorite impact.

Dark Flight: is the last leg of the meteoroid atmospheric flight. It occurs when the ablation is over, and there is no related emission of light.

Filament: is the cometary material that was detached from its parent comet so long ago that gravitational and non-gravitational effects have effectively distributed it along the orbit, or an evolved one, of the parent comet.

Fireball: is a meteor whose brightness magnitude reaches or overcomes that of Venus (-4). It can also be referred as bolide.

Fireball Network: is a group of stations that are arranged under the same acquisition and reduction software and procedures, and are usually ruled by the same organization. They often comply with the same institutional requirements.

Flow Regime: is a classification used in fluid dynamics to outline the state of a fluid and the physical and mathematical approach to be implemented related studies in that state.

Halley Type Comet, HTC: is a comet with an orbital period smaller than 250 years, usually between 20 and 200 years. These comets are thought to be originated in the Oort Cloud and are controlled by the gravitational influence of Jupiter.

Hydrodynamic shielding: is a local increase of the air density in the front face of a meteoroid that impacts the Earth at hypersonic velocities. The incoming air flux that a meteoroid encounters either removes or ionize the meteoroid surface particles at a high rate, and so these particles have not enough time to move away from the surface, thus increasing the local density and hindering further high-energy impacts of air molecules.

International Astronomical Union, IAU: is a scientific entity born in 1919 devoted to promoting and safeguarding the science of astronomy in all its aspects through international cooperation.

Infrasound: is a low-frequency (< 20 Hz) sound lying below the human hearing range and above the natural oscillation frequency of the atmosphere.

Interplanetary Dust or Zodiacal Dust: is finely divided solid matter, with particle sizes in general smaller than meteoroids, moving in, or coming from, interplanetary space.

Jupiter Family Comet, JFC: is a short period comet controlled by the gravitational influence of Jupiter. These comets are originated in the Kuiper Belt.

Kirkwood gap: is a regions within the mean asteroid belt where the density of asteroid is lower, probably depleted by the effect of gravitational resonances.

Knudsen Number, Kn: is a fluid dynamics dimensionless number that compares the molecular mean free path of the fluid to a characteristic size. When there is an object immersed in the gas the characteristic size corresponds to one size of the object.

Kuiper Belt: is a disk-like region between 30 and 55 UA (beyond Neptune) that consists of small icy bodies.

Long Period Comet: is a comet with an orbital period greater than 200 years. These comets are thought to be originated in the Oort Cloud.

Mach Number, Ma**:** is a fluid dynamics dimensionless parameter that compares the velocity of an object immersed in a fluid to the local sound speed in the fluid.

Mean Asteroid Belt, MAB: is one region of the Solar System where the density of asteroids orbiting the Sun is larger. It is located between 2 and 4 AU, this is, between Mars and Jupiter.

Mean Motion Resonance: is an orbital resonance where the ratio of the orbital periods of two bodies is a small integer.

Meteor: is the bright phenomenon associated with the atmospheric passage of a meteoroid through the Earth atmosphere.

Meteor Shower: is the sudden increase of meteor events occurring during a period of time and apparently radiating from the same point in the sky.

Meteor Shower Outburst: is defined as a notable increase in the annual meteor shower activity.

Meteorite: is a meteoroid that survived the atmospheric passage and reaches the Earth's surface.

Meteorite-dropper: refers to those superbolides that may be followed by a meteorite fall.

Meteoroid: is a solid natural object of a size roughly between 30 micrometers and 1 meter moving in, or coming from, interplanetary space.

Micrometeorite: is that interplanetary dust that may survive to atmospheric deceleration with partial or no surface melting at all and can be deposited on the Earth's surface.

Near Earth Asteroid, NEA: refer to those NEOs which are asteroids.

Near Earth Comet, NEC: refer to those NEOs which are comets.

Near Earth Object, NEO: are comets and asteroids that orbit in the near-Earth environment, this is with perihelion distances below 1.3 AU.

Oort Cloud: is a theoretical spherical distribution of mainly icy debris that is located in the edge of the solar system. Between $5,000$ and $100,000$ AU. The bodies within this cloud are, in average, as separated one to another as the Earth is to Jupiter.

Orbital Resonance: is the mutual periodical gravitational influence of two or more celestial bodies.

Ordinary Chondrites: is the major (therefore the classification of ordinary) class of chondritic meteorites that are characterized by a high abundance of chondrules. Ordinary chondrites are divided into three different groups: H, L and LL.

Plume: is a hot gas jet able to reach back to higher atmospheric altitudes from where the energetic event took place.

Population Index, r: is a factor that indicates how many times bigger is the meteor population of a magnitude regarding the population with a lower magnitude.

Potential Hazardous Asteroid, PHA: refers to those PHOs which are asteroids.

Potential Hazardous Object, PHO: are those NEOs that can approach hazardously to Earth and thus become a potential threat. Their minimum orbit intersection distance (MOID) shall be of 0.05 AU or less and show an absolute magnitude (H) of 22.0 or less.

Reynold Number, Re: is a fluid dynamics dimensionless parameter that compares the convective forces to the viscous forces in a fluid.

Rubble Pile: a celestial body (generally an asteroid) that consists of several large rocky chunks linked gravitationally.

Secular Resonance: is the orbital resonance where the precession of two bodies is synchronized.

Shock layer: is the gas region between the shock wave and the meteoroid surface.

Shock wave: is a singularity created in the atmosphere by supersonic or hypersonic flying objects. As the object moves through the atmosphere, the air molecules have no time to adapt to the incoming object. The result is a discontinuity region that creates a jump in the air pressure, temperature and density values at both sides of the discon-

tinuity.

Short Period Comet: is a comet with an orbital period smaller than 200 years. These comets are thought to be originated in the Kuiper Belt.

Stream: is a group of meteoroids with similar orbits and common origin.

Superbolide: is a very bright fireballs which is generally able to get to much lower altitudes and can emit a continuous very bright light, at mid-way between the luminosity of the Moon and the Sun (absolute magnitude -16 or brighter).

Swarm: is a group of meteoroids resulting from the breakup of a larger particle.

Tektite: is a gravel-sized natural glass formed on the ground due to the local high temperatures reached due to a meteorite impact or a low-atmospheric airburst.

Tisserand Parameter: is a value calculated from the comparison of the orbital semi-major axis, eccentricity and inclination of a large perturbing celestial body (i.e., a planet) and a smaller body. It is generally used to state close encounters with solar planets.

Trailet: is a group dust trails that remain undistorted over long orbital times.

Trans-Neptunian Object, TNO: are those celestial bodies that orbit the Sun beyond the orbit of Neptune.

Visible Magnitude, M_V: is the measure of the brightness of an object in the visible range (between 390 and 700 nanometers) as it was observed from a distance of 10 parsecs (32.6 light-years) with interstellar particle's light extinction.

Yarkovsky Effect: is the thermal unbalance that occurs between two faces of a celestial rotating body. The Sun radiation absorbed in one face of the body is then slowly emitted at a different time rate by each face due to the differential Sun incidence on the different meteoroid faces (the body's self-thermal radiation shall be also considered here). This effect causes long-term orbit variations to meteoroids and small asteroids (between 10 cm to 10 km in diameter).

Yarkovsky - O'Keefe - Radzievskii – Paddack, YORP: is a derived effect of the Yarkovskt effect. The radiation (either self-thermal radiation or sun radiation) emitted by each face of the celestial body might differ in terms of magnitude and direction, thus creating a slight torque. Among other consequences, in the very long-term such torques could speed up the body cause fragmentation, and also change the rotation pole of the body.

Zenith Hourly Rate, ZHR: is the number of meteors that would be observed under good observing conditions in one hour if the radiant was at the zenith.

C

PUBLICATIONS

The publications which have resulted from the work carried out in this thesis are the following:

- Moreno-Ibáñez, M., Silber, E. A., Gritsevich, M., Trigo-Rodríguez, J. M., 2018, Verification of the flow regimes based on high fidelity observations of bright meteors, *The Astrophysical Journal*, Vol. 863, Issue 2, p. 174.
- Moreno-Ibáñez, M., Trigo-Rodríguez, J. M., Madiedo, J. M., Vaubaillon, J., Williams, I. P., Gritsevich, M., Morillas, L. G., Blanch, E.; Pujols, P., Colas, F., Dupouy, P., 2017, Multi-instrumental observations of the 2014 Ursid meteor outburst, *Monthly Notices of the Royal Astronomical Society*, Vol. 468, Issue 2, p. 2206-2213.
- Moreno-Ibáñez, M., Gritsevich, M., Trigo-Rodríguez, J. M., 2017, Measuring the Terminal Heights of Bolides to Understand the Atmospheric Flight of Large Asteroidal Fragments, *Assessment and Mitigation of Asteroid Impact Hazards, Astrophysics and Space Science Proceedings*, Vol. 46. ISBN 978-3-319-46178-6. Springer International Publishing Switzerland, 2017, p. 129.
- Trigo-Rodriguez, J. M., Lyytinen, E., Gritsevich, M., Moreno-Ibáñez, M., Bottke, W. F., Williams, I., Lupovka, V., Dmitriev, V., Kohout, T., Grokhovsky, V., 2015, Orbit and dynamic origin of the recently recovered Annama's H5 chondrite, *Monthly Notices of the Royal Astronomical Society*, Vol. 449, Issue 2, p. 2119-2127.
- Moreno-Ibáñez, M., Gritsevich, M., Trigo-Rodriguez, J. M., 2015, New methodology to determine the terminal height of a fireball, *Icarus*, Vol. 250, p. 544-552.

BIBLIOGRAPHY

Abedin, A., Wiegert, P., Janches, D., et al. 2018, Icarus, 300, 360

Anders, E., & Grevesse, N. 1989, Geochimica et Cosmochimica Acta, 53, 197

Asher, D. J. 2000, in Proceedings of the International Meteor Conference, 18th IMC, Frasso Sabino, Italy, 1999, ed. R. Arlt, 5–21

Asher, D. J., Bailey, M. E., & Emel'Yanenko, V. V. 1999, Monthly Notices of the Royal Astronomical Society, 304, L53

Babadzhanov, P. B. 1990, in Asteroids, Comets, Meteors III, ed. C. I. Lagerkvist, H. Rickman, & B. A. Lindblad, 497

Babadzhanov, P. B. 1991, in LPI Contributions, Vol. 765, Asteroids, Comets, Meteors 1991, 7

Babadzhanov, P. B., & Kokhirova, G. I. 2009, Astronomy & Astrophysics, 495, 353

Babadzhanov, P. B., & Obrubov, Y. V. 1989, Highlights of Astronomy, 8, 287

Baggaley, W. J. 2002, in Meteors in the Earth's Atmosphere, ed. E. Murad & I. P. Williams (Cambridge, UK: Cambridge University Press), 123

Bailey, M. E., & Emel'Yanenko, V. V. 1996, Monthly Notices of the Royal Astronomical Society, 278, 1087

Becvár, A. 1946, International Astronomical Union Circular, 1026

Beitz, E., Blum, J., Parisi, M. G., & Trigo-Rodriguez, J. 2016, The Astrophysical Journal, 824, 12

Ben-Menahem, A. 1975, Physics of the Earth and Planetary Interiors, 11, 1

Berezhnoy, A. A., & Borovička, J. 2010, Icarus, 210, 150

Betlem, H., Jenniskens, P., van't Leven, J., et al. 1999, Meteoritics & Planetary Science, 34, 979

Bevan, A. W. R., & Binns, R. A. 1989, Meteoritics, 24, 127

Binzel, R. P. 2000, Planetary and Space Science, 48, 297

Binzel, R. P., Rivkin, A. S., Stuart, J. S., et al. 2004, Icarus, 170, 259

Bischoff, A., & Geiger, T. 1995, Meteoritics, 30, 113

Bischoff, A., Jersek, M., Grau, T., et al. 2011, Meteoritics & Planetary Science, 46, 793

Blanch, E., Trigo-Rodríguez, J. M., Madiedo, J. M., et al. 2017, in Assessment and Mitigation of Asteroid Impact Hazards: Proceedings of the 2015 Barcelona Asteroid Day, ed. J. M. Trigo-Rodríguez, M. Gritsevich, & H. Palme, Vol. 46 (Springer International Publishing Switzerland), 185

Bland, P. A. 2004, Astronomy and Geophysics, 45, 5.20

Bland, P. A., & Artemieva, N. A. 2003, Nature, 424, 288

Bland, P. A., Zolensky, M. E., Benedix, G. K., & Sephton, M. A. 2006, in Meteorites and the Early Solar System II, ed. D. S. Lauretta & H. Y. McSween (University of Arizona Press, Tucson), 853–867

Bland, P. A., Spurný, P., Greenwood, R. C., et al. 2009, Meteoritics & Planetary Science Supplement, 72, 5292

Bland, P. A., Towner, M. C., Sansom, E. K., et al. 2016, in LPI Contributions, Vol. 1921, 79th Annual Meeting of the Meteoritical Society, 6265

Blum, J., Schräpler, R., Davidsson, B. J. R., & Trigo-Rodríguez, J. M. 2006, The Astrophysical Journal, 652, 1768

Borovicka, J. 1993, Astronomy & Astrophysics, 279, 627

—. 1994, Planetary and Space Science, 42, 145

Borovicka, J., & Kalenda, P. 2003, Meteoritics & Planetary Science, 38, 1023

Borovicka, J., Spurný, P., Kalenda, P., & Tagliaferri, E. 2003, Meteoritics & Planetary Science, 38, 975

Borovicka, J., Spurny, P., & Keclikova, J. 1995, Astronomy & Astrophysics Supplement, 112, 173

Borovička, J., & Spurný, P. 2008, Academy of Sciences, Fričova 298, 25165 Ondřejov Observatory, Czech Republic) Publication: Astronomy & Astrophysics, 485, L1

Borovička, J., Spurný, P., & Brown, P. 2015a, in Asteroids IV, ed. P. Michel, F. E. DeMeo, & W. F. Bottke (University of Arizona Press, Tucson), 257–280

Borovička, J., Spurný, P., Brown, P., et al. 2013a, Nature, 503, 235

Borovička, J., Spurný, P., & Koten, P. 2007, Astronomy & Astrophysics, 473, 661

Borovička, J., Tóth, J., Igaz, A., et al. 2013b, Meteoritics & Planetary Science, 48, 1757

Borovička, J., Spurný, P., Šegon, D., et al. 2015b, Meteoritics & Planetary Science, 50, 1244

Boslough, M., Brown, P., & Harris, A. 2015, in 2015 IEEE Aerospace Conference, 1–12

Boslough, M., & Crawford, D. A. 2008, International Journal of Impact Engineering, 35, 1441

Bottke, W. F., Jedicke, R., Morbidelli, A., Petit, J.-M., & Gladman, B. 2000, Science, 288, 2190

Bottke, W. F., Morbidelli, A., Jedicke, R., et al. 2002, Icarus, 156, 399

Bottke, Jr., W. F., Vokrouhlický, D., Rubincam, D. P., & Nesvorný, D. 2006, Annual Review of Earth and Planetary Sciences, 34, 157

Bouquet, A., Baratoux, D., Vaubaillon, J., et al. 2014, Planetary and Space Science, 103, 238

Boyd, I. D. 2000, Earth Moon and Planets, 82, 93

Brearley, A. J., & Jones, R. H. 1998, in Planetary Materials, vol. 36: Reviews in Mineralogy, ed. J. J. Papike (Mineralogical Society of America), 3–001–3–398

Britt, D. T., & Consolmagno, G. J. 2003, Meteoritics & Planetary Science, 38, 1161

Britt, D. T., Yeomans, D., Housen, K., & Consolmagno, G. 2002, in Asteroids III, ed. W. F. Bottke, Jr., A. Cellino, P. Paolicchi, & R. P. Binzel (University of Arizona Press, Tucson), 485–500

Bronshten, V. A. 1965, Problems of motion of large meteoritic bodies in the atmosphere, Memorandum RM-4257-PR (Santa Monica, California: The Rand Corporation), translation

—. 1983, Physics of meteoritic phenomena (Dordrecht: Reidel), translation

Brož, M., Vokrouhlický, D., Morbidelli, A., Nesvorný, D., & Bottke, W. F. 2011, Monthly Notices of the Royal Astronomical Society, 414, 2716

Brown, P., Ceplecha, Z., Hawkes, R. L., et al. 1994, Nature, 367, 624

Brown, P., Marchenko, V., Moser, D. E., Weryk, R., & Cooke, W. 2013a, Meteoritics & Planetary Science, 48, 270

Brown, P., Pack, D., Edwards, W. N., et al. 2004, Meteoritics & Planetary Science, 39, 1781

Brown, P., ReVelle, D. O., Silber, E. A., et al. 2008, Journal of Geophysical Research (Planets), 113, E09007

Brown, P., Spalding, R. E., ReVelle, D. O., Tagliaferri, E., & Worden, S. P. 2002a, Nature, 420, 294

Brown, P., Vaubaillon, J., Jenniskens, P., & Yrjola, I. 2015, Central Bureau Electronic Telegrams, 4041

Brown, P., McCausland, P. J. A., Fries, M., et al. 2011, Meteoritics & Planetary Science, 46, 339

Brown, P. G., Edwards, W. N., Revelle, D. O., & Spurny, P. 2007, Journal of Atmospheric and Solar-Terrestrial Physics, 69, 600

Brown, P. G., Revelle, D. O., Tagliaferri, E., & Hildebrand, A. R. 2002b, Meteoritics & Planetary Science, 37, 661

Brown, P. G., Assink, J. D., Astiz, L., et al. 2013b, Nature, 503, 238

Campbell-Brown, M. D., & Koschny, D. 2004, Astronomy & Astrophysics, 418, 751

Campins, H., & Swindle, T. D. 1998, Meteoritics & Planetary Science, 33, 1201

Capozzi, D. 2018, Master's thesis, International University of Valencia, in Spanish

Cassidy, W., Harvey, R., Schutt, J., Delisle, G., & Yanai, K. 1992, Meteoritics, 27, 490

Ceplecha, Z. 1951, Bulletin of the Astronomical Institutes of Czechoslovakia, 2, 156

—. 1957, Bulletin of the Astronomical Institutes of Czechoslovakia, 8, 51

—. 1961, Bulletin of the Astronomical Institutes of Czechoslovakia, 12, 21

—. 1967, Smithsonian Contributions to Astrophysics, 11, 35

—. 1968, SAO Special Report, 279

—. 1987, Bulletin of the Astronomical Institutes of Czechoslovakia, 38, 222

—. 1988, Bulletin of the Astronomical Institutes of Czechoslovakia, 39, 221

Ceplecha, Z., Borovička, J., Elford, W. G., et al. 1998, Space Science Reviews, 84, 327

Ceplecha, Z., & McCrosky, R. E. 1976, Journal of Geophysical Research, 81, 6257

Ceplecha, Z., & Revelle, D. O. 2005, Meteoritics & Planetary Science, 40, 35

Chambers, J. E. 1999, Monthly Notices of the Royal Astronomical Society, 304, 793

Chapman, C. R., Morrison, D., & Zellner, B. 1975, Icarus, 25, 104

Chen, J., Elmi, C., Goldsby, D., & Gieré, R. 2017, Geophysical Research Letters, 44, 8757

Chesley, S. R., Chodas, P. W., Milani, A., Valsecchi, G. B., & Yeomans, D. K. 2002, Icarus, 159, 423

Chyba, C. F., Thomas, P. J., & Zahnle, K. J. 1993, Nature, 361, 40

Colas, F., Zanda, B., Bouley, S., et al. 2014, in Proceedings of the International Meteor Conference, Giron, France, 18-21 September 2014, ed. J.-L. Rault & P. Roggemans, 34–38

Consolmagno, G. J., & Britt, D. T. 1998, Meteoritics & Planetary Science, 33, 1231

D'Abramo, G., Harris, A. W., Boattini, A., et al. 2001, Icarus, 153, 214

de la Fuente Marcos, C., & de la Fuente Marcos. 2018, Research Notes of the American Astronomical Society, 2, 131

de la Fuente Marcos, C., de la Fuente Marcos, R., & Mialle, P. 2016, Astrophysics and Space Science, 361, 358

de León, J., Campins, H., Tsiganis, K., Morbidelli, A., & Licandro, J. 2010, Astronomy & Astrophysics, 513, A26

Delbo', M., Walsh, K., Bolin, B., Avdellidou, C., & Morbidelli, A. 2017, Science, 357, 1026

Delbo, M., Libourel, G., Wilkerson, J., et al. 2014, Nature, 508, 233

DeMeo, F. E., Binzel, R. P., Slivan, S. M., & Bus, S. J. 2009, Icarus, 202, 160

Denning, W. F. 1912, The Observatory, 35, 90

Devillepoix, H. A. R., Sansom, E. K., Bland, P. A., et al. 2018, Meteoritics & Planetary Science, arXiv:1803.02557

Dmitriev, V., Lupovka, V., & Gritsevich, M. 2015, Planetary and Space Science, 117, 223

Dyl, K. A., Benedix, G. K., Bland, P. A., et al. 2016, Meteoritics & Planetary Science, 51, 596

Egal, A., Gural, P. S., Vaubaillon, J., Colas, F., & Thuillot, W. 2017, Icarus, 294, 43

Engrand, C., & Maurette, M. 1998, Meteoritics & Planetary Science, 33, 565

Flynn, G. J., Moore, L. B., & Klöck, W. 1999, Icarus, 142, 97

Froeschle, C., & Scholl, H. 1986, Astronomy & Astrophysics, 166, 326

Gaffey, M. J., Bell, J. F., Brown, R. H., et al. 1993, Icarus, 106, 573

Gajdoš, Š., Tóth, J., & Kornoš, L. 2015, in International Meteor Conference Mistelbach, Austria, ed. J.-L. Rault & P. Roggemans, 133–135

Gounelle, M., Spurný, P., & Bland, P. A. 2006, Meteoritics & Planetary Science, 41, 135

Grady, M. M. 2000, Catalogue of Meteorites (Cambridge, UK: Cambridge University Press), 696

Granvik, M., Morbidelli, A., Jedicke, R., et al. 2016, Nature, 530, 303

Greely, A. W. 1915, Science, 41, 360

Grewal, M., & Andrews, A. P. 1993, Kalman filtering: Theory and practice (Upper Saddle River, NJ: Pearson Prentice Hall)

Gritsevich, M., & Koschny, D. 2011, Icarus, 212, 877

Gritsevich, M., Lyytinen, E., Hankey, M., et al. 2017, in LPI Contributions, Vol. 1987, 80th Annual Meeting of the Meteoritical Society, 6188

Gritsevich, M., Lyytinen, E., Moilanen, J., et al. 2014, in Proceedings of the International Meteor Conference, Giron, France, 18-21 September 2014, ed. J.-L. Rault & P. Roggemans, 162–169

Gritsevich, M. I. 2007, Solar System Research, 41, 509

—. 2008a, Doklady Physics, 53, 588

—. 2008b, Moscow University Mechanics Bulletin, 63, 1

—. 2008c, Solar System Research, 42, 372

—. 2008d, Doklady Physics, 53, 97

—. 2009, Advances in Space Research, 44, 323

—. 2010, Moscow University Mechanics Bulletin, 65, 94

Gritsevich, M. I., Lukashenko, V. T., & Turchak, L. I. 2016, Mathematical Models and Computer Simulations, 27

Gritsevich, M. I., & Popelenskaya, N. V. 2008, Doklady Physics, 53, 88

Gritsevich, M. I., & Stulov, V. P. 2006, Solar System Research, 40, 477

—. 2007, Physics - Doklady, 52, 219

—. 2008, Solar System Research, 42, 118

Gritsevich, M. I., Stulov, V. P., & Turchak, L. I. 2012, Cosmic Research, 50, 56

Gural, P. S. 2012, Meteoritics & Planetary Science, doi:10.1111/j.1945-5100.2012.01402.x

Haack, H., Michelsen, R., Stober, G., et al. 2011, in LPI Contributions, Vol. 1639, Workshop on Formation of the First Solids in the Solar System, 9100

Halliday, I. 1987, Icarus, 69, 550

—. 1988, Icarus, 76, 279

Halliday, I., Blackwell, A. T., & Griffin, A. A. 1977, Meteoritics, 12, 248

—. 1978, Journal of the Royal Astronomical Society of Canada, 72, 15

—. 1989a, Journal of the Royal Astronomical Society of Canada, 83, 49

—. 1989b, Meteoritics, 24, 65

Halliday, I., Griffin, A. A., & Blackwell, A. T. 1981, Meteoritics, 16, 153

—. 1996, Meteoritics & Planetary Science, 31, 185

Hasegawa, I. 1990, Astronomical Society of Japan, 42, 175

Hedin, A. E. 1991, Journal of Geophysical Research, 96, 1159

Hildebrand, A. R., McCausland, P. J. A., Brown, P. G., et al. 2006, Meteoritics & Planetary Science, 41, 407

Hillestad, T. E. 1987, WGN, Journal of the International Meteor Organization, 15, 59

Hoffmeister, C. 1948, Meteorstrome (Verlag Johann Ambrosious Barth, Leipzig)

Hoppe, J. 1937, Astronomische Nachrichten, 262, 169

Howie, R. M., Paxman, J., Bland, P. A., et al. 2017, Experimental Astronomy, 43, 237

Hughes, D. W. 1994, Contemporary Physics, 35, 75

Huss, G. R., Rubin, A. E., & Grossman, J. N. 2006, in Meteorites and the Early Solar System II, ed. D. S. Lauretta & H. Y. McSween (University of Arizona Press, Tucson), 567–586

Imoto, S., & Hasegawa, I. 1958, Smithsonian Contributions to Astrophysics, 2, 131

Jacchia, L., Verniani, F., & Briggs, R. E. 1967, Smithsonian Contributions to Astrophysics, 10, 1

Jacchia, L. G., & Whipple, F. L. 1956, Vistas in Astronomy, 2, 982

Jenniskens, P. 1994, Astronomy & Astrophysics, 287, 990

—. 1995, Astronomy & Astrophysics, 295, 206

—. 1998, Earth, Planets, and Space, 50, 555

—. 2004a, The Astronomical Journal, 127, 3018

—. 2004b, Advances in Space Research, 33, 1444

—. 2006, Meteor Showers and their Parent Comets (Cambridge, UK: Cambridge University Press)

—. 2008, Icarus, 194, 13

Jenniskens, P., Gural, P. S., Dynneson, L., et al. 2011, Icarus, 216, 40

Jenniskens, P., & Lyytinen, E. 2005, The Astronomical Journal, 130, 1286

Jenniskens, P., Lyytinen, E., Nissinen, M., Yrjola, I., & Vaubaillon, J. 2007, WGN, Journal of the International Meteor Organization, 35, 125

Jenniskens, P., & Vaubaillon, J. 2010, The Astronomical Journal, 139, 1822

Jenniskens, P., Lyytinen, E., de Lignie, M. C., et al. 2002, Icarus, 159, 197

Jenniskens, P., de Kleer, K., Vaubaillon, J., et al. 2008, Icarus, 196, 171

Jenniskens, P., Shaddad, M. H., Numan, D., et al. 2009, Nature, 458, 485

Jenniskens, P., Fries, M. D., Yin, Q.-Z., et al. 2012, Science, 338, 1583

Jenniskens, P., Rubin, A. E., Yin, Q.-Z., et al. 2014, Meteoritics & Planetary Science, 49, 1388

Jewitt, D. 2008, in Saas-Fee Advanced Course 35: Trans-Neptunian Objects and Comets, ed. D. Jewitt, A. Morbidelli, & H. Rauer (Society for Astrophysics and Astronomy), 132

Jewitt, D. 2012, The Astronomical Journal, 143, 66

Jones, D. C. 2007, PhD thesis, Queen Mary, University of London

Jones, D. C., & Williams, I. P. 2008, Earth Moon and Planets, 102, 35

Jopek, T. J., Valsecchi, G. B., & Froeschle, C. 1999, Monthly Notices of the Royal Astronomical Society, 304, 751

Jopek, T. J., & Williams, I. P. 2013, Monthly Notices of the Royal Astronomical Society, 430, 2377

Josyula, E., & Burt, J. 2011, DTIC Document RTO-EN-AVT-194-01. NATO S&T, 40

Kenkmann, T., Artemieva, N. A., Wünnemann, K., et al. 2009, Meteoritics & Planetary Science, 44, 985

Kero, J., Fujiwara, Y., Abo, M., Szasz, C., & Nakamura, T. 2012, Monthly Notices of the Royal Astronomical Society, 424, 1799

Kingery, A., & Blaauw, R. C. 2017, Planetary and Space Science, 143, 67

Kohout, T., Gritsevich, M., Lyytinen, E., et al. 2015, in LPI Contributions, Vol. 1856, 78th Annual Meeting of the Meteoritical Society, 5209

Kohout, T., Meier, M. M. M., Maden, C., et al. 2016, in LPI Contributions, Vol. 1921, 79th Annual Meeting of the Meteoritical Society, 6316

Kohout, T., Haloda, J., Halodová, P., et al. 2017, Meteoritics & Planetary Science, 52, 1525

Kulakov, A. L., & Stulov, V. P. 1992, Solar System Research, 26, 478

Langbroek, M. 1997, Radiant, Journal of the Dutch Meteor Society, 19, 39

Le Pichon, A., Antier, K., Cansi, Y., et al. 2008, Meteoritics & Planetary Science, 43, 1797

Levin, B. I. 1961, Physikalische Theorie der Meteore und die meteoritische Substanz im Sonnensystem (Berlin, Akademie-Verlag)

Levin, B. J. 1956, Bulletin of the Astronomical Institutes of Czechoslovakia, 7, 58

Lidov, M. L. 1961, Iskusstvennie Sputniki Zemli (Artificial Earth's Satellites), 8, 5, in Russian

—. 1962, Planetary and Space Science, 9, 719

Lindblad, B. A. 1971a, Smithsonian Contributions to Astrophysics, 12, 14

—. 1971b, Smithsonian Contributions to Astrophysics, 12, 1

Llorca, J., Trigo-Rodríguez, J. M., Ortiz, J. L., et al. 2005, Meteoritics & Planetary Science, 40, 795

Lyytinen, E., & Gritsevich, M. 2016, Planetary and Space Science, 120, 35

Lyytinen, E. J., & Van Flandern, T. 2000, Earth Moon and Planets, 82, 149

Macke, R. J., Consolmagno, G. J., & Britt, D. T. 2011, Meteoritics & Planetary Science, 46, 1842

Madiedo, J. M., Espartero, F., Trigo-Rodríguez, J. M., et al. 2016, Icarus, 275, 193

Madiedo, J. M., & Trigo-Rodríguez, J. M. 2008, Earth Moon and Planets, 102, 133

Madiedo, J. M., Trigo-Rodríguez, J. M., Castro-Tirado, A. J., Ortiz, J. L., & Cabrera-Caño, J. 2013a, Monthly Notices of the Royal Astronomical Society, 436, 2818

Madiedo, J. M., Trigo-Rodriguez, J. M., & Lyytinen, E. 2011, in Meteoroids: The Smallest Solar System Bodies, ed. W. J. Cooke, D. E. Moser, B. F. Hardin, & D. Janches, 330

Madiedo, J. M., Trigo-Rodríguez, J. M., Ortiz, J. L., & Morales, N. 2010, Advances in Astronomy, 2010, 167494

Madiedo, J. M., Trigo-Rodríguez, J. M., Williams, I. P., Ortiz, J. L., & Cabrera, J. 2013b, Monthly Notices of the Royal Astronomical Society, 431, 2464

Madiedo, J. M., Trigo-Rodríguez, J. M., Zamorano, J., et al. 2013c, Monthly Notices of the Royal Astronomical Society, 436, 3656

—. 2014, Monthly Notices of the Royal Astronomical Society, 445, 3309

Martínez-Jiménez, M., Moyano-Cambero, C. E., Trigo-Rodríguez, J. M., Alonso-Azcárate, J., & Llorca, J. 2017, in Assessment and Mitigation of Asteroid Impact Hazards: Proceedings of the 2015 Barcelona Asteroid Day, ed. J. M. Trigo-Rodríguez, M. Gritsevich, & H. Palme, Vol. 46 (Springer International Publishing Switzerland), 73

McCrosky, R. E., & Boeschenstein, Jr., H. 1965, SAO Special Report, 173

McCrosky, R. E., & Posen, A. 1968, SAO Special Report, 273

McCrosky, R. E., Posen, A., Schwartz, G., & Shao, C.-Y. 1971, Journal of Geophysical Research, 76, 4090

McCrosky, R. E., Shao, C.-Y., & Posen, A. 1978, Meteoritika, 37, 44

—. 1979, Meteoritika, 38, 106

McNaught, R. H., & Asher, D. J. 1999, WGN, Journal of the International Meteor Organization, 27, 85

McSween, H. Y. J., & Huss, G. R. 2010, Book Review: Cosmochemistry (Cambridge: Cambridge University Press)

Meier, M. M. M., Welten, K. C., Riebe, M. E. I., et al. 2017, Meteoritics & Planetary Science, 52, 1561

Michel, P., Benz, W., Tanga, P., & Richardson, D. C. 2001, Science, 294, 1696

Michel, P., Tanga, P., Benz, W., & Richardson, D. C. 2002, Icarus, 160, 10

Milley, E. P. 2010, Master's thesis, University of Calgary

Molau, S., Kac, J., Crivello, S., et al. 2015, WGN, Journal of the International Meteor Organization, 43, 62

Morbidelli, A., Bottke, Jr., W. F., Froeschlé, C., & Michel, P. 2002, in Asteroids III, ed. W. F. Bottke, Jr., A. Cellino, P. Paolicchi, & R. P. Binzel (University of Arizona Press, Tucson), 409–422

Morbidelli, A., Gonczi, R., Froeschle, C., & Farinella, P. 1994, Astronomy & Astrophysics, 282, 955

Morbidelli, A., & Nesvorný, D. 1999, Icarus, 139, 295

Morbidelli, A., & Vokrouhlický, D. 2003, Icarus, 163, 120

Moreno-Ibáñez, M., Gritsevich, M., & Trigo-Rodríguez, J. M. 2015a, Icarus, 250, 544

Moreno-Ibáñez, M., Gritsevich, M., & Trigo-Rodríguez, J. M. 2016, in International Meteor Conference Egmond, the Netherlands, 2-5 June 2016, ed. A. Roggemans & P. Roggemans, 197–201

Moreno-Ibáñez, M., Gritsevich, M., & Trigo-Rodríguez, J. M. 2017a, in Assessment and Mitigation of Asteroid Impact Hazards: Proceedings of the 2015 Barcelona Asteroid Day, ed. J. M. Trigo-Rodríguez, M. Gritsevich, & H. Palme, Vol. 46 (Springer International Publishing Switzerland), 129

Moreno-Ibáñez, M., Silber, E. A., Gritsevich, M., & Trigo-Rodríguez, J. M. 2018, The Astrophysical Journal, 863, 174

Moreno-Ibáñez, M., Trigo-Rodriguez, J. M., Rodriguez, D., & Sanchez, A. 2015b, in Lunar and Planetary Science Conference, Vol. 46, Lunar and Planetary Science Conference, 1138

Moreno-Ibáñez, M., Trigo-Rodríguez, J. M., Madiedo, J. M., et al. 2017b, Monthly Notices of the Royal Astronomical Society, 468, 2206

Moyano-Cambero, C. E., Trigo-Rodríguez, J. M., Benito, M. I., et al. 2017, Meteoritics & Planetary Science, 52, 1030

Müller, T. G., Marciniak, A., Butkiewicz-Bąk, M., et al. 2017, Astronomy & Astrophysics, 598, A63

Neslusan, L., Svoren, J., & Porubcan, V. 1998, Astronomy & Astrophysics, 331, 411

Neslušan, L., Svoreň, J., & Porubčan, V. 1995, Earth Moon and Planets, 68, 427

Nesvorný, D., & Morbidelli, A. 1998, The Astronomical Journal, 116, 3029

Oberst, J., Molau, S., Heinlein, D., et al. 1998, Meteoritics & Planetary Science, 33, 49

Ohtsuka, K. 1994, Tokyo Meteor Network Rep., No. 14, p. 85 - 87, 14, 85

Ohtsuka, K., Shioi, H., & Hidaka, E. 1995, WGN, Journal of the International Meteor Organization, 23, 69

Ortiz, J. L., Aceituno, F. J., Quesada, J. A., et al. 2006, Icarus, 184, 319

Palme, H., & Zipfel, J. 2017, in Assessment and Mitigation of Asteroid Impact Hazards: Proceedings of the 2015 Barcelona Asteroid Day, ed. J. M. Trigo-Rodríguez, M. Gritsevich, & H. Palme, Vol. 46 (Springer International Publishing Switzerland), 33

Pauls, A., & Gladman, B. 2005, Meteoritics & Planetary Science, 40, 1241

Pecina, P., & Ceplecha, Z. 1983, Bulletin of the Astronomical Institutes of Czechoslovakia, 34, 102

—. 1984, Bulletin of the Astronomical Institutes of Czechoslovakia, 35, 120

Picone, J. M., Hedin, A. E., Drob, D. P., & Aikin, A. C. 2002, Journal of Geophysical Research (Space Physics), 107, 1468

Popelenskaya, N. V. 2010, Moscow University Mechanics Bulletin, 65, 90

Popova, O., Borovička, J., Hartmann, W. K., et al. 2011, Meteoritics & Planetary Science, 46, 1525

Popova, O. P., Sidneva, S. N., Shuvalov, V. V., & Strelkov, A. S. 2000, Earth Moon and Planets, 82, 109

Popova, O. P., Sidneva, S. N., Strelkov, A. S., & Shuvalov, V. V. 2001, in ESA Special Publication, Vol. 495, Meteoroids 2001 Conference, ed. B. Warmbein, 237–245

Popova, O. P., Jenniskens, P., Emel'yanenko, V., et al. 2013, Science, 342, 1069

Porubčan, V., & Kornoš, L. 2002, in ESA Special Publication, Vol. 500, Asteroids, Comets, and Meteors: ACM 2002, ed. B. Warmbein, 177–180

Porubčan, V., Williams, I. P., & Kornoš, L. 2004, Earth Moon and Planets, 95, 697

Pravec, P., Harris, A. W., Kušnirák, P., Galád, A., & Hornoch, K. 2012, Icarus, 221, 365

Probstein, R. F. 1961, Aerospace Research Central Journal, 31, 185

Rabinowitz, D., Helin, E., Lawrence, K., & Pravdo, S. 2000, Nature, 403, 165

Rajchl, J. 1969, Bulletin of the Astronomical Institutes of Czechoslovakia, 20, 363

—. 1972, Bulletin of the Astronomical Institutes of Czechoslovakia, 23, 357

Reid, A. M., Jakes, O., Zolensky, M. E., & Miller, R. M. 1995, Meteoritics, 30, 781

Rendtel, J., Arlt, R., & Beath, A. 1995, Handbook for visual meteor observers (Belgium: International Meteor Organization)

Revelle, D. O. 1974, PhD thesis, University of Michigan

—. 1976, Journal of Geophysical Research, 81, 1217

—. 1979, Journal of Atmospheric and Terrestrial Physics, 41, 453

—. 1980, Journal of Geophysical Research, 85, 1803

ReVelle, D. O. 1993, in Meteoroids and their Parent Bodies, ed. J. Stohl & I. P. Williams, 343

Revelle, D. O. 2002, in ESA Special Publication, Vol. 500, Asteroids, Comets, and Meteors: ACM 2002, ed. B. Warmbein, 127–136

Revelle, D. O., & Rajan, R. S. 1979, Journal of Geophysical Research, 84, 6255

Rickman, H. 2014, Meteoritics & Planetary Science, 49, 8

Rieger, L. A., Bourassa, A. E., & Degenstein, D. A. 2014, Atmospheric Measurement Techniques, 7, 777

Rietmeijer, F. J. M. 2000, Meteoritics & Planetary Science, 35, 1025

Roggemans, P. 1987, Handbook for visual meteor observations (Belgium: International Meteor Organization)

Rubin, A. E., Trigo-Rodríguez, J. M., Huber, H., & Wasson, J. T. 2007, Geochimica et Cosmochimica Acta, 71, 2361

Rudawska, R., Vaubaillon, J., & Atreya, P. 2012, Astronomy & Astrophysics, 541, A2

Sansom, E. K., Bland, P., Paxman, J., & Towner, M. 2015, Meteoritics & Planetary Science, 50, 1423

Sansom, E. K., Bland, P. A., Rutten, M. G., Paxman, J., & Towner, M. C. 2016, The Astronomical Journal, 152, 148

Sansom, E. K., Rutten, M. G., & Bland, P. A. 2017, The Astronomical Journal, 153, 87

Sekanina, Z. 1982, in IAU Colloq. 61: Comet Discoveries, Statistics, and Observational Selection, ed. L. L. Wilkening, 251–287

Sekhar, A., & Asher, D. J. 2013, Monthly Notices of the Royal Astronomical Society, 433, L84

Sekhar, A., Asher, D. J., & Vaubaillon, J. 2016, Monthly Notices of the Royal Astronomical Society, 460, 1417

Silber, E., & Brown, P. G. 2019, in Infrasound and middle-atmospheric monitoring: Challenges and Perspectives, Le Pichon et al. (eds.). (New York: Springer), 9, 202, in press

Silber, E., Niculescu, M., Butka, P., & Silber, R. 2018a, Atmosphere, 9, 202

Silber, E. A., Boslough, M., Hocking, W. K., Gritsevich, M., & Whitaker, R. W. 2018b, Advances in Space Research, 62, 489

Silber, E. A., & Brown, P. G. 2014, Journal of Atmospheric and Solar-Terrestrial Physics, 119, 116

Silber, E. A., Brown, P. G., & Krzeminski, Z. 2015, Journal of Geophysical Research (Planets), 120, 413

Silber, E. A., Hocking, W. K., Niculescu, M. L., Gritsevich, M., & Silber, R. E. 2017, Monthly Notices of the Royal Society, 469, 1869

Silber, E. A., ReVelle, D. O., Brown, P. G., & Edwards, W. N. 2009, Journal of Geophysical Research (Planets), 114, E08006

Simek, M. 1985, Bulletin of the Astronomical Institutes of Czechoslovakia, 36, 270

Smirnov, E. A., & Shevchenko, I. I. 2013, Icarus, 222, 220

Southworth, R. B., & Hawkins, G. S. 1963, Smithsonian Contributions to Astrophysics, 7, 261

Spurny, P., Bland, P. A., Borovicka, J., et al. 2012, in LPI Contributions, Vol. 1667, Asteroids, Comets, Meteors 2012, 6369

Spurný, P., Bland, P. A., Shrbený, L., et al. 2011, Meteoritics & Planetary Science Supplement, 74, 5101

Spurny, P., Borovicka, J., Haloda, J., Shrbeny, L., & Heinlein, D. 2016, in LPI Contributions, Vol. 1921, 79th Annual Meeting of the Meteoritical Society, 6221

Spurný, P., Borovička, J., Baumgarten, G., et al. 2017a, Planetary and Space Science, 143, 192

Spurný, P., Borovička, J., Kac, J., et al. 2010, Meteoritics & Planetary Science, 45, 1392

Spurný, P., Borovička, J., Mucke, H., & Svoreň, J. 2017b, Astronomy & Astrophysics, 605, A68

Spurný, P., Haloda, J., Borovička, J., Shrbený, L., & Halodová, P. 2014, Astronomy & Astrophysics, 570, A39

Spurný, P., Oberst, J., & Heinlein, D. 2003, Nature, 423, 151

Steel, D. I., Asher, D. J., & Clube, S. V. M. 1991, Monthly Notices of the Royal Astronomical Society, 251, 632

Steyaert, C. 1990, Photographic astrometry (Belgium: International Meteor Organization)

Stulov, V. P. 1997, Applied Mechanics Reviews, 50, 671

—. 1998, Planetary and Space Science, 46, 253

—. 2004, Planetary and Space Science, 52, 459

Stulov, V. P., Mirskii, A. N., & Vislyi, A. I. 1995, Aerodinamika bolidov (Aerodynamics of Bolides) (Moscow: Nauka)

Sutherland, W. 1893, Philosophical Magazine, 36, 507

Tancredi, G., Ishitsuka, J., Schultz, P. H., et al. 2009, Meteoritics & Planetary Science, 44, 1967

Tapia, M., & Trigo-Rodríguez, J. M. 2017, in Assessment and Mitigation of Asteroid Impact Hazards: Proceedings of the 2015 Barcelona Asteroid Day, ed. J. M. Trigo-Rodríguez, M. Gritsevich, & H. Palme, Vol. 46 (Springer International Publishing Switzerland), 199

Tauzin, B., Debayle, E., Quantin, C., & Coltice, N. 2013, Geophysical Research Letters, 40, 3522

Taylor, G. 1950, Proceedings of the Royal Society of London Series A, 201, 175

Tóth, J., Vereš, P., & Kornoš, L. 2011, Monthly Notices of the Royal Astronomical Society, 415, 1527

Tóth, J., Kornoš, L., Zigo, P., et al. 2015, Planetary and Space Science, 118, 102

Trigo-Rodríguez, J. M. 2000, Astronomy & Astrophysics, 355, 1160

Trigo-Rodriguez, J. M. 2002, PhD thesis, Universitat de Valencia

Trigo-Rodríguez, J. M. 2012, Meteoritos (Madrid, Spain: Editorial Catarata-CSIC, colección ¿Qué sabemos de?, Consejo Superior de Investigaciones Científicas)

Trigo-Rodríguez, J. M., Betlem, H., & Lyytinen, E. 2005, The Astrophysical Journal, 621, 1146

Trigo-Rodríguez, J. M., & Blum, J. 2009a, Planetary and Space Science, 57, 243

—. 2009b, Publications of the Astronomical Society of Australia, 26, 289

Trigo-Rodríguez, J. M., Borovička, J., Llorca, J., et al. 2009a, Meteoritics & Planetary Science, 44, 175

Trigo-Rodríguez, J. M., Borovička, J., Spurný, P., et al. 2006, Meteoritics & Planetary Science, 41, 505

Trigo-Rodríguez, J. M., García-Hernández, D. A., Sánchez, A., et al. 2010, Monthly Notices of the Royal Astronomical Society, 409, 1682

Trigo-Rodríguez, J. M., & Llorca, J. 2006, Monthly Notices of the Royal Astronomical Society, 372, 655

—. 2007, Monthly Notices of the Royal Astronomical Society, 375, 415

Trigo-Rodríguez, J. M., Llorca, J., Borovicka, J., & Fabregat, J. 2003, Meteoritics & Planetary Science, 38, 1283

Trigo-Rodríguez, J. M., Llorca, J., Borovička, J., & Fabregat, J. 2004a, Earth Moon and Planets, 95, 375

Trigo-Rodríguez, J. M., Llorca, J., Lyytinen, E., et al. 2004b, Icarus, 171, 219

Trigo-Rodriguez, J. M., Madiedo, J. M., Gural, P. S., et al. 2008, Earth Moon and Planets, 102, 231

Trigo-Rodríguez, J. M., Madiedo, J. M., Williams, I. P., & Castro-Tirado, A. J. 2009b, Monthly Notices of the Royal Astronomical Society, 392, 367

Trigo-Rodríguez, J. M., Madiedo, J. M., Williams, I. P., et al. 2009c, Monthly Notices of the Royal Astronomical Society, 394, 569

Trigo-Rodríguez, J. M., & Williams, I. P. 2017, in Assessment and Mitigation of Asteroid Impact Hazards: Proceedings of the 2015 Barcelona Asteroid Day, ed. J. M. Trigo-Rodríguez, M. Gritsevich, & H. Palme, Vol. 46 (Springer International Publishing Switzerland), 11

Trigo-Rodríguez, J. M., Castro-Tirado, A. J., Llorca, J., et al. 2004c, Earth Moon and Planets, 95, 553

Trigo-Rodríguez, J. M., Lyytinen, E., Jones, D. C., et al. 2007, Monthly Notices of the Royal Astronomical Society, 382, 1933

Trigo-Rodríguez, J. M., Madiedo, J. M., Williams, I. P., et al. 2013, Monthly Notices of the Royal Astronomical Society, 433, 560

Trigo-Rodríguez, J. M., Moyano-Cambero, C. E., Llorca, J., et al. 2014, Monthly Notices of the Royal Astronomical Society, 437, 227

Trigo-Rodríguez, J. M., Lyytinen, E., Gritsevich, M., et al. 2015, Monthly Notices of the Royal Astronomical Society, 449, 2119

Tsien, H. S. 1946, Aerospace Research Central Journal, 13, 653

Tubiana, C., Snodgrass, C., Michelsen, R., et al. 2015, Astronomy & Astrophysics, 584, A97

Šimek, M., & Pecina, P. 2002, Earth Moon and Planets, 88, 115

Van Schmus, W. R., & Wood, J. A. 1967, Geochimica et Cosmochimica Acta, 31, 747

Vasilyev, N. V. 1998, Planetary and Space Science, 46, 129

Vaubaillon, J. 2002, in Proceedings of the International Meteor Conference, 20th IMC, Cerkno, Slovenia, 2001, ed. M. Triglav, A. Knöfel, & C. Trayner, 76–81

Vaubaillon, J. 2003, PhD thesis, l'Observatoire de Paris

Vaubaillon, J., Colas, F., & Jorda, L. 2005a, Astronomy & Astrophysics, 439, 751

—. 2005b, Astronomy & Astrophysics, 439, 761

Vaubaillon, J., Koten, P., Margonis, A., et al. 2015, Earth Moon and Planets, 114, 137

Vinković, D. 2007, Advances in Space Research, 39, 574

Vinnikov, V. V., Gritsevich, M. I., & Turchak, L. I. 2016, in American Institute of Physics Conference Series, Vol. 1773, American Institute of Physics Conference Series, 110016

Weisberg, M. K., McCoy, T. J., & Krot, A. N. 2006, in Meteorites and the Early Solar System II, ed. D. S. Lauretta & H. Y. McSween (University of Arizona Press, Tucson), 19–52

Wetherill, G. W., & Revelle, D. O. 1981, Icarus, 48, 308

Whipple, F. L. 1938, in Proceedings of the American Philosophical Society, Vol. 79, 499–548

Whipple, F. L., & Jacchie, L. G. 1957, Smithsonian Contributions to Astrophysics, 1, 183

Wiegert, P., Vaubaillon, J., & Campbell-Brown, M. 2009, Icarus, 201, 295

Wilkison, S. L., & Robinson, M. S. 2000, Meteoritics & Planetary Science, 35, 1203

Williams, I. P. 1993, in Meteoroids and their Parent Bodies, ed. J. Stohl & I. P. Williams, 31

Williams, I. P. 1997, Monthly Notices of the Royal Astronomical Society, 292, L37

—. 2001, Celestial Mechanics and Dynamical Astronomy, 81, 103

Williams, I. P. 2002, in Meteors in the Earth's Atmosphere, ed. E. Murad & I. P. Williams (Cambridge, UK: Cambridge University Press), 332

—. 2004, WGN Journal, International Meteor Organization, 32, 11

Williams, I. P., Johnson, C., & Fox, K. 1986, in Asteroids, Comets, Meteors II, ed. C.-I. Lagerkvist, H. Rickman, B. A. Lindblad, & H. Lundstedt, 559–563

Williams, I. P., & Wu, Z. 1993, Monthly Notices of the Royal Astronomical Society, 262, 231

Ye, Q., Brown, P. G., Campbell-Brown, M. D., & Weryk, R. J. 2013, Monthly Notices of the Royal Astronomical Society, 436, 675

Yomogida, K., & Matsui, T. 1983, Journal of Geophysical Research, 88, 9513

Yoshida, M., Omoto, K., Naruse, R., & Ageta, Y. 1971, Antarctic Record, 39, 62

Zhdan, I. A., Stulov, V. P., Stulov, P. V., & Turchak, L. I. 2007, Solar System Research, 41, 505

Öpik, E. J. 1933, Acta et Commentationes Universitatis Tartuensis, 33, 1

—. 1958, Physics of Meteor Flight in the Atmosphere (New York: Interscience), 1–179